RUPRECHT-KARLS-UNIVERSITÄT HEIDELBERG

Klaus Urban

Measurement of Inclusive and DiJet $D^{\star}$-Meson Photoproduction at the H1 Experiment at HERA

Dissertation

HD-KIP-09-13

KIRCHHOFF-INSTITUT FÜR PHYSIK

INAUGURAL - DISSERTATION

zur

Erlangung der Doktorwürde

der

Naturwissenschaftlich - Mathematischen

Gesamtfakultät

der Ruprecht - Karls - Universität

Heidelberg

vorgelegt von

Dipl.-Phys. Klaus Urban

aus Dortmund (Nordrhein - Westfalen)

Tag der mündlichen Prüfung: 28. Januar 2009

Measurement of Inclusive and DiJet $D^{\star}$-Meson Photoproduction at the H1 Experiment at HERA

Gutachter: Prof. Dr. Hans-Christian Schultz-Coulon
Prof. Dr. Ulrich Uwer

Kurzfassung

In der vorliegenden Arbeit wird der Produktionsmechanismus von Charm-Quarks in Elektron-Proton-Streuungen am Speicherring HERA untersucht. Der analysierte Datansatz entspricht Luminositäten von 30.68 pb^{-1}, 68.23 pb^{-1} und 93.39 pb^{-1}. Der Nachweis von Ereignissen mit Charm-Quarks erfolgt durch die Rekonstruktion von $D^\star$-Mesonen im kinematischen Bereich der Photoproduktion. $D^\star$-Mesonen werden erstmals mit Hilfe der dritten Stufe des Fast-Track-Triggers des H1-Experiments selektiert. Hierdurch konnte der Phasenraum im Vergleich zur vorangegangenen Messung entscheidend erweitert und die Statistik um einen Faktor acht erhöht werden. Der untersuchte kinematische Bereich erstreckt sich über eine Photonvirtualität von $Q^2 < 2$ GeV^2 und eine Schwerpunktsenergie des Photon-Proton-Systems von $100 < W_{\gamma p} < 285$ GeV. $D^\star$-Mesonen werden mit einem minimalen transversalen Impuls von 1.8 GeV im Bereich der Pseudorapidität $|\eta| < 1.5$ untersucht. Die Messung in Photoproduktion und kleinen $p_t(D^\star)$ liegt an der Grenze zur Gültigkeit der pertubativen QCD und ist daher von besonderem Interesse.

In einer weiterführenden Messung werden, basierend auf den Ereignissen mit $D^\star$ Mesonen, mindestens zwei Jets selektiert. Es werden Jets mit $p_t > 4$ GeV bzw. $p_t > 3$ GeV im Bereich der Pseudorapidität $|\eta| < 1.5$ untersucht. Hierbei wird verlangt, dass einer der selektierten Jets mit dem $D^\star$-Meson assoziiert ist. Die Rekonstruktion von zwei harten Partonen ermöglicht einen tieferen Einblick in den Produktionsmechanismus der Charm-Quarks. Diese Messung zeigt, dass Prozesse mit aufgelösten Photonen im untersuchten Phasenraum eine entscheidene Rolle bei der Photoproduktion von Charm-Quarks spielen. Einfach- und doppeltdifferentielle Wirkungsquerschnitte beider Ereignismengen werden mit Vorhersagen der pertubativer QCD in führender und nächsthöherer Ordnung verglichen.

Abstract

In the present analysis the production mechanism of charm quarks in electron proton scattering at the HERA collider is investigated using 30.68 pb^{-1}, 68.23 pb^{-1} and 93.39 pb^{-1} of data collected with the H1 experiment. Events containing charm quarks are detected by the reconstruction of $D^\star$ mesons in the kinematic domain of photoproduction. For the first time $D^\star$ mesons are selected on the basis of the third level of the H1 Fast Track Trigger. Compared to the previous analysis the phase space studied was extended significantly and the data statistics increased by a factor of eight. The investigated kinematic region covers photons of virtuality of $Q^2 < 2$ GeV^2 and photon-proton center-of-mass energies in the range of $100 < W_{\gamma p} < 285$ GeV. $D^\star$ mesons are measured with transverse momenta of at least 1.8 GeV and pseudorapidities $|\eta| < 1.5$. The measurement in photoproduction and low $p_t(D^\star)$ is of particular interest since it allows the test of different theoretical models at the limit of applicability of pertubative QCD.

In a further measurement, which is based on the events with $D^\star$ mesons, at least two jets are selected. Jets with $p_t > 4$ GeV and $p_t > 3$ GeV, are studied in the pseudorapidity range of $|\eta| < 1.5$, where one of the selected jets is associated with the $D^\star$ meson. The investigation of two hard partons, by means of the jets, results in an improved understanding of the pr oduction mechanism of charm quarks. This measurement demonstrates that resolved photon processes play an important role in the photoproduction of charm quarks. Single and double differential cross sections of both event samples are compared to predictions of pertubat ive QCD in leading and next to leading order.

Contents

Chapter 1

Introduction

The Standard Model comprises the current knowledge of particle physics. It describes the interaction between the elementary particles very successfully within field theories by emission and absorption of gauge bosons. The field theory describing the interaction between quarks is the Quantum Chromodynamic (QCD). The force is mediated by gluons g which carry color charge and are in contrast to the mediator of electromagnetic force selfinteracting. This leads to a characteristic of QCD theory given by a rising coupling constant α_s with increasing distances of the quarks. Since calculations are performed in power series of α_s (perturbative QCD), the predictive power is restricted to regimes of low distances (large scales μ) where α_s is small and the quarks can be treated as quasi free (asymptotic freedom) [Gro73, Pol73]. Towards large distances, α_s rises and a process referred to as confinement takes place. The rules of confinement prohibit to observe free quarks in nature, quarks are always found in colorless compounds (hadrons) of two or three, respectively. The measurement of hadrons or bunches of hadrons (jets) produced in high energy particle collision experiments allows to test the QCD theory.

The H1 experiment located at the collider HERA provides ideal conditions to test pQCD. At H1 electrons and protons are collided at a center of mass energy of $\sqrt{s} = 318$ GeV. The kinematic regime of photoproduction, studied in this thesis, is characterized by electrons scattered under low angles (low virtualities) such that they escape the H1 detector volume undetected. The large scale usually given by the high virtuality of the exchanged photon can not be the appropriate choice in the photoproduction regime. Perturbative calculations are possible in processes in which heavy quarks are produced. Here the mass of the quarks provides the hard scale necessary to perform pQCD. The dominant production mechanism for heavy quarks at HERA is the Boson Gluon Fusion (BGF). In this process a heavy quark pair is produced in the interaction of a virtual photon with a gluon emitted by the proton. In addition to the BGF, processes in which the partonic structure of the photon is resolved, have to be considered as well.

In the present analysis charged $D^\star$ mesons are used to tag events containing charm quarks in the kinematic regime of photoproduction. In particular $D^\star$ mesons are analyzed which have decayed in the Golden Decay Channel: $D^{\star\pm} \to D^0\pi^\pm_{slow} \to K^\mp\pi^\pm\pi^\pm_{slow}$. The characteristic feature of this decay mode is the low mass difference between the D^0 and the $D^\star$ meson, which results in a small momentum of the pion (π_{slow}) emerged from the $D^\star$ decay. The invariant mass difference between the three and two body decay $\Delta M = M(K\pi\pi_{slow}) - M(K\pi)$ is used to determine the number of $D^\star$ mesons. With the new level three system of the Fast Track Trigger (FTT), which has been used in this analysis, it is for the first time possible to select events containing $D^\star$ mesons during the data taking procedure.

On the one hand the measurement of $D^\star$ mesons with low transverse momentum in photoproduction is of particular interest since it allows to test pQCD at its limit of applicability, on the other hand unfortunately the tag of only one hard parton produced in the interaction is insufficient to derive a complete picture of the production mechanism. A more detailed

picture is obtained in further measurement in which in addition to the $D^\star$ meson two jets are selected.

The aim of the analysis presented in this thesis is to improve the knowledge of charm photoproduction. Previous measurements by the H1 [Adl99, Akt07] and ZEUS collaboration [Bre99, Che03] proved that the charm photoproduction is reasonably described by QCD theory. The presented measurement supports these findings. However, the accuracy of the previous measurements were restricted by limited statistics and phase space. The investigation of $D^\star$ mesons in an extended phase space and on the basis of a significantly larger statistics gives new insights and shows that $D^\star$ meson photoproduction is not fully understood.

This thesis is structured as follows: In the second chapter an overview of the theoretical aspects of the QCD theory is given. The emphasis is placed on the $D^\star$ meson production in photoproduction. Subsequently, an introduction of the HERA collider and the detector components of the H1 experiment relevant for this analysis are presented. In the fourth chapter the discussion focuses on the reconstruction method of $D^\star$ mesons followed by the event selections and analysis strategy in the fifth chapter. Chapter six is devoted to the preparation of the cross section measurement. This chapter includes comparisons of Monte Carlo and data and detector effect corrections. The systematic uncertainties are discussed in chapter seven. In chapter eight the results of the cross section measurement in the inclusive sample are presented. Chapter nine is dedicated to the DiJet cross section measurement. In chapter 10 the results of the cross section measurement of the DiJet sample are presented. The thesis closes with a summary and conclusion in chapter eleven.

Chapter 2

Theoretical Overview

This chapter gives a general overview on the theoretical aspects of $D^\star$ meson production in photoproduction at the HERA collider. Beginning with the basic properties of electron-proton (ep) scattering and an introduction to the relevant kinematic quantities, the fundamental principles of Quantum Chromodynamics (QCD) are briefly summarized. The discussion then focuses on the heavy quark production in the kinematic region of photoproduction. The transition from the heavy quark to the $D^\star$ meson is described afterwards. The chapter closes with an overview over the theoretical models used in the context of this analysis.

2.1 Electron Proton Scattering

Electron proton scattering $ep \to lX$ is mediated via the exchange of a virtual photon a Z or W boson, respectiveley. Depending on the charge of the exchanged boson, the process is divided into neutral (NC) $ep \to e'X$ or charged currents (CC) $ep \to \nu_e X$. Figure 2.1 shows the corresponding Feynman diagrams. The incoming electron, with momentum $\boldsymbol{k}$, interacts via the exchange of a virtual boson with the incoming proton, with momentum $\boldsymbol{P}$. The transfered momentum is given by the variable $\boldsymbol{q}$. The momentum of the outgoing lepton is denoted with $\boldsymbol{k}$'.

The processes shown in figure 2.1 are described by four Lorentz invariant variables s, Q^2, x and y. These variables are defined as follows:

$$s = (\boldsymbol{P} + \boldsymbol{k})^2 \tag{2.1}$$

$$Q^2 = -\boldsymbol{q}^2 = -(\boldsymbol{k} - \boldsymbol{k}')^2 \tag{2.2}$$

$$y = \frac{\boldsymbol{P} \cdot \boldsymbol{q}}{\boldsymbol{P} \cdot \boldsymbol{k}} \tag{2.3}$$

$$x = \frac{Q^2}{2\boldsymbol{P} \cdot \boldsymbol{q}} \tag{2.4}$$

The inelasticity y corresponds to the relative energy loss of the electron in the proton rest frame; the Bjorken scaling variable x represents the four momentum fraction of the proton carried by the struck parton; both quantities are defined in the range $(0 < y < 1)$ and $(0 < x < 1)$, respectively. The above quantities are related via

$$Q^2 = sxy. \tag{2.5}$$

For fixed beam energies and neglecting the particle masses [1] the squared center-of-mass energy s is given by

$$s \simeq 4E_e E_p. \tag{2.6}$$

[1] Equation 2.6 does not hold for fixed target experiments

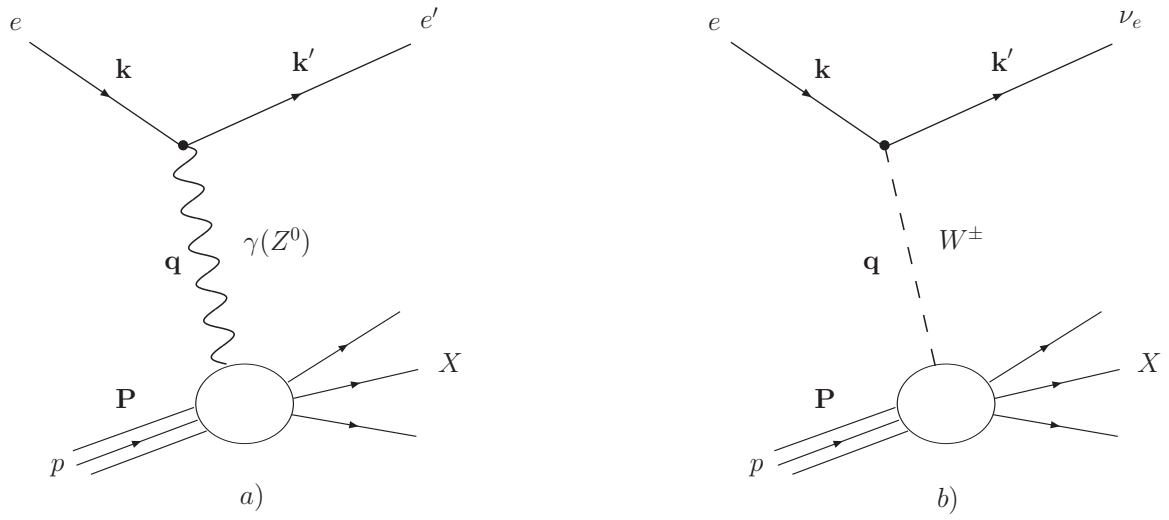

Figure 2.1: *Feynman diagrams of lowest order for electron proton scattering. On the left (a) the neutral current process and on the right (b) the charged current process is shown.*

E_e denotes the electron beam energy and E_p the proton beam energy. According to equation 2.5 the kinematics of deep inelastic scattering is determined by two Lorentz invariant quantities. The cross section σ of the ep scattering is described by $\sigma \sim \mathcal{L}_{\alpha\beta}\mathcal{W}^{\alpha\beta}$. The electromagnetic part is given by the lepton tensor $\mathcal{L}_{\alpha\beta}$ which is precisely calculable in the framework of QED. The hadronic part is given by the QCD theory and includes the photon proton interaction. Since it is not possible to calculate the hadronic tensor from first principles, it is expressed in terms of proton structure functions. Under the assumption of Lorentz invariance, current conservation at the hadronic vertex [2] and parity conservation the differential cross section is given by two independent structure functions F_2 and F_L:

$$\frac{d^2\sigma}{dxdQ^2} = \frac{2\pi\alpha^2}{Q^4 x} Y_+ [F_2(x,Q^2) - \frac{y^2}{Y_+} F_L(x,Q^2)] \quad \text{with} \quad Y_+ = 1 + (1-y)^2. \tag{2.7}$$

F_2 and F_L are related to the γp cross sections of longitudinal and transverse polarized virtual photons. The structure function F_2 includes contributions of both, longitudinally and transversely polarized photons, whereas F_L solely includes contributions of longitudinal polarized photons. According to equation 2.7, sizeable effects of F_L are only expected at large inelasticities y. A recent measurement of F_L by the H1 collaboration is given in [Aar08].

2.2 Quantum Chromodynamics

This section deals with the principles of Quantum Chromodynamics (QCD). In the framework of QCD theory, interactions between quarks are described by emission and absorption of gluons. Gluons are massless spin one particles which carry no electrical charge but an additional quantum number, referred to as the color charge. One of the main differences compared to the QED theory is that the gluons are unlike the photons selfinteracting.

In QED vacuum polarisations $\gamma \rightarrow e^+e^-$ lead to a screening effect of the probed charge. This effect can be understood as a shielding of the bare charge by a charged cloud induced

[2] $q_\alpha \mathcal{W}^{\alpha\beta} = q_\beta \mathcal{W}^{\alpha\beta} = 0$

Figure 2.2: *Loops in Quantum Chromodynamics. On the left: fermion loop. On the right: gluon loop.*

by the vacuum polarizations. More and more of the charge becomes visible by probing it with higher energies (lower scales), leading to a rising coupling constant α_{em} with the scale. However, due to the gluon self-coupling, in QCD the opposite effect is observed. Towards higher energies, processes like $g \rightarrow gg$ start to dominate and lead to an anti-screening and decrease of α_s with the scale. This leads to a characteristic of QCD theory, which is given by the fact that at small scales (large distances), where α_s becomes large, the partons are bound together into colourless states (confinement), whereas at high scales (short distances) and low α_s, the partons can be treated as quasi-free particles [Gro73, Pol73] (asymptotic freedom).

Similar to QED, in QCD ultra violet divergencies occur, which are related to infinite momenta in loop diagrams, as displayed in figure 2.2. A renormalization of the theory is nessescary and performed by the introduction of an arbitrary renormalization scale μ_r, which absorbs the divergencies into the running of α_s. The requirement that any physical observable should not depend on the arbitrary scale μ_r leads to the renormalization equation for $\alpha_s(\mu_r^2)$. In the leading logarithmic approximation the strong coupling is given by:

$$\alpha_s(\mu_r^2) = \frac{12\pi}{(33 - 2n_f)\ln(\frac{\mu_r^2}{\Lambda_{QCD}^2})} \tag{2.8}$$

The variable n_f denotes the number of active flavors present in the proton and the parameter Λ_{QCD} represents the scale where α_s becomes large. It has been experimentally determined to $\Lambda_{QCD} \approx 200$ MeV. In pratice, μ_r is chosen close to the physical scales characterizing the process under study. In inclusive ep scattering μ_r is set to Q^2, which is usually the only choice in this case. In QCD calculations are performed in power series of α_s (perturbative QCD). The predictive power of QCD is therefore restricted to the regime of asymptotic freedom, where α_s is small and the power series of α_s converges.

At low scales α_s is large and the perturbative series diverges. This part can be absorbed in non-perturbative functions that have to be determined experimentally. The cross section is factorized into a long distance and a short distance part, as expressed by the factorization theorem [Bar78]. This introduces a new scale, the factorization scale μ_f, separating the two regimes. Particles with virtualities larger than μ_f^2 are taken into account in the perturbative calculation of the short distance part, while the emmision of of particles with lower virtualities is treated in the non-perturbative function.

Applying the factorization theorem, the structure function F_2 can be written as a convolution of pertubatively calculable coefficient functions C^i and parton density functions (PDF) f_i^p summing over all partons i in the proton p. The structure function F_2 can be expressed by [Bro94]:

$$F_2(x, Q^2) = \sum_i \int_0^1 dz\, C^i\left(\frac{x}{z}, \frac{Q^2}{\mu_r^2}, \frac{\mu_f}{\mu_r}, \alpha_s(\mu_r^2)\right) f_i^p(z, \mu_f^2, \mu_r^2). \tag{2.9}$$

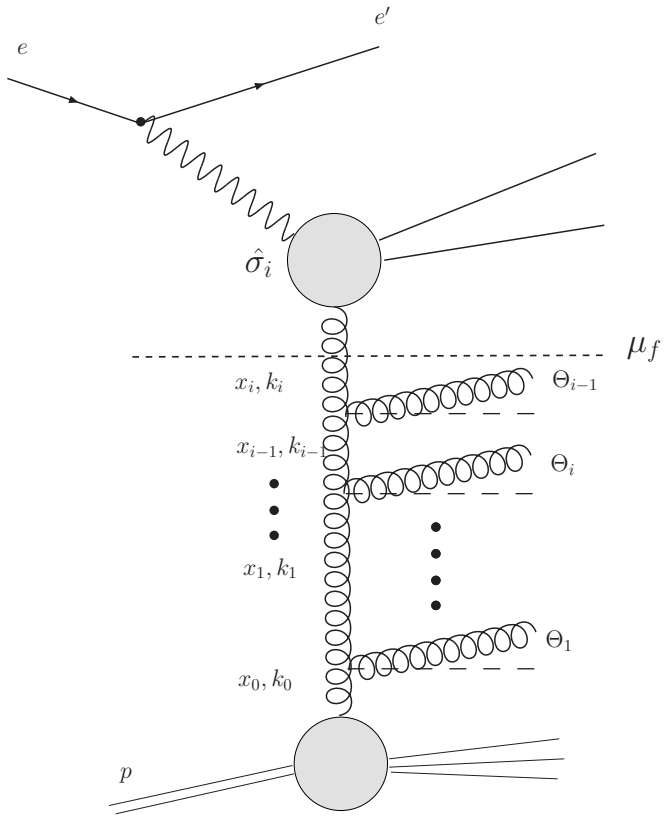

Figure 2.3: *Illustration of the factorization approach which separates the hard matrix element $\hat{\sigma}_i$ from the parton evolution at the cut of scale μ_f. The variable x_i denotes the longitudinal momenta, k_i the transverse momenta and θ_i the emission angle.*

The PDFs $f_i^p(z, \mu_f^2, \mu_r)$ represent the probability of finding a parton i carrying a fraction z of the proton momentum. But now, they additionally depend on the scales. The short distance parts are represented in the coefficient function C^i which include the interaction between the exchanged boson and the parton of the proton. Several approaches exist to separate the long distance and short distance parts. The most commonly applied are the deep inelastic scattering scheme DIS [Alt79] and the modified minimal substraction scheme $\overline{\text{MS}}$ [Bar78]. In inclusive ep scattering the usual choice for the factorisation scale is $\mu_f^2 = Q^2$.

Based on equation 2.9 it is in principle possible to extract the parton density functions at a certain scale μ by measurements of the structure function F_2. In practice the PDFs are obtained by fitting the structure functions to the data at a given starting scale μ. With so-called evolution equations it is possible to predict the PDFs measured at a certain μ to a different scale as long as α_s is reasonably small and reliable pQCD calculations are possible. Various approaches exist, which will be introduced in the following.

Evolution Schemes

Evolution equations form the link between the measured PDFs at a certain scale μ to the hard matrix element at any other scale μ'. The existing evolution schemes consider possible processes like gluon radiation and splitting of gluons into quark or gluon pairs, respectively. Since such radiations can occur several times, this circumstance is summarized in a so called parton ladder. Within the evolution scheme an integration over all radiated partons is

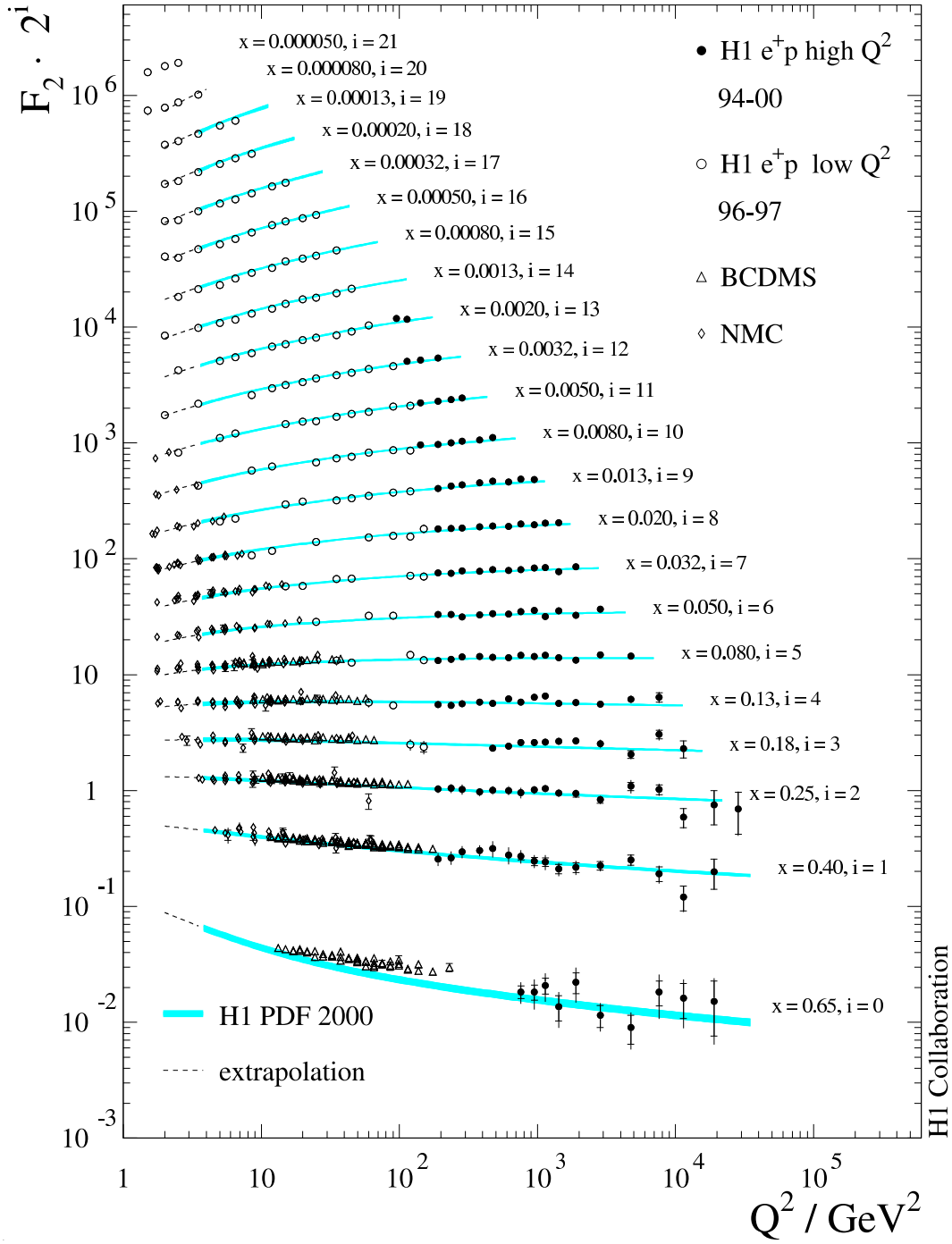

Figure 2.4: *Summary of measurements of the proton structure function F_2 as a function of x and Q^2 [Adl03] by the H1 and ZEUS collaboration and fixed target experiments. The results are compared with the Standard Model expectations based on the DGLAP approach (error bands).*

performed. In figure 2.3 an illustration of the parton ladder and the factorization ansatz is given.

DGLAP: The DGLAP (Dokshitzer-Gribov-Lipatov-Altarelli-Paresi) approach [Dok77, Gri72, Lip75, Alt77] is based in first order of α_s on four splitting functions $P_{ij}(z)$ which give the probability for a parton i to emit a parton j with the momentum fraction z of the parent parton. Within the DGLAP approach the longitudinal momenta x_i of the radiated gluons are strongly k_t ordered. Furthermore it is assumed that the momenta x_i are large compared to the transverse momenta $k_{t,i}$. The k_t dependence is integrated out within the summation over all radiated partons. This approach is also referred to as the collinear evolution scheme, since the k_t is small in comparison to the scale μ. It is expected that the DGLAP approach breaks down at very low x.

CCFM: Within the CCFM (Ciafolani, Catani, Fiorani, Marchesini) approach [Cat90a, Cia88, Cat90b, Mar95], the radiated partons are ordered on the basis of the emission angles $\theta_i > \theta_{i-1}$. In the approximation used here only gluons are considered. For radiations under small angles and not too small x the momentum fraction $z_i = x_i/x_{i-1}$ is close to one and the ordering of the gluon ladder is similar to the DGLAP approach. For low values of x a much faster rise of the parton density distribution is predicted by the CCFM approach compared to the DGLAP approach. The CCFM approach is based on a k_t unintegrated parton density distribution $\mathcal{A}(x_g, k_t^2, \mu_f^2)$ which describes the probability of finding a parton carrying the longitudinal momentum fraction x_g and transverse momentum k_t at the factorization scale μ_f.

The DGLAP approach covers most of the phase space accessible by *ep* scattering experiments at HERA and has been successfully tested down to values of $x \simeq 1 \cdot 10^{-4}$ by measurements of the proton structure function F_2 [Adl03, Che04] (see figure 2.4). At lower values of x the DGLAP formalism is expected to break down. In this regime a third approach, the BFKL [Kur77, Bal78] formalism describing an evolution in x at fixed Q^2 is expected to work. The CCFM approach interpolates between DGLAP and BFKL. Hints for a better agreement of the HERA data with the CCFM approach than with predictions based on DGLAP have been found so far in forward jet production [Adl97]. In heavy quark production relatively low values of x are reached in certain regions of phase space, thus a comparison of the heavy quark production with QCD models incorporating both approaches might resolve some open questions.

2.3 Photoproduction of Heavy Quarks at HERA

The following discussion concentrates on the heavy quark production mechanism at HERA in the kinematic regime of photoproduction. In general a quark is denoted as a heavy quark if the quark mass exceeds the Λ_{QCD} parameter such that the mass can be used as a hard scale. Heavy quarks are the charm, beauty and top quark. At HERA only the charm and the beauty quarks are denoted as heavy quarks since the energy necessary to produce the top quark is far beyond the energy provided by the HERA collider.

Photoproduction

Two kinematic regions are defined at the HERA collider which are referred to as the kinematic regimes of photoproduction and Deep Inelastic Scattering (DIS). Experimentally the

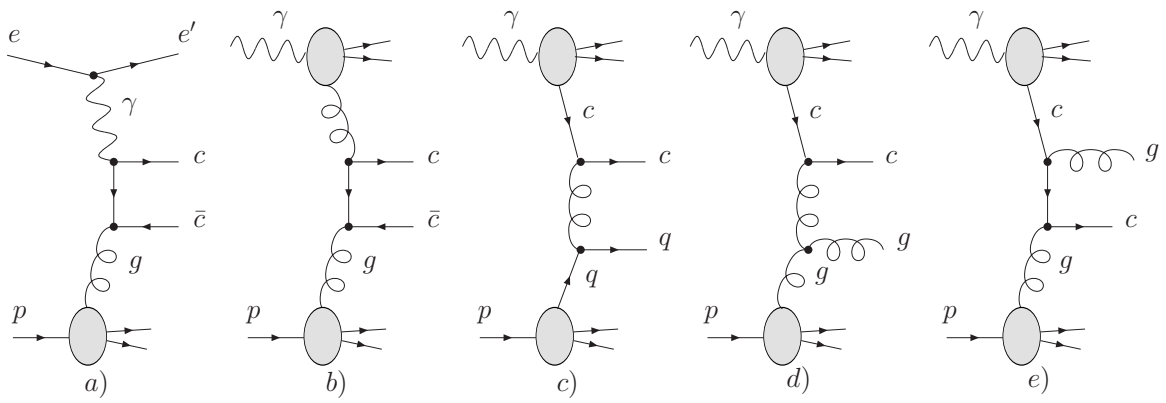

Figure 2.5: *The production processes for heavy quarks relevant for this analysis. The BGF process is shown a), the resolved processes are depicted in b)-e). Process b) is referred to as hadron like and c)-e) show the charm excitation processes.*

regimes are defined by a tag of the scattered electron in DIS $2 < Q^2 < 1000$ GeV^2 and the anti-tag in photoproduction $0 < Q^2 < 2$ GeV^2, respectively. The definition of the Q^2 ranges are given by the acceptance of the H1 detector. In photoproduction the electron is scattered at such low angles that it escapes the detector volume undetected.

Apparently, the photoproduction regime dominates the production since the cross section rises with $1/Q^4$ (see equation 2.7). The characteristic feature of the photoproduction regime is the exchange of almost real photons. The *ep* scattering can be simplified by separating the emission of quasi real photons from the electron from the subsequent interaction of the photon with the proton. The flux of photons $f_\gamma(y, Q^2_{max})$ can be calculated in the framework of QED and is given as a function of the inelasticity y by the Weizsäcker Williams approximation [vW34, Wil34]. An important observable in photoproduction is the center-of-mass energy of the photon-proton system $W_{\gamma p}$ which is defined as

$$W^2_{\gamma p} = (q + P)^2 = y \cdot s - Q^2 \simeq y \cdot s. \tag{2.10}$$

Here P denotes the four momentum of the incoming proton and q the four momentum of the photon. In photoproduction and at high center-of-mass energies s the contribution of Q^2 is negligible.

Heavy Quarks

A very early measurement at the H1 experiment [Adl96] showed that the dominant production mechanism for heavy quarks is the Boson Gluon Fusion (BGF) process. In this process a heavy quark pair is produced by the interaction of the virtual photon and a gluon emitted by the proton ($\gamma g \rightarrow c\bar{c}$), see figure 2.5 a). The cross section for beauty pair production in comparison to charm pair production is suppressed by two orders of magnitude due to the larger mass of the beauty quarks $m_{c\,(b)} \simeq 1.5\,(4.75)$ GeV and the smaller charge of the beauty quarks $|q_{c\,(b)}| = 2/3(1/3)$[3].

From the theoretical point of view the photoproduction regime is one of the biggest challenges of pQCD. The hard scale given by Q^2 in the DIS case can not be the appropriate

[3]In the following only the charm and anticharm quarks are considered since the contribution of beauty quarks is negligible in the scope of this analysis

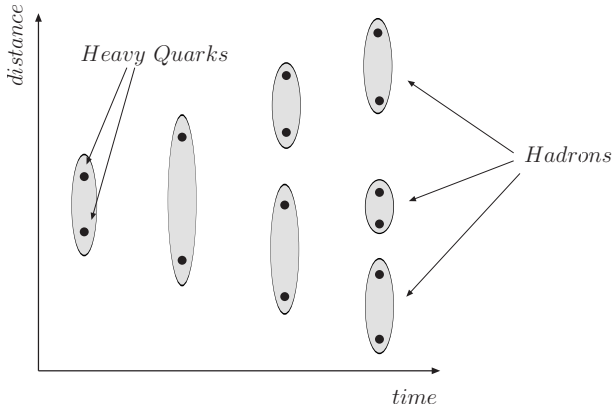

Figure 2.6: *Illustration of break up of color strings according the Lund String model.*

choice in the photoproduction regime. In processes in which heavy quarks are produced, the scale is usually given by a combination of the transverse momentum and the mass of the heavy quarks $m_t^2 = m_c^2 + (p_{t,c}^2 + p_{t,\bar{c}}^2)/2$. In the leading order (LO) picture it has to be considered that the exchanged photon becomes quasi real and processes, in which the partonic structure of the photon is resolved, lead to relevant contributions to the cross section. Indications for the need of resolved components in the charm production mechanism have been found in [Che03]. Figure 2.5 shows a summary of the processes relevant for this analysis. The processes labeled with a) represents the already discussed BGF process. In b)-e) the resolved photon processes are depicted. Process b) is referred to as the hadron like and c)-e) are the charm excitation processes. A gluon or a charm quark enters the hard interaction from the photon side in the hadron like or charm excitation processes, respectively. The characteristic feature of the BGF process is that the complete photon energy is transfered into the hard interaction, whereas in the resolved case only a fraction x_γ of the photon momentum carried by the gluon or charm quarks is transfered to the interaction. The above described separation into direct and resolved processes is not unique and holds only in the LO picture. In the next-to-leading order (NLO) picture the process $\gamma g \to c\bar{c}g$ for instance leads to the same final state as the charm excitation processes displayed in figure 2.5 d) and e).

2.4 Fragmentation

Due to the rules of colour confinement single quarks can not be observed in nature. The transition from colored quarks to colorless hadrons is described by the fragmentation. The process of fragmentation was first measured at e^+e^- collider experiments and then applied under the assumption of universality to ep scattering experiments.

The fragmentation procedure is divided into three parts which are described by pQCD, phenomenological models and a non perturbative part. In the first step soft QCD radiation, referred to as parton showers (PS), are applied to the quarks. This process can be calculated in the framework of pQCD. The technique used here is based on similar evolution equations as given by the DGLAP approach. Several phenomenological models exist to describe the transition from the quark to a hadron. These are in particular the independent fragmentation [Fie78], the Lund String [And83] and the cluster model [Mar88]. Since the Lund String model is the most commonly used, a short description will be given on the basis of the BGF process. In the leading order picture, the quarks produced in the BGF process are expected to be back-to-back, in the center-of-mass frame of the $g\gamma$ system. Thus it is not very likely that they form a bound $c\bar{c}$ state. The Lund String model assumes a color field between the two

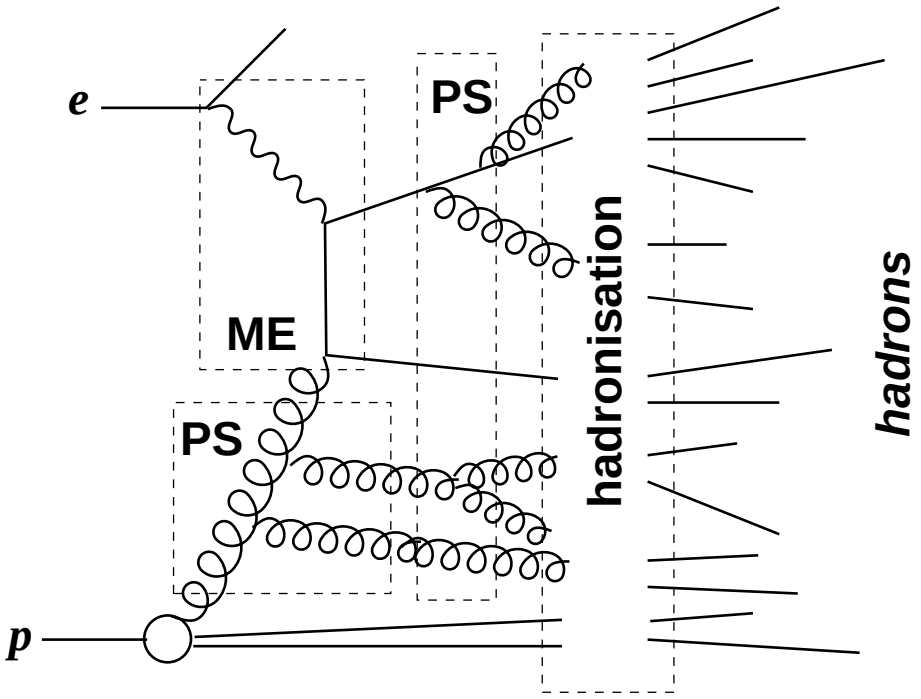

Figure 2.7: *Schematic overview of an event generator. Depicted is the hard matrix element (ME), initial and final state radiation are incorporated by parton showers (PS). The last step is the hadronisation.*

quarks, which is bounded in a so-called colour string. This string is elongated with increasing distance of the quarks and expressed by the QCD potential:

$$V = \frac{4\alpha_s}{3r} + \kappa r. \tag{2.11}$$

The colour confinement is given by the second term κr, which takes into account that the strong force arises with increasing distance. Accordingly the energy saved in the colour string arises with increasing distance of the quarks. The string breaks up, if the energy saved in the string becomes high enough two produce new $q\bar{q}$ pairs. The above described procedure is repeated with the newly produced $q\bar{q}$ pairs and goes on until the the energy is exhausted. The principle idea of the Lund String model is depicted in figure 2.6. The Lund String model describes the creation of particles in the hadronisation process, but makes no prediction about the energy transfer from the quarks to the hadrons.

The longitudinal momentum transfer z from the string to the hadron is given by different models Bowler [Bow81], Kartvelishvili [Kar78] or Peterson [Pet83]. A brief description of the Peterson model is given in the following.

The Peterson fragmentation is based on the assumption that the fragmentation solely depends on the longitudinal energy transfer from the initial heavy quark Q to the hadron $H = Q\bar{q}$. Thereby the light quark $\bar{q}$ is assumed to be produced in spontaneous $q\bar{q}$ production. The energy transfer between the initial and the final state can be expressed by the relation $\Delta E = E_H + E_q - E_Q$. Here E_H and E_q denotes the energies of the produced hadron H and the light quark q. The energy of the initial quark Q is given by E_Q. Based on this assumption the functional form of the Peterson fragmentation can be derived to:

$$D^{np}_{Q\to H} = \frac{N}{z(1 - \frac{1}{z} - \frac{\epsilon_Q}{(1-z)})^2} \tag{2.12}$$

	Pythia(massless)	*Pythia(massive)*	*Cascade*
Proton PDF	CTEQ6L LO	CTEQ6L LO	A0
Photon PDF	GRV LO	GRV LO	
Renorm. scale	m_t	m_t	m_t'
Factor. scale	m_t	m_t	$\sqrt{\hat{s}+Q_t^2}$
m_c [GeV]	1.5	1.5	1.5
Fragmentation	Bowler	Peterson $\epsilon_{pet} = 0.035$	Peterson $\epsilon_{pet} = 0.035$

Table 2.1: *Parameters used in the pQCD calculations where m_c denotes the charm quark mass. The "transverse mass" variables are defined as $m_t^2 = m_c^2 + (p_{t,c}^2 + p_{t,\bar{c}}^2)/2$ and $m_t'^2 = 4m_c^2 + p_{t,c}^2$. The squared invariant mass and the transverse momentum squared of the $c\bar{c}$ pair are denoted by $\hat{s}$ and Q_t^2, respectively. ϵ_{pet} is the Peterson fragmentation parameter.*

With the parameter N the probability distribution is normalized to one. The Peterson parameter ϵ_Q describes the scale for the "hardness" of the produced hadron, since it is related to the energy of the hadron. The Peterson parameter has to adjusted to the data. A recent measurement of charm fragmentation functions by the H1 collaboration is given in [H108] and by the ZEUS collaboration in [ZEU00]. In both measurements the fragmentation of charmed D mesons is investigated.

In the analysis presented in this thesis events with charm quarks are tagged using $D^{\star\pm}$ mesons. Charm quarks fragment with a probability of $\mathcal{P}(c \to D^{\star+}) = 23.5 \pm 0.5 \pm 0.5\%$ [Yao06] into charged $D^\star$ mesons. In the context of this analysis only $D^\star$ mesons decaying via the chain $D^{\star\pm} \to D^0\pi^\pm_{slow} \to K^\mp\pi^\pm\pi^\pm_{slow}$ are analyzed (inclusive sample). In a further measurement, based on the events of the inclusive sample, events are selected containing at least two jets. This sample forms the so-called DiJet sample. In first approximation a jet can be seen as a bunch of particles created in the hadronisation process. Relatively high transverse momentum of the jets ($p_t(Jet_{1,(2)}) > 4(3)$ GeV) are requirered and reliable pQCD calculations are possible. Summing up the theoretical aspects discussed so far the production cross section of $D^\star$ mesons can be written as a convolution of the proton structure, the photon structure, the hard matrix element and the fragmentation:

$$\sigma_{D^\star}(ep \to eX) = \sum_i f_i^p(\mu_f, \mu_r^2) \otimes \hat{\sigma}_i(\mu_f, \mu_r, \hat{s}) \otimes f_i^\gamma(\mu_f, \mu_r^2) \otimes D(z). \tag{2.13}$$

The proton structure is given by f^p, the photon structure f^γ, the hard matrix element by $\hat{\sigma}$ and the fragmentation is given by $D(z)$. The variable $\hat{s}$ corresponds to the center-of-mass energy of the hard partons produced in the hard interaction.

2.5 LO Event Generators

In high energy physics Monte Carlo techniques are widely used for theory predictions and detector simulation. The event generation is in principle subdivided into parts given by the factorization theorem. A schematic sketch of the event generating procedure on the basis of the BGF process is illustrated in figure 2.7.

The parton which enters the hard interaction from the proton side is given by the parton density functions. The PDFs define the flavor, the energy and the flux of the parton and

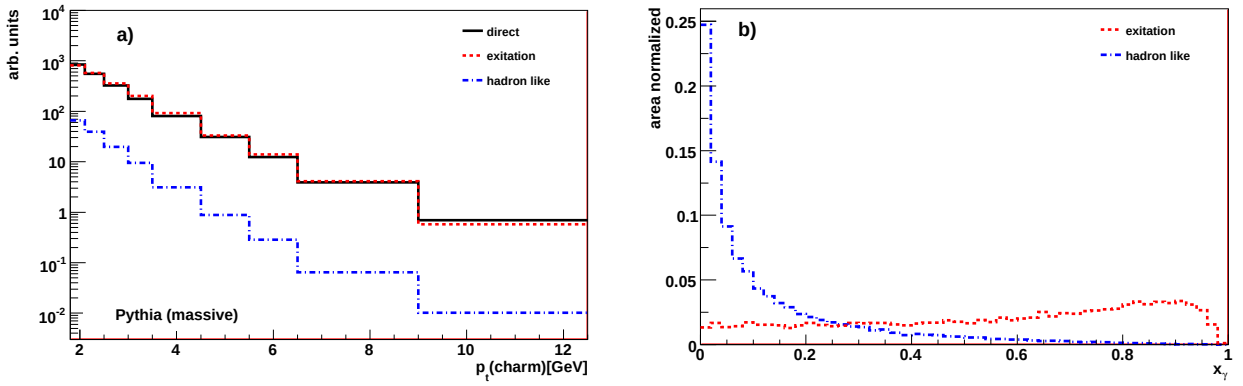

Figure 2.8: *Contributions of different processes predicted by the Pythia (massive) leading order Monte Carlo simulation. As a function of the transverse momentum of the charm quarks a) and as a function of the variable x_γ b). Note that the p_t distributions are normalized to the cross section of the processes and the x_γ distributions are area normalized.*

are evolved according the DGLAP or CCFM evolution equations to the appropriate scale, which is given by the transverse mass m_t. Before the parton enters the hard interaction possible higher order effects are simulated by parton showers (PS). The parton showers are incorporated as soft gluon radiation and gluon splitting $g \rightarrow gg$ and are calculated on the basis of similar techniques as given by the evolution equations.

The emission of the virtual photon from the electron is described within the framework of QED. The photon flux $f_{\gamma/e}(y, Q^2)$ is defined by the Weizsäcker-Williams approximation and the partonic behavior of the photons by the photon structure functions. The matrix element (ME) of the hard interaction is calculated in leading order. Finally the two hard partons and all other partons which have been produced by the PS enter the hadronisation procedure. Note that the PS which are applied on the outgoing quarks are equivalent to the first step of the fragmentation procedure described in section 2.4.

The generation procedure leads to sets of particle four vectors, which are used as input for the detector simulation. The simulation software provides the calculation of the detector response, including the simulation of efficiencies, resolutions and the dead material of the detector devices. Subsequently the data and the Monte Carlo can be treated as equal and both the data and Monte Carlo samples are fully reconstructed by the same reconstruction software.

Two event generators, Pythia and Cascade, have been used in the context of this analysis. The models differ significantly in the treatment of the proton structure. Pythia is based on the DGLAP approach, whereas in Cascade the CCFM evolution equations are implemented. In both generators the charm mass has been set to 1.5 GeV. All Monte Carlo samples used in this analysis are so-called signal Monte Carlos, where during the generation process only those events are selected which contain $D^\star$ mesons decaying via $D^{\star\pm} \rightarrow D^0\pi^\pm_{slow} \rightarrow K^\pm\pi^\mp\pi^\pm_{slow}$.

PYTHIA: In the regime of photoproduction Pythia [Sjo94] is the most frequently used event generator at HERA. The proton and photon PDFs used are CTEQ6L [Lai00] and GRV LO [Glu92], respectively. Pythia can either be run in the so-called massive or in the massless mode. The latter is often referred to as the full inclusive mode. The Lund string fragmentation model [And83] together with the Peterson[Pet83] in the massive

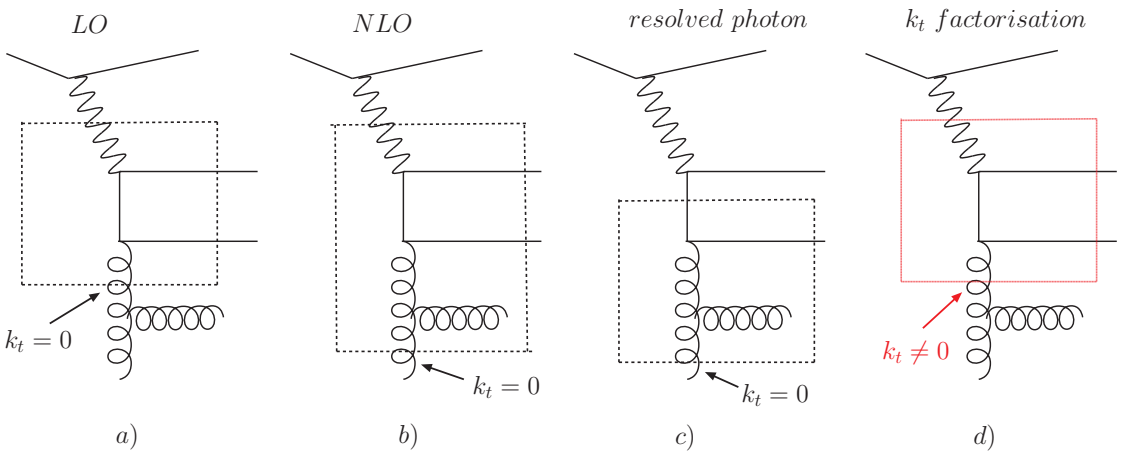

Figure 2.9: *Comparison of the DGLAP and CCFM approach. The three processes on the left a)-c) are intrinsicly implied by the CCFM approach d).*

mode or the Bowler[Bow81] fragmention model in the massless mode is used to simulate the hadronisation process.

massive: In this mode three different types of processes are generated separately using leading order matrix-elements. The processes have been introduced in figure 2.5 and correspond to the BGF, the charm excitation and 'hadron like' processes. Note that the charm quark is treated as massive particle in the calculation of the BGF process, whereas it is treated as massless in the resolved case.

massless: In this approach Pythia is run in the full inclusive mode ('MSTP(14) = 30'). Direct and resolved processes are calculated using massless matrix elements.

CASCADE: The CASCADE [Jun01, Jun02] program is used for calculations in the k_t-factorization approach. The quarks are treated as massive partons in the hard matrix element and the incoming gluon is treated off mass-shell and can have a finite transverse momentum. The unintegrated PDF set A0 [Han03] used in Cascade has been obtained from an analysis of the inclusive structure function F_2 in the CCFM approach. The initial state radiation is performed according the CCFM equations and the final state radiation of the gluons or quarks as well as the fragmentation is performed with Pythia. A photon PDF is not needed, parts of the resolved processes are taken into account by the k_t-factorization.

A summary of the used proton and photon PDFs as well as the applied fragmentation models is given in table 2.1.

In figure 2.8 a) the distribution of the transverse momentum of the charm quarks as predicted by the Pythia (massive) simulation is displayed for the three different processes (see figure 2.5) separately. The contributions of the BGF (direct) process and excitation processes are of similar size and exceed the hadron like contribution by far. In figure 2.8 b) the x_γ distribution is depicted for the excitation and hadron like processes as predicted by the Pythia (massive) simulation. In the LO direct case x_γ is by definition equal to one; this is therefore not shown.

The definition of the resolved processes depends on the way the hard matrix element is calculated. In Cascade for instance, part of the higher order terms and the charm excitation

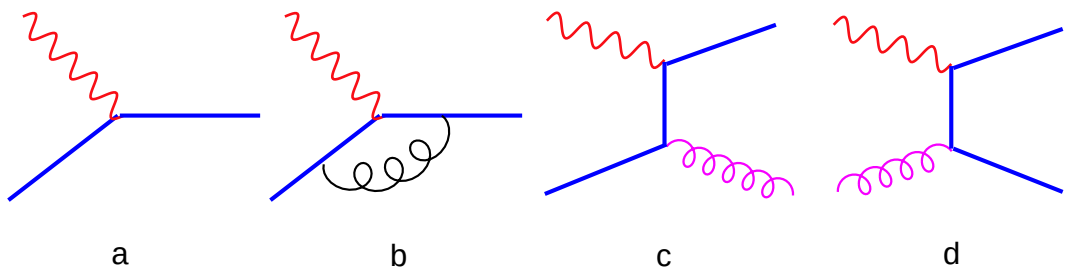

Figure 2.10: *A selection of processes implemented in the massless calculation scheme. The figure is adopted from [Tun02].*

processes are taken into account by the non-vanishing virtuality of the gluon. Figure 2.9 shows a comparison between the DGLAP approach and the CCFM approach. The processes a)-c) calculated in the DGLAP approach are intrinsicly covered by the k_t factorization in the CCFM.

2.6 NLO calculations

In contrast to inclusive analyses, where usually only one hard scale is present by Q^2, the scale is no more unique in processes in which heavy quarks are produced. Here the hard scale can either be the mass, the transverse momenta or a combination of both. This circumstance is often referred to as the multi hard scale problem and treated by applying different calculation schemes. Presently three different calculation schemes are available which differ basically in the treatment of the heavy quark mass.

Within the massless Zero-Mass-Variable-Flavor-Number-Scheme (ZMVFNS) approach-[Bin98], the heavy quarks are treated as massless partons in the hard matrix element. Heavy quarks are considered as active partons in the proton, that means that the heavy quark is treated as part of the sea quarks and their calculation is partially absorbed in the PDF. Some of the next-to-leading order diagrams are shown in figure 2.10. Since terms of the order m_c^2/μ^2 are neglected in the calculation, this scheme is expected to work as long as the hard scale is large compared to the heavy quark mass.

Within the massive Fixed-Flavor-Number-Scheme (FFNS) approach [Fri95a, Fri95b], the heavy quarks are treated as massive particles. In this approach only light quarks and gluons are considered as active partons in the proton, while the heavy quarks are produced dynamically in the BGF. Some of the diagrams are shown in figure 2.11. In this scheme the heavy quark mass provides an additional hard scale. Thus it is expected to work for low scales.

The General-Mass-Variable-Flavor-Number-Scheme (GMVFNS) approach [Tun02] is an attempt of an unified description both for small and large scales. The massive scheme is applied for low scales and the massless scheme at high scales. Various attempts exist how to perform the interpolation in the transition regime between the massless and massive calculation. In addition to the light partons also charm and bottom quarks are considered as active partons in the proton in this approach.

In the context of this analysis the measurement of the inclusive sample is compared to a FFNS and GMVFNS calculation. A GMVFNS calculation is presently not available for two partons in the final state. Hence it is not possible to compare the results obtained in the DiJet sample with this calculation. In order to take into account that the FFNS calculation only considers three active flavors in the proton, an appropriate fixed flavor parton

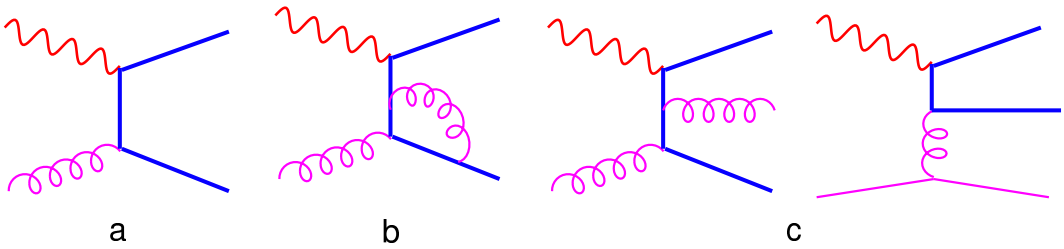

Figure 2.11: *A selection of processes implemented in the massive calculation scheme. The figure is adopted from [Tun02].*

	GMVFNS	*FFNS*
Proton PDF	CTEQ6.5M	CTEQ5F3
Λ_{QCD}	328 MeV	390 MeV
Photon PDF	GRV LO	GRV LO
Renorm. scale	$0.5 \cdot m_t < m_t < 2 \cdot m_t$	$0.5 \cdot m_t < m_t < 2 \cdot m_t$
Factor. scale	$0.5 \cdot m_t < m_t < 2 \cdot m_t$	$0.5 \cdot m_t < m_t < 2 \cdot m_t$
m_c [GeV]	m_c	$1.3 < m_c < 1.7$
Fragmentation	KKKS 2008[Kne08]	Peterson $\epsilon_{pet} = 0.035$

Table 2.2: *Summary of the QCD parameters used in the NLO calculation. The parameter m_c denotes the charm quark mass. The transverse mass m_t is defined as $m_t^2 = m_c^2 + (p_{t,c}^2 + p_{t,\bar{c}}^2)/2$. ϵ_{pet} is the Peterson fragmentation parameter.*

density given by CTEQ5F3 [Lai00] has been used. The CTEQ6.5M is used in the GMVFNS calculation, which incorporates also contributions from charm and bottom. In figure 2.12 the distribution of the gluon density functions CTEQ5F3 and CTEQ6.5M are displayed at a scale $\mu_f = 10$ GeV^2. In addition to the NLO PDFs the CTEQ6L parameterization, which is used in the LO generator Pythia, is depicted. Both the CTEQ5F3 and CTEQ6.5M are in general lower than the leading order PDF CTEQ6L. This is not surprising since it takes into account that the next-to-leading order cross section is higher than the leading order cross section.

The GMVFNS calculation has been provided by [Spi08b, Spi08a]. The FFNS calculation is accessible for the H1 collaboration by the program FMNR, which provides full user control on the outgoing partons. A summary of the used QCD parameters in the NLO calculations is given in table 2.2.

FMNR

The FMNR program [Fri95a] provides weighted parton level events with two or three outgoing partons, which are for instance a $c\bar{c}$-quark pair and possibly one additional light parton. In FMNR the direct and resolved processes are calculated separately. The transition from the charm quark to the $D^\star$ mesons is treated by downscaling of their three-momenta according the Peterson fragmentation function [Pet83] in a frame where the quark-antiquark pair is back-to-back. Figure 2.13 shows the relative contributions to the cross of the direct and resolved processes as a function of the transverse momentum of the charm quarks.

The value of the Λ_{QCD} parameter used has to be consistend with the value used in the

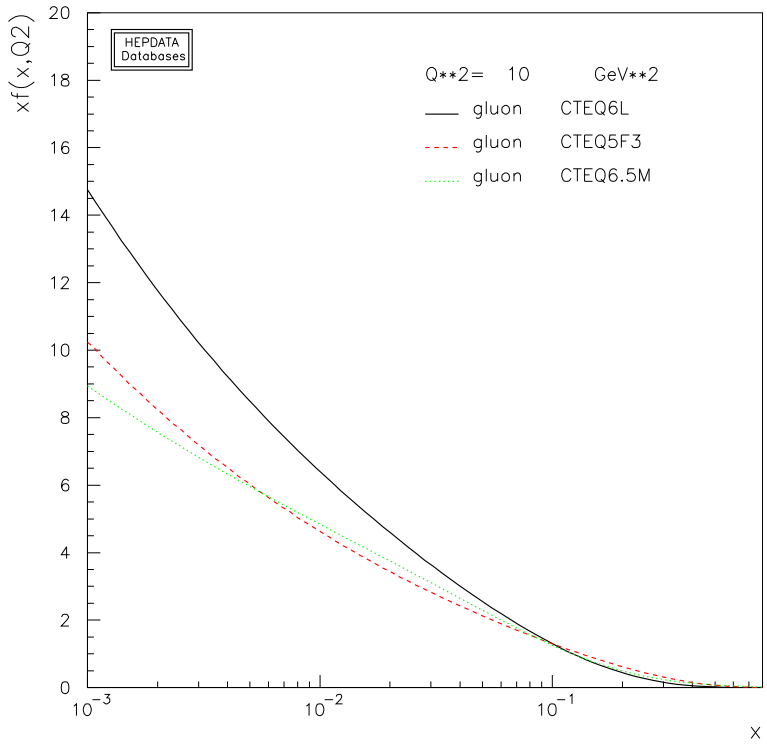

Figure 2.12: *Gluon densities at the scale $\mu_f = 10$ GeV^2. The CTEQ6L parameterization is used in the leading order generator PYTHIA. The CTEQ5F3 parameterization is used in the NLO FFNS calculation and takes into account three active flavors in the proton which are the up, down and the strange quark. The CTEQ6.5M parameterization is used in the NLO GMVFNS calculation.*

fitting procedure to determine the PDF and therefore set to 390 MeV. The value for the Peterson fragmentation ϵ_{Pet} has been set to $\epsilon_{Pet} = 0.035$. The value of the pole mass 1.5 GeV is used for the charm quark mass. The renormalization and factorization scales are set to the transverse mass of the charm quark $m_t = \sqrt{m_c^2 + (p_{t,c}^2 + p_{t,\bar{c}}^2)}$.

The reliability of a prediction is usually estimated by varying renormalization and factorization scales by $1/2 \cdot m_t$ and $2 \cdot m_t$ as well as the charm mass by ± 0.2 . The resulting uncertainty corresponds to missing higher oder terms in the matrix calculation.

In the following the uncertainty due to a variation of the factorization (μ_f) and renormalization (μ_r) scales as well as the charm mass is studied as a function of the transverse momentum of the $D^\star$ meson and the jet associated to the $D^\star$ meson. The calculations are performed within the visible range of this measurement (see table 6.1 and table 10.1).

In the figures 2.14 a)-c) the effect of the scale and mass variation for the $D^\star$ meson and in figures 2.14 d)-f) for the jet associated with the $D^\star$ meson are illustrated. The uncertainties observed in the visible range of the inclusive sample are in general higher than in the phase space of DiJet sample. This can be explained by the larger scale provided by the higher p_t of the jet.

Two effects are competing against each other by varying the charm mass. On the one hand, the downward variation of the charm mass leads to an increase of cross section due to the lower mass, on the other hand simultaneously the strong coupling constant α_s becomes larger, which leads to a reduction of the cross section, since $\sigma \sim \alpha_s^2$. Figure 2.14 a) and d) shows the result of the downward and upward variation of the charm mass. The downward

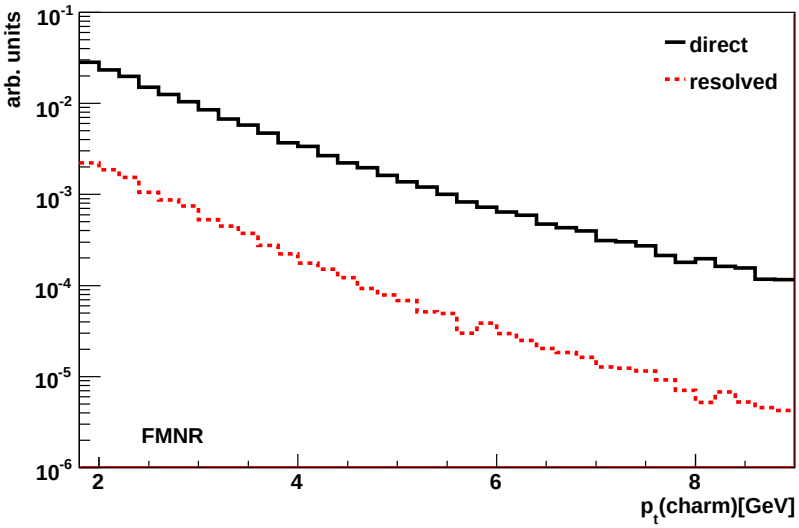

Figure 2.13: *Contributions of direct and resolved processes as a function of the transverse momentum of the charm quarks as predicted by the FFNS calculation provided by the program FMNR.*

variation leads to an increase of the cross section, thus it can be concluded that the effect of the rising α_s is low compared to the effect of the decreased mass. The uncertainty is highest at low p_t and becomes small at high p_t. The maximal uncertainty due to the variation of the charm mass is 30% in the phase space of the inclusive sample and 15% in the phase space of DiJet sample.

The effect of a variation of the factorization scale is displayed in figure 2.14 b) and e). At low x, an increase of the factorization scale leads in general to an increasing parton density and therefore to an increase of the cross section. However, the effect on the cross section is in both cases small and amounts in average to 10%.

The increase or decrease of the cross section by an upward or downward variation of the renormalization scale can be understood as an increase or decrease of the strong coupling constant given by equation 2.8. The influence on the cross section by a variation of the renormalization scale is much larger than a variation of the factorization scale. Especially at low p_t the downward variation by $0.5 \cdot \mu_r$ leads to a deviation from the nominal cross section of more than a factor of two for both the $D^\star$ meson and the jet. In the presented analysis, the uncertaintanties are used for the comparison of the NLO calculation with the data. They are determined independently and afterwards added in quadrature.

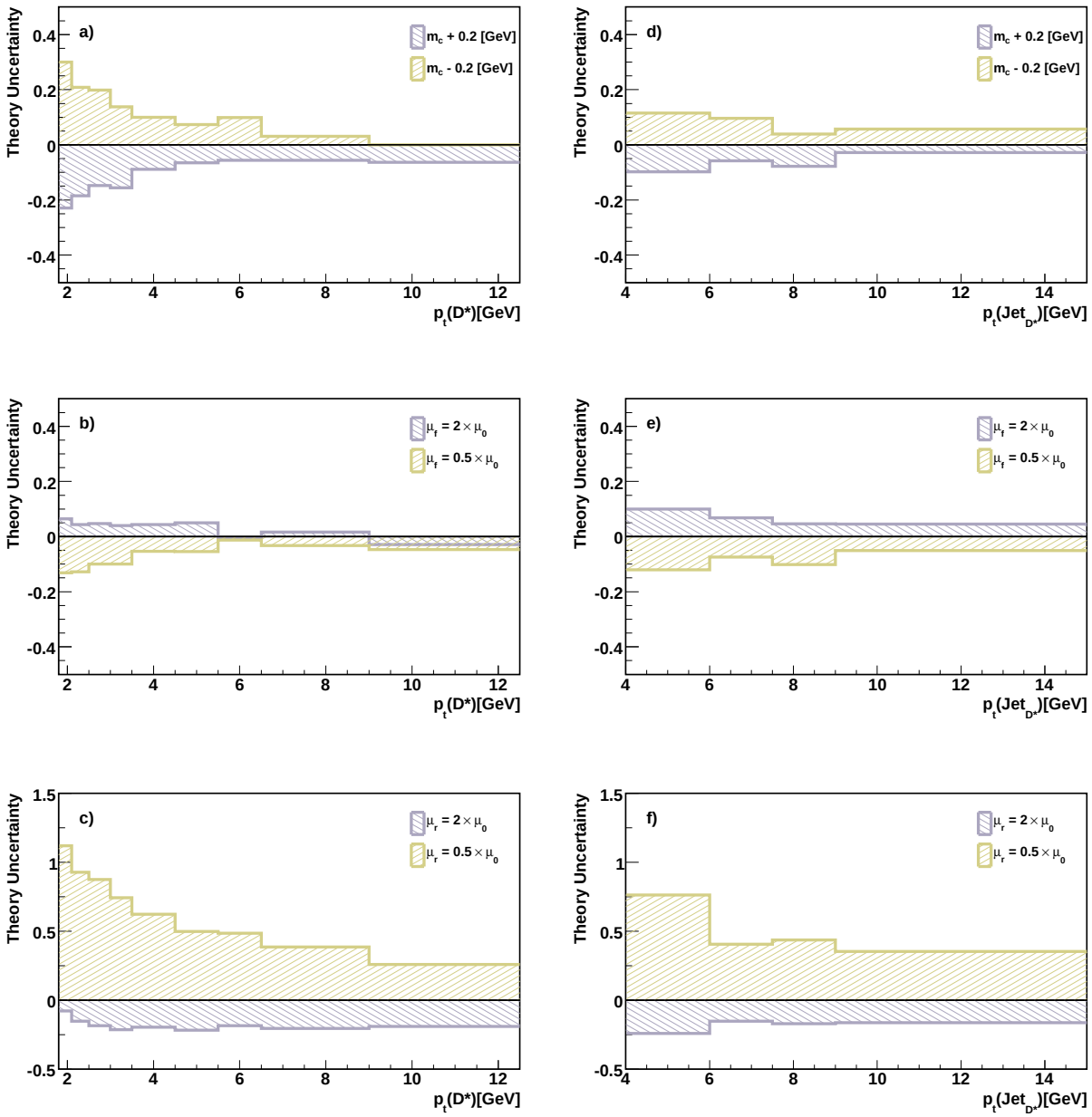

Figure 2.14: *Uncertainties due to the next to leading order calculation given by the FMNR program as a function of the transverse momentum of the $D^\star$ meson a)-c) and the jet associated to $D^\star$ meson d)-f). The uncertainties are determined by a variation of the charm mass, renormalization and factorization scales.*

Chapter 3

The H1 Experiment at the HERA Accelerator

The analysis presented in this thesis is based on data which have been recorded with the H1 detector at the HERA collider in the time period of september 2006 till june 2007. After an introduction of the HERA collider the dicussion focuses on the H1 experiment. Emphasis is placed on the detector components relevant for this analysis. These are in particular the tracking devices and the trigger system. In particular the Fast Track Trigger (FTT) played an important role for this analysis. The FTT has been fully commissioned in September 2006 and allowed a selection of exclusive final states, such as $D^\star$ mesons, at an early stage of the data taking procedure. Employing the FTT in this analysis allows for the first time to investigate the photoproduction $D^\star$ mesons in almost the full phase space covered by the H1 experiment.

3.1 HERA Accelerator

The HERA accelerator has been in operation since 1991 till 2007. The HERA accelerator had an circumference of around 6.3 km and formed the last phase of a multistage accelerator system. Within the HERA accelerator system protons and electrons or positrons were accelerated in bunches in opposite directions inside separate beampipes. The electron[1] and proton bunches are collided at two interaction points. The time interval between two bunches amounted to 96 ns. The protons and electrons were accelerated to energies of 920 GeV and 27.5 GeV, respectively. A schematic illustration of the accelerator and its experiments is given in figure 3.1.

From the experiments located at the HERA accelerator H1 and ZEUS used the electron beam as well as the proton beam, while the HERMES and HERA-B experiments made only use of the electron or proton beam, respectively. The HERA-B experiment was in operation until the year 2003 and used the proton beam to investigate the properties of heavy B meson production, with the aim to measure the CP-violation. In the HERMES experiment the electron beam was collided with polarized gas targets in order to investigate the spin structure of protons. The experiments H1 and ZEUS were ep scattering experiments in which the electrons and protons were collided at a center-of-mass energy of $\sqrt{s} = 318\,\text{GeV}$. Both experiments were multipurpose experiments which allowed various studies concerning the strong and electroweak interaction.

[1] In the data taking period relevant for this analysis positrons have been accelerated.

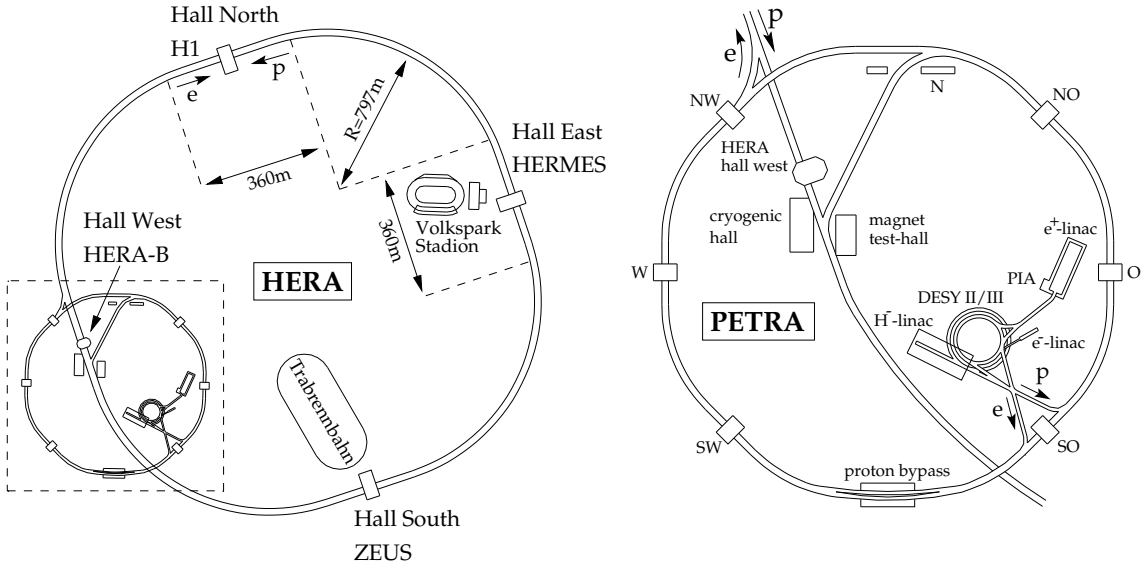

Figure 3.1: Schematic overview of the HERA accelerator and the pre-accelerator facilities

3.2 Detector Overview

The H1 detector [Abt97a, Abt97b] was designed to give a precise identification and reconstruction of the particles produced particles in the ep collisions. Of particular interest for the analysis presented in this thesis is the precise track measurement in the central tracking devices. Figure 3.2 shows the configuration of the main detector. The H1 detector was composed of a number of subdetector devices which cover almost the whole angular range around the nominal interaction point.

In the schematic overview shown in figure 3.2 the proton beam enters the detector volume from the top and the electron beam from the bottom. The beams were collided at the interaction point (IP) [1]. Due to the different beam energies the bulk of the produced particles were expected in the direction of the proton beam. This had been considered by an asymmetric design of the experiment and a finer instrumentation in direction of the proton beam. In the following this direction is referred to as the forward direction. The backward direction has been optimized to allow a precise reconstruction of the energy and angle of the scattered electron.

The H1 coordinate system is defined as follows. The origin of the right handed cartesian coordinate system is defined by the interaction point. The z axis is given by the symmetry axis of the H1 experiment while its direction is defined by the proton beam direction. The x axis points to the center of the HERA collider and the y axis points upwards. It is often more convenient to describe the event kinematics in polar coordinates. In this case the azimuthal angle ϕ is defined in the xy plane and the polar angle θ is given with respect to the z axis. It is common to express the polar angle θ by the pseudorapidity η. Both quantities are related via $\eta = -\ln(\tan(\theta/2))$.

The interaction point was surrounded by the Central Silicon Detector (CST) [2], which allowed a precise reconstruction of the interaction point. The CST covered an angular range of $30° < \theta < 150°$. In the Backward region the CST was complemented by the Backward Silicon Tracker (BST) [3] and in the forward region by the Forward Silicon Tracker (FST) [4]. In the radial direction the tracking system was continued by the Central Chambers (CJC). Consisting of the inner and outer Central Chambers CJC1 [7] and CJC2 [8]. The

proportional chambers CIP [5] and COP [6] were located at the inner part of the CJC1 or outer part of the CJC2, respectively. The multiwire proportional chamber CIP encloses the CST. Since the measurement of the z-coordinate provided by the CJC was not very precise, the signals provided by the COZ were used to support the z measurement of the CJC. The tracking system was completed with the track chambers FTD [9] and BPC [10] located in the forward and backward direction, respectively.

The tracking system was enclosed by the calorimetry. The Liquid Argon (LAr) [12,13] calorimeter covered the central and forward region and the Spaghetti Calorimetry (SpaCal) [14,15] closed the acceptance gap in the backward region. The primary task of the SpaCal was the identification of the scattered electron at low Q^2.

The tracking system and the calorimetry were surrounded by a super conducting solenoid [18]. With the arrangement of the magnet outside of the calorimeter volume the amount of dead material was minimized. The magnetic field induced by the solenoid was almost homogeneous and parallel to the z axis. The strength of the field amounted to 1.16 T. The outermost detector component was the muon system. The central muon system (CMD) [19] covered an angular range of $4° < \theta < 171°$. The CMD was complemented by the forward muon system (FMD) [21] which had an angular acceptance of $3° < \theta < 17°$.

A further detector component which is not visible in figure 3.2 is the luminosity system, located at $z = -101.8$ m.

3.3 Central Tracking Devices

The purpose of the central tracking devices (CDT) was to measure the momenta of charged particles in the central region of the H1 experiment. The CTD were placed within the magnetic field of the solenoid and the measured tracks consequently curved depending on the transverse momentum. The components of the CTD are displayed in figure 3.2.

Central Silicon Detector

The Central Silicon Detector (CST) [Pit00] provided precise vertex and track information based on the track measurement of charged particles close to the interaction point. The CST had been designed with an elliptic form, to take into account the elliptic form of the beampipe. The CST was used to improve the tracks measured in the CJC1 or CJC2 by providing precise track points in the $r\phi$ plane as well as in the z coordinate.

Central Inner Proportional Chamber

The Central Inner Proportional chamber (CIP) [Urb04] was a multiwire proportional chamber and consisted of five detector layers. The wires of the CIP were strung parallel to the beam direction. The CIP had a radius of $r = (15.7 - 19.3)$ cm and covered an angular range of $11° < \theta < 169°$. Due to the fast response time of the CIP of around ~ 75 ns the CIP was used for the online event selection. The z vertex position of the events is defined by the intersection of the tracks with the z-axis and was determined on the basis of pre-calculated masks and used to derive the trigger decision.

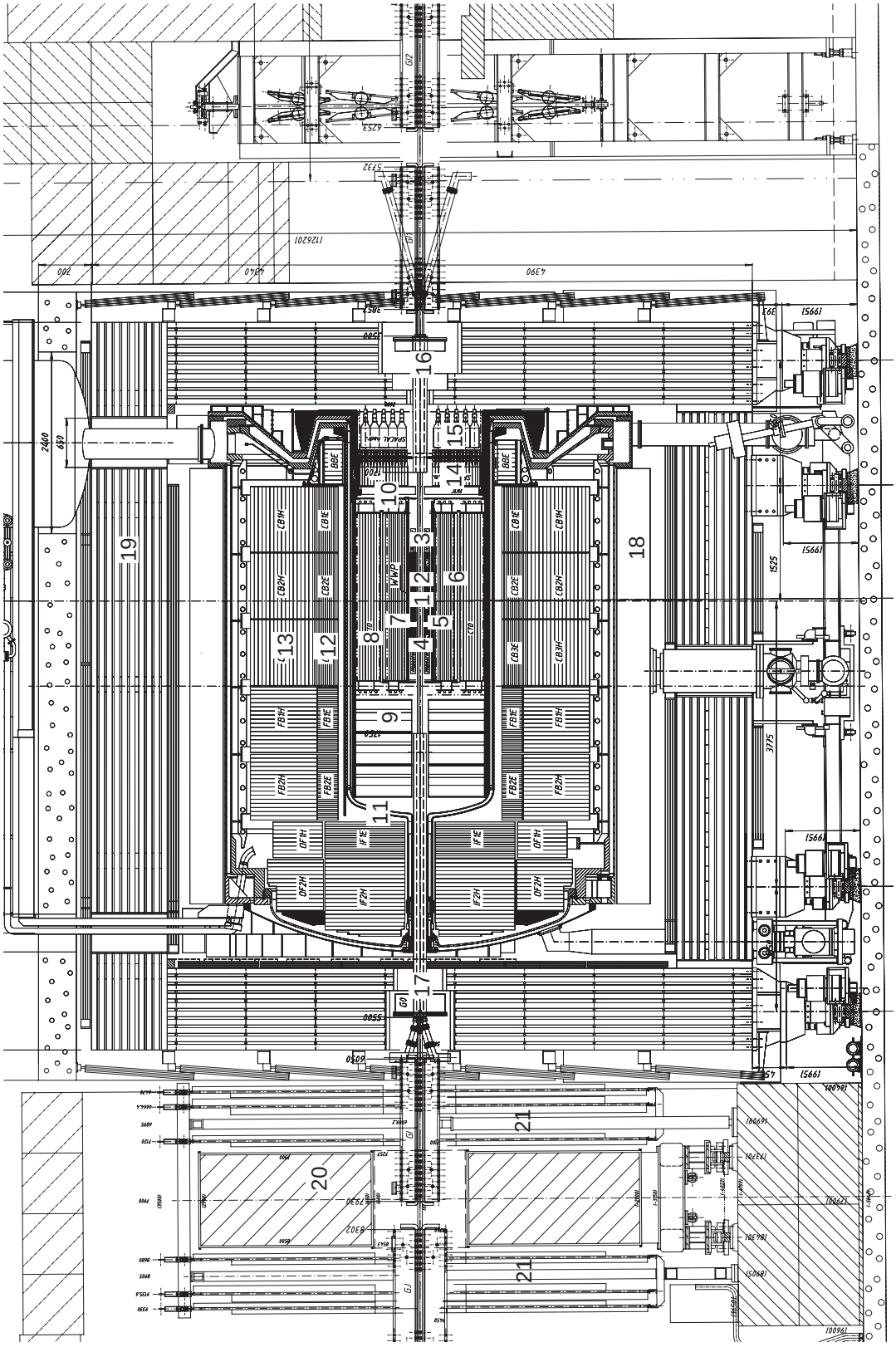

Figure 3.2: *Schematic side view of the H1 experiment. The numbers are explained in table 3.1.*

Number		
1	Interaction Point	IP
	Tracking	
2	Central Silicon Detector	CST
3	Backward Silicon Detector	BST
4	Forward Silicon Detector	FST
5	Central inner proportional Chamber	CIP
6	Central outer proportional Chamber	COP
7	inner Central jet chamber	CJC1
8	outer Central jet chamber	CJC2
9	Forwards Tracker	FTD
10	Backward proportional chamber	BPC
	Calorimetry	
11	Liquid Argon Cryostat	LAr-Cryostat
12	electrom. liquid Argon Calorimetry	LAr(em)
13	hadronic liquid Argon Calorimetry	LAr(had)
14	electrom. Spaghetti Calorimeter	SpaCal(em)
15	hadronic Spaghetti Calorimeter	SpaCal(had)
	Other subsystems	
16	super conducting focus Magnet	GG
17	super conducting focus Magnet	GO
18	super conducting Solenoid	
19	Central Muon Detector	CMD
20	Muon Toroid Magnet	
21	Forward Muon Detector	FMD

Table 3.1: *Summary of the main detector components of the H1 experiment (see figure 3.2).*

Central Jet Chambers

The Central Jet Chambers (CJC1&2) were the main components of the central tracking system of the H1 experiment. The CJC consisted of two separated chambers: the inner CJC1 and the outer CJC2. The radius of the inner chamber amounts to $r = 45.0$ cm and both chambers together had a radius of $r = 85.5$ cm. The CJC1 was separated in 30 drift cells and the CJC2 in 60 cells, respectively. Each cell consisted of 24 signal wires in the CJC1 and 32 signal wires in the CJC2. The cells were tillted by 30° to ensure that the straight tracks cross at least two cells. The position of the tracks was determined by analysing the drift times of the charges, produced in the ionization procedure, to the signal wires. The precise track coordinates were calculated by the position of the charge, the drift time and the drift velocity.

Since the particle trajectories were curved by the magnetic field, the reconstruction allowed to deduce the transverse momenta of the tracks. The resolution of the momentum measurement in the CJC was given by $\sigma_{p_t}/p_t^2 = 0.005\ \text{GeV}^{-1} \oplus 0.015$ [Kle06]. The CJC provided the input signals for the Fast Track Trigger (FTT). The FTT will be explained in detail in section 3.7. More information about the CJC can be found in [Erd96].

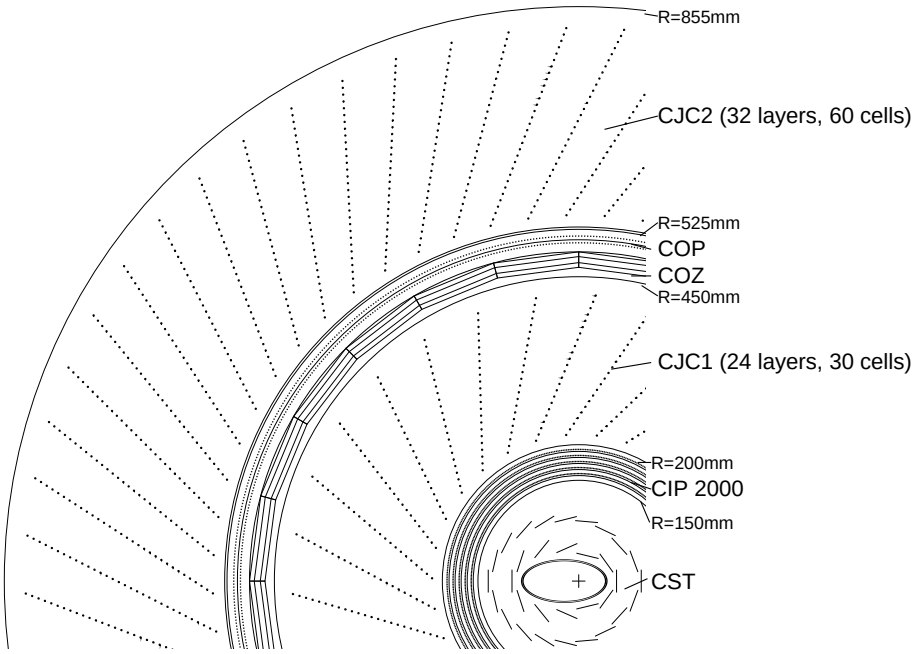

Figure 3.3: *Radial view of the central tracking system of the H1 experiment. Depicted is the CST* [1]*, CIP* [2]*, CJC1* [3]*, COZ, COP* [6] *and CJC2* [5]*. The signal wires of the CJC1&2 are depicted as points.*

3.4 Calorimetry

The most important calorimeters at H1 were the Liquid Argon (LAr) and the scintillating fiber (SpaCal) calorimeter. The main purpose of the SpaCal was to measure the scattered electron in the backward region of the experiment at low Q^2. The informations provided by the LAr were used to reconstructed the scattered electron at higher Q^2 and the hadronic final state.

Liquid Argon Calorimeter

The Liquid Argon Calorimeter (LAr) [And93] is a finely segmented non-compensating sampling calorimeter with an angular acceptance of $4° < \theta < 154°$. The main design goals were a good separation of electrons and pions and a precise reconstruction of the electron energy. The energy resolution for electrons amounts to $\sigma(E)/E = 12\%\sqrt{E} \oplus 1\%$ and for pions to $\sigma(E)/E = 50\%\sqrt{E} \oplus 2\%$. The LAr is divided into an inner electromagnetic [12] and an outer hadronic [13] section. A side view of the upper part of the LAr is given in figure 3.4. The LAr was subdivided into 108 independent modules which were combined into eight octants. In both sections liquid argon was used as active material. The absorber used in the electromagnetic and hadronic section is lead and stainless steal, respectively. Both sections were cooled by a cryostat [11] filled with liquid argon.

SpaCal

The SpaCal [App97] provides an energy measurement in the backward region of the H1 detector. The SpaCal is divided into a hadronic and an electromagnetic section. The geometrical acceptance is restricted to $153° < \theta < 177.5°$. In this region the electron is scattered

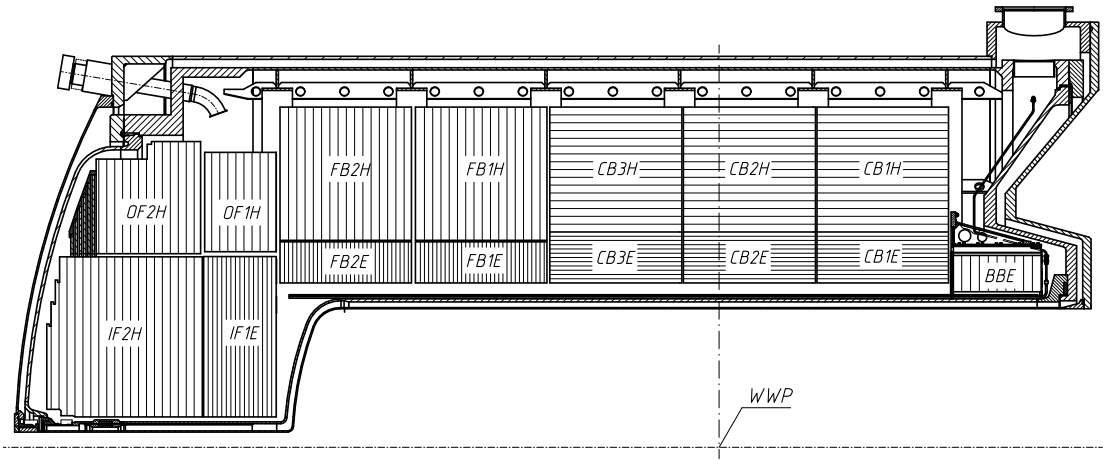

Figure 3.4: *Side view of the liquid argon calorimeter. Visible are the eight electromagnetic and the hadronic modules. The modules which are labeled with 'E' correspond to the electromagnetic section and the parts labeled with 'H' to the hadronic section.*

for squared momentum transfers of $2 < Q^2 < 100\,\mathrm{GeV}^2$. The main design goals were a good energy and position reconstruction of the scattered electron. The relative energy resolution reached by the SpaCal was $(7.1 \pm 0.2)\%/\sqrt{E/GeV} \oplus 1.0 \pm 0.1)\%$ [Nic96]. Further construction goals had been a high time resolution (≤ 1 ns) [Nic96] and an efficient lepton hadron separation[App96]. Furthermore the SpaCal provided the possibility to detected the hadronic energy flux in the backward region of the detector.

3.5 Luminosity System

The luminosity measurement at the H1 experiment was based on the Bethe-Heitler-Process(BH) $\sigma_{BH}(ep \to e\gamma)$ which can be precisely calculated in the framework of the QED theory [Bet34]. The integrated $\mathcal{L}$ in a certain time interval is given by:

$$\mathcal{L} = \frac{N_{BH}}{\sigma_{BH}}. \tag{3.1}$$

Here N_{BH} is the number of BH events in a certain time interval. The BH photon is measured in the photon detector, which was located at $z = -101.8$ m. The detector was a sampling calorimeter consisting of quartz fibers and tungsten. A beryllium filter and a water Cerenkov counter were located in front of the detector to suppress background events [Adl98]. The BH electron could be measured in the so-called electron tagger, which was located at $z = -5.4$ m. The measurement of the electron in coincidence with the photon was used to control the photon measurement; it was not used for the determination of the luminosity.

3.6 Trigger System

The nominal bunch-crossing rate at HERA amounted to 10.4 MHz whereas the expected rate of electron-proton-scattering events was about 1 kHz. This means that background events occur about a thousand times more often than events of a physical relevance. The readout of the H1 detector took in averrage about 1.4 ms. During this time the detector was not able

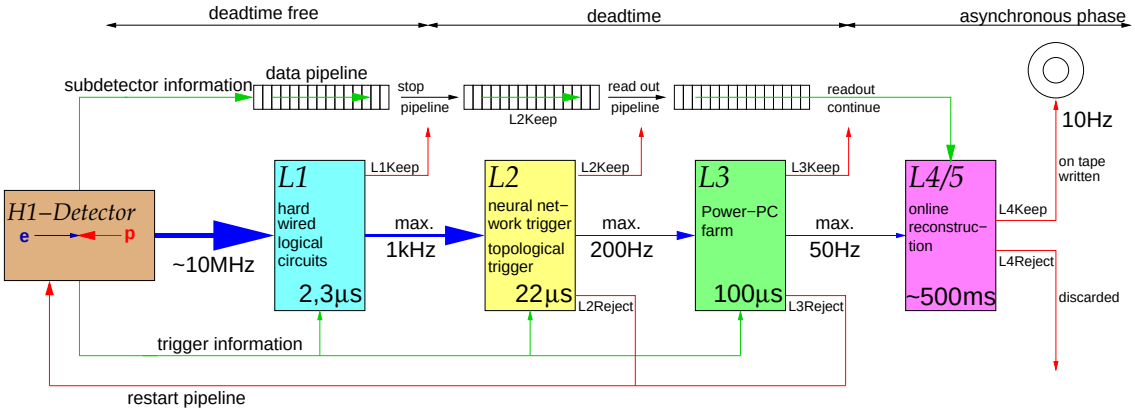

Figure 3.5: *A schematical sketch of the four level trigger system of the H1 experiment. The first three levels are synchronous to the data taking. The first level is deadtime free. Typical input rates are shown for each level.*

to record any further events. The maximal readout rate was restricted to at most 50 Hz to achieve a deadtime of less than 10%. Due to this limited bandwith, the challenge for the H1 trigger system was to eliminate background events and simultaneously select physical events of interest. This was realized with the help of a four-level trigger system [Els92]. Figure 3.5 shows a schematic overview of the trigger system. On each level the trigger rate was gradually reduced and the decision time increased. The fourth trigger level selected events after the full readout and had no influence on the deadtime. In total a rate reduction from 10 MHz to 10 Hz was achieved.

The task of the first trigger level (L1) was to reduce background events at an early stage of the data acquisition. Here the emphasis was placed on speed rather than on accuracy. The L1 system was synchronized to the bunch crossing rate of 96 ns. The data of the subdetector systems were fed into a ring buffer system, in order to keep the first trigger level deadtime free. The decision of the L1-system was based on the digitized signals of the subdectectors (trigger elements). Up to 256 trigger elements were combined via logical operations to 128 so-called subtriggers. If, after the latency of 2.3 μs, an event satisfied the trigger conditions the L1-Keep signal was set, the ring buffers were frozen and the deadtime began. Subsequently the trigger signals were sent to the second trigger level (L2).

After a positive decision of the L1 system (L1-Keep) the operation of the second trigger level (L2) began. The task of the L2 system was to validate the L1 decision within 22 μs based on the information provided by the L1 System. Compared to the L1 decision the L2 decision was based on more sophisticated algorithms which allowed a more precise analysis of the event signature. Three independent systems were available, the topological trigger L2TT [Biz97], the neural net trigger L2NN [Köh97] and the FTT. These systems provided their decision in the form of 96 trigger elements which were again combined via logical operations to L2 subtriggers. After a positive decision of the L2 subtriggers the L2-Keep signal was set and the readout of the H1 detector began. Otherwise (L2-Reject) the event was no longer stored and the ring buffer system was again enabled.

The third trigger level (L3) was implemented within the FTT. The task of the L3 system was to identify, within a latency of about 130 μs, exclusive final states using track based event informations including invariant mass calculations. The FTT-L3 consisted of five PowerPCs where the decision was derived on the basis of the information provided by the L2-system. In particular these were the track based information of the FTT-L2 system but

also information from other systems were taken into account. Up to 48 trigger elements were provided by the FTT. The L3 reject stops the readout and starts the pipeline.

After the readout the whole data was sent to the fourth trigger level (L4). The L4 system consisted of a processor farm where the events were fully reconstructed and afterwards classified into so called event classes. Due to the deadtime requirement, the input rate of the L4 system was limited to 50 Hz. On the basis of this classification the final decision, if an event was stored (L4-Keep) or thrown away (L4-Reject), was performed. To allow L4 efficiency studies, a small fraction of the rejected events was marked and stored. In the end the data were stored permanently on tapes with a rate of 10 Hz.

Since the input rates of the different subtriggers were strongly coupled to the instantaneous luminosity and the background conditions, it was not always possible to achieve the required rate reduction with the trigger system. To assure that the constant bandwidth was optimally exploited during varying conditions so-called prescale factors had been implemented to the trigger system. To each subtrigger i a prescale factor d_i was assigned. This means that only one out of d_i events satisfying the conditions of subtrigger i lead to a positive L1 decision. In this case a so-called $actual - bit$ was set to one and the event was recorded. For the case that an event did satisfy the conditions of the subtrigger i a so called $raw - Bit$ was set, if the $actual - bit$ of at least one other subtrigger set. More information about prescaling can be found in [Urb05].

3.7 Fast Track Trigger

In the years 2001-2002 the HERA collider has been upgraded to achieve a higher interaction rate in the experiments. To make the best possible use of the higher luminosity, the Fast Track Trigger (FTT) [Bai99a, Bai99b] had been built. The FTT was the only triggersystem which operated on three trigger levels. The trigger decision was based on informations provided by selected wires of the central jet chambers (CJC1 & CJC2). Due to the low latency of 2.3 μs only coarse track parameters in the $r\phi$-plane had been calculated on the first trigger level. The higher latency on the second trigger level allowed to perform three dimensional track fits. On the third trigger level the precise track parameters obtained on the second level and in addition information of other trigger systems were used to search for exclusive final states within a latency of 100 μs.

FTT-L1

The FTT decision was based on 12 out of 56 wire layers of the CJC, the wire-layers were organized in four trigger layers, each trigger layer consisted of three wire-layers (see figure 3.7). The first three trigger layers were located in the CJC1, the fourth layer in the CJC2. Wires of the same drift cell and the same triggerlayer formed so-called trigger-cells. The information from five trigger-cells was digitized with a 80 MHz sampling rate. Hits were identified by a fast Qt algorithm and transfered into shift registers, synchronized with 20 MHz. At the same time a second shift register was filled for the Level 2 system which was synchronized with 80 MHz. While the shift registers were filled the z-position was determined using the method of charge division [Sch04].

The patterns in the shift registers were compared to pre-calculated masks. Tracks originating from the interaction point showed a characteristic pattern in the shift registers so that one could easily distinguish them from random coincidences. The track segments were then filled into a $\kappa - \phi$ histogram, which consisted of 16×60 bins. With a so-called sliding window

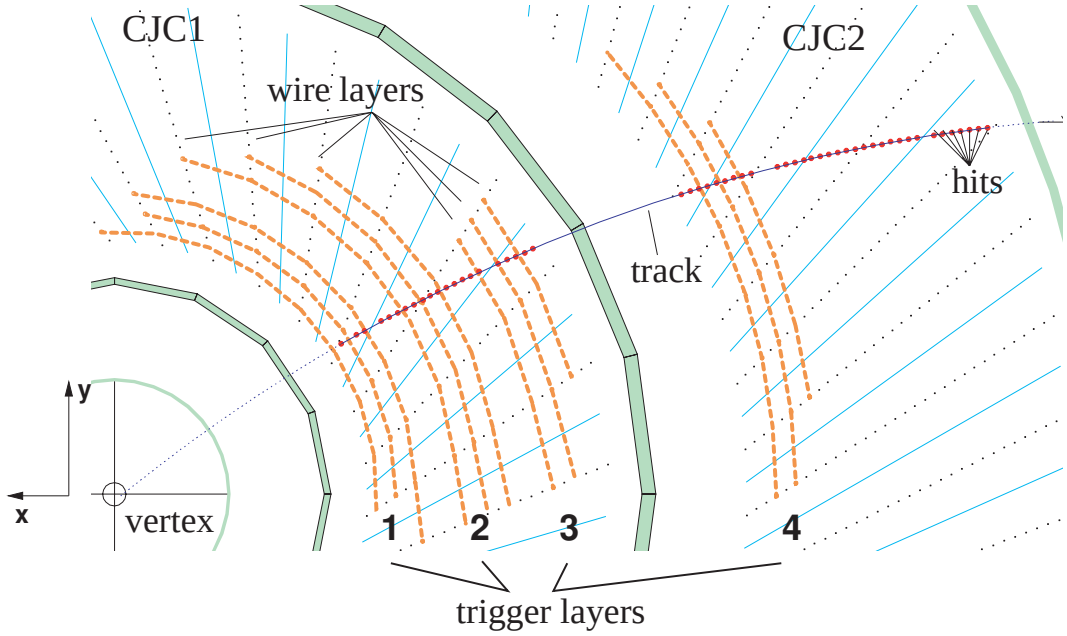

Figure 3.6: *Sector of the CJC in $r\phi$ view. Visualized are the four trigger layers of the FTT consisting of three wires each.*

technique these $\kappa - \phi$ histograms of the four trigger layers were analyzed and coincidences found were compared. The resolution of the tracks is limited by the low amount of bins. For the trigger decision the amount of tracks above a certain p_t threshold is used. These information are then coded in trigger elements, which are combined via boolean operations with trigger elements of other trigger subsystems.

FTT-L2

After a positive L1 decision the FTT starts immediately with the calculation of the L2 decision which has to be derived within 22 μs. Compared to FTT-L1 the larger decision time allows a more precise reconstruction of the tracks. In particular this was achieved by employing shift registers filled with a sampling rate of 80 MHz and taking into account more precalculated masks. The track segments were transfered to finer binned $\kappa - \phi$ histogram, which consisted of 40×640 bins. The resolution of the track segments was further increased by an additional track fit in the $r\phi$-plane [Wis03, Kar91]. The track is fully reconstructed by an additional linear fit in the rz-plane, which is based on the z-position determined on Level 1. On the basis of the fully reconstructed tracks it was possible to search for exclusive final states. However, the low latency of L2 allowed only to search for two particle exclusive final states.

FTT-L3

For the case that an event was excepted by Level 2 all tracks were transfered to the third level. In addition data of other trigger subsystems, for example of the muon system were made available to Level 3. The main purpose of the L3 system was the identification of processes including charm and beauty quarks. The final states were found within a time period of

100 μs. The selection algorithms which had been implemented, allowed to perform searches for $D^\star$ mesons and inelastic J/Ψ mesons with different p_t thresholds and for electrons and muons in the final state. In the following the $D^\star$ algorithm which is relevant for this thesis will be presented.

The $D^\star$ mesons are selected in the Golden Decay Channel ($D^{\star\pm} \rightarrow D^0\pi^\pm_{slow} \rightarrow K^\mp\pi^\pm\pi^\pm_{slow}$). In the first step of this algorithm two tracks were combined under the mass hypothesis of decay products of the D^0 meson. In the case that the invariant mass of the decay products is consistent with the mass of the D^0 meson, within a mass window of 180 MeV, the algorithm proceeds with the search of the track corresponding to the π_{slow} meson. The invariant mass difference ΔM between the three tracks corresponding to $D^0\pi_{slow}$ and the two tracks corresponding to the decay products of the D^0 was calculated for all track combinations. Real $D^\star$ mesons are expected around $\Delta M = m_{D^{\star\pm}} - m_{D^0} = 145.421 \pm 0.010$ MeV [Yao06]. In practice a combination of an upper ΔM cut as well as a cut on the transverse momentum of the $D^\star$ above a certain p_t threshold ($> 1.5, > 2.5$ and > 4.5 GeV) is applied. In order to cope with increasing combinatorics towards lower $p_t(D^\star)$ the two lower p_t cuts were combined with a ΔM cut of < 180 MeV and the high p_t cut with < 280 MeV. For the case that the algorithm has not terminated with a positive decision after $100\mu s$ the event is rejected and the readout stopped. A detailed description of the FTT L3 system can be found in [Jun04] and [Nau03].

3.8 HFS Reconstruction

The tracks of the hadronic final state (HFS) particles and their energy is measured in the trackers and the calorimeters, respectively.

The 'Hadroo2' algorithm [MP05] realizes the reconstruction of the HFS particles by combining the informations of the tracker and calorimeter with simultaneously keeping the best measurement. The biggest problem while combining the tracks and clusters is to avoid double counting of the energy. This problem occurs when the energy is measured in the calorimeter and in the tracking devices. The decision criteria whether to use the cluster or track information is given by the energy resolution of the corresponding devices. In order to derive a unique decision criteria, the algorithm assumes that each track originated from a pion. The energy of the track is given by $E_{track} = \sqrt{p^2_{track} + M_\pi}^2$ and the error on the track can be calculated using standard error propagation and depends on the uncertainty of the measurement of the transverse momentum p_t and the angle θ of the track. The expected error of the cluster is estimated under the assumption that this track would be measured with the track energy E_{track} in the calorimeters. By comparing both errors a decision is derived whether to use the tracker or calorimeter measurement.

Chapter 4

Reconstruction of $D^\star$ Mesons

In this analysis charm quarks are tagged by $D^\star$ mesons which decay via the Golden Decay Channel: $D^{\star\pm} \to D^0\pi^\pm_{slow} \to K^\mp\pi^\pm\pi^\pm_{slow}$. This decay mode has a comparatively low branching ratio. Nevertheless, it has an advantage concerning the reconstruction of $D^\star$ mesons given by the fact that all particles in the final state cary an electrical charge and are therefore measurable in the tracking devices. A further characteristic feature of this decay mode is, that due to the low mass difference between the $D^\star$ and the D^0 meson the pion from the $D^\star$ decay is produced just above its mass threshold. This results in a low transverse momentum of the pion[1] which is precisely measureable. This circumstance is exploited during the reconstruction of the $D^\star$ meson signal within the so-called Mass Difference (ΔM) method. On the basis of this method, the resolution of the extracted $D^\star$ meson signal is dominated by the resolution of the π_{slow} track measurement. Since all sets of three tracks with correct charges in the events are used the $D^\star$ signal is superimposed by a large amount of combinatorial background.

In the beginning of this chapter the ΔM method is introduced. Subsequently, this chapter concentrates on the extraction of the $D^\star$ meson signal. Here the advantages and disadvantages of different techniques will be discussed. The chapter closes with a discussion of the selection criteria which have been applied to reduce the combinatorial background.

4.1 The Mass Difference Method

The $D^\star$ mesons which decay via ($D^{\star\pm} \to D^0\pi^\pm_{slow} \to K^\mp\pi^\pm\pi^\pm_{slow}$) are reconstructed using the so-called Mass Difference Method (ΔM), which allows a signal measurement of the $D^\star$ mesons with a high resolution. In the beginning of the reconstruction procedure the decay of the D^0 meson into a kaon and an oppositely charged pion is reconstructed. For this purpose the invariant mass is calculated for all possible combinations of two tracks in the event under the mass hypothesis of a kaon or pion candidate, respectively. Subsequently, those combinations are selected which correspond to the mass of the D^0 meson of $M(D^0) = 1864.5 \pm 0.4$ MeV [Yao06] within a mass window of 400 MeV. A third track is added to the tracks of the already identified kaon and pion candidates with the attempt to find the track which corresponds to the slow pion. Hence only tracks are added under the mass hypothesis of a pion which have the same charge sign as the pion track from the D^0 decay. In the invariant mass distribution of the three track system a peak due to real $D^\star$ mesons is expected at the nominal mass of the $D^\star$ meson. In practice unfortunately a high amount of combinatorial background and bad resolution makes it nearly impossible to resolve a $D^\star$ meson signal in this distribution.

At this stage of the reconstruction procedure the inherent advantage of the Golden Decay Channel, which is given by the fact that the slow pion has a relatively low momentum and

[1] The pion is therefore referred to as the slow pion (π_{slow}).

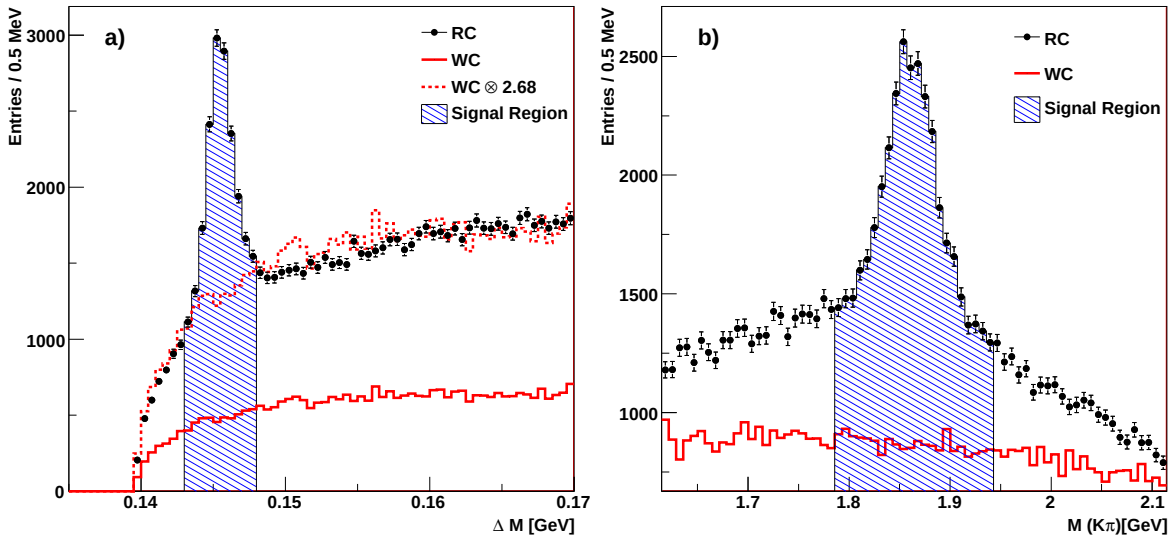

Figure 4.1: *ΔM (a) and (b) $M(K\pi)$ distributions determined after all selection cuts applied in this analysis. The RC distribution is represented by the points and the WC by the solid histogram. The signal region in the ΔM and $M(K\pi)$ distribution is displayed by the dashed area. The dashed histogram in the ΔM distribution represents the WC distribution scaled to the height of the RC distribution.*

can therefore be precisely measured is exploited. The invariant mass difference between the three body decay of the $D^\star$ and the two body decay of the D^0 meson is calculated:

$$\Delta M = M(K\pi\pi_{slow}) - M(K\pi). \tag{4.1}$$

By this method the experimental uncertainties of the kaon and pion candidates cancel to a large extent, such that the uncertainty of the measurement is approximately given by the uncertainty of the slow pion track. Nevertheless the amount of combinatorial background is still too large to resolve a significant signal. In the context of this analysis the combinatorial background has been further suppressed by a stronger restriction of the mass window to ± 80 MeV around the nominal D^0 mass. On the one hand this additional requirement improves the signal to combinatorial background ratio of the ΔM distribution significantly. On the other hand it has to be considered that the width of the D^0 signal amounts to $\simeq 30$ MeV, hence a fraction of events containing real $D^\star$ mesons is rejected from the analysis due to this tightened D^0 mass window selection. Since Monte Carlo simulations are used to correct for these losses, it is essential that the width of the D^0 signal is described in the simulation. The influence of this cut on the final measurement is studied in detail in section 7.4.

The data sample obtained with the above described algorithm will be called the right charged (RC) sample. Figure 4.1 a) shows the ΔM distribution of the RC sample (points) after all selection cuts applied in this analysis. Due to a minimal energy necessary to produce the slow pion the ΔM distribution shows a threshold behavior at the pion mass $m_{\pi^\pm} = 139.5702 \pm 0.0004$ MeV [Yao06]. A clear signal, which corresponds to $D^\star$ mesons decayed in the Golden Decay Channel, is observed at the position of the invariant mass difference $m_{D^{\star\pm}} - m_{D^0} = 145.421 \pm 0.010$ MeV. The width of the signal is given by the limited detector resolution and amounts to $\simeq 0.8$ MeV. The shape of the signal is not symmetric, the left side can be described by a gaussian whereas a tail towards higher values of ΔM is observed. This can be explained by the fact that the energy provided by the $D^\star$ meson

decay is just above the mass threshold which is needed to produce the slow pion. The signal can therefore only be shifted towards higher masses. Figure 4.1 b) shows the $M(K\pi)$ distribution of the $D^\star$ candidates, without a cut on D^0, found in the signal region of the ΔM ($143 < \Delta M < 148$ MeV) distribution. A clear peak is observed at the invariant mass of the D^0 meson at $m(D^0) = 1.8645$ GeV. Due to a cut on the invariant mass of the D^0 meson in the online selection by the level 3 system of the FTT (see section 3.7) the combinatorial background is falling on the left and right side of the signal. The events in the signal region $m(D^0) \pm 80$ MeV, illustrated by the dashed area, correspond to the events in the ΔM distribution in figure 4.1 a).

In addition to the RC sample a second sample is reconstructed in the context of this analysis. In contrast to the reconstruction of the RC sample, the tracks of the kaon and pion candidates from the D^0 decay are combined such, that the same charge for these tracks is required. The third has to have the opposite charge sign as the pion track. This particle combination does not correspond to any decay mode of the $D^\star$ meson and is referred to as the wrong charged sample (WC). Nevertheless it is expected that the shape of the WC distribution is similar to the shape of the combinatorial background of the RC distribution since it is based on the same track combinatoric. In figure 4.1 a) the ΔM distribution of the WC sample is displayed by the solid histogram. As expected no $D^\star$ signal is found in this distribution. The amount of events is significantly lower than the amount of events found in the RC sample. This can be explained by the fact that the algorithm used in the online selection of the level 3 system of the FTT does not select wrong charged pion and kaon candidates. The $D^\star$ meson candidates in the WC distribution are found in events in which the level 3 system triggered on a RC $D^\star$ candidate. The dashed histogram in figure 4.1 a) represents the WC distribution scaled to the height of the combinatorial background of the RC distribution. The scale factor is determined to 2.68 by comparing the last 30 intervals of the RC and WC distribution. It can be seen that the WC distribution has a very similar shape as the combinatorial background of the RC distribution. In the context of this analysis the WC distribution is used in the process of the $D^\star$ signal extraction to determine the combinatorial background in the signal region of the right charged distribution.

4.2 Determination of the number of $D^\star$ Mesons

The ΔM distribution depicted in figure 4.1 shows that the $D^\star$ signal is superimposed by a large amount of combinatorial background. In order to determine the number of real $D^\star$ mesons the amount of underlying combinatorial background in the signal region has to be determined and subtracted from the RC distribution. In the context of this analysis two methods have been used. These are the so-called statistical substraction method and a method which parameterizes the ΔM-distribution.

Statistical Subtraction Method

The statistical substraction method makes use of the fact that the WC distribution has a similar shape as the combinatorial background in the RC distribution. The number of $D^\star$ mesons is determined by statistically subtracting the combinatorial background of the WC distribution from the RC distribution, where the WC distribution has been scaled to the height of the combinatorial background of the RC distribution beforehand. This subtraction is performed for each interval i of a certain variable x seperately. That means in particular that the normalization factor R^i_{norm}, used to scale the WC distribution, is calculated for

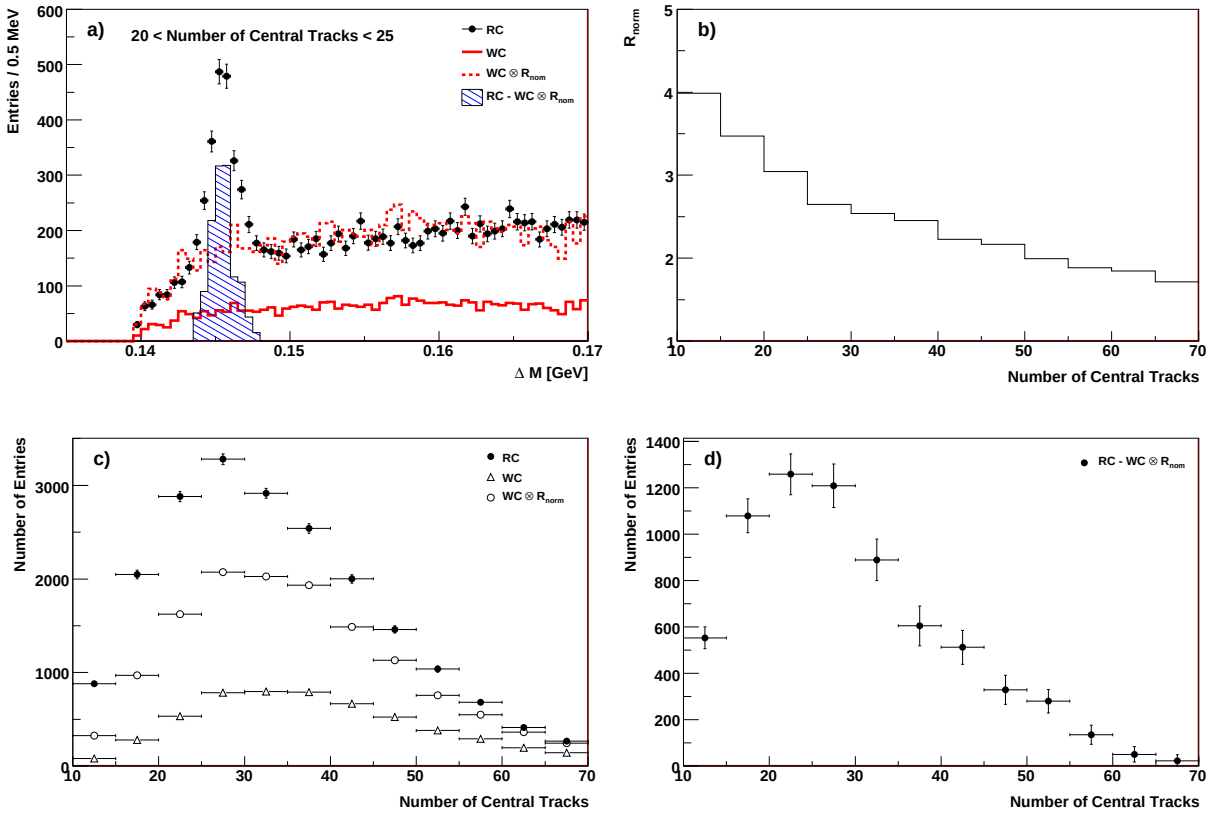

Figure 4.2: *Illustration of the statistical substraction method on the basis of the number of tracks in the central track detector n_{tracks}. Figure (a) shows the ΔM distribution determined in the interval $25 < n_{track} < 30$ for the RC (points), WC (solid histogram) and the scaled WC (dashed histogram) sample. The $D^\star$ signal determined by subtracting the scaled WC from the RC distribution is illustrated by the dashed area. (b) R_{norm} as function of n_{tracks}. (c) RC (points), WC (open triangles) and scaled WC (open circles) distribution as function of n_{tracks}. The $D^\star$ signal distribution as function of n_{tracks} is displayed in (d).*

each individual interval i. This procedure ensures that possible deviations in the kinematic behavior of the $D^\star$ meson candidates in the right charged background and the wrong charged distribution are absorbed in the normalization factor. The normalization factor is determined by adding the content a_j^{RC} and b_j^{WC} of the last thirty bins j of the right charged and the wrong charged ΔM distribution in the interval i of the variable x, respectively. The ratio of these quantities defines the normalization factor in the interval i:

$$R_{norm}^i = \left. \frac{\sum_j^{30}(a_j^{RC})}{\sum_j^{30}(b_j^{WC})} \right|_i \tag{4.2}$$

In order to avoid subtracting large numbers, which would result in large statistical errors, only $D^\star$ meson candidates in the signal region ($143 < \Delta M < 148$ MeV) of the ΔM distribution are taken into account in the subtraction. The statistical error of the number of $D^\star$ mesons in interval i is calculated on the basis of Gaussian error propagation.

In figure 4.2 the statistical subtraction method is illustrated for the number of central tracks n_{track} measured in the CJC. In figure 4.2 (a) the RC and WC distribution is displayed for the interval $20 < n_{track} < 25$. The normalization factor R_{norm} in this interval is calculated to 3.04. The $D^\star$ signal which has been determined by subtracting the scaled WC

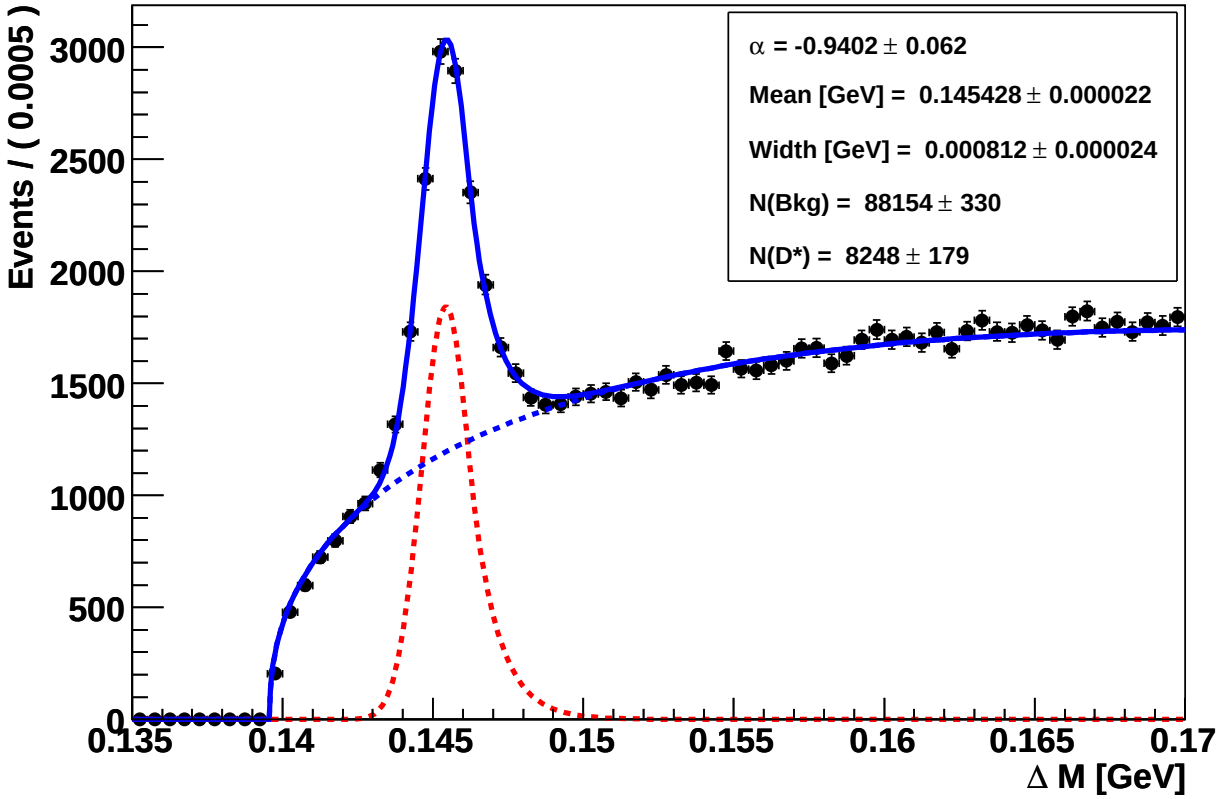

Figure 4.3: *ΔM distribution of all selected $D^\star$ meson candidates in the inclusive sample with the fitted parameterization described in the text.*

distribution from the RC distribution is illustrated by the dashed area. The factor R_{norm} differs from the factor for the total sample (see figure 4.1) which had been calculated to 2.68. The normalization factor R_{norm} as function of n_{track} is displayed in figure 4.1 b). This distribution shows that the amount of events in the WC sample compared to the combinatorial background in the RC sample is rising towards higher values of n_{track}. In figure 4.2 (c) the RC, WC and the scaled WC distribution is displayed. Figure 4.2 (d) shows the final distribution of the $D^\star$ meson signal as function of n_{track}.

The advantage of the method of statistical subtraction is that it is applicable in cases where the statistics of the ΔM distribution is not adequate for a parameterization. A disadvantage of this method is that the subtraction of the two distributions leads to large statistical errors. The more precise method given by a parameterization of the ΔM distribution is introduced in the following.

Parameterization of the ΔM distribution in Data

The parameterization used, to determine the number of $D^\star$ mesons, consists of a sum of two functions. One function is used to describe the combinatorial background and the second to describe the signal. This parameterization has first been used in a previous analysis of $D^\star$ production in DIS and is in detail described in [Boe07].

The function implemented to describe the signal is given by the asymmetric density function[2] $f_{CB}(\Delta M)$. This parameterization takes the asymmetric behavior of the $D^\star$ meson

[2]This function was first used by the Crystal Ball Collaboration to describe the tail in $J/\psi \to e^+e^-$.

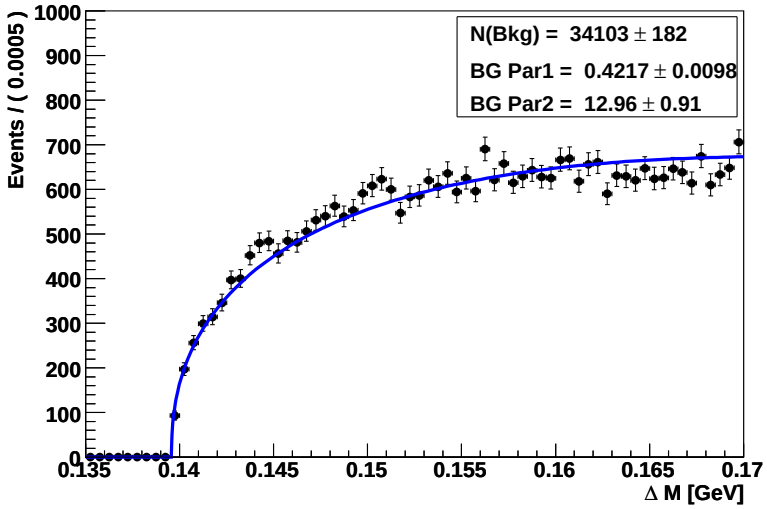

Figure 4.4: ΔM *distribution of all selected WC candidates in the inclusive sample with the fitted parametrization described in the text.*

signal observed in figure 4.1 into account. It is composed of a gaussian function, to describe the behavior towards low values of ΔM and the peak region and a power law to describe the asymmetry of the $D^\star$ signal towards large values of ΔM. The function is given by the following formula:

$$f_{CB}(\Delta M) = N \cdot \begin{cases} \exp\left(-\frac{1}{2}\left(\frac{\Delta M-\mu}{\sigma}\right)^2\right) & \text{if } \frac{\Delta M-\mu}{\sigma} \leq \alpha \\ \frac{\left(\frac{n}{|\alpha|}\right)^n \exp\left(-\frac{1}{2}\alpha^2\right)}{\left(\frac{n}{|\alpha|}-|\alpha|-\frac{\Delta M-\mu}{\sigma}\right)^n} & \text{if } \frac{\Delta M-\mu}{\sigma} > \alpha. \end{cases} \tag{4.3}$$

Here N denotes the normalization parameter of the function, the parameter μ corresponds to the most probable value and σ denotes the width of the Gaussian part of the distribution. The variables n and α define the form of the tail. The falling power law is located on the right side of the signal for negative values of α and on the left side for positive values of α. The amount of $D^\star$ mesons is determined by a numeric integration of the signal function.

A good description of the shape of the combinatorial background is given by the Granet parameterization [Gra78]:

$$f_{Gr}(m) = p_0 \cdot (m - m_\pi)^{p_1} \cdot e^{(-p_2 m - (p_3 \cdot m^2))} \tag{4.4}$$

Here p_0 denotes the normalization while p_1, p_2 and p_3 define the shape of the distribution. The parameter p_3 is not used and set to zero. The wrong charge distribution helps to constrain the parameters p_1 and p_2. Therefore the sum of both functions 4.3 and 4.4 is fitted to the right charge distribution and simultaneously function 4.4 is fitted to the WC distribution, whereby only the parameter p_0 of equation 4.4 is allowed to vary between the RC and the WC parameterization. An additional constraint is given by the condition that the integral of the sum of the two functions is consistent with the number of entries in the histogram. The parameterization is provided by the software package `RooFit`. The parameters are determined by an unbinned negative log likelihood fit. The `RooFit` package

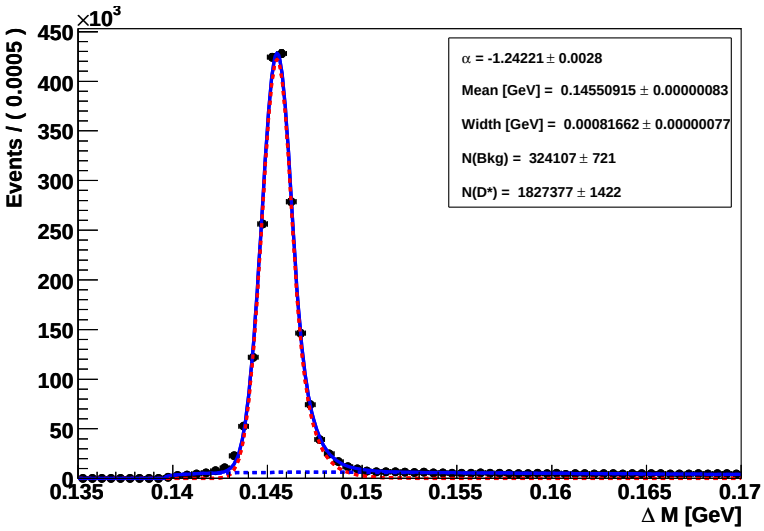

Figure 4.5: *ΔM distribution of all selected $D^\star$ meson candidates in the Pythia (massless) simulation. The number of signal events is extracted by the parameterization described in section 4.2.*

provides the numeric integration of the signal and the combinatorial background for each iteration step. The result of the fit to the total data sample is depicted in figures 4.3 for the RC and in 4.4 for WC distribution. The asymmetric signal parameterization as well as the parameterization of the combinatorial background gives a good description of the data. The fit yields a number of $D^\star$ mesons of 8249 ± 179. The width is determined to 0.812 ± 0.024 MeV.

Monte Carlo Treatment

The Monte Carlo samples used in this analysis are so-called signal Monte Carlos samples, which contain only events with charm quarks produced in the processes depicted in figure 2.5. Processes with only light flavors in the final state are not generated. Furthermore only those events are selected on generator level which contained $D^\star$ mesons decayed in the Golden Decay Channel. That means in particular that each event of the Monte Carlo samples contains at least one $D^\star$ meson decayed via $D^{\star\pm} \to \pi^\pm_{slow}\pi^\pm K^\mp$ [3]. The amount of combinatorial background is therefore only caused by additional random combinations in these events. It is therefore stronger suppressed over the whole ΔM spectrum and has also a different shape than the combinatorial background in the data. This has been taken into account by a different parameterization of the combinatorial background in the Monte Carlo than in the data. The following parameterization has been chosen (for details see [Boe07]):

$$f_{MC}(m) = p_0 \cdot (m - m_\pi)^{p_1} \cdot e^{(-p_2(m-m_\pi) - p_3(m-m_\pi)^2)} \tag{4.5}$$

In comparison to equation 4.4 an additional parameter p_3 has been introduced. This, together with the quadratic term leads to a stronger damping for large values of ΔM, which results in a better description of the ΔM distribution. For the signal the same parameterization (see equation 4.3) as for the data has been used. The result of the fit to a sample provided by the Pythia (massless) simulation is depicted in figure 4.5. The asymmetric signal parameterization as well as the parameterization of the combinatorial background gives

[3] In a very small fraction of events two $D^\star$ mesons are found.

a good description of the ΔM spectra. Furthermore it is remarkable that the determined width of 0.8166 ± 0.0008 MeV of the signal is within the uncertainties consistent with the width determined in data (see figure 4.3).

4.3 Quality of the Track Simulation

As described in section 4.1 the measurement of $D^\star$ mesons is solely based on the measurement of the three tracks of the corresponding decay particles. Thus a precise reconstruction of the tracks is essential to determine a $D^\star$ meson signal with a high resolution. Furthermore a good description of track parameters by the Monte Carlo simulation is important since Monte Carlo simulations are used to correct for inefficiencies in the track finding. Deviations in control distributions of track parameters indicate that inefficiencies of the track finding in the data are not correctly simulated in the Monte Carlo.

The hit information provided by the central tracking devices, CJC, CST and CIZ are the basis of the track reconstruction. In figure 4.6 a)-c) the distributions of the number of reconstructed hits n_{hit} corresponding to the tracks of the daughter particles of the $D^\star$ meson are displayed. In these distributions a double peak structure is observed. The peaks are located at $n_{hit} \simeq 22$ and $n_{hit} \simeq 55$. The second peak is much more prominent in the n_{hit} distributions corresponding to the pion and kaon than in the distribution of the slow pion candidate. The peaks are reproduced for the kaon and pion distribution by the Monte Carlo simulation, whereas the first peak is overestimated and the second peak is underestimated in the Monte Carlo for the slow pion candidate.

In order to understand the different height and shape of the slow pion distribution compared to the pion and kaon distribution it is useful to investigate a further variable given by the radial track length r_{rad}. The radial track length of the three decay particles of the $D^\star$ meson is displayed in figure 4.6 d)-f). Both quantities, n_{hit} and r_{rad}, are related to each other since a longer track corresponds in general to a higher amount of hits. Hence also in the r_{rad} distributions a double peak structure is observed. The two peaks at 20 cm and 60 cm can be explained with the radial size of the CJC1 and CJC2, respectively. The first peak is caused by particles which are not reaching the CJC2, because they are absorbed or scattered in the dead material between both trackers. The size of the first peak is small compared to the peak at 60 cm, from this it can be concluded that the particles reach the CJC2 in most of the cases. Since it is more likely that particles with low momentum are absorbed or scattered in the dead material, the first peak is significantly higher for the π_{slow} candidate than for the kaon or pion candidate. The second peak in the n_{hit} distribution of the slow pion is broader in Monte Carlo than in data, whereas a similar width is observed for the first peak in data and Monte Carlo. Since the track efficiency is mainly influenced by tracks with small n_{hit} values, only a marginal influence of the second peak on the efficiency is expected.

Further important track parameters are the reconstructed transverse momentum and the polar angle θ of the tracks. The corresponding control distributions are displayed in figure 4.7. Since the amount of statistic in the individual intervals is large, the combinatorial background has been subtracted according the parameterization described in section 4.2. The amount of tracks is decreasing, for large and small values of θ. This can be explained on the one hand by the fact that the acceptance of the CJC is reached in the first and last bin, on the other hand by the requirement that the $D^\star$ is measured in the central region. The applied cut on the $D^\star$ corresponds to $|\eta(D^\star)| < 1.5$, which restricts the $D^\star$ to the central region. Within this analysis only tracks which are measured within the central

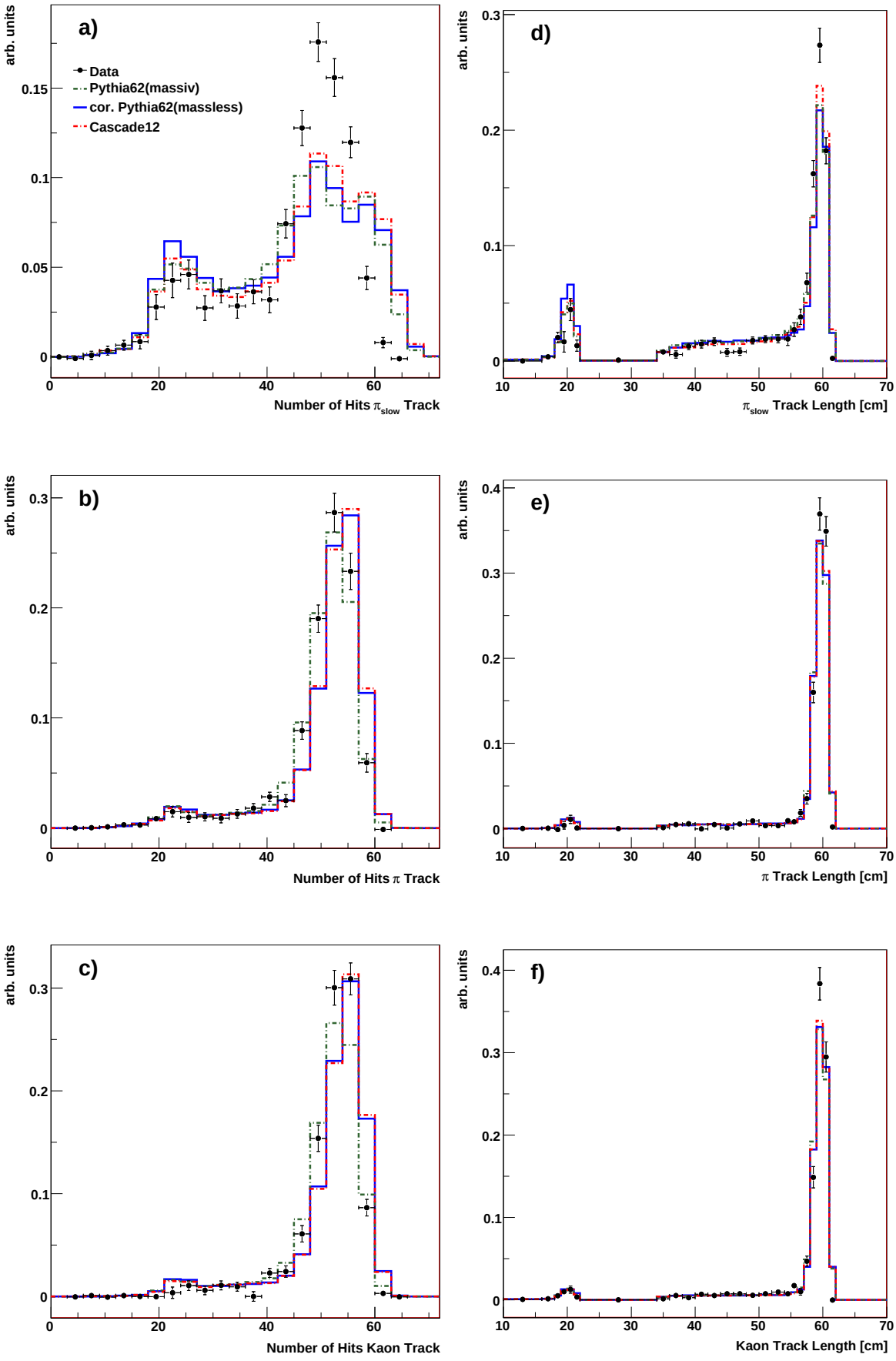

Figure 4.6: *Control distribution as a function of the number of track hits a)-c) and the radial track length d)-f) for the π_{slow}, π and the kaon candidate. The data (points) is compared to the prediction given by the Pyhtia (massless), Pythia (massive) and Cascade simulation. The combinatorial background is statistically subtracted (see section 4.2).*

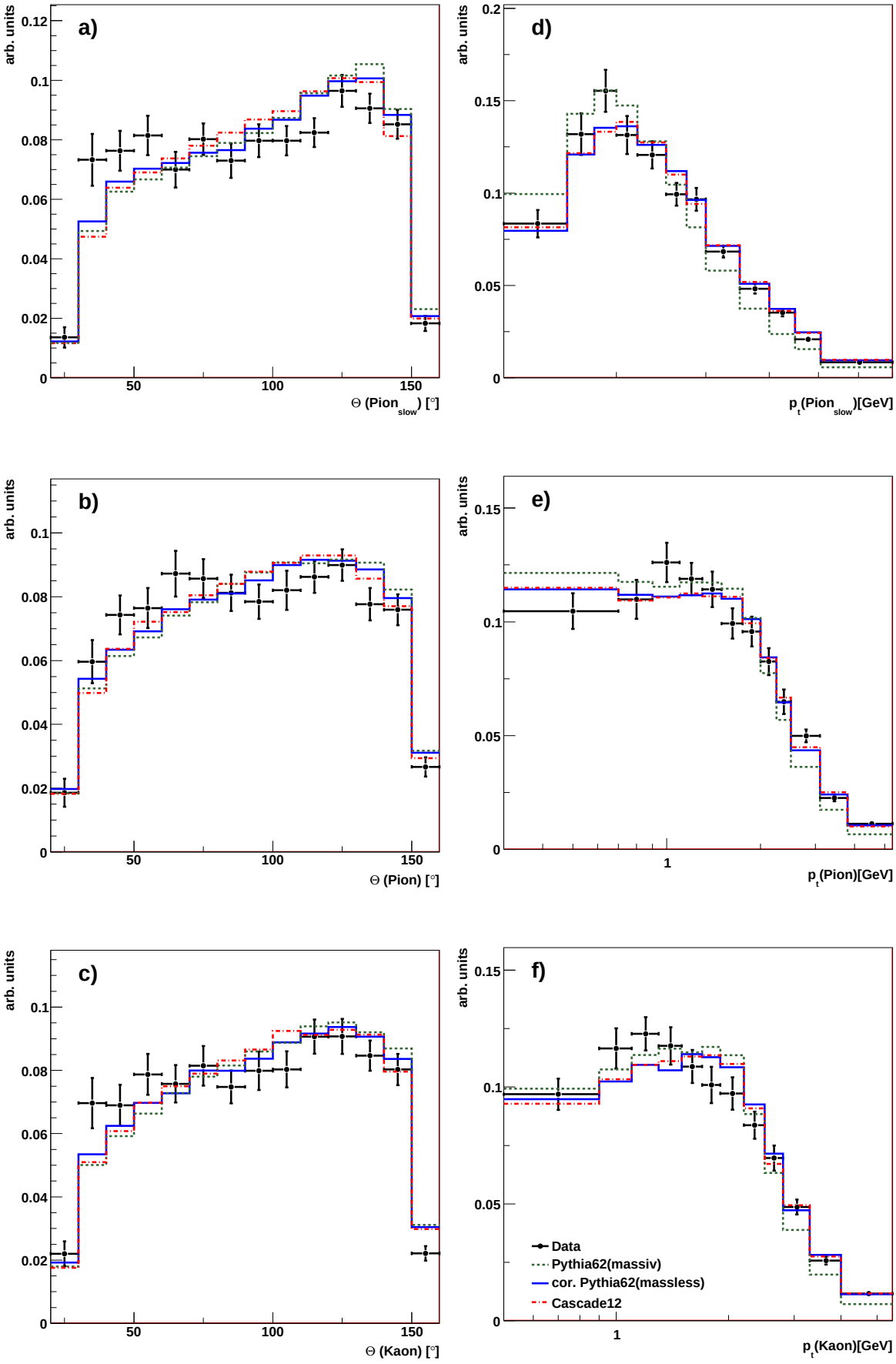

Figure 4.7: *Control distribution for the decay products of the $D^\star$ meson as a function of the polar angle Θ of the tracks a)-c) and the transverse momentum d)-f). The data is compared to the prediction provided by the Pythia (massless), Pythia (massive) and Cascade prediction. The signal is determined by the parameterization described in section 4.2.*

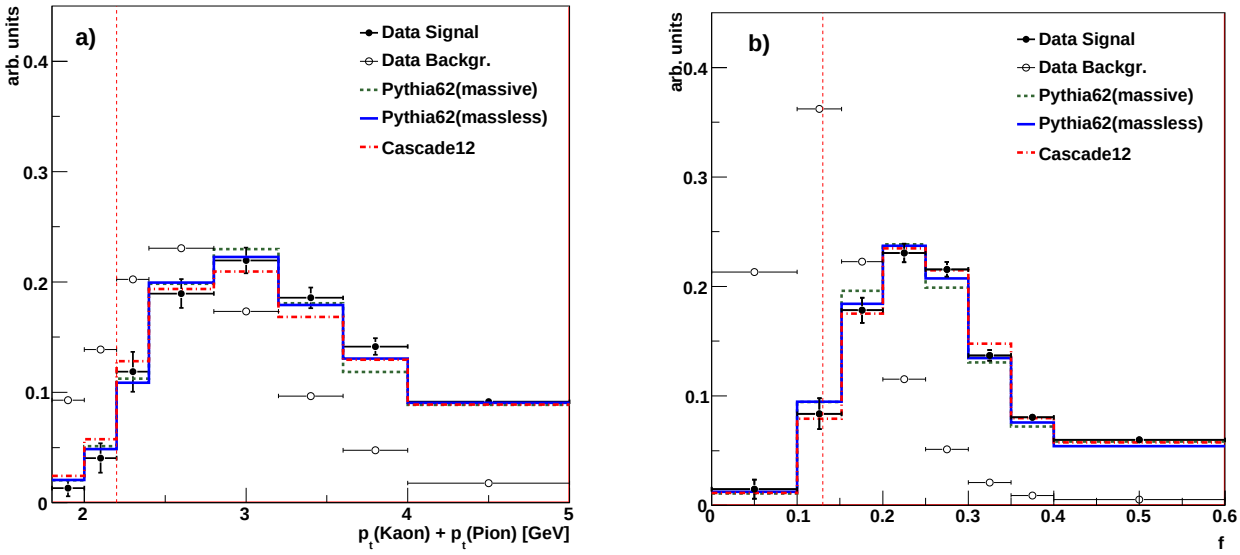

Figure 4.8: *Control distributions as function of the the variables $p_t(K)+p_t(\pi)$ (a) and f (b) The $D^\star$ signal distribution determined in the data is represented by the full points and the Monte Carlo predictions by the lines. The combinatorial background of the right charge data sample is shown by the open circles. The cut values applied in this analysis are indicated by the vertical dotted line. All distributions are area normalized.*

tracking devices are taken into account. Thus only tracks with a polar angle Θ in the range of $20^\circ - 160^\circ$ are selected. The transverse momentum spectra of the daughter particles of the $D^\star$ meson are displayed in figure 4.7 d)-f). The distributions are in general well described by the Monte Carlo. In particular a good description of the low momentum region by the Monte Carlo is important, since here the detector inefficiencies are largest.

Due to the observed deviations concerning the number of track hits and the track length a systematic uncertainty corresponding to the track finding efficiency is expected. This uncertainty is one of the dominant uncertainty sources of this analysis. If for instance, the track finding efficiency is systematically too high or too low in the Monte Carlo, presumably all tracks are affected and the uncertainty is assumed to be correlated. That means in particular for this analysis, that this error has to be multiplied with three, due to the three daugther particles of the $D^\star$ mesons (see section 7).

4.4 Background Reduction

The amount of combinatorial background in the differential ΔM distribution increases towards low transverse momenta of the $D^\star$ mesons and the forward region of the H1 experiment due to steeper rising rates of of light quark production compared heavy quark production in this regime of phase space. Neglecting the small transverse momentum of the slow pion candidate a strong correlation between the scalar sum of the transverse momentum of the pion and kaon candidate and the transverse momentum of the $D^\star$ meson candidate is expected. Figure 4.8 shows the control distribution as function of the variable $p_t(K) + p_t(\pi)$. The Monte Carlo describes the data reasonably well. In addition to the signal distribution the distribution of the combinatorial background of the data is displayed. The comparison of the signal and background distribution shows that the signal to background ratio decreases

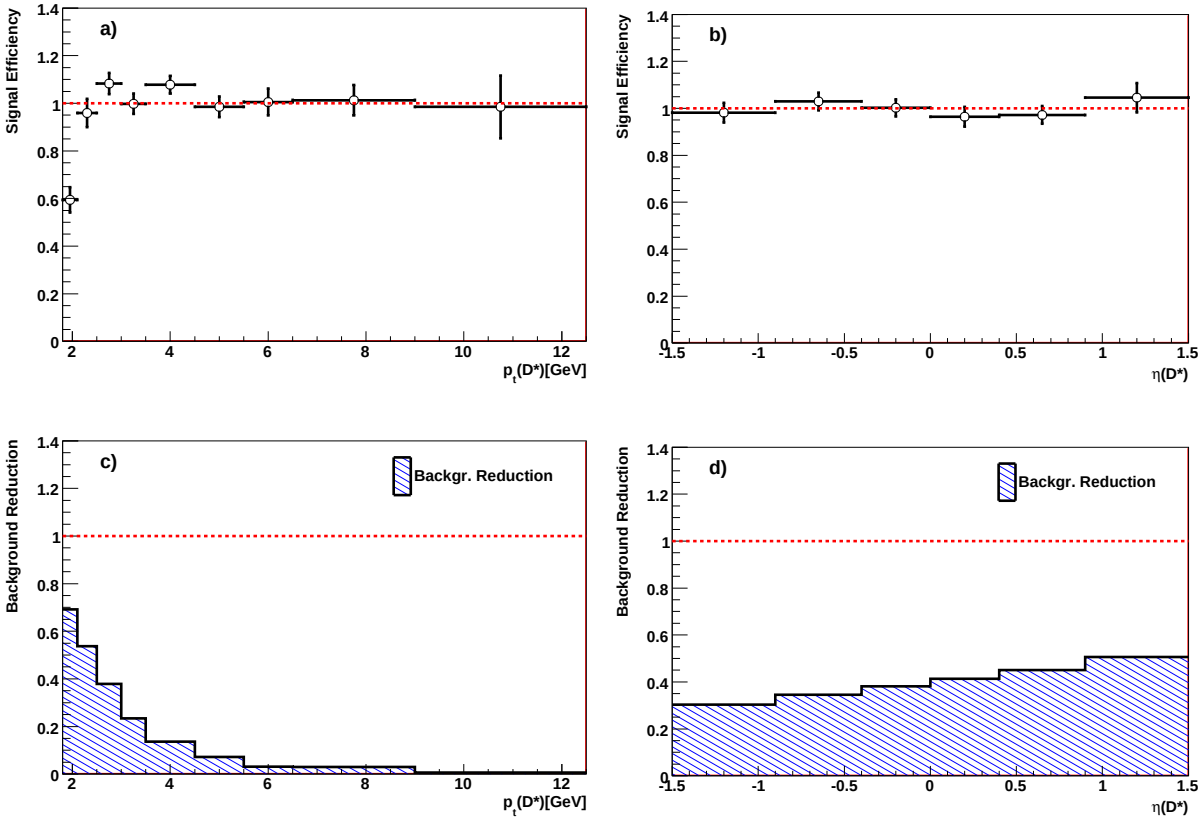

Figure 4.9: *Signal efficiency a)-b) and reduction of the combinatorial background c)-d), due to a cut on the quantity f, as a function of the transverse momentum and the pseudorapidity of the $D^\star$ meson.*

towards small values of $p_t(K) + p_t(\pi)$ and that on average an improvement of the ratio is possible by a cut on this quantity. In the context of this analysis only $D^\star$ meson candidates are taken into account with $p_t(K) + p_t(\pi) > 2.2$ GeV.

Due to a harder fragmentation of charm compared to light flavors, it is expected that $D^\star$ mesons carry a large part of the hadronic final state energy of the event. Thus a further reduction of the combinatorial background can be achieved by constraining the transverse momentum of the $D^\star$ meson to the sum of the transverse momenta of all particles in the hadronic final state by the quantity f:

$$f = \frac{p_t(D^\star)}{\sum_i^{\theta>10^\circ} E_i \cdot \sin\theta_i}. \tag{4.6}$$

Here E_i denotes the energy and θ_i the polar angle of a particle i in the hadronic final state. By selecting only particles with a polar angle $\theta > 10^\circ$, contributions from the proton remnant are reduced. Figure 4.8 b) shows the $D^\star$ signal as a function of the variable f for data and the Monte Carlo prediction given by the Pythia (massless), Pythia (massive) and Cascade simulation. The combinatorial background in the data and Monte Carlo distribution has been subtracted for each interval of the distribution by the parameterization as described in section 4.2. The Monte Carlo predictions are in good agreement with the data within the uncertainties. The distribution of the $D^\star$ signal is rising towards larger values of f with a maximum at around $f_{max} \simeq 0.20 - 0.25$. In addition to the $D^\star$ signal distribution, the combinatorial background of the right charge data sample is shown in figure 4.8. The

distribution of the combinatorial background is located at small values of the quantity f with a maximum at around $f = 0.10 - 0.15$. Therefore the quantity f is well suited to separate the signal from the combinatorial background. Within this analysis a cut $f > 0.13$ is applied. According to figure 4.8 a small reduction of the total $D^\star$ meson signal and a drastically reduction of the combinatorial background of around 55% is expected.

Figure 4.9 shows the influence of the cut $f > 0.13$ as a function of the transverse momentum and the pseudorapidity of the $D^\star$ mesons. In particular the efficiency of the $D^\star$ meson signal 4.9 as a function of p_t a) and η b) is displayed. The reduction of the combinatorial background is shown in 4.9 c) and 4.9 d). Here the number of $D^\star$ mesons before and after the cut on the quantity f is determined on the basis of the statistical substraction method, since the large amount of combinatorial background towards low p_t in the sample without a requirement on f does not allow parameterization. A significant signal loss of $\simeq 40\%$ is observed in the first p_t bin. The absolut number of $D^\star$ mesons, with a cut on $f > 0.13$, in this bin yields $N(D^\star) = 442 \pm 60$ and without a cut on f it amounts to 618 ± 122. Compared to the total number of $D^\star$ mesons, the reduction in this bin corresponds to a reduction of 2.0% of the total sample. Within the statistical error no signal loss is observed in the $\eta(D^\star)$ distribution. The combinatorial background reduction is highest at low transverse momenta, where it amounts to $\simeq 70\%$ in the first bin, and in the forward region, where it amounts to $\simeq 50\%$ in the last η bin.

A further background reduction could be achieved by using the information of the specific energy loss dE/dx of the charged particles in the tracking detectors. The combinatorial background reduction power of the dE/dx information has been studied within this analysis (see chapter A). However, since no dE/dx simulation is available, the cuts applied in data must be so efficient that the signal loss is negligible. Thus the cuts are so loose that only a small background reduction is achieved. Accordingly, the cuts were not applied in the order to keep the systematic uncertainty small.

Chapter 5

Data Selection

To introduce the data analysis procedure the selection criteria will be discussed in this chapter. In the beginning of the selection procedure, problematic parts of the data taking period are excluded from the analysis. Afterwards the selection of photoproduction events will be discussed. Subsequently this chapter deals with the trigger selection. In the end of The chapter closes with a presentation of the final data selection strategy.

5.1 Selection of the Runperiod

The analysis presented in this thesis is based on a data sample which was recorded with the H1 experiment from September 2006 to June 2007.

Events were collected in so called luminosity fills. A luminosity fill started with the filling of electron and proton bunches into the HERA accelerator and it ended when the beams were lost or dumped. The luminosity fills are divided in luminosity runs. A luminosity run is a part of the data taking period in which the status of the H1 detector was stable. Depending on the detector status the luminosity runs were classified into three categories: *good*, *medium* and *poor*. In runs classified as *good* the subdetectors, which are important for the event reconstruction, were fully operational. If for example the CJC had to be switched off during data taking because of high currents the corresponding run was classified as *poor*. In this analysis only runs with the classification *good* or *medium* were used. Furthermore it is required that the following subdetectors were in operation: CJC1, CJC2, TOF, LAr, SpaCal and Lumisystem. In addition only runs which correspond to an integrated luminosity of more than 0.1 μb^{-1} are considered in the analysis, this ensures furthermore the stability of the data taking. The selected data sample corresponds to an integrated luminosity of 113.14 pb^{-1}.

5.2 Selection of Photoproduction Events

In case of the HERA2 setup of the H1 detector the kinematic region of photoproduction is defined as $Q^2 < 2\ \text{GeV}^2$. From the experimental point of view the characteristic of the photoproduction regime is that the electron is scattered under such low angles that it escapes the detector volume undetected. Hence the definition of the photoproduction regime is given by the SpaCal geometry, which is restricted by the beam pipe for the low Q^2. Photoproduction events can therefore be identified by a veto of electron candidates (untagged photoproduction) measured in the SpaCal. In the SpaCal, a scattered electron is defined by a cluster energy deposition greater than 8 GeV and a cluster radius of less than 4 cm. Figure 5.1 a) shows the Q^2 distribution for generated events, with and without an electron veto. The corresponding electron veto efficiency is displayed in figure 5.1 b). The veto efficiency amounts to $\simeq 50\%$ at $Q^2 = 2\ \text{GeV}^2$.

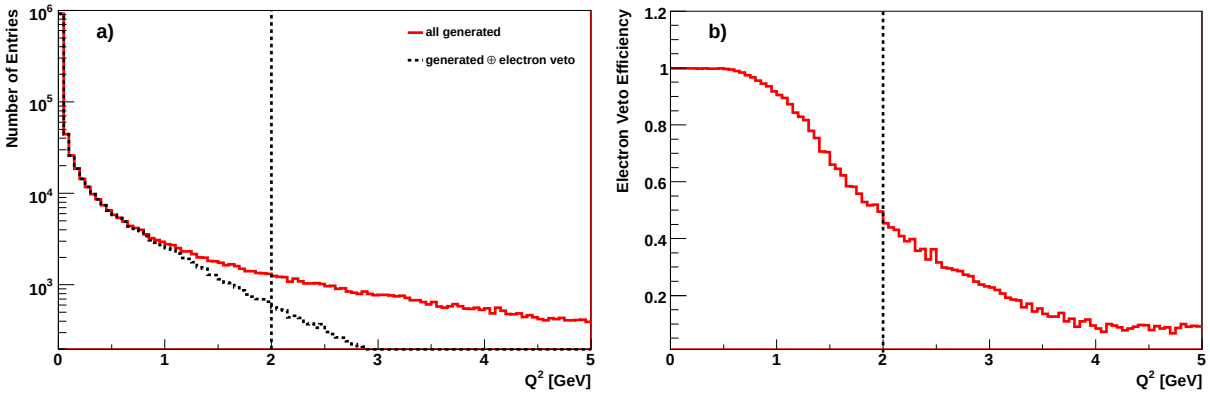

Figure 5.1: *Displayed is the Q^2 distribution (a) without (continuous line) and with an electron veto (dashed line) determined on the basis generated events with the Pythia (massless) simulation. The corresponding electron veto efficiency is depicted in (b). The dashed line indicates the border of the visible range.*

Since the scattered electron is not measured, the kinematic quantities are calculated by means of the HFS particles according the Jaquet-Blondel method [AB79]. In practice unfortunately, some hadrons of the HFS escape the detector volume undetected due to the uncovered regions of the H1 detector. Nevertheless, it was shown in [AB79] that the event kinematic can be calculated using the variable $(E - p_z)_{had}$, which is defined as the difference between the energy E_{had} and the longitudinal momentum $p_{z,had}$ of all particles in the HFS. The characteristic of the quantity $(E - p_z)_{had}$ is that it is by definition insensitive to particle losses in the forward direction, where the particle losses are largest. The quantity y_{had} is defined as $y_{had} = (E - p_z)_{had}/(2E_e)$. The selected range of this analysis is given by $0.1 < y_{had} < 0.8$, which is equivalent to $100 < W_{\gamma p} < 285$ GeV (see equation 2.10). The upper cut ensures that background from deep inelastic scattering is removed from the analysis and the lower cut rejects events in the extreme forward region of the detector. This cut is necessary to guarantee a complete reconstruction of the final state.

In order to inspect the selection of photoproduction events, the quantity $E - p_z$ is investigated. It is expected, that in the case of photoproduction, the quantity $E - p_z$ is distributed below values of 55 GeV. In DIS, where energy and momentum conservation is applicable, a peak is expected at $2E_e$. The peak in DIS normally has a tail towards lower values, since often not all particles are reconstructed. Thus, the variable $E - p_z$ can be used to identify DIS background events in photoproduction analyses and vice versa. Figure 5.2 shows the $E - p_z$ distribution for data and different Monte Carlo Models for all events selected in this analysis. No peak at $2E_e$ is visible in figure 5.2, therefore it can be concluded that the veto on the scattered electron in the calorimeters leads to an efficient selection of photoproduction events.

5.3 Interaction Vertex

The interaction point of an event is determined by reconstructing all tracks of an event and extrapolating them to their origin or vertex. The position of the interaction vertex in the xy plane is given by the beam size and varies only by a few μm, whereas the z coordinate of the reconstructed interaction point is approximately given by a Gaussian distribution, which is extended $\simeq 10$ cm. The reason for this, is the spacial resolution of the proton bunches, which

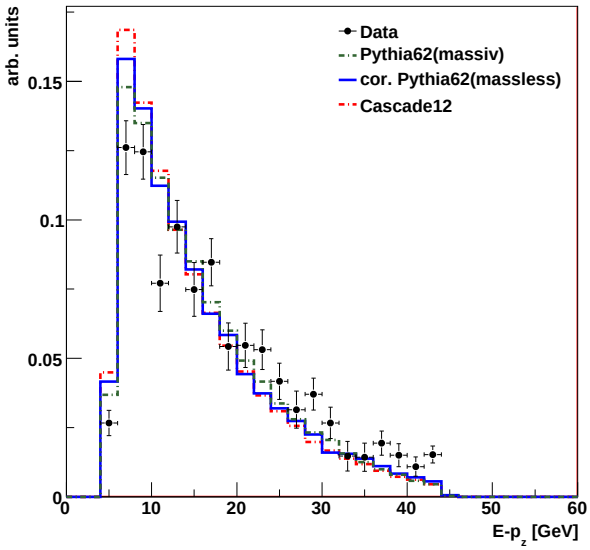

Figure 5.2: *Distribution of the quantity $E-p_z$, the data (points) is compared to the Pythia (massless), Pythia (massive) and Cascade prediction. The number of $D^\star$ mesons is determined on the basis of the statistical substraction method. The Pythia (massless) distribution is corrected as discussed in the next chapter.*

extends over a few micrometers. In addition, the proton bunches are characterized by so-called satelite bunches before and after the nominal proton bunch at approximately ± 70 cm. These satelite bunches are not sufficiently simulated in the Monte Carlo simulation. Thus, a cut on the $z_{vertex} = \pm 35$ cm has been applied in order to suppress events which correspond to interactions with these bunches. Furthermore this cut ensures that interactions with gas molecules or the beampipe are excluded as well. In figure 5.3 a) the z vertex distribution is shown for the data and the Monte Carlo simulation given by the Pythia (massless) prediction. Both distribution are normalized to the amount of events found in data. It can be seen that the z_{vertex} distribution in the simulation (dotted line) is much broader than in data. This takes into account that the width of the z_{vertex} distribution in data varies with the selection applied in a certain analysis. The broader width in the Monte Carlo allows a reweighting of the distribution with small correction factors. Since the description of the z_{vertex} distribution has a direct influence on the detector efficiencies (see chapter 6) of the $D^\star$ mesons, the simulation has been reweighted within this analysis. Figure 5.3 b) shows the ratio of data to Monte Carlo as a function of z_{vertex}. This ratio has been parameterized with a polynominal function and afterwards used to reweight the Monte Carlo on the parton, hadron and detector level. The solid histogram in figure 5.3 a) represents the z_{vertex} distribution after this reweighting. A much better description of the data is achieved after the reweighting, which is essential for a correct determination of the detector efficiencies.

5.4 Trigger Selection

In the kinematic phase space covered by this analysis the scattered electron is not detected. Therefore the online event selection is based on the selection of $D^\star$ meson candidates by the third level of the Fast Track Trigger. On the first and second trigger level, trigger conditions are implemented to achieve an appropriate input rate for the third trigger level. A mix of three subtriggers is used in the context of this analysis, which are referred to as the s55, s53 and s122. They are mainly composed of triggerelements provided by the FTT trigger. In addition CIP triggerelements are in operation on the first trigger level to support the rate reduction capability of the FTT trigger. Table 5.1 gives a summary of the trigger conditions of these subtriggers.

The purpose of the three triggers was to select events containing $D^\star$ meson with different

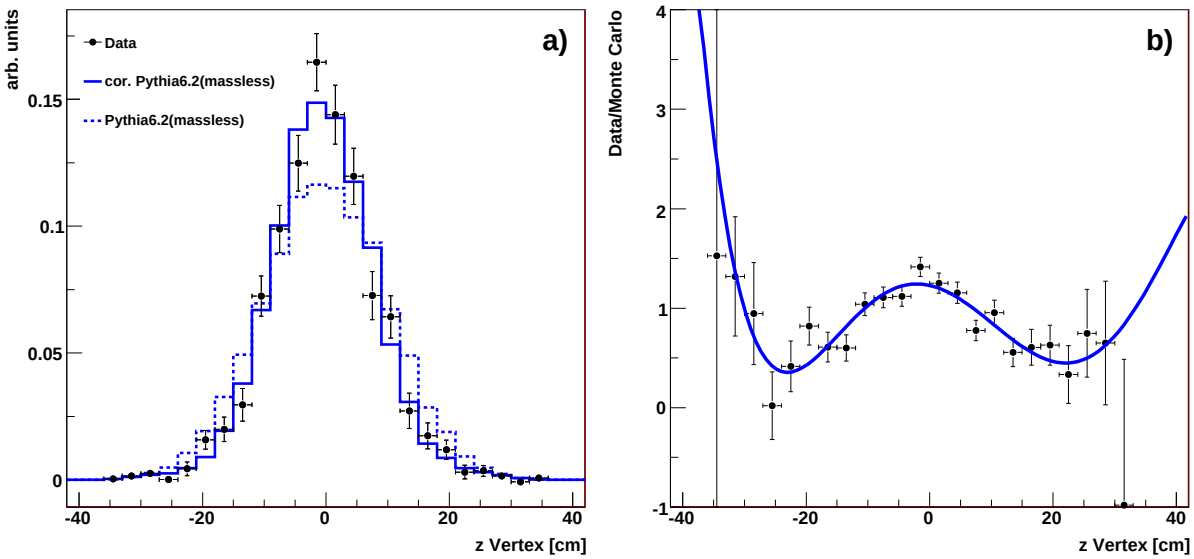

Figure 5.3: *(a) z Vertex distribution for data (points) and for the Pythia Monte Carlo before (dotted histogram) and after (solid histogram) reweighting. The number of $D^\star$ mesons is determined on the basis of the statistical substraction method. Figure (b) shows the ratio Data/MC before correction as a function of the z Vertex, the parameterization (solid line) is used to correct the Monte Carlo.*

transverse momenta. In particular the s55 was designed to select $D^\star$ mesons with low, the s53 with medium and the s122 with high transverse momenta. Due to the rising rates towards low transverse momenta the design focus of the low and medium triggers was placed more on an efficient rate reduction than on a high efficiency, whereas the conditions of the high p_t trigger have been adjusted with the goal to achieve a high efficiency.

An usual event with a $D^\star$ meson candidate consists of a compareable high track multiplicity in the central region. An online selection of those events is possible by triggerelements provided by the CIP trigger. The triggerelements used in this analysis are the so-called *cipmul* and *cipsig* triggerelements. The purpose of the latter is to select events with tracks pointing to the nominal interaction point. It is available in four possible states, which correspond to the ratio between the number of central tracks pointing to the interaction point $N(ctr)$ versus the number of background tracks, which are usually pointing to forward $N(fwd)$ or backward $N(bwd)$ z-direction on the beam line. The triggerelement $cipsig > 2$ means in particular, that the ratio of the amount of central tracks to the amount of background tracks, exceeds a factor of two. The triggerelement $cipmul > 4$ is correlated to the number of central tracks measured by the CIP trigger. Only those events are selected in which the track multiplicity exceeds at least 10 tracks. More information about the CIP trigger can be found in [Urb04]. In coincidence to the CIP trigger elements FTT trigger elements are required on the first level. These triggerelements allow a selection of events based on the amount of tracks above a certain p_t threshold. The condition $FTT\_mul\_Ta > 5$ for instance fires, if an event contains more than five tracks with a transverse momentum of more than 100 MeV. The aim of the conditions on the first level is on the one hand to select events of physical interest at an early stage of the data taking and on the other hand to achieve a significant rate reduction. Note that all three subtriggers used in this analysis are composed of the same triggerelements on the first level. All triggerelements are combined by a logical AND operation.

Subtrigger	*triggerelement*	*definition*
	level 1	
s55, s53, s122	cipmul>4	$N(ctr) + N(bwd) + N(fwd) > 10$
	& cipsig>2	$N(ctr) > 2 \cdot (N(bwd) + N(fwd))$
	& FTT_mul_Ta>5	#tracks > 5, with $p_t > 100$MeV
	& FTT_mul_Tc>2	#tracks > 2, with $p_t > 400$MeV
	& FTT_mul_Td>1	#tracks > 1, with $p_t > 900$MeV
	& FTT_mul_Te>0	#tracks > 0, with $p_t > 1.8$GeV
	level 2	
s55	& FTT_Et_1	total transverse energy > 5.0GeV
	& FTT_mul_Te>1	#tracks > 1, with $p_t > 900$MeV
	& FTT_zVtx>2	
s53	& FTT_Et_2	total transverse energy > 6.5GeV
	& FTT_mul_Te>1	#tracks > 1, with $p_t > 900$MeV
	& FTT_zVtx>2	
s122	& FTT_mul_Te>1	#tracks > 1, with $p_t > 900$MeV
	& FTT_zVtx>2	
	level 3	
s55	& low_pt_D^*_untagged	$p_t(D^*) > 1.5$ GeV with $\Delta M \leq 180$ MeV
s53	& medium_pt_D^*_untagged	$p_t(D^*) > 2.5$ GeV with $\Delta M \leq 180$ MeV
s122	& high_pt_D^*_untagged	$p_t(D^*) > 4.5$ GeV with $\Delta M \leq 280$ MeV

Table 5.1: *Definition of the subtriggers s55, s53 and s122 used in this analysis. Note that the L2 condition FTT_Et_2 of s53 has not been active within the run range* 488631 – 489128*.*

To achieve a further rate reduction, three triggerelements are used on the second triggerlevel, which are all provided by the FTT trigger. These are the conditions FTT_Et_n, $FTT\_mul\_Te > 1$ and $FTT\_zVtx > m$. The latter provides the possibility to use the information of the vertex position of the event, which is determined by extrapolating the tracks reconstructed on the second trigger level to their origin (for details see [Ber06]). The variable m is an index for the quality of the determined vertex. The triggerelement FTT_Et_n fires if the sum of the transverse momentum of all tracks exceeds 5.0GeV or 6.5GeV for $n = 1$ or $n = 2$, respectively. These conditions came into operation for the s55 and s53 in order to cope with the high input rates to the third level. The high rates are caused by the rising rates and larger combinatorics towards low transverse momenta of the $D^\star$ meson candidates.

Based on the preselection on the first and second trigger level, the final search for the exclusive final states of $D^\star$ mesons is performed on the third trigger level. The $D^\star$ meson candidates are identified on the basis of the invariant mass hypothesis of the decay products of the $D^\star$ meson. Three different triggerelements came into operation for the different subtriggers, these differ in the minimal transverse momentum required for the $D^\star$ candidates (see section 3.7) and the allowed ΔM range.

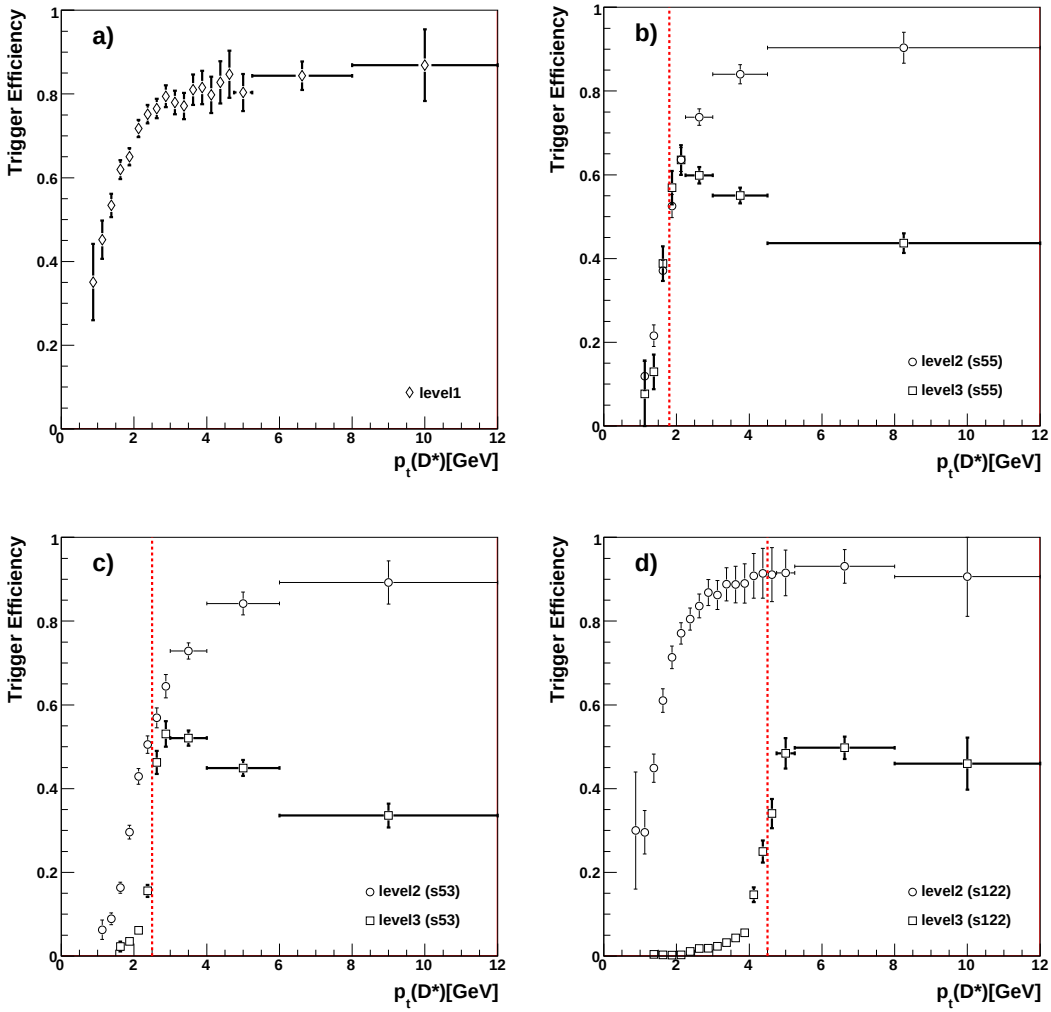

Figure 5.4: *Efficiencies for the triggerelements implemented the subtriggers s55, s53 and s122 as function of the transverse momentum of $D^\star$ meson. The efficiencies are shown for each level and each subtrigger, separately. Efficiency of the first level is shown in (a). The efficiency of the second and third level is shown in figure (b), (c) and (d) for the subtriggers s55, s53 and s122. The dotted line in b)-d) indicates final slection cut applied in this analysis.*

5.5 Trigger Efficiency

To calculate the trigger efficiency an independent sample of signal events is needed, which is selected by so-called monitor subtriggers. To guarantee the independence, the monitor subtriggers must not contain trigger elements of which the analysis subtriggers are built of. Since no such subtrigger for inclusive $D^\star$ meson production in photoproduction exists, DIS subtriggers have been used as monitor subtriggers. DIS subtriggers are defined by selection criteria, which are mainly given by a detection of the scattered electron in the calorimeters. The monitor subtriggers used in this analysis are referred to as s0 and s3. The conditions of these subtriggers use to the energy and position of the scattered electron in the SpaCal. The level one conditions of both s0 and s3 are given by triggerelements of the Inclusive Electron Trigger (IET) [V.B95]. The condition used by s0 is $SPCLe\_IET > 1$ and s3 consist of the condition $SPCLe\_IET > 2$. These trigger elements fire if the cluster energy measured in the SpaCal exceeds 6 GeV or 9 GeV, respectively. On the second trigger level the conditions

$SPCL\_R20$ and $SPCL\_R30$ are implemented to achieve further rate reductions of s0 and s3. These conditions are topological triggerelements which are based on the informations provided by the IET trigger. They select events with at least one energy deposition in SpaCal with a distance to the beampipe of $r \geq 20$ cm or $r \geq 30$ cm, respectively.

Since the decision criteria of the subtriggers s55, s53 and s122 are based on informations of the central tracking devices (see section 3.7) the independence of the above defined monitor sample is ensured. The trigger efficiency is given by the following formula:

$$\epsilon_{trig} = \frac{raw_{Bit}^{signal} \;\&\&\; act_{Bit}^{monitor}}{act_{Bit}^{monitor}} \tag{5.1}$$

In order not to misinterpret effects of the prescaling as an inefficiency of the investigated subtrigger the signal sample is defined by the *raw bit*, that means that this sample includes also events which had been vetoed by the autoprescale tool. Whereas the monitor sample is given by all events in which the *actual bit* of the monitor triggers is set. All analysis cuts are performed except the veto against the scattered electrons which can't be applied due to the use of DIS monitor triggers.

Figure 5.4 shows the efficiencies for all trigger levels separately as a function of the transverse momentum of the $D^\star$ mesons. The efficiency of the level 1 triggerelements determined for the run range of s122 is depicted in figure 5.4 (a). Note that this efficiency corresponds also to the level 1 efficiencies of s55 and s53, since all subtriggers are built of the same level1 conditions. It can be seen that the efficiency reaches 85% towards high transverse momenta of the $D^\star$ meson. Towards low transverse momenta the efficiency decreases to $\simeq 40\%$, due to the track p_t conditions of the FTT triggerelements. In figure 5.4 b)-d) the efficiency for the triggerelements of the second and third triggerlevel of the subtrigger s55 (b), s53 (c) and s122 (d) are displayed. These efficiencies are determined for events triggered by the previous level, such that they correspond to the pure efficiency of the investigated level. Hence, the total efficiency can be derived by a multiplication of the level one, two and three efficiencies.

It can be seen that the efficiencies of the level two conditions show in principle the same behavior as the level one efficiency. For subtrigger 122 (d) this behavior is caused by the $FTT\_mul\_Te > 1$ condition, which requires at least two tracks above a p_t threshold of 900 MeV. A high efficiency is observed above a transverse momentum of the $D^\star$ meson of 4 GeV. In this region the efficiency reaches values of 90%. Below 4 GeV the efficiency drops down to 30% at a p_t of 1 GeV. By comparing the level 2 efficiency of subtrigger 122 with the level 2 efficiencies of the subtriggers s55 and s53 it can be seen that the position of the level 2 threshold of these subtriggers is shifted towards larger values of the transverse momentum of the $D^\star$ meson. This can be explained by the additional $FTT\_Et\_1(2)$ conditions, which have been applied to cope with the higher rates at low transverse momenta. The efficiencies of the level 3 triggerelements show as expected a sharp threshold at 1.5 GeV for the s55 (b), 2.5 GeV for the s53 (c) and 4.5 GeV for the s122 (d). The efficiencies are reaching values between 55% and 65% right after the threshold and are than again decreasing towards higher transverse momenta of the $D^\star$ meson. This effect is most prominent for the level 3 triggerelements used in the subtriggers s55 and and s53 and can be explained by the strict ΔM cut applied in the triggerelements of the third level (see table 5.1) and the deterioration of the track resolution towards high transverse momentum of the tracks [Jun07].

The total efficiency of the three triggers is dominated by the efficiency of the level 3 triggerelements. Furthermore figure 5.4 shows that the threshold of the level 1 triggerelements is far away from the thresholds of the level 3 triggerelements of the triggers s53 and s122, thus no influence on the threshold of the total efficiency is expected for these trigger.

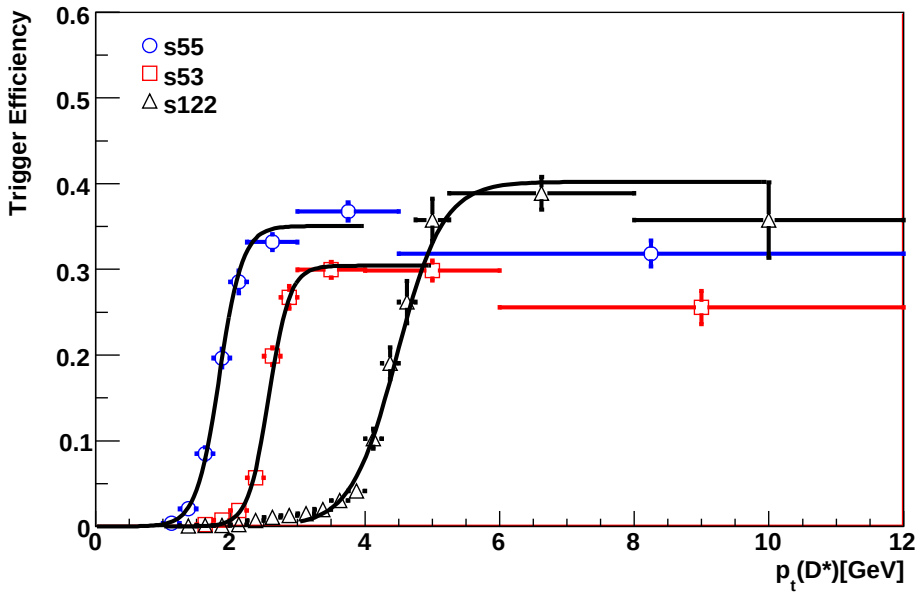

Figure 5.5: *Total trigger efficiencies as function of the transverse momentum of $D^\star$ meson. For the subtriggers s55 (circles), s53 (squares) and s122 (triangles). The efficiencies have been parameterized with a Fermi function (see 5.2). Note that the parameterization has been restricted to low values of the transverse momentum of the $D^\star$ meson, in order to avoid a bias by the decreasing efficiency at high p_t.*

An influence on the total efficiency of the level 2 triggerelements is expected in particular for the total efficiency of subtrigger s55. Unfortunately, the threshold of the level 2 triggerelements of subtrigger s55 is at the same position as the threshold of the level 3 triggerelement. Only a marginal effect on the threshold of the final efficiency is expected by the level 2 triggerelements and no effect is expected for s122, since here the level 2 threshold is far away from the level 3 threshold. Figure 5.5 shows the total efficiency as a function of the transverse momentum of the $D^\star$ meson for the subtriggers s55, s53 and s122. In order to determine the position and width of the threshold, the efficiencies have been parameterized with a Fermi function:

$$f(p_t) = \frac{p_0}{e^{\frac{p_1 - p_t}{p_2}} + 1} \tag{5.2}$$

The parameter p_0 denotes the efficiency in the plateau region, p_1 the position of the threshold and p_2 the width of the threshold. In order to avoid a bias of the falling efficiency at high transverse momenta the parameterization has been restricted to low values of the transverse momentum as shown in figure 5.5. The p_t threshold of the subtrigger s55 is determined to $p_1^{s55} = 1.84 \pm 0.02$ GeV with a width of $p_2^{s55} = 0.17 \pm 0.01$ GeV. This threshold is, as expected, located above the threshold of the level3 triggerelement since it is defined by a convolution of the level 2 and level 3 efficiencies. A summary of the position and width of the three subtriggers can be found in table 5.2.

5.6 Analysis Strategy

The output rates of the subtriggers s55, s53 and s122 are comparatively large due to the high rate of photoproduction events. In order to cope with these rates the subtriggers have been prescaled (see section 3.5). In the final cross section measurement the recorded

Subtrigger	*Position* $p_t(D^\star)$ [GeV]	*Width* $p_t(D^\star)$ [GeV]
s55	1.84 ± 0.02	0.17 ± 0.01
s53	2.57 ± 0.02	0.15 ± 0.01
s122	4.48 ± 0.05	0.34 ± 0.02

Table 5.2: *Summary of the position and the width of the trigger thresholds.*

event samples have to be corrected by the fraction of events, which have been discarded due to the prescaling. The average prescales P of the subtriggers used in this analysis are $P(s55) = 2.01$, $P(s53) = 1.33$ and $P(s122) = 1.21$. The different size of the prescales is approximately reflecting the magnitude of the output rates of the different subtriggers which are given by the different p_t thresholds and the rising rates towards low transverse momenta of the $D^\star$ meson. In addition to the correction for the prescale, the event samples have to be corrected for those events which are lost due the inefficiencies of the subtriggers. Both effects can be taken into account by applying weights to the accepted events. The total number of events is then given by the sum of weights W. If only one subtrigger is used in the analysis, the determination of W would be trivial. In this case W is defined by all of those events i in which the actual bit act_{Bit} of the investigated subtrigger has been set to one, weighted with the average prescale factor and the trigger efficiency: $W = \sum_i act^i_{Bit} \cdot P \cdot \epsilon^{trig}$. However, the situation becomes more complicated if more than one subtrigger is used in the analysis. In this case it is possible that the phase spaces covered by specific subtriggers are interfering with each other. The question arises how the correction factors for the events in the overlap region are calculated.

At the H1 experiment two methods are commonly used to combine subtriggers. Neither of these methods can be applied to this analysis. Nevertheless, both methods played an important role in the considerations of finding a combination strategy for this analysis, therefore they will be briefly introduced in the following. One method is mainly used within analyses which deal with measurements of the proton structure functions, the other method is based on an H1 internal note [Ric97]. In the following the latter will be referred to as the inclusive method and the other to as the exclusive[1] method. Both methods differ in the treatment of the events in the interfering phase space of the subtriggers and describe the combination of n subtriggers.

In the case of the exclusive method, a priority is assigned to each subtrigger. The highest priority is assigned to the subtrigger with the lowest prescale factor. Gradually, lower priorities are assigned to those subtriggers with higher prescale factors. The assignment of the highest priority to a subtrigger means that all events, in which the actual bit of this subtrigger is set are selected and weighted with the prescale factor of this subtrigger. For the case that in an event the actual of the subtrigger with the highest priority is not set, it is checked if the actual or raw bit of the subtrigger with the second highest priority is set. If this is the case the event is weighted with the corresponding prescale factor. If this is not the case the actual or raw bits of subtriggers with lower priorities are proved successively till a subtrigger is found which has triggered the event. If the event is not incorporated in the phase space of any of the used subtriggers the event is thrown away.

In contrast to the exclusive method all subtriggers are treated equally within the inclusive method. Events of the common phase space are considered with an averaged event weight.

[1] The name exclusive method is commonly used in analyses which deal with measurements of the proton structure function.

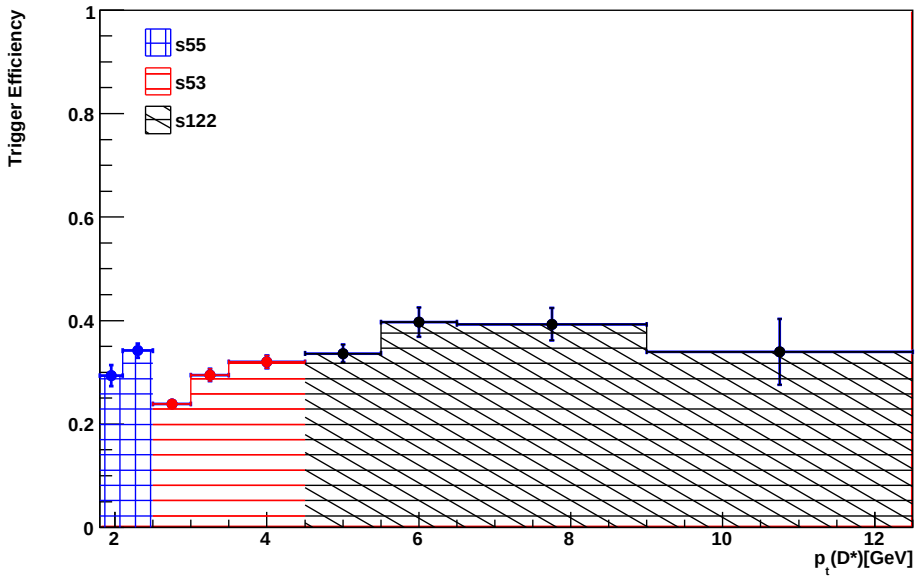

Figure 5.6: *Trigger efficiency as a function of the p_t of all $D^\star$ candidates in the inclusive sample. The phase space covered by the different subtriggers is distinguished by variably hatched histogram areas.*

The advantage of this method is that all events are considered in the event weight calculation and a lower error on the final sum of event weights is expected. A more detailed description of both methods can be found in [Urb05].

Unfortunately, neither of these methods can be applied to this analysis, since both methods assume that the different subtriggers fire entirely independent and a statistical distribution of the accepted and rejected events by the prescaling can be assumed. Since the subtriggers used in this analysis are composed of the same triggerelements on the first trigger level, it is not assured that the prescale factors are independent. Therefore, the trivial case of only one-subtrigger is considered again. The idea, which has been realized within this analysis, is a clean separation of the event samples in phase space regions, such that combining the subtriggers is trivial. The disadvantage of this method is that it is unavoidable that a fraction of events is excluded from the analysis. The rejected events correspond to those events, which are for instance solely triggered by subtrigger s122, but not incorporated in the selected phase space of this subtrigger. Fortunately, the subtriggers used in this analysis are composed of similar triggerelements. Thus it is expected that the overlap between the event samples of the different subtriggers in interfering regions of phase space is large. That means that a separation in phase space is causing only marginal loses of events in the final sample.

The main goal selecting appropriate phase space regions for the specific subtriggers was to maximise the statistic of the $D^\star$ mesons with simultaneous consideration of a preferably high efficiency. The latter is necessary to keep the systematic uncertainties due the determination of the trigger efficiency low. Despite these, additional constraints are given by the different p_t thresholds of the total efficiencies (see figure 5.5) and the different amount of luminosities collected by the various subtriggers. The latter is caused by the different commissioning times of the different subtriggers. The first subtrigger which has been fully commissioned was the subtrigger s122. This subtrigger has been active within the run range 477240−500611 which corresponds to a prescale corrected integrated luminosity of about $\mathcal{L}_{s122} = 93.39$ pb^{-1}.

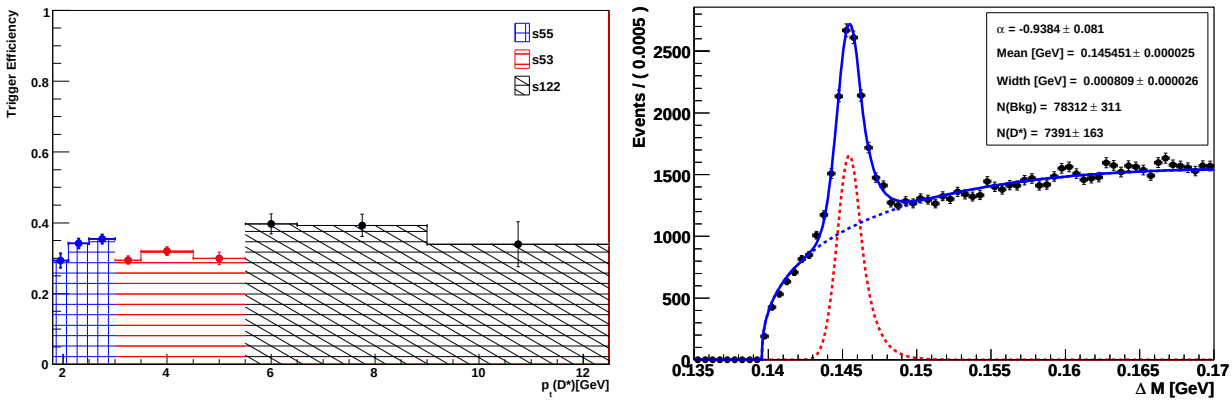

Figure 5.7: *On the left: Trigger efficiency as a function of the transverse momentum of the $D^\star$ meson with a varied phase space definition of the subtriggers. On the right the corresponding total $D^\star$ signal in the inclusive sample.*

Subsequently, the other subtriggers had been commissioned, s53 had been active in the run range 482535−500611 and s55 in 489125−500611. These run ranges correspond to integrated luminosities of $\mathcal{L}_{s53} = 68.23$ pb^{-1} and $\mathcal{L}_{s55} = 30.68$ pb^{-1}, respectively. An overview of the luminosity taken by different subtriggers can be found in table 5.3.

Subtrigger	$p_t(D^\star)$ [GeV]	*Luminosity* $\mathcal{L}$ [pb^{-1}]	*Run Number Range*	*Prescale*
s55	1.8 – 2.5	30.68	489125 – 500611	2.01
s53	2.5 – 4.5	68.23	482535 – 500611	1.33
s122	4.5 – 12.5	93.39	477240 – 500611	1.21

Table 5.3: *Overview of the different subtriggers and the phase space in which they are used.*

In the following, the phase space regions for the subtriggers are separated by the transverse momentum of the $D^\star$ mesons, such that there is no overlap of the event samples of the different subtriggers. Concerning the results obtained in this chapter, it is evident that the subtriggers s55 is used in the low, s53 for the medium and s122 in the high p_t regime. The lower border of the low $p_t(D^\star)$ range is restricted by the p_t threshold of the subtrigger s55 to 1.8 GeV. In addition this border is also enforced by the detorating signal-to-combinatorial background ratio as described in section 4.4. The upper border of the s55 region is defined by the threshold of s53 to 2.5 GeV. In figure 5.5 it can be seen, that it could make sense to extend the phase space of s55 towards higher values of the transverse momentum of the $D^\star$ meson, since the efficiency of s55 is about 10% higher than the efficiency of subtrigger s53 in the p_t range $2.5 < p_t(D^\star) < 3.0$ GeV. However, it has to be kept in mind that the prescale corrected luminosity of s55 is a factor two lower than the prescale corrected luminosity of subtrigger s53. The gain in the amount of measured $D^\star$ mesons due to the higher efficiency, by using s55 towards higher transverse momenta, is negligible compared to the gain due to the larger run range of s53. For the same reason the upper border of the phase space of s53 is restricted by the lower luminosity of s53 compared to the luminosity of s122. As soon as the efficiency of subtrigger s122 reaches reasonable high values the phase space of s53 is restricted and the phase space of s122 begins. The upper border of s53 or lower border of s122, respectively, is defined by the threshold of s122 at 4.5 GeV. Figure 5.6 shows the

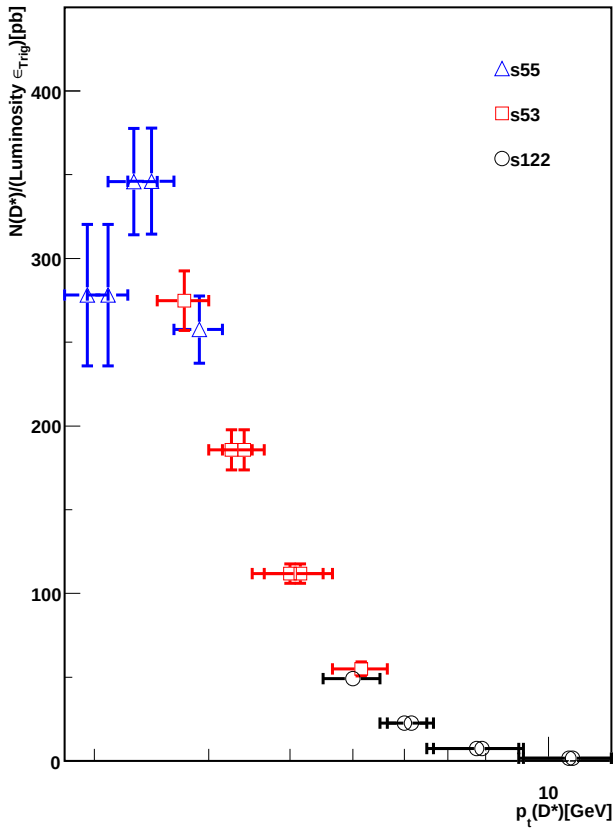

Figure 5.8: *Comparison of $N(D^\star)$ as a function of the p_t of the $D^\star$ mesons. $N(D^\star)$ is determined according the phase space separation summarized in table 5.3 and the alternative phase space definition according figure 5.7 (left). $N(D^\star)$ is corrected by the corresponding efficiency and luminosity in a certain interval. Note that the result obtained with the modified phase space definition is shown shifted towards higher $p_t(D^\star)$ values for better visibility.*

efficiency according to this phase space definition as a function of the transverse momentum of the $D^\star$ mesons. The first two bins correspond to the efficiency of s55, the following three bins to s53 and the remaining four bins to s122. The total $D^\star$ meson signal obtained with this phase space definition is depicted in figure 4.3 and yields a total number of $D^\star$ mesons of 8240 ± 173. The chosen p_t ranges and the relevant characteristics of the subtriggers are summarized in table 5.3.

Since the analysis strategy given by the phase space separation described above is not common at H1 and the event sample is triggered with the new level 3 system of the FTT trigger, it is cross-checked that the result obtained with the phase space definition introduced above, is consistent with results obtained with a modified phase space definition. The phase spaces are modified such that the $p_t(D^\star)$ ranges of the subtriggers s55 and s53 are shifted towards higher transverse momenta by one bin. In this alternative definition the $p_t(D^\star)$ range of subtrigger s55 is given by the range $1.8 < p_t(D^\star) < 3.0$ GeV, the range of subtrigger s53 by $3.0 < p_t(D^\star) < 5.5$ GeV and the range of s122 by $5.5 < p_t(D^\star) < 12.5$ GeV. Figure 5.7 (left) shows the efficiency for this phase space separation. In comparison to the efficiency depicted in figure 5.6 it can be seen that the average efficiency is higher than the efficiency shown in figure 5.6. Nevertheless, the total amount of $D^\star$ mesons obtained with this definition is as expected lower than the number of $D^\star$ mesons obtained in the default definition of the phase spaces. The corresponding $D^\star$ meson signal obtained with the modified phase space definition is shown in figure 5.7 (right) and yields a total number of $D^\star$ mesons of 7391 ± 163. In order to check that the results obtained with both phase space separations are consistent, the number of $D^\star$ meson as a function of the transverse momentum is investigated. The amount of $D^\star$ mesons is determined in each interval according the parameterization as described in section 4.2 and afterwards corrected by the efficiency in the corresponding interval and the prescale corrected luminosity of the corresponding subtrigger used in a

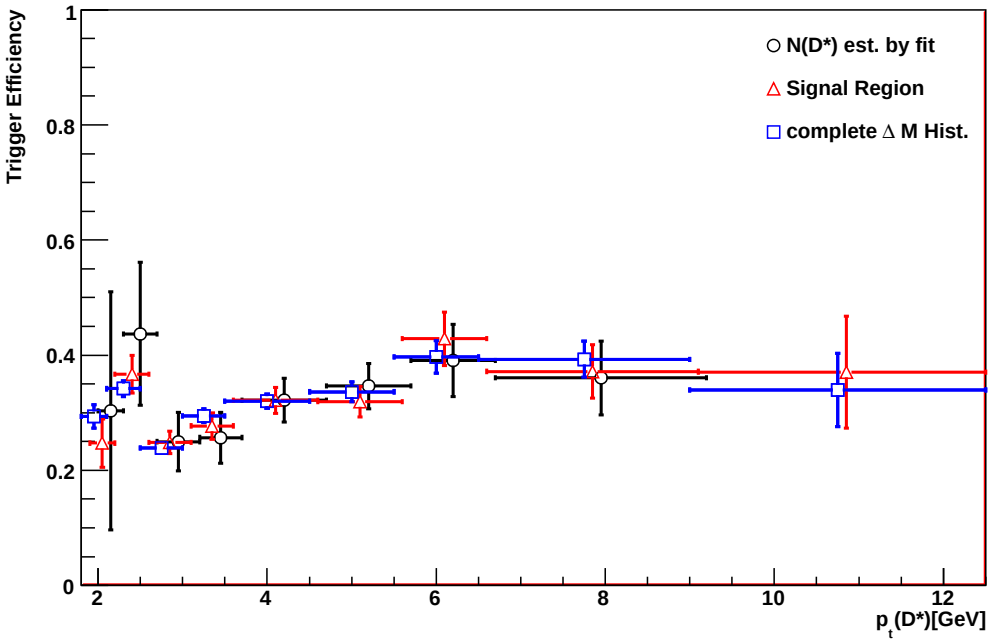

Figure 5.9: *Trigger efficiency as a function of* $p_t(D^\star)$. *The efficiency which corresponds to the total* ΔM *histogram is displayed by the open squares. The efficiency which takes only into account the events of the signal region* $(143.0 < \Delta M < 148.0)$ MeV *is represented by the triangles. The circles correspond to the efficiency determined on the basis of real* $D^\star$ *mesons, which have been determined on the basis of a parameterization of the* ΔM *signal for each interval. Note that the statistic in the highest* p_t *bin in the reference sample is to small to perform a parameterization.for better visibility*

specific p_t range. Figure 5.8 shows the number of $D^\star$ mesons as a function of the transverse momentum corrected by the the efficiency and the luminosity. In the intervals in which the phase space definition is not changed, the same result of corrected number of $D^\star$ mesons is found. The bin from $2.5 < p_t(D^\star) < 3.0$ GeV corresponds to a measurement with subtrigger s53 in the default phase space definition (see figure 5.6) and to a measurement with subtrigger s55 in the modified definition. Both results in this interval are consistent within the statistical uncertainty. The same can be concluded for the bin $4.5 < p_t(D^\star) < 5.5$ GeV, which is once measured with s53 and s122. This shows that reliable results can be obtained with the chosen analysis strategy.

A further test of the reliability of the efficiency determined above has been performed within this thesis. In the previous discussion it was assumed that it is possible to determine the efficiency on the basis of the $D^\star$ meson candidates of the whole ΔM distribution. This implies that the efficiency depends in the same way on real $D^\star$ mesons as on the combinatorial background. In order cross check this hypothesis, the trigger efficiency shown in figure 5.7 has been determined again on the basis of a data sample enriched with real $D^\star$ mesons. Therefore only $D^\star$ meson candidates are taken into account which are found in the signal region $(143 < \Delta M < 148$ MeV) of the ΔM distribution. Figure 5.9 shows that the efficiency based on events found in the signal region (triangles) is within the errors in agreement with the efficiency determined on the basis of the whole ΔM distribution (squares). In a further study the amount of combinatorial background has been completely subtracted by a parameterization of the ΔM distributions for each p_t interval of the monitor

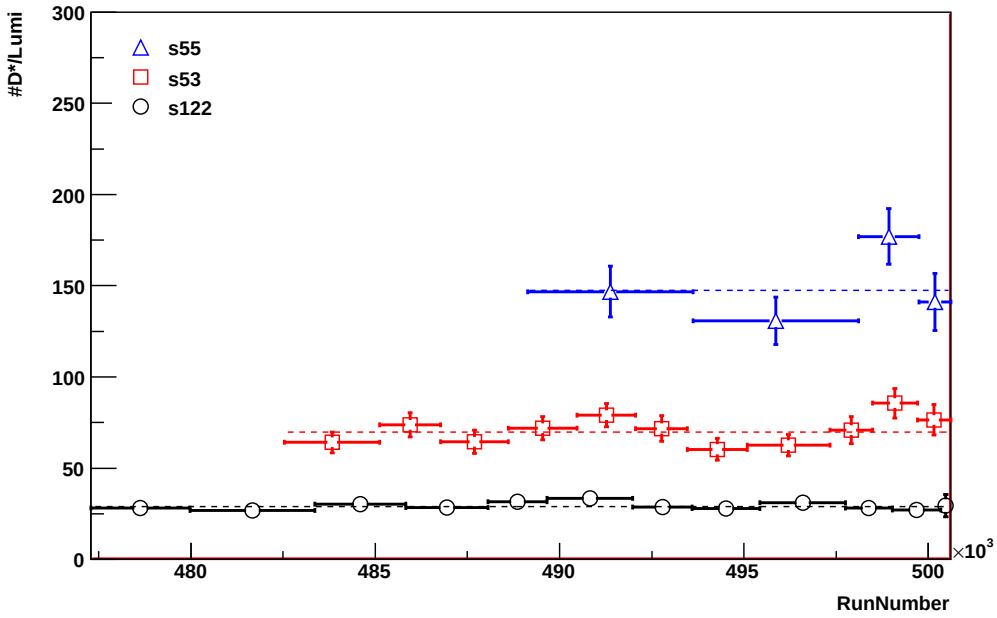

Figure 5.10: *N(D⋆) yields for the subtriggers used in this analysis. Depicted is the number of $D^\star$ mesons as a function of the runnumber. The bin width is chosen such that it corresponds to a constant amount of luminosity. For s122 this is* 6 pb^{-1}*, for s53* 8 pb^{-1} *and for s55* 10 pb^{-1}*. The number of $D^\star$ mesons is determined by a parameterization and divided by the luminosity.*

and signal sample. The corresponding efficiency, see 5.9 (circles), is as well in agreement with the efficiency determined on the basis of all events in the ΔM distribution. Thus it can be concluded that the combinatorial background has the same influence on the efficiency as real $D^\star$ mesons and can therefore be used to determine the efficiency. This has the advantage that the amount of statistic is increased and the systematic uncertainty due to the trigger efficiency is reduced.

5.7 Data Stability

The stability of the production rate of a subtrigger is an important index for the quality of the data. For the following stability studies the final selection criteria discussed so far have been applied, these include the phase space separation described above. The production rate is defined as $N(D^\star)/\mathcal{L}$ and is analyzed in intervals of constant luminosity. Figure 5.10 shows the $D^\star$ production yield for the three subtriggers used in this analysis as function of the run number for intervals of constant luminosity. The different ranges of the distributions correspond to the different commissioning times of the subtriggers. The production rate is largest for s55 due to the rising rates towards small transverse momenta. The number of $D^\star$ mesons has been determined with the parameterization described in section 4.2. Thus the interval sizes are restricted by a reasonable high signal to combinatorial background ratio, which is necessary to perform a parameterization of the ΔM distribution. This ratio is lowest for the s55 and the chosen interval sizes of 10 pb^{-1} therefore largest. The interval size for the s53 corresponds to 8 pb^{-1} and to 6 pb^{-1} for the s122. However, it can be seen that the production rate is stable within the statistical errors, no time dependence is observed.

Chapter 6

Cross Section Determination

This chapter is devoted to the analysis procedure of the cross section measurement. The fundamental issues of a cross section determination can be summarized to three basic ingredients. These are the number of measured events N, the total integrated luminosity $\mathcal{L}$ and the detector effects ϵ_{det}. Since the luminosity is a quantity for the amount of events which occurred in a certain time interval, N and $\mathcal{L}$ are related to the cross section σ via $\sigma \sim N/\mathcal{L}$. Due to inefficiencies of the used detector devices, the number of measured particles N will always be too low. This is comprised in the variable ϵ_{det} which is used to correct for these particle losses. In addition, the uncertainty on the number of measured events N has to be estimated. The uncertainty incorporates the statistical error as well as systemtic uncertainties caused by the limited resolution of the detector devices. The extraction of the number of measured $D^\star$ mesons and the corresponding statistical error has already been discussed in section 4.2.

This chapter deals with the remaining ingredients to extract the cross sections. In the beginning a detailed definition of the cross section is given. Afterwards, detector resolutions are investigated with the aim to determine appropriate interval sizes of the investigated variables. Subsequently, the discussion focuses on the determination of the detector effect corrections. The systematic uncertainties are discussed in the next chapter.

6.1 Cross Section Definition

The total cross section for $D^\star$ mesons, which have decayed via the Golden Decay Channel $D^{\star\pm} \to D^0\pi^\pm_{slow} \to \pi^\mp K^\pm \pi^\pm_{slow}$, is given by the total number of measured $D^\star$ mesons N in the visible range, the total integrated luminosity $\mathcal{L}$ and detector effects ϵ_{det}. It is common to separate the detector effects into the acceptance $\mathcal{A}$, the reconstruction efficiency ϵ_{rec} and trigger efficiency ϵ_{trig}. The total cross section within the visible range is then given by the following formula:

$$\sigma^{\text{vis}}_{\text{tot}}(ep \to e' D^\star X) = \frac{N_{D^\star} \cdot (1-r)}{\mathcal{L} \cdot \mathcal{BR}(D^\star \to K\pi\pi_{\text{slow}}) \cdot \mathcal{A} \cdot \epsilon_{rec} \cdot \epsilon_{trig}} \; . \tag{6.1}$$

Here the correction constant r is applied to account for reflections from other D^0 decays, which contribute to the D^0 signal within the D^0 mass window. $\mathcal{BR}(D^\star \to K\pi\pi_s)$ is the branching ratio of the analyzed $D^\star$ decay chain and amounts to 3.8% [Yao06]. The definition and determination of the acceptance and reconstruction efficiency is described in section 6.4. The triggerefficiency has already been discussed in the previous chapter. The cross section is defined as the sum of the $D^{\star+}$ and $D^{\star-}$ cross sections and includes $D^\star$ mesons from b-quark decays.

The definition of the visible range of this measurement is given in table 6.1. The minimal transverse momentum of the $D^\star$ meson is restricted to 1.8 GeV, due to the limited trigger

visible range	
Q^2	< 2 GeV
$W_{\gamma p}$	$(100 - 285)$ GeV
$\|\eta(D^\star)\|$	< 1.5
$p_t(D^\star)$	> 1.8 GeV

Table 6.1: *Definition of the visible range in the inclusive sample.*

efficiency. Furthermore, it has been shown in section 4.4 that the ratio of the signal to the combinatorial background rapidly deteriorates towards low values of the transverse momentum of the $D^\star$ meson. Thus, it becomes impossible to extract a significant $D^\star$ meson signal below 1.8 GeV. The direction of the $D^\star$ meson is strongly correlated to the direction of the decay products. Since the tracks of the decay products of the $D^\star$ meson are restricted to the central region, the region of the $D^\star$ meson has to be restricted as well. With the applied track cuts it is only possible to identify $D^\star$ mesons in the region of $|\eta < 1.5|$. The Q^2 range is given by the geometrical acceptance of the backward calorimeter (SpaCal). The upper border of the $W_{\gamma p}$ range is restricted by a worse signal to combinatorial background ratio and the lower border rejects events in the extreme forward region and ensures a good reconstruction of the events. The differential cross section is defined along the lines of equation 6.1, with the exception, that the number of $D^\star$ mesons and the detector correction factors are determined for each interval ΔY of the investigated quantity Y. Thus, equation 6.1 has to be divided by the width ΔY of a certain interval:

$$\frac{d\sigma^{\text{vis}}(ep \to e' D^\star X)}{dY} = \frac{N_{D^\star} \cdot (1 - r)}{\Delta Y \cdot \mathcal{L} \cdot \mathcal{BR}(D^\star \to K\pi\pi_{\text{slow}}) \cdot \mathcal{A} \cdot \epsilon_{rec} \cdot \epsilon_{trig}} \,. \tag{6.2}$$

The appropriate interval width for the differential cross section measurement has to be determined for each investigated quantity.

6.2 Purity and Resolution

On the one hand the interval width of a certain investigated variables is limited by the amount of statistics in data and finally by the significance of the number of $D^\star$ mesons in the parameterization, used to fit the ΔM distribution. The approach is to achieve a binning which is as fine as feasible in order derive as much information about the $D^\star$ meson kinematics as possible. On the other hand this approach is limited by migration effects, which degrade the reliability of the measurement. Migrations are the result of the limited detector resolution. They are determined on the basis of Monte Carlo samples and describe the transition of events from one interval to another. This means for example, that a $D^\star$ meson with a true transverse momentum of $p_t^{gen}(D^\star) = 2.5$ GeV is reconstructed with a $p_t^{rec}(D^\star) = 3.1$ GeV. If the interval borders had been chosen like $(2.0 - 3.0 - 4.0)$ GeV, the $D^\star$ meson would end up in the wrong interval. It is possible to reduce the effect of the migrations by increasing the interval size. Thus, a compromise has to be found in the choice of appropriate interval width. The migrations are quantified in the purity $\mathcal{P}$, which is given by the following formula:

$$\mathcal{P} = \left. \frac{N_{gen \;\&\&\; rec}}{N_{rec}} \right|_{bin} \tag{6.3}$$

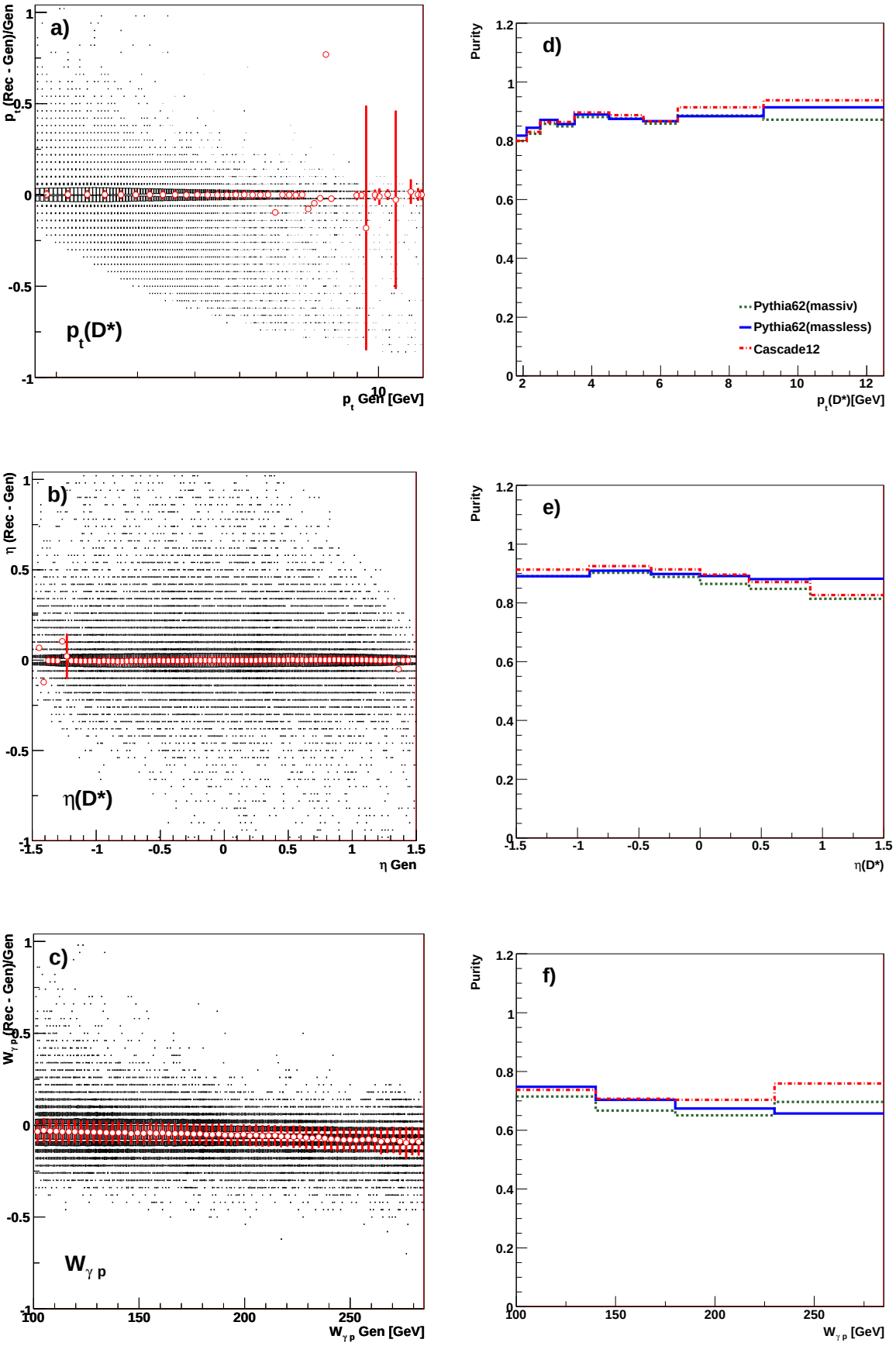

Figure 6.1: *The resolution as function of the transverse momentum a), the pseudorapidity b) of the $D^\star$ meson and the quantity $W_{\gamma p}$ c), obtained on the basis of the Pythia (massless) simulation. The open circles represent the mean and the error bar the width of gaussian parameterization of the corresponding slice. The corresponding purities $\mathcal{P}$ d)-f) are calculated on the basis of the Pythia (massless), Pythia (massive) and Cascade simulation.*

The denominator represents the total amount of reconstructed $D^\star$ mesons in a certain bin of the investigated quantity. The numerator is a subset of the denominator and denotes the amount of events, in which the reconstructed quantity appears in the same bin as the generated. The visibility cuts are not applied in equation 6.3. This ensures that the purity takes also into account migrations of $D^\star$ mesons from the outside of the visible range. In both cases (numerator and denominator) the number of $D^\star$ mesons is determined on the basis of the parameterization described in 4.2.

In the ideal case of perfect resolution the purity would be equal to one. It is not possible to achieve this in reality. Nevertheless, a large fraction of events should originate from the bin they are measured in. In practice a purity of at least 70% is chosen.

The resolutions as a function of the transverse momentum, the pseudorapidity of the $D^\star$ meson and the photon-proton center-of-mass energy are depicted in figure 6.1 a)-c). The resolution is determined on the basis of the Pythia (massless) Monte Carlo. For p_t and $W_{\gamma p}$ the relative resolutions, defined as the difference between the generated and reconstructed quantities divided by the generated quantity, are shown. For $\eta(D^\star)$ the absolute resolution defined as the difference between the generated and reconstructed quantities, is diplayed. In order to avoid biases, no visibility cuts have been applied on the generator level. In addition the cuts on the detector level have been lowered in order to avoid influences at low p_t and at the phase space edges of $\eta(D^\star)$. Thus the cut on the transverse momentum has been reduced to 1.5 GeV and the $\eta(D^\star)$ range extended to $|\eta(D^\star)| < 1.7$. For the same reason, no upper or lower cuts are required on the quantity $W_{\gamma p}$ on the detector level. Figure 6.1 a)-c) shows the correlation between the resolutions and the generated quantities. In order to make the resolution better visible the correlations have been divided into equidistant so-called slices. A slice is defined by the projection of the entries of the x axis to the y axis for a certain section of the distribution. Subsequently, these projections are parameterized by a gaussian function. The large points in the correlation distributions represent the mean, the width is displayed as error bar. It can be seen that a high resolution is found for $p_t(D^\star)$ and $\eta(D^\star)$ and a low resolution for $W_{\gamma p}$.

In figure 6.1 d)-f) the purity is depicted as a function of $p_t(D^\star)$, $\eta(D^\star)$ and $W_{\gamma p}$. The purity has been determined on the basis of the Pythia (massless), the Pythia (massive) and the Cascade simulation. The bin sizes have been adjusted such that the purities as a function of the transverse momentum and the pseudorapidity exceed in average 80% for both quantities. A finer binning in the p_t distribution is not posible, since towards low $p_t(D^\star)$ the signal to background ratio is decreasing and towards large p_t the amount of statistics. Due to the worse resolution, the purity as a function of the quantity $W_{\gamma p}$ is as expected much lower than the purity as a function of p_t and η. The interval sizes have been increased till the purity exceeded 70%. With the finally chosen interval sizes an average purity of 75% is reached.

6.3 Comparison of Data and Simulation

A Monte Carlo sample is used to correct the measured $D^\star$ meson quantities for detector effects. In order to determine reliable results it has to be ensured, that the Monte Carlo simulation describes the shape of the data. In the previous section it has been shown that the migrations have been reduced to 20% by the choice of appropriate interval sizes. It has to be considered that the remaining migrations can have a large influence on the extraction of the cross section. In particular steeply falling or rising distributions and phase space regions where the correction factors are large have to be handled with care. The following discussion focuses on control distribution in which the data is always compared

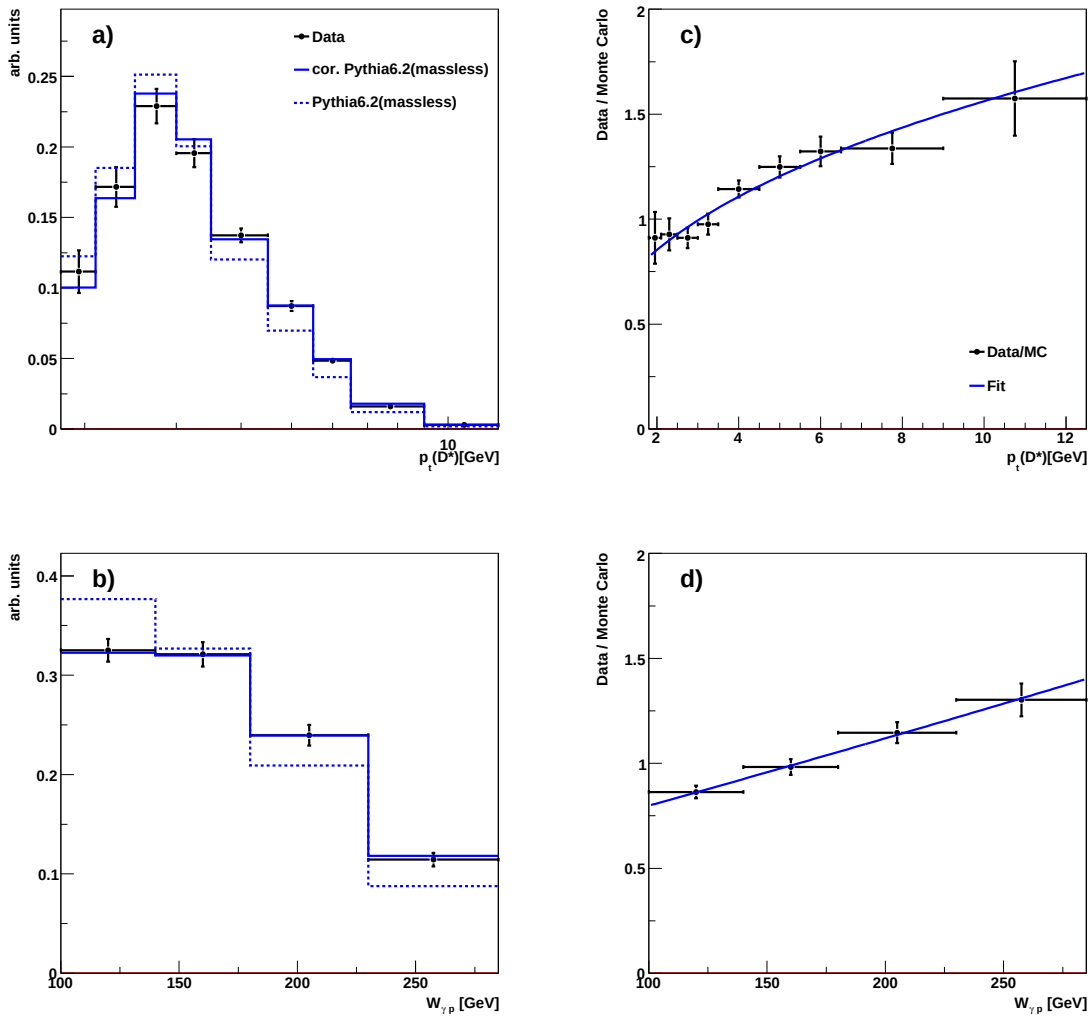

Figure 6.2: *Control distributions for $p_t(D^\star)$ a) and $W_{\gamma p}$ b). The data is compared to the Monte Carlo predictions given by the Pyhtia (massles) simulation, before (dotted line) correction and after (continuous line). The distributions are normalized on the amount data statistics. In c) and d) the ratio between the data and Monte Carlo before correction is displayed. The parameterization used for the correction is depicted by a line.*

to the prediction provided by the Pythia (massless) simulation, since this Monte Carlo simulation has finally been used to correct for the detector effects.

Due to low efficiencies of the track reconstruction towards low transverse momenta of the $D^\star$ meson the correction factors in this regime are large. Furthermore this distribution is exponentially rising towards low transverse momenta. Therefore emphasis is placed on a good description of the p_t spectra, especially at low transverse momenta.

As already mentioned, a simulation of the level 3 trigger elements is currently not available in the Monte Carlo simulation. In order to be able to compare the data with Monte Carlo simulation the effects caused by the trigger selection, in particular the trigger inefficiencies and the varying luminosity as a function of the transverse momentum, have to be considered in the Monte Carlo. The trigger inefficiency has been taken into account by downscaling the Monte Carlo events on the detector level according to the efficiency depicted in figure 5.6. Furthermore it has to be considered that the data sample corresponds to different

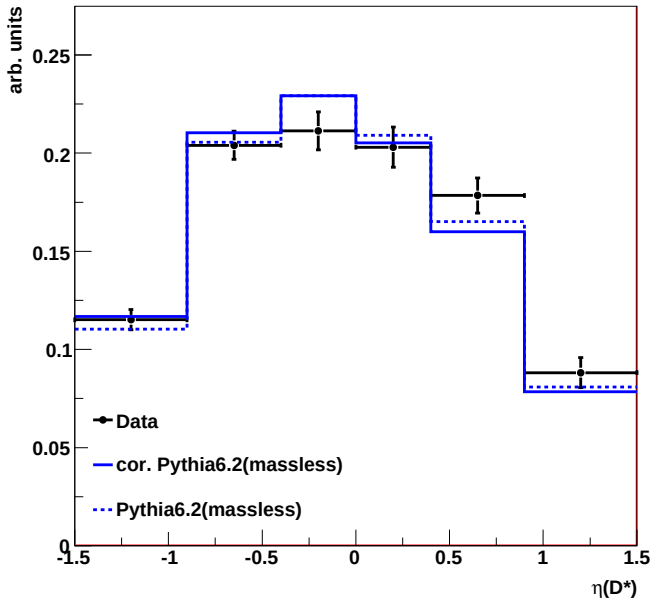

Figure 6.3: *Control distribution as a function of the pseudorapidity of the $D^\star$ meson. The data, represented by the points, is compared to the prediction provided by the Pythia (massless) prediction, before (dotted line) and after correction (continuous line), repsectively.*

amounts of luminosities in certain p_t ranges of the $D^\star$ mesons. This has been considered by p_t-dependend correction factors $L(p_t)$. The following correction factors have been applied: In the p_t range from 1.8 GeV to 2.5 GeV the correction factor amounts to $L = 30.68$, in the range from 2.5 GeV to 4.5 GeV to $L = 68.23$ and in the range from 4.5 GeV to 12.5 GeV the factor amounts to $L = 93.39$. These factors match exactly to the luminosities summarized in table 5.3 and regard the different run ranges in which the subtriggers had been active. Together with the luminosity of the Monte Carlo $\mathcal{L}_{MC}$, the total weight factors $w(p_t)$ applied to the Monte Carlo events is thus given by $w(p_t) = L(p_t) \cdot \epsilon_{trig}^{incl}(p_t)/\mathcal{L}_{MC}$. After applying these correction factors to the Monte Carlo events the data and the Monte Carlo simulation can be compared.

Figure 6.2 a) and b) shows the control distributions as function of $p_t(D^\star)$ and $W_{\gamma p}$. The data is represented by the points and the Monte Carlo simulation by the dashed histogram. It can be seen that the prediction overestimates the data for low transverse momenta of the $D^\star$ meson and underestimates it in the regime of high transverse momenta, this tendency has already been observed in a previous analysis [Flu05]. A similar behavior is observed, in figure 6.2 b), as a function of $W_{\gamma p}$. Here the prediction underestimates the data in the first bin and overestimates it in the last two bins. This effect could not been seen in [Flu05], due to a stronger restricted phase space in $W_{\gamma p}$. A similar behaviour of $W_{\gamma p}$ has been observed in a measurement of Jets with high transverse momentum in photoproduction [Str04].

The observed description of the data by the Monte Carlo simulation is not satisfying. Thus, the simulation has been corrected within this analysis by reweighting the events in the Monte Carlo sample. The reweighting factors are determined on the basis of the data and the Monte Carlo events on the detector level and afterwards applied to each Monte Carlo event on the parton, hadron and detector level. In order to determine the reweighting factors the ratio *Data/Monte Carlo* has been investigated. Figure 6.2 c) shows this ratio as function of the transverse momentum of the $D^\star$ meson. It can be seen that the deviation

between the data and the Monte Carlo is largest at high transverse momenta. The ratio has been parameterized by a polynomial of second order, which has been used to reweight the Monte Carlo events. After the p_t correction, the ratio *Data/Monte Carlo* as a function of the variable $W_{\gamma p}$ has been investigated figure 6.2 d), which has been parameterized by a polynomial function of first order. This function has been used to reweight the Monte Carlo in addition to the p_t correction.

In figure 6.2 a) and b) the finally corrected Monte Carlo, represented by the continuous line, is compared to the data. A good agreement is found for the transverse momentum and a perfect agreement is found for the $W_{\gamma p}$ distribution.

Furthermore it is necessary to check whether the applied corrections have an influence on the pseudorapidity of the $D^\star$ meson. Especially $\eta(D^\star)$ and $W_{\gamma p}$ are correlated to each other. Figure 6.3 shows the control distribution as a function of the pseudorapidity. The Monte Carlo simulation is displayed before and after the correction. It can be seen that the influence of the correction on this distribution is marginal and a reasonable agreement is found before and after the correction. In summary, after correction a good agreement between the data and the corrected Monte Carlo is found. It has been checked the the control distributions shown before have not significantly changed after the reweighting. Thus the Monte Carlo can be used to calculate the detector effect correction factors.

6.4 Detector Effect Corrections

The technique used in this analysis to correct the measured data points to the hadron level is the so-called bin by bin method. Within this method the correction factors due to the geometrical acceptance $\mathcal{A}$ and the reconstruction efficiencies ϵ_{rec} are determined by the use of Monte Carlo simulations. Therefore events are first generated and afterwards linked to the full detector simulation, the correction factors are determined by comparing the generated events and the corresponding events after the full detector response as a function of each investigated variable and interval. However, this method only holds if the Monte Carlo simulation used for the unfolding gives a sufficient description of the data and if the resolutions and migrations are of the order of the chosen bin size of the investigated variable. That these conditions are fullfilled has been shown above. The migrations are below 20% and the corrected simulation given by Pythia (massless) prediction sufficiently describes the data.

Detector Acceptance

The acceptance $\mathcal{A}$ denotes the particle losses due to the geometry of the H1 detector. The acceptance is defined as the ratio of all generated $D^\star$ mesons $N_{gen}^{acc}\,|_{vis}$ in the visible range, surviving the acceptance cuts and the amount of all generated $D^\star$ mesons $N_{gen}\,|_{vis}$ in the visible range:

$$\mathcal{A} = \left.\frac{N_{gen}^{acc}}{N_{gen}}\right|_{vis} \tag{6.4}$$

The acceptance cuts for the decay particles of the $D^\star$ meson are defined by the geometric acceptance and the cuts applied to reduce the combinatorial background, which have been introduced in section 4.4. The acceptance cuts are summarized in table 6.2. Figure 6.4 a)-c) shows the acceptance as a function of $p_t(D^\star)$, $\eta(D^\star)$ and $W_{\gamma p}$. The acceptance distributions have been determined on the basis of the Monte Carlo simulation given by the Pythia

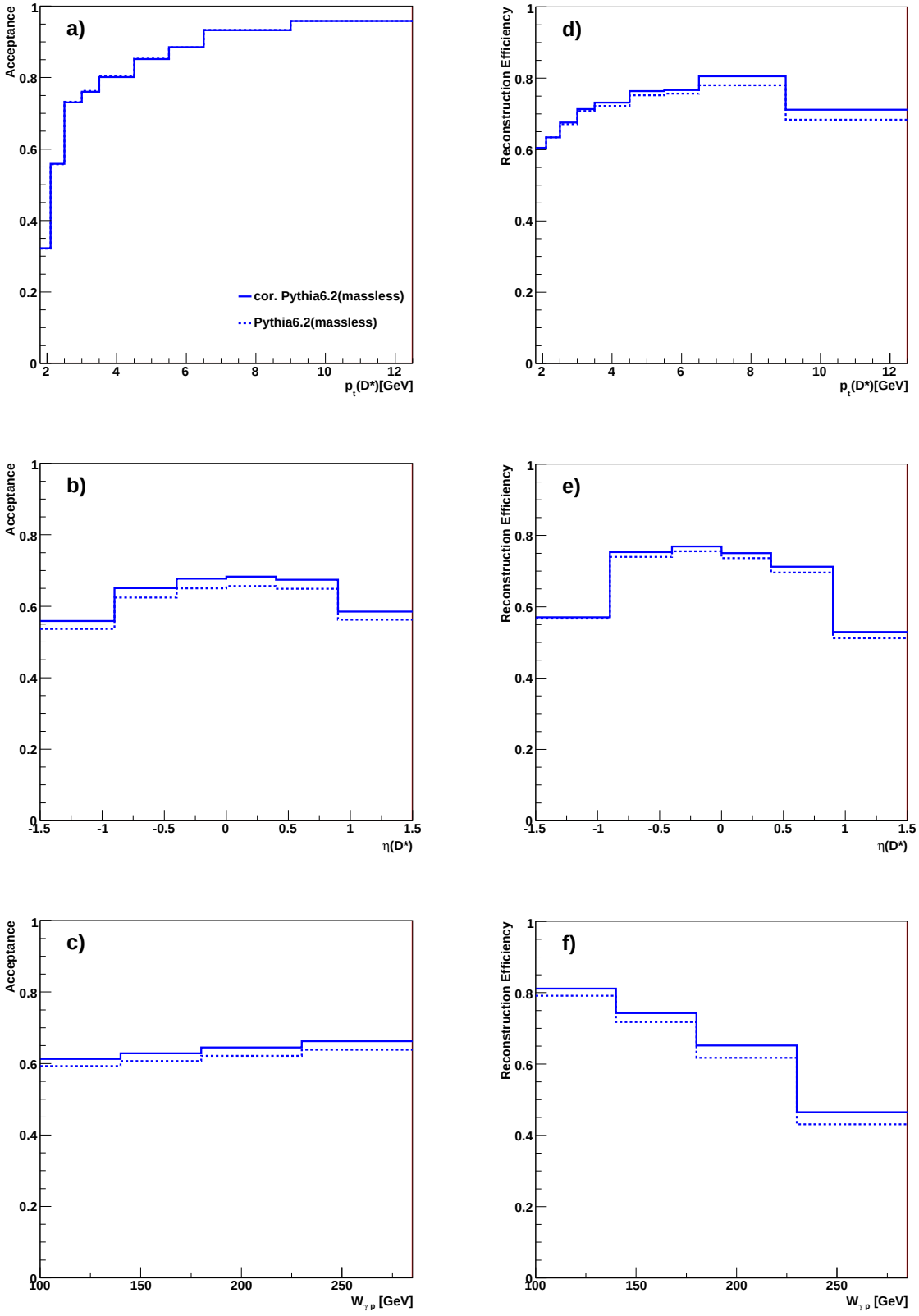

Figure 6.4: *Correction factors due to the acceptance $\mathcal{A}$ and reconstruction efficiency ϵ_{rec} determined on the basis of the corrected and uncorrected Monte Carlo simulation given by the Pythia (massless) prediction. The distributions are determined as a function of $p_t(D^\star)$, $\eta(D^\star)$ and $W_{\gamma p}$.*

acceptance range	
$p_t(K)$	> 0.5 GeV
$p_t(\pi)$	> 0.3 GeV
$p_t(\pi_{\text{slow}})$	> 0.12 GeV
$\theta(\text{Track})$	$20^\circ < \theta < 160^\circ$
$p_t(K) + p_t(\pi)$	> 2.2 GeV
$p_t(D^\star)/\sum_{\theta>10^\circ} E_i \cdot \sin\theta_i$	> 0.13

Table 6.2: *Definition of the detector acceptance.*

(massless) prediction. It is expected that the correction of the Monte Carlo simulation, described in the previous section, has only a small influence on the acceptance distribution. However, it can be seen that the acceptance, as a function of η and $W_{\gamma p}$, based on the corrected simulation is in average 3% higher than the uncorrected because of the large acceptance at high transverse momenta.

Figure 6.4 a) shows that the acceptance as function of the transverse momentum of the $D^\star$ meson drops down towards low values of p_t to about 32%. This can be explained with the relatively high cut on the transverse momentum on the π_{slow}. The acceptance as a function of the pseudorapidity of the $D^\star$ meson decreases towards low or high values of η. In this region it is likely that one of the decay products of the $D^\star$ meson escapes the acceptance of the central tracking devices. The acceptance as function of $W_{\gamma p}$ shown in figure 6.4 (c) is as expected approximately flat.

Reconstruction Efficiency

The reconstruction efficiency is defined as the number of reconstructed particles N_{rec} after all analysis cuts and the full detector response, divided by the number of generated and accepted $D^\star$ mesons N_{gen}^{acc} in the visible range:

$$\epsilon_{\text{rec}} = \left.\frac{N_{rec}}{N_{gen}^{acc}}\right|_{vis} \tag{6.5}$$

In order to substract the combinatorial background the number of reconstructed $D^\star$ mesons N_{rec} is determined by the parameterization described in section 4.2 in each interval of the investigated variable. The reconstruction efficiency as a function of $p_t(D^\star)$, $\eta(D^\star)$ and $W_{\gamma p}$ for the corrected and uncorrected Monte Carlo simulation is depicted in figure 6.4 d)-f). It can be seen that both distributions differ by a few percent from each other. Altogether, the influence on the final measurement amounts to a few percent. The distributions as a function of p_t (d) and η (e) show a similar behavior as already observed in the acceptance distributions. Towards low values of the transverse momentum of the $D^\star$ meson the reconstruction efficiency drops down to 50%. This is due to the fact that it becomes more difficult to identify the π_{slow} in this regime. Towards high transverse momenta the efficiency rises, till the track resolution becomes worse and the efficiency begins to fall again in the last interval. The reconstruction efficiency as a function of the pseudorapidity of the $D^\star$ meson is flat in the central region and drops to around 65% in the first and last bin. This can be explained by the fact, that the decay particles traverse only a small part of the CJC and it becomes more difficult to reconstruct the tracks. The reconstruction efficiency as a function of $W_{\gamma p}$ shows a significant different behavior as the corresponding acceptance distribution. The distribution drops towards high values of the $W_{\gamma p}$.

Chapter 7

Systematic Uncertainties

In addition to the statistical error various sources of systematic uncertainties have to be taken into account. They are added in quadrature to the statistical error and result in a total systematic uncertainty of about 10.6%. The dominant uncertainty sources are the luminosity measurement and the determination of the trigger efficiency. These and further uncertainty sources will be discussed in the following.

7.1 Luminosity

The uncertainty due to the determination of the integrated luminosity is one of the dominant uncertainty sources of this analysis. In previous analyses the uncertainty amounted to 1.5% and dominant uncertainties were due to the geometric acceptance of the photon detector and the estimation of non-ep background on the basis of proton pilot bunches [Lev06]. However, in the end of the year 2006 a significant increase of the luminosity corrected event yield occurred. This increase has been confirmed by several independent analyses. Figure 7.1 shows the event yield as a function of the run number for the data taking period 2004-2007. The yield has been obtained on the basis of an event sample measured with the backward calorimeter (SpaCal). It can be seen that an increase in the yield occurred approximately at the run number 477000. So far it was not possible to clarify the origin of this increase. The analysis presented in this thesis is based on a data sample which has been recorded in the time when the step in the luminosity measurement occurred. As up to now it was not possible to decide whether the yield measured before run 477000 or after this run is correct, the H1 collaboration thus decided to assign an uncertainty of 5.0% for the data taking period of this measurement.

7.2 Trigger efficiency

The trigger efficiency has been determined on the basis of the inclusive $D^\star$ data sample (see section 5.5). As a consequence, the precision of the trigger efficiency determination is limited by the amount of statistics available in the data. As discussed in section 5.6 a trigger efficiency as a function of the transverse momentum of the $D^\star$ meson, determined in data, has been used within this analysis to simulate the subtriggers in the Monte Carlo simulation. The efficiency displayed in figure 5.6 is determined in the same intervals as the final cross section measurement, thus the relative uncertainty due to the trigger efficiency could be calculated on the basis of figure 5.6 and afterwards assigned as uncertainty to each bin of the transverse momentum measurement of the $D^\star$ meson. However the distribution 5.6 makes no prediction how the error propagates into other variables, like for instance the $\eta(D^\star)$ distribution. To estimate the uncertainty in the other distributions it is exploited that a variation of the trigger efficiency has a direct influence on the extracted cross section.

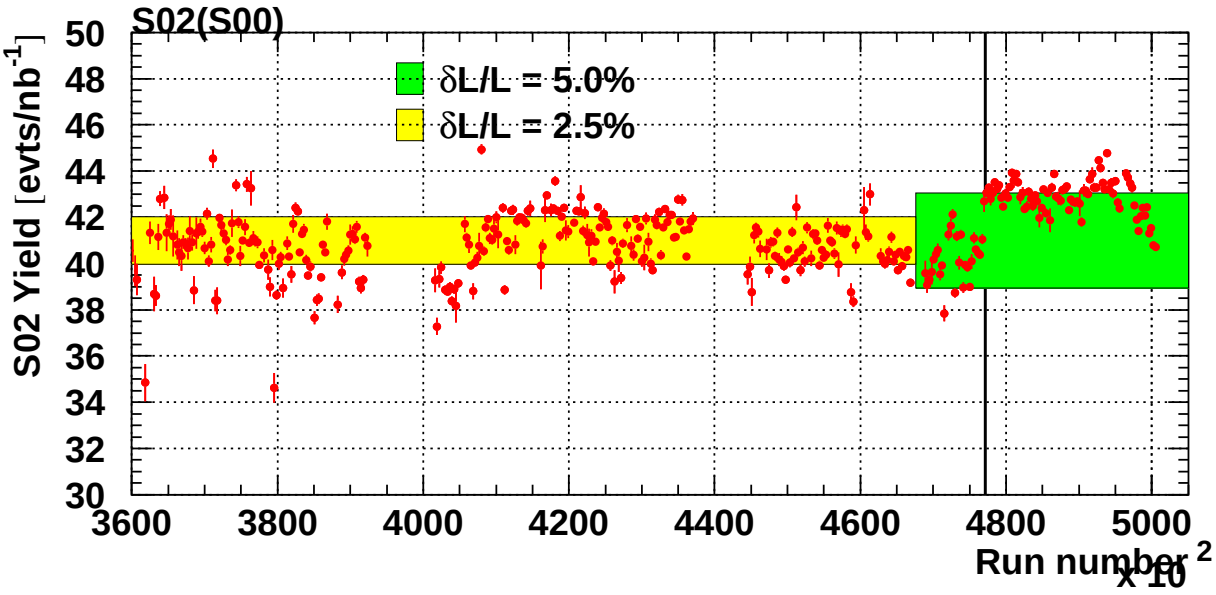

Figure 7.1: *Event yield as a function of the run number determined on the basis of events measured with the SpaCal The increase in the yield is indicated by a straight line. Figure adopted from [Sch08].*

In the first step the cross sections are calculated on the basis of the efficiency correction factors depicted in figure 5.6. Afterwards, the calculation is repeated, but this time the efficiency correction factors are increased or decreased by the upward or downward errors depicted in figure 5.6. The results are compared and the relative deviations between the default result and the result coresponding to the increased or decreased trigger efficiency defines the uncertainty due to the trigger efficiency determination.

The figures 7.2 a)-c) show the relative uncertainty due to the determination of the trigger efficiency as a function of p_t and η of the $D^\star$ mesons and as a function of $W_{\gamma p}$. The relative statistical uncertainty is displayed for reference. It can be seen that the uncertainty is smallest at medium values of p_t and increases towards high transverse momentum of the $D^\star$ meson. In the last interval an uncertainty of around $\simeq 20\%$ is observed. However, towards low transverse momenta the uncertainty is again increasing. This can be explained by the smaller run range seen by subtrigger s55, which results in a smaller amount of statistics, in this regime. The statistical uncertainty depicted below shows in principle the same behavior. This shows furthermore that the observed structure is given by the amount of statistics in a specific p_t range. The uncertainties as a function of the pseudorapidity of the $D^\star$ meson and the center-of-mass energy of the proton-photon system amount in average to $\simeq 5\%$. The distributions show as expected a flat behavior with a small rise towards large η and $W_{\gamma p}$ values, which can be explained by correlations between the transverse momentum and these variables. Furthermore, it can be seen that these uncertainties are of the same size as the statistical errors. On average the uncertainty due to the trigger efficiency amounts to 4.8% in the inclusive sample.

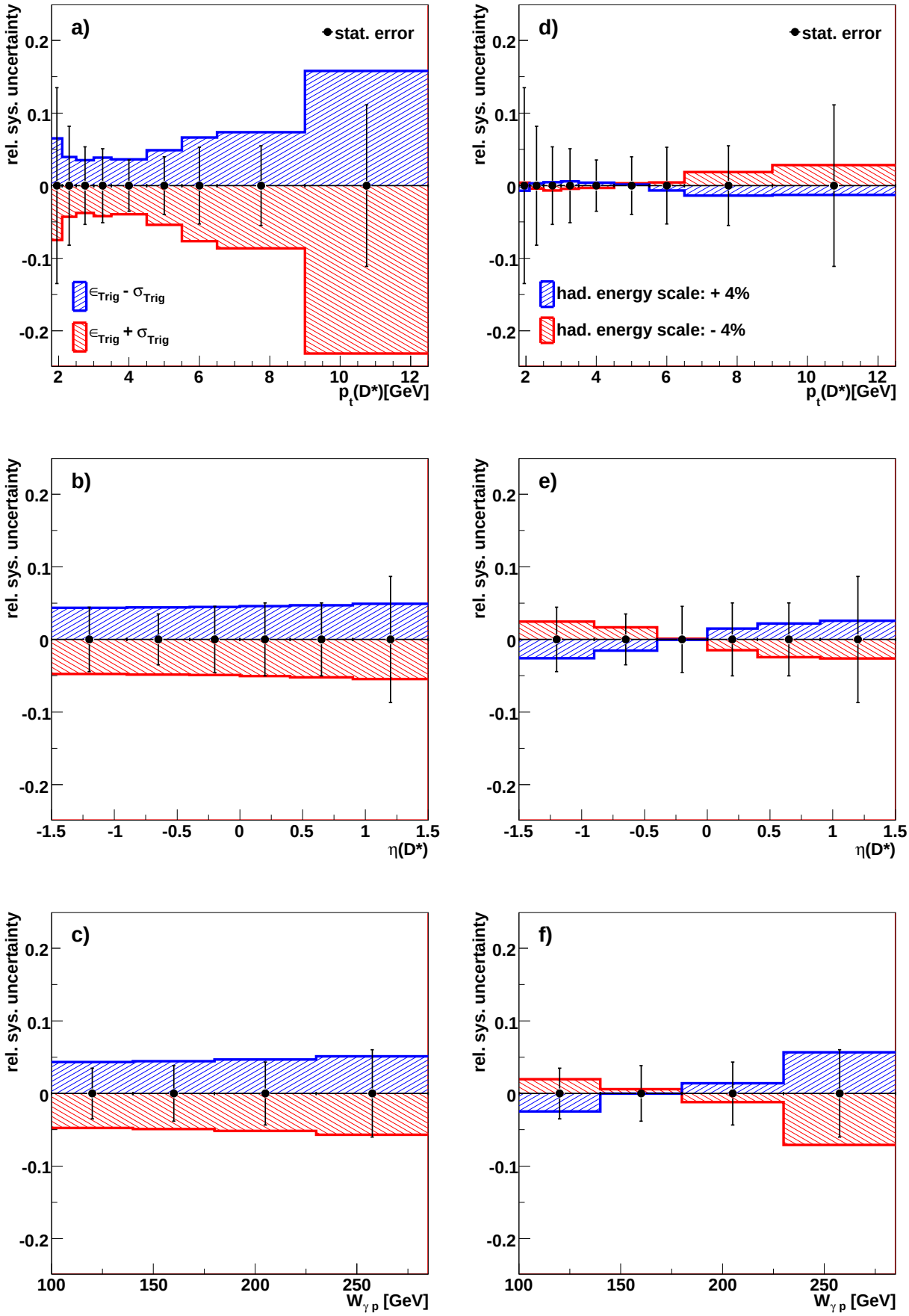

Figure 7.2: *Systematic uncertainties due to trigger efficiency a)-c) and the uncertainty of the hadronic energy scale d)-f) as a function of p_t, η and $W_{\gamma p}$. The relative statistical error is shown for comparison.*

7.3 Hadronic Energy Scale

The hadronic energy measurement in the LAr calorimeter is known to a precision of 4%. In order to estimate the influence of this uncertainty on the cross section measurement a variation of the energy of all HFS particles by the energy uncertainty of the calorimeter measurement is performed. Since the HFS particles are formed by using the tracker and the calorimeter information (see section 3.8), this variation leads to an upper limit of the uncertainty.

Two quantities are used in this analysis which depend directly on the energies of the HFS particles. These are the variable f and y_{had}. The latter is used to suppress DIS background background and events in the extreme forward region, whereas a cut on the variable f is performed to reduce the combinatorial background. The uncertainty due to the hadronic energy scale is estimated in a similar way as the uncertainty due to the trigger efficiency. The following calculations are performed on the basis of the corrected Pythia (massless) prediction. The result of the measurement is calculated twice once with the increased energy of all HFS particles by 4% and once with the decreased values. The quantity y_{had} is defined as $y_{had} = (E - p_z)_{had}/2E_e$. Thus, y_{had} is directly correlated to the particle energies and the variation by the hadronic uncertainty is taken into account by $y^{\pm} = y_{had} + y_{had} \cdot (\pm 4\%)$. Simultaneously the particle energies which are used to calculate the variable f are modified accordingly:

$$f^{\pm} = \frac{p_t(D^{\star})}{\sum^{\theta>10^{\circ}} (E_i + E_i \cdot (\pm 4\%)) \cdot \sin\theta_i} \tag{7.1}$$

The results obtained by the upward and downward variation are compared to the default result. The relative deviations are taken as systematic uncertainty.

Figure 7.2 d)-f) shows the uncertainty as function of the transverse momentum and the pseudorapidity of the $D^{\star}$ meson and for the center-of-mass energy of the proton-photon system. The upward variation (+4%) is displayed by the right hatched and the downward variation (−4%) by the left hatched histogram. Positive values of the uncertainty correspond to an increase and negative to a decrease of the cross section. By comparing these uncertainties with the uncertainties due to the trigger efficiency (see figure 7.2, left), it can be seen that the uncertainty due to the variation of the hadronic energy is in general a factor two lower than the uncertainty due to the trigger efficiency. Furthermore a turnover of the direction of the uncertainty is observed in all distributions. These turnovers can be explained by considering that the applied method corresponds to a shifting of events into the measured phase space or out of the measured phase space. In figure 6.2, it has been shown that the quantity $W_{\gamma p}$ is steeply falling towards high values of $W_{\gamma p}$. Since $W_{\gamma p}$ is directly proportional to the energies of the HFS particles, this explains why at low values of the quantity $W_{\gamma p}$ a downward variation of the particle energies leads to an increase of the cross section. The pseudorapidity of the $D^{\star}$ meson is correlated to the quantity $W_{\gamma p}$. Since $W_{\gamma p}$ denotes the energy of the photon proton system, it is expected that the particles produced in the interaction are mostly found in the forward direction (positive η) of the calorimeter for low values of $W_{\gamma p}$, whereas they are boosted to the backward direction for high values of $W_{\gamma p}$. This is in agreement with the behavior observed in the η distribution. The uncertainty is largest in the highest $W_{\gamma p}$ bin where it reaches −8%. On average the uncertainty due to the hadronic energy scale amounts to 2.0% in the inclusive sample.

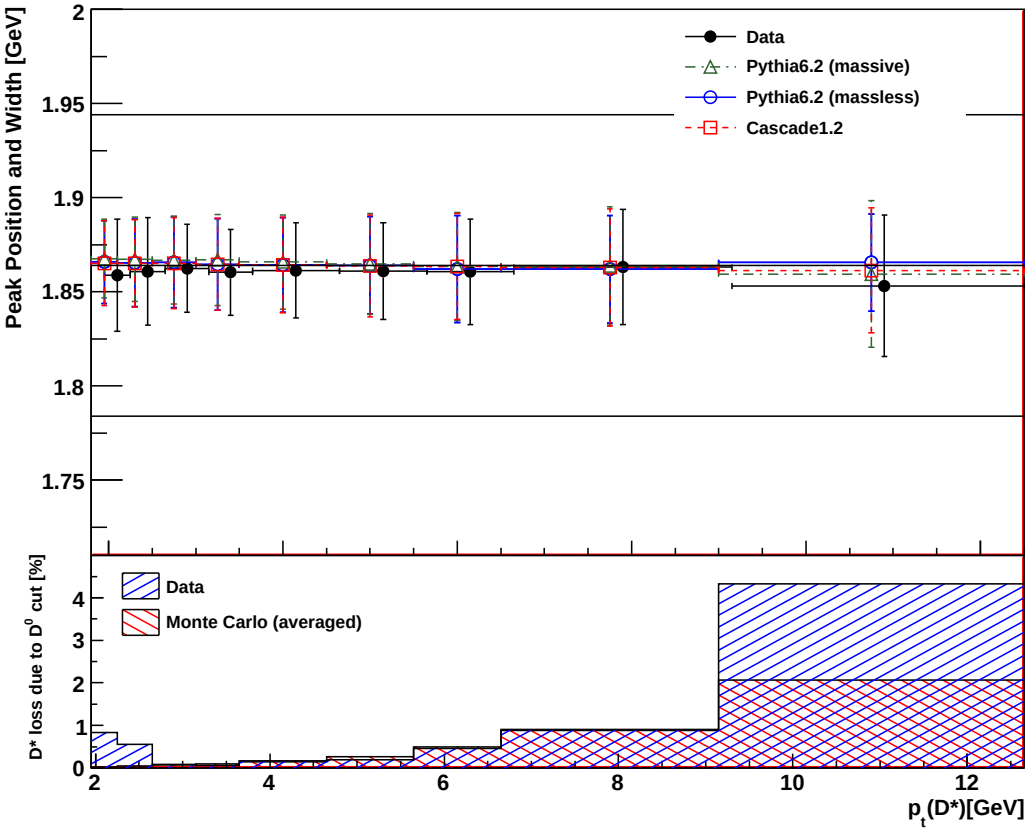

Figure 7.3: *In the upper part, the mean (points) and width (error bar) of the D^0 signal as a function of the transverse momentum of the $D^\star$ meson are displayed. The values are obtained for data and the Monte Carlo simulations given by Pythia(massless), Pythia (massive) and Cascade simulation. The outer lines denote the position of the cut on the D^0 mass. The data points are shifted slightly to the left. In the lower part, the relative discrepancy of the full integration of the D^0 signal and the integration within the range ± 80 MeV around the nominal D^0 mass is shown. The three Monte Carlo predictions are averaged.*

7.4 D^0-mass cut

It is the first time that the amount of statistics in an inclusive $D^\star$ photoproduction analysis is large enough to investigate the influence of the D^0-mass cut on the cross section measurement in detail. The D^0-mass cut has been introduced in section 4.1 and is applied within a window of ± 80 MeV around the nominal D^0 mass in order to reduce the combinatorial background in the ΔM distribution. Unfortunately, a small fraction of $D^\star$ mesons are reconstructed outside the D^0 mass window and are rejected from the analysis. Due to a slightly different track resolution found in the data and the Monte Carlo simulation, it is expected that the amount of rejected $D^\star$ meson is varying between data and Monte Carlo. Since Monte Carlo samples are used to correct for the losses in data, it is necessary to estimate the uncertainty due to this cut. Therefore, the position and the width of the D^0 signal has been investigated as a function of the transverse momentum of the $D^\star$ meson. The values have been determined for the data sample and for the Monte Carlo predictions given by Pythia (massive), Pythia (massless) and Cascade. In the upper part of figure 7.3 the position of the D^0 signal is

represented by the points and the width by the error bar. The nominal position is indicated by the dashed line and the mass window cut values by the upper and lower solid lines. It can be seen that the position of the D^0 signal in data and Monte Carlo is found in agreement with the nominal D^0 peak position over the full $p_t(D^\star)$ range. Due to the lower resolution of the measured tracks at high transverse momentum, it is expected that the width increases towards large transverse momenta of the $D^\star$ meson. This dependence is observed in all Monte Carlo simulations and in data in the range $2.5 < p_t(D^\star)$ GeV < 12.5. However, in the first two bins the width in data is again increasing towards lower p_t and a significantly larger width is found in data than in the Monte Carlo simulations is found. The observed discrepancy is probably caused by an insufficient description of the multiple interactions in the Monte Carlo simulations, which dominate the resolution in the low p_t regime. The discrepancy could be explained by too little dead material in the detector simulation, which would cause an overestimated track finding efficiency.

In order to quantify the influence of the different width of the D^0 signal in data and the Monte Carlo simulation, the fraction of $D^\star$ mesons found outside the mass D^0 window of ± 80 MeV are compared. In both cases the number of $D^\star$ mesons is determined by an integration of the signal parameterization in the corresponding range. The lower part of figure 7.3 shows the fractional loss found in the data and the Monte Carlo simulations. The Monte Carlo distribution represents the averaged result of all three models. It can be seen that a perfect agreement between the data and the Monte Carlo is found in the p_t range $2.5 < p_t(D^\star)$ GeV < 9.0, whereas deviations are found at low transverse momentum, where they amount to 1% and in the last bin, where the discrepancy between the data and the Monte Carlo amounts to 2%. The observed deviation is taken into account by applying a global uncertainty of 1%.

7.5 Model Uncertainty

In this analysis three different leading order Monte Carlo models are investigated. As already discussed in this chapter, the prediction given by the Pythia (massless) simulation has been used to correct the data to the hadron level. According to equation 6.1 the chosen Monte Carlo model has a direct influence on the extracted cross section, by means of the acceptance and the reconstruction efficiency. Thus it is evident, that different cross section results might be obtained if the correction factors would be determined on the basis of a another Monte Carlo model. This circumstance is referred to as model dependence. The deviations in the correction factors, determined on the basis of different models, are used to estimate the model uncertainty. The appropriate correction factor to estimate the model dependence is the acceptance $\mathcal{A}$, since this incorporates the different physical models whereas the reconstruction efficiency reflects mainly detector effects. The largest deviations are found between the acceptance determined between the Pythia (massless) and the Cascade simulation. Thus, the total deviation between these acceptances is taken as relative uncertainty on the cross section measurement. Figure 7.4 shows the model uncertainty as a function of the transverse momentum and the pseudorapidity of the $D^\star$ meson. For comparison the statistical error is displayed. It can be seen that the uncertainty due to the model dependence is small compared to the already discussed uncertainties. On average the uncertainty due to the model dependence amounts to 1.0% in the inclusive sample.

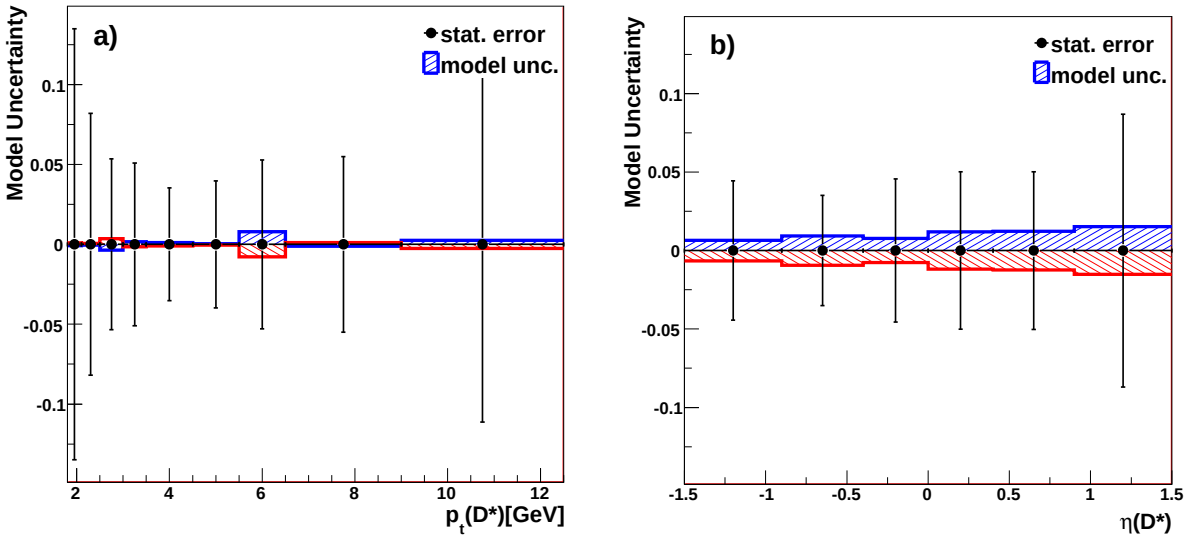

Figure 7.4: *Systematic uncertainties due to model dependence as a function of the transverse momentum a), the pseudorapidity b) of the $D^\star$ mesons. The relative statistical error is shown for comparison (points).*

7.6 Signal Extraction

The global uncertainty due to the signal extraction has been estimated by using different functions to parameterize the signal and the combinatorial background in the ΔM distribution. This procedure allows to approximate the influence of the chosen parameterization on the extracted number of $D^\star$ mesons. In addition to the already introduced Crystal Ball and Granet parameterizations (see section 4.2) one other function for the background and one for the signal has been used. For the combinatorial background the parametrization given by $f(\Delta M) = u_n(\Delta M - m_\pi)^{u_e} \cdot (1 - u_s(\Delta M)^2)$ is used. The pion mass m_π defines the threshold border of the function. The rise is given by the exponential parameter u_e and the quadratic correction term with the parameter u_s improves the description of the data in the high ΔM region. A more detailed description of this function is given in [Flu05]. The additional function used for the signal parameterization is given by a variation of the Novosibirsk parameterization [Ver] which is in detail described in [Boe07]. With the parameterizations introduced in section 4.2 four different combinations of the signal and background parameterizations are possible. The variously combined functions are used to parametrize the ΔM distribution determined for all events found in the inclusive data sample. A bin by bin investigation of the effect of the different parametrizations is not possible, since the effect would be small compared to the statistical error. The largest deviations in the number of extracted $D^\star$ mesons are found between the Crystal Ball parameterization for the signal and Granet for the background and the Novsibirsk parameterization for the signal and the alternative parametrization for the background. In the latter case the number of extracted $D^\star$ mesons is obtained to $N(D^\star) = 8440 \pm 168$ and for the Crystal Ball and Granet combination to $N(D^\star) = 8357 \pm 179$. The relative deviation of these numbers is taken as uncertainty for all bins.

7.7 DIS-Background

To quantify the amount of DIS events which influence this analysis a DIS Monte Carlo sample has been used. The amount of DIS events which survive the photoproduction selection cuts has been determined to $\frac{N_{MC}(D^*)}{\mathcal{L}} = 7.9$ pb. To the total production yield of the analyzed photoproduction data integrated over the full phase space amounts to $\frac{N(D^*)}{\mathcal{L}} = 750$ pb. The comparison of both quantities results to a contribution of 1% to the total cross section, which has been subtracted from the data.

7.8 Branching ratio

$D^\star$ mesons originating from the so-called Golden Decay Channel $D^{*\pm} \to D^0\pi_s^\pm \to K^\mp\pi^\pm\pi_s^\pm$ are analyzed in this thesis. In order to determine $D^\star$ cross sections the number of $D^\star$ mesons has to be corrected for the branching ratio of this decay chain (see equation 6.1). The branching ratio $\mathcal{BR}$ has been determined to $\mathcal{BR} = (2.57 \pm 0.06)\%$ [Yao06]. This results to a relative uncertainty on the cross section measurement of 2.57%.

7.9 Reflections

In addition to the Golden Decay Channel further decay modes of the D^0 with two charged particles in the final state exist, which contribute to the cross section. These decay modes are referred to as reflections r and consist mainly of the decay modes:

$$D^0\pi_{slow}^\pm \to (K^\pm K^\mp,\, \pi^\pm\pi^\mp,\, \pi^\pm\pi^\mp\pi^0)\pi_{slow}^\pm. \tag{7.2}$$

The invariant mass difference ΔM of the three particle system of the reflections is compareable to the invariant mass difference reconstructed on the basis of the decay particles of the Golden Decay channel. Hence the reflections are reconstructed in the signal region of the ΔM distribution. The contribution of the reflections to the cross section is small, due to the D^0 mass window cut. Nevertheless, their contribution has to be subtracted, since the final cross sections presented in this thesis are only corrected for $D^\star$ mesons decaying in the Golden Decay Channel. The correction factor and the corresponding uncertainty has been studied in detail in [Jun08]. In [Jun08] a full inclusive charm Monte Carlo sample, which contains events of all possible decay modes of the $D^\star$ meson, is used to estimate the influence of the reflections. It is not expected that the correction factors change from the DIS to the photoproduction regime, the values obtained in [Jun08] are applied to this analysis. The correction factor r due to the reflections has been determined to be 4.0% with a corresponding error of 1.0%.

7.10 Primary Vertex Fit Efficiency

The primary vertex is determined by fitting the tracks measured in the CJC1, CJC2 CST and CIZ to their origin. The vertex fit efficiency is defined as the probability to find a primary vertex and to fit the tracks of $D^\star$ decay particles to this origin. Deviations of the primary vertex fit efficiency in data and Monte Carlo are taken into account by applying a global correction factor to each event. The influence of a different primary vertex fit efficiency found in data and Monte Carlo to the cross section has been studied in detail in [Boe07].

Source	*Uncertainty*
Luminosity	5.0%
Signal Extraction	1.2%
D^0-meson mass cut	1.0%
DIS Background	1.0%
Branching ratio	2.3%
Reflections	1.0%
Primary vertex fit efficiency	2.5%
Track finding efficiency	6.0%
Trigger Efficiency	4.7%
Model Dependence	1.0%
Hadronic energy scale	2.0%
Sum	10.6%

Table 7.1: *Summary of all identified systematic uncertainty sources. The latter three uncertainties correspond to bin by bin uncertainties.*

In this analysis the correction factor has been determined to 2.5%. Since the analysis is statistically limited a corresponding error of 100% on the correction factor is assumed.

7.11 Track Uncertainty

The track finding efficiency corresponds to the probability that a track is found by the used algorithms in the tracking devices. Since Monte Carlo samples are used to correct for particle losses, deviations in the track finding efficiency between data and Monte Carlo simulation have therefore a direct influence on the cross section. The uncertainty due to the track finding efficiency is one of the dominant sources of systematic uncertainties. Three independent error sources have been identified, which are discussed in detail in [Boe07]. The estimation of the track finding uncertainty is based on an analysis of K^0 decays in which the uncertainty is determined to 2% per track. This results in an uncertainty of 6% for the $D^\star$ meson, since it is assumed that the tracks of the decay particles of the $D^\star$ meson are correlated.

7.12 Summary Uncertainties

A summary of the different uncertainty sources is listed in table 7.1. The uncertainties listed in the upper part of the table correspond to global uncertainties which are applied to each event. The uncertainty sources listed in the lower part correspond to uncertainties which have been determined in each interval of the measured variables. The denoted values correspond to the average uncertainties in the inclusive sample. The luminosity, the track finding efficiency and the trigger efficiency are identified as the dominant uncertainty sources.

Chapter 8

Results: Inclusive sample

In this chapter the results of the inclusive $D^\star$ meson cross section measurement are presented. The cross section are determined in the visible range, which covers a range of the photon virtuality of about $Q^2 < 2$ GeV^2 and photon-proton center-of-mass energies of $100 < W_{\gamma p} < 285$ GeV. $D^\star$ mesons are measured with a transverse momenta of at least 1.8 GeV and pseudorapidities $|\eta(D^\star)| < 1.5$. The total cross sections have been calculated according to equation 6.1 and the differential cross section according to equation 6.2. The measurement is compared to leading order Monte Carlo models given by the Pythia (massive), the Pythia (massless) and the Cascade prediction. The measurement is further compared to next-to-leading order predictions based on a Fixed-Flavor-Number-Scheme (FFNS) as well as to a prediction based on a General-Mass-Variable Flavor-Number-Scheme (GMVFNS) calculation.

8.1 Total Inclusive Cross Section

The total cross section is given by the total amount of measured $D^\star$ mesons which yield 8248 ± 179 (see figure 4.3), the corrected integrated luminosity of 30.68 pb^{-1}, 68.23 pb^{-1} and 93.39 pb^{-1} and the detector efficiency and acceptance correction determined in chapter 6. The total visible cross section is determined to:

$$\sigma^{tot}_{vis}(e^\pm p \to e^\pm D^{\star\pm} X) = 38.60 \pm 2.04 \pm 4.25 \text{ nb} \tag{8.1}$$

The first error denotes the statistical and the second the systematic uncertainty. By comparing the statistical with the systematic uncertainty it can be seen that the precision of the measurement is dominated by the systematic uncertainty. A summary of the total cross section predicted by the leading and next to leading order QCD models can be found in table 8.1. The total cross section calculated by the Pythia (massless) simulation amounts to $\sigma^{tot}_{vis} = 38.47$ nb and is in agreement with the measurement within the uncertainties, whereas the Pythia (massive) prediction overestimates and the Cascade prediction underestimates the measurement by around $\simeq 7$ nb or $\simeq 13$ nb, respectively. A summary of the used PDFs and relevant QCD parameters used in the LO models can by found in table 2.1.

The total cross section predicted by the next to leading order FFNS [Fri95a, Fri95b] and GMVFNS [Spi08b] calculation result to $\sigma^{tot}_{vis} = 34.52^{+21.85}_{-6.69}$ nb and $\sigma^{tot}_{vis} = 32.60^{+19.45}_{-11.78}$ nb, respectively. The central values are compatible with the measurement. The theoretical uncertainties are estimated by varying the renormalization and factorization scales. In addition to the scales the charm mass is varied for the FFNS calculation. The theoretical uncertainties exceed the uncertainties of the measurement by far. A summary of the used PDFs and relevant QCD parameters of both NLO models can by found in table 2.2.

	tot. cross section [nb]
data	$38.60 \pm 2.04 \pm 4.25$
Pythia(massive)	45.25
Pythia(massless)	38.47
Cascade12	25.59
FFNS	$34.52^{+21.85}_{-6.69}$
GMVFNS	$32.60^{+19.45}_{-11.78}$

Table 8.1: *Total $D^\star$ meson cross sections determined in the visible range of the inclusive sample. The statistical error coresponds to the error of the fit used to parametrize the ΔM distribution, as described in 4.2. The systematic uncertainty is determined as discussed in section 7. The theoretical uncertainty of the FFNS prediction corresponds to a scale and mass variation and the uncertainty of the GMVFNS is estimated by scale variation.*

8.2 Differential inclusive Cross Sections

Differential cross sections have been measured as a function of $p_t(D^\star)$, $\eta(D^\star)$ and $W_{\gamma p}$. The cross sections are compared to LO order predictions given by the Pythia (massive), Pythia (massless), Cascade and to NLO predictions given by a FFNS and GMVFNS calculation. In the following discussed distributions the statistical error of the data points is represented by the inner and the square sum of the statistical and systematic uncertainty by the outer error bar. In order to make a comparison of the shape of the extracted cross sections between the data and the theory predictions easier, the normalized ratio R is calculated:

$$R = \frac{\frac{d\sigma^{calc}}{dY}}{\frac{d\sigma^{data}}{dY}} \cdot \frac{\sigma^{data}_{vis}}{\sigma^{calc}_{vis}} \tag{8.2}$$

The variable Y denotes any measured quantity. The variable $\frac{d\sigma^{calc}}{dY}$ and $\frac{d\sigma^{calc}}{dY}$ corresponds to the cross section of a certain theory prediction and the data divided by the bin width dY. With the first term the cross section of a certain theory prediction in the bin dY is normalized to the measured cross section in the corresponding bin. The factors σ^{calc}_{vis} and σ^{data}_{vis} correspond to the total visible cross section calculated for the theory prediction and the data, respectively. With this term, the theory predictions are normalized on the total visible cross section of the data. For the FFNS calculation R is calculated for the central value and each variation separately and afterwards added in quadrature. For the GMVFNS calculation only the central value and the combined uncertainty consisting of the variation of the factorization and renormalization scale are available, thus a correct calculation of the theoretical errors is not possible and therefore only the central values are shown in the ratio distributions for the GMVFNS calculation.

Transverse Momentum of the D* meson

Figure 8.1 shows the extracted cross section as a function of the transverse momentum of the $D^\star$ meson. The corresponding ratio R is displayed below. Neither of the leading order predictions is able to describe the whole observed p_t spectrum of the $D^\star$ mesons, see figure 8.1 a). However, at low p_t, in the range of $1.8 < p_t(D^\star) < 3.0$ GeV, a good agreement

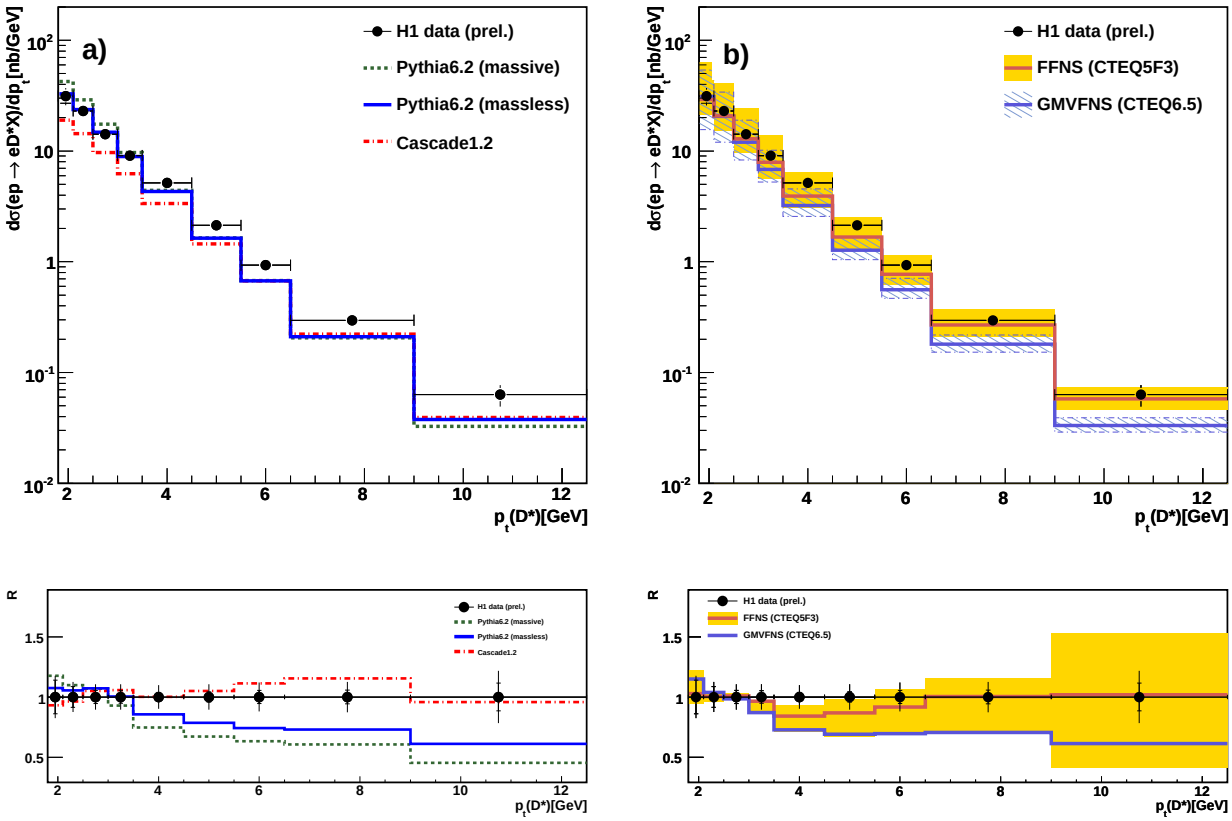

Figure 8.1: *Differential cross section distributions for the inclusive $D^\star$ sample as a function of $p_t(D^\star)$. On the left the data is compared to leading order Monte Carlo predictions given by Pythia(massless), Pythia(massive) and Cascade. On the right the data is compared NLO calculations based on a FFNS (solid) and a GMVFNS (dashed). The corresponding normalized ratios of the MC to the data are displayed in the lower figures.*

is found with the prediction provided by the Pythia (massless) simulation. The Pythia (massive) overestimates and the Cascade prediction underestimates the measurement in this regime. Towards large transverse momenta above a $p_t(D^\star)$ of 3.0 GeV the measurement is underestimated by all three predictions. All predictions show the same normalization above a transverse momentum of 4.5 GeV. The ratio R shows that both Pythia predictions are too steep and can not describe the shape of the $p_t(D^\star)$ spectra. The intrinsic k_t of the gluon in the Cascade Monte Carlo simulation leads to a steeper p_t distribution and a good description of the p_t shape.

In figure 8.1 b) the measurement is compared to the NLO calculations. A good description of the $p_t(D^\star)$ distribution over the full investigated range is given by the FFNS calculation. The GMVFNS calculation is in agreement with the measurement at low transverse momenta ($1.8 < p_t(D^\star) < 3.0$ GeV) and underestimates the measurement towards large $p_t(D^\star)$. As expected the theoretical uncertainties decrease towards higher p_t. For a discussion of the different theoretical uncertainties sources see section 2.6. The ratio distribution shows that a good agreement in shape is found with the FFNS calculation within the uncertainties. The uncertainty increases towards large p_t, which reflects that the shape is constraint by the low $p_t(D^\star)$ bins due to the larger cross section. The shape of the GMVFNS prediction is too steep.

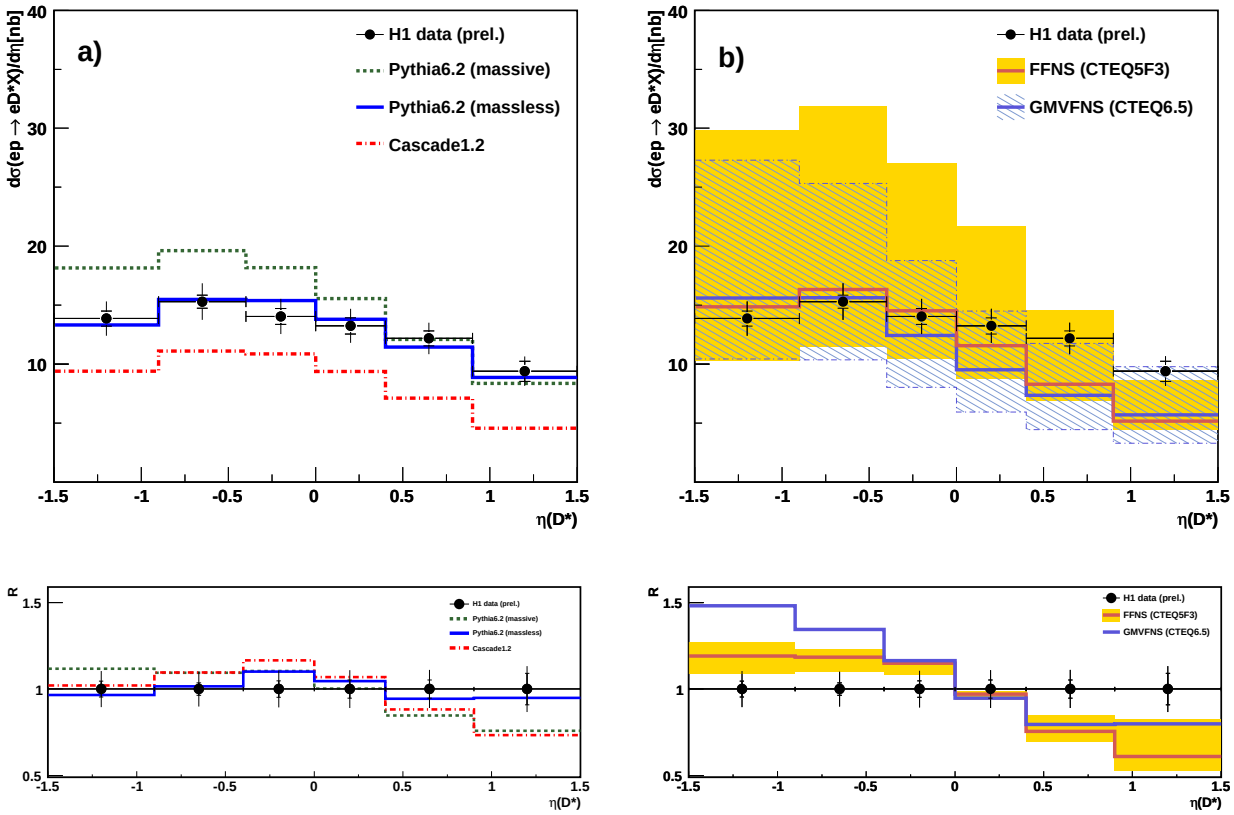

Figure 8.2: *Differential cross section distributions for the inclusive $D^\star$ sample as a function of $\eta(D^\star)$. On the left the data is compared to leading order Monte Carlo predictions given by Pythia(massless), Pythia(massive) and Cascade. On the right the data is compared NLO calculations based on a FFNS (solid) and a GMVFNS(dashed). The corresponding normalized ratios of the MC to the data are displayed in the lower figures.*

Pseudorapidity of the D* meson

In figure 8.2 the cross section as a function of $\eta(D^\star)$ is displayed. The distribution is slightly falling towards positive η and shows a maximum at $-1 < \eta(D^\star) < -0.5$. The Pythia (massless) prediction is in good agreement with the measurement over the full η range. The prediction provided by the Pythia (massive) simulation is compatible with the data in the forward region ($\eta > 0.4$), but overestimates the measurement in the backward region. The Cascade simulation underestimates the measurement over the full range. The normalized ratio shows that the Pythia (massless) prediction describes the shape reasonable over the full η range. The Pythia (massive) and Cascade prediction describe the shape in the backward region, but are too steep in the very forward bin ($0.9 < \eta(D^\star) < 1.5$).

The comparison of the measurement with the NLO predictions is shown in figure 8.2 b). A reasonable agreement with central values of both calculations is found in the backward direction, whereas the predictions underestimate the measurement in the forward direction. Both predictions show large theoretical uncertainties, which are largest in the backward direction and decrease towards the forward direction. In figure 8.4 the theoretical uncertainty sources of the FFNS calculation are shown separately as a function of the pseudorapidity of the $D^\star$ meson. The largest uncertainty is given by the variation of the renormalization scale. In particular the uncertainty in the upward direction reaches values of $\simeq 100\%$ in the

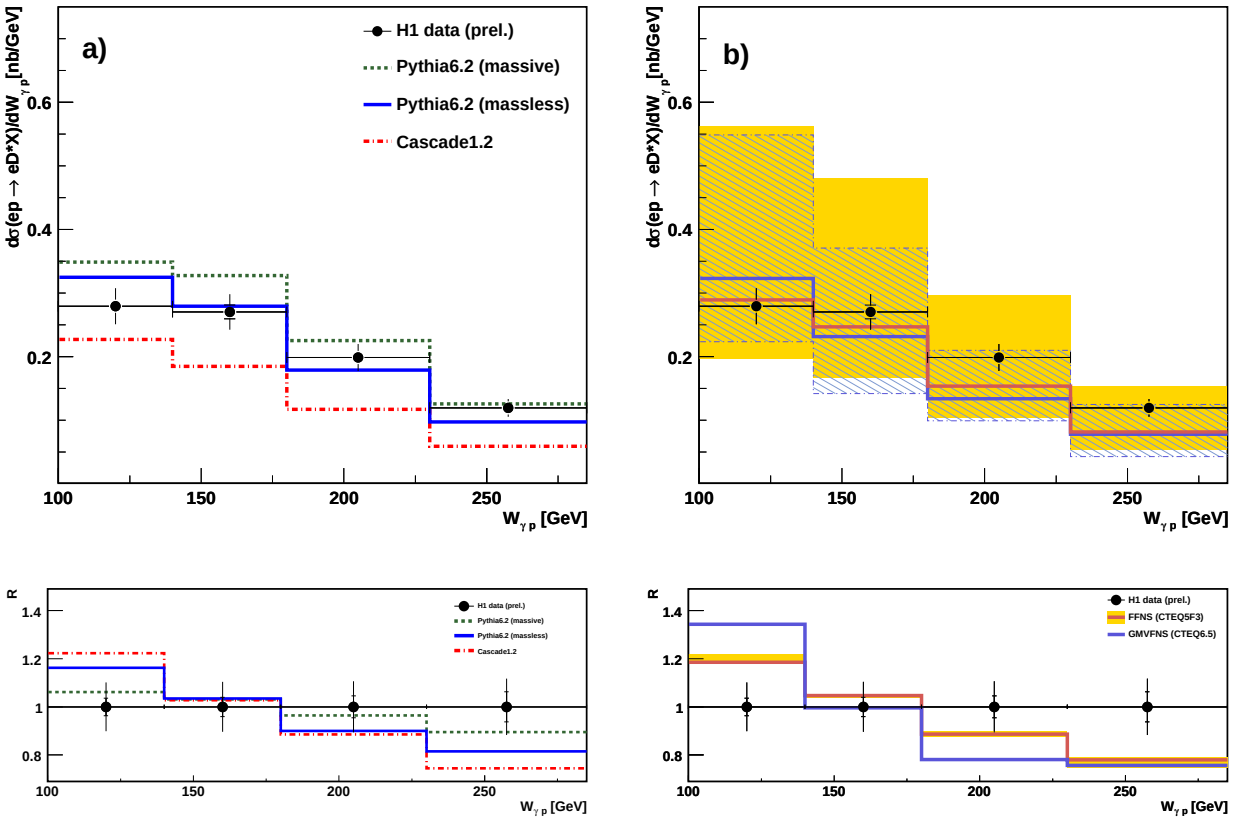

Figure 8.3: *Differential cross section distributions for the inclusive $D^\star$ sample as a function of $W_{\gamma p}$. On the left the data is compared to leading order Monte Carlo predictions given by Pythia(massless), Pythia(massive) and Cascade. On the right the data is compared NLO calculations based on a FFNS (solid) and a GMVFNS(dashed). The corresponding normalized ratios of the MC to the data are displayed in the lower figures.*

backward direction. The normalized ratio distribution shows that the shape is not described by the NLO calculations. Both prediction are too steep falling towards positive $\eta(D^\star)$.

Center-of-Mass Energy of Photon-Proton System

In figure 8.3 the cross section measurement of the variable $W_{\gamma p}$, measured for the first time in this large region, is displayed. Neither of the leading order predictions is able to describe the $W_{\gamma p}$ spectra completely. However, the best agreement is found with the Pythia (massless) prediction. The normalized ratio shows that the shape is good described by the Pythia (massive) prediction. The Pythia (massless) and the Cascade predictions are both too steep.

The data is well compatible with the NLO calculations within the uncertainties. The central values are compareable with the measurement in the first two bins and underestimate the measurement at large values of $W_{\gamma p}$. In figure 8.4 the uncertainties of the FFNS calculation are shown separately. The largest uncertainty is given by the variation of the renormalization scale. The uncertainties are almost flat and have therefore no influence on the shape. This can be seen in the normalized ratio distribution, where the theoretical uncertainties are small. Neither of the NLO calculations is able to describe the $W_{\gamma p}$ shape.

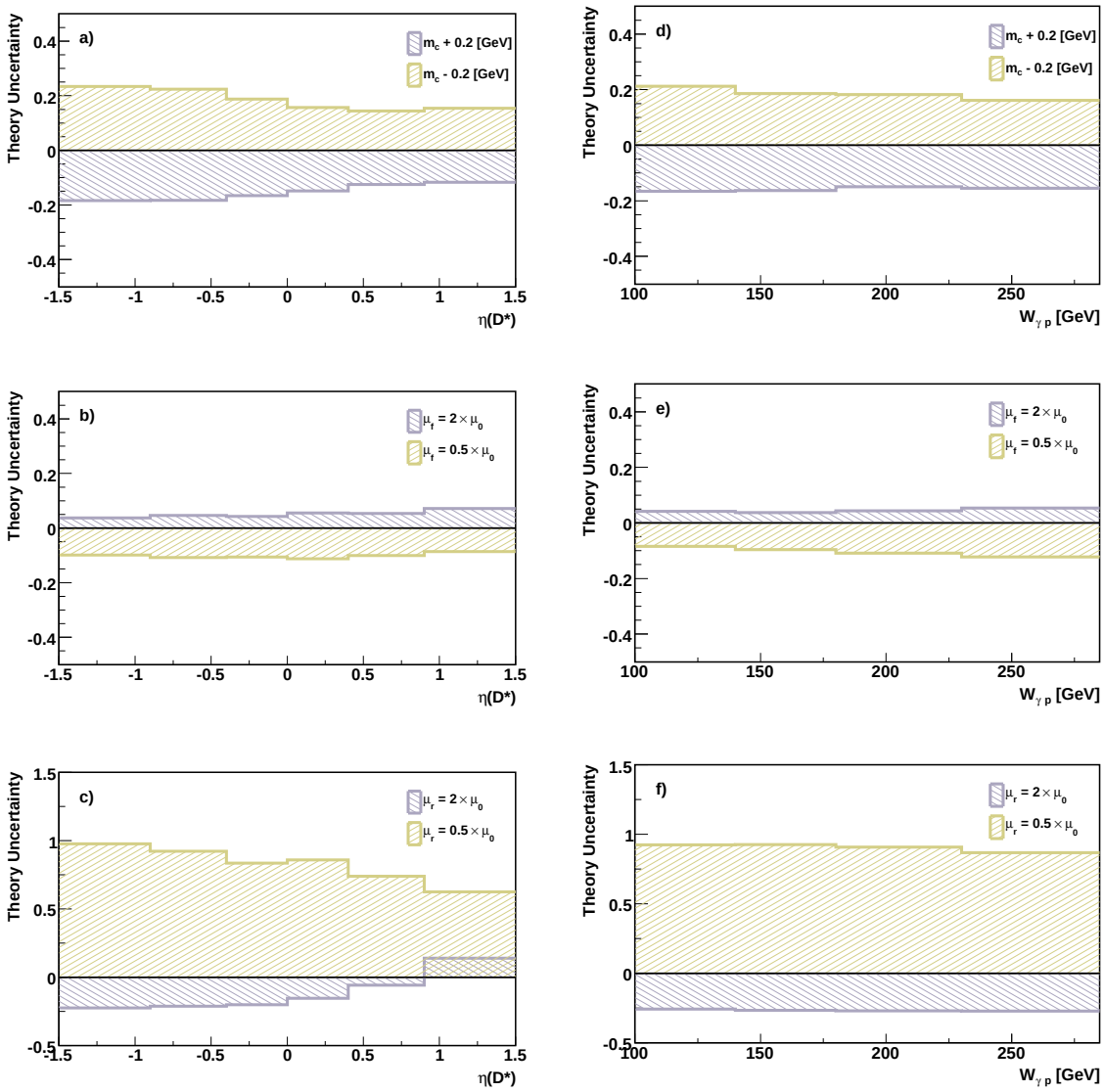

Figure 8.4: *Relative theoretical uncertainties as a function of $\eta(D^\star)$ a)-c) and $W_{\gamma p}$ d)-f), as predicted by the FFNS next-to-leading order calculation provided by the program FMNR.*

8.3 Double Differential Cross Sections

In order to study the observed excess at high transverse momenta and in the forward region in more detail double differential cross sections as a function of the transverse momentum and the pseudorapidity of the $D^\star$ meson have been extracted. The pseudorapidity of the $D^\star$ mesons has been measured in three different $p_t(D^\star)$ ranges. The chosen p_t ranges correspond to the ranges introduced in section 5, such that each range corresponds to a measurement with one of the three subtriggers used in this analysis. In figure 8.5 the double differential cross section as a function of $\eta(D^\star)$ in bins of $p_t(D^\star)$ are displayed.

$D^\star$ mesons with low p_t are primarily observed in the backward region. Towards larger $p_t(D^\star)$ more and more $D^\star$ mesons are measured in the forward region. The different interval sizes consider the decreasing signal to background ratio towards the forward region and low p_t.

In general the theory predictions reproduce the tendency, that $D^\star$ mesons are located more

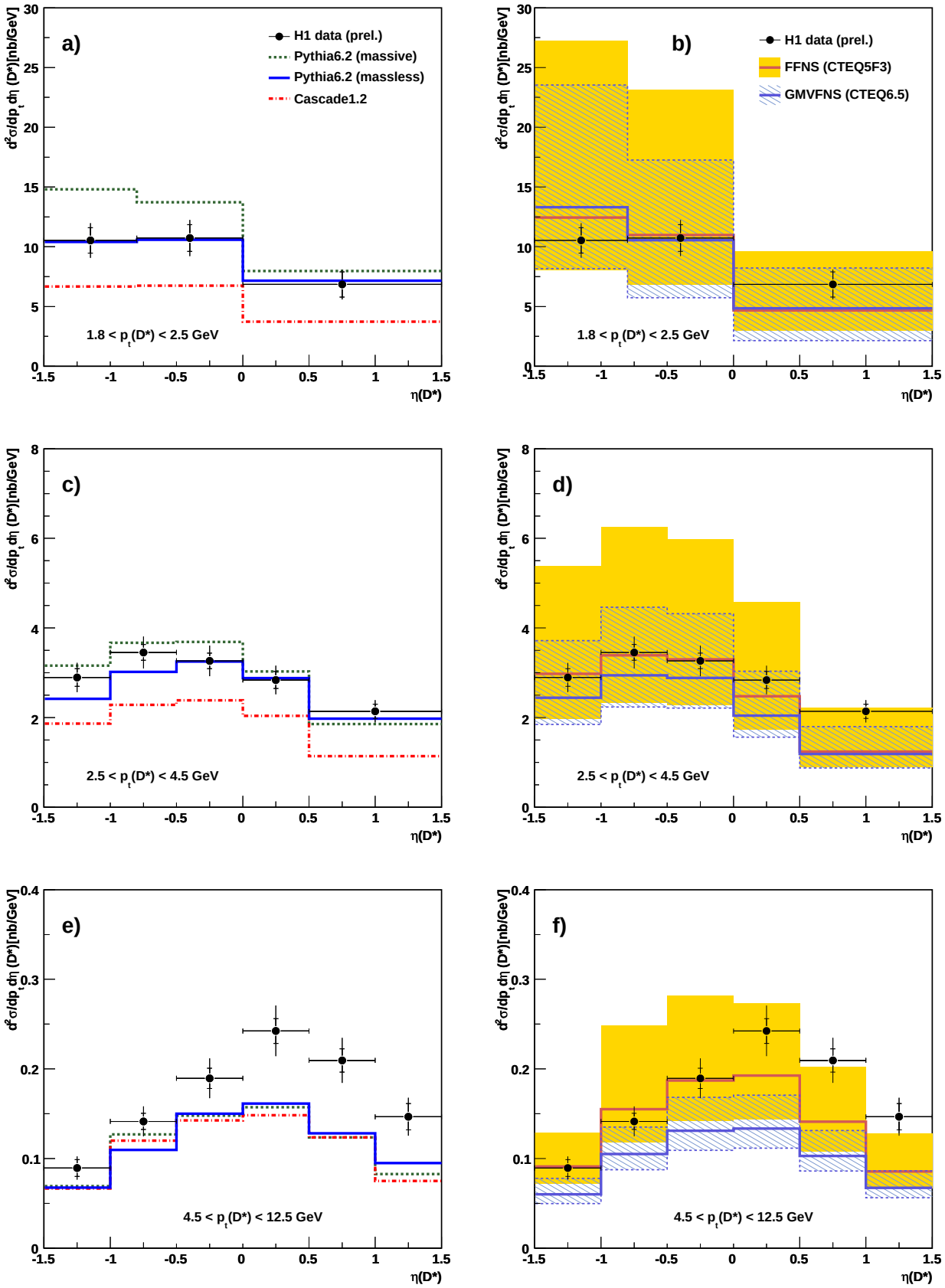

Figure 8.5: *Double differential cross section distributions for the inclusive $D^\star$ sample as a function of p_t and η of the $D^\star$ meson. On the left the data is compared to leading order Monte Carlo predictions given by Pythia(massless), Pythia(massive) and Cascade. On the right the data is compared to next to leading order calculations given by FMNR and(solid) and GMVFNS(dashed).*

in the forward region with increasing p_t. However, the rise of the theory prediction in the forward region towards large p_t is not strong enough to describe the data. The measurement is compatible with the Pythia (massless) simulation at low p_t, but does not describe the shape and normalization at large p_t. Pythia (massive) and Cascade are always too low, except in the lowest p_t interval, in the forward region. In the highest p_t range all three LO predictions are very similar in shape and normalization.

Both NLO calculation show the tendency to underestimate the measurement in the forward region. This is most prominent for large p_t. In the highest p_t range the shape of the NLO distributions is similar to the shape of the of the LO order predictions.

An interpretation of the excess in the forward region and especially at large p_t is difficult. It has to be considered that the theoretical models are influenced by a various number of input parameters, which are in particular the proton and photon PDF, the different treatment of the resolved components in the different models, the calculation of the hard matrix element and the applied fragmentation model. However, the measurement shows, that the naive assumption that NLO should describe the high p_t range better than LO, does not hold.

8.4 Summary Inclusive Results

The precision of the measurement is much higher than the accuracy of the NLO calculations. The theoretical uncertainties are estimated by scale variations and amount to $^{+63\%}_{-19\%}$ for the FFNS and to $^{+60\%}_{-36\%}$ for the GMVFNS calculation. The measurement is best reproduced by the leading order Pythia (massless) simulation and the next to leading order FFNS prediction. The shapes are in general reasonbly described by the LO and NLO predictions deviations are observed in the shape at large p_t, in the forward region. Neither of the models is able to describe the shape of the $W_{\gamma p}$ distribution. A clear excess is observed in the double differential cross section measurement at large p_t and in the forward direction.

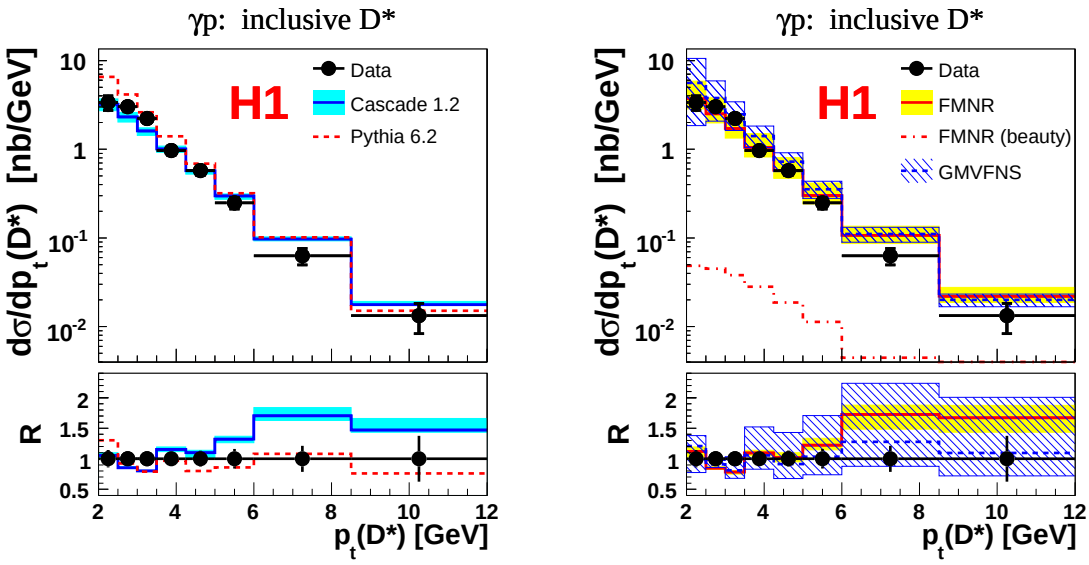

Figure 8.6: *Inclusive $D^\star$ meson cross sections as a function of the transverse momentum of the $D^\star$ mesons [Akt07]. The measurement is compared with the leading order predictions of the Pythia (massive) and the Cascade simulation (on the left) and to a FFNS (FMNR) and a GMVFNS next to leading order calculation (on the right).*

8.5 Comparison to Previous Measurements

It is interesting to see how the results obtained in this analysis compare to previous measurements of the H1 and ZEUS collaboration. Both measurements are based on significantly lower statistics and are performed in a smaller phase space compared to the present analysis.

Previous Measurement by the H1 collaboration

Differential photoproduction cross sections for events containing $D^\star$ mesons had been measured by the H1 collaboration in [Akt07]. The data sample analyzed corresponds to an integrated luminosity of 51 pb^{-1}. The investigated kinematic region covers range of a photon-proton center of mass energy of $172 < W_{\gamma p} < 256$ GeV and photon virtualities of $Q^2 < 0.01$ GeV^2. The phase space is significantly stronger restricted than the phase space investigated in this analysis. The restriction in the $W_{\gamma p}$ and Q^2 range in the previous analysis corresponds to the acceptance of the electron tagger, located close to the beam pipe at $z = -33.4$ m, which has been used to select photoproduction events. $D^\star$ mesons had been investigated in the Golden Decay Chanel with a transverse momentum of $p_t(D^\star) > 2.0$ GeV and in the pseudorapidity range of $|\eta(D^\star)| < 1.5$. The total number of $D^\star$ mesons amounted to 1166 ± 82. Figure 8.6 shows the cross section measurement of the $D^\star$ mesons as a function of the transverse momentum and pseudorapidity of the $D^\star$ mesons. The measurement is compared to leading order Monte Carlo predictions given by the Pythia (massive) and Cascade simulation as well to a FFNS calculation (provided by FMNR) and a GMVFNS calculations.

Note that the FFNS and the GMVFNS calculations differ from the calculation presented in this thesis. The GMVFNS calculation is based on [Kni05b, Kni05a] and the FFNS uses the CTEQ6M PDF in contrast to the CTEQ5f3 PDF used in the present analysis. The different PDF could explain why the normalization of the GMVFNS and the FFNS calculations are

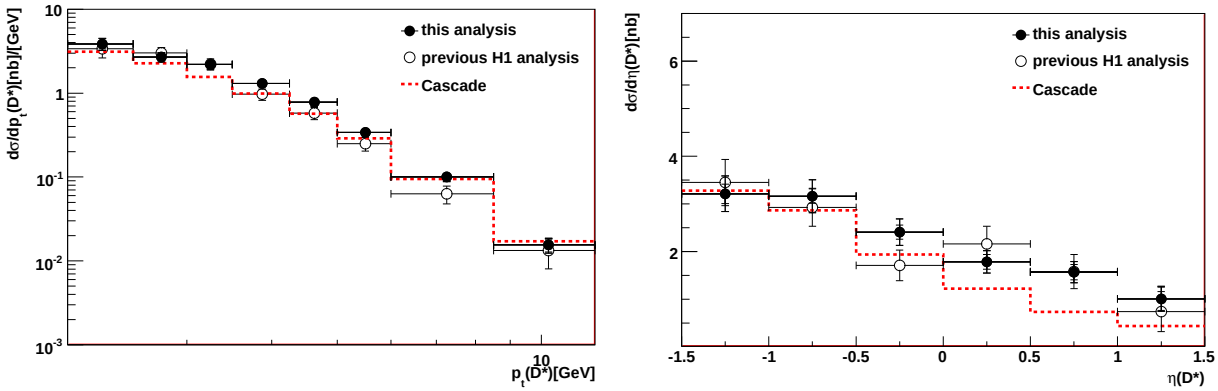

Figure 8.7: *Inclusive $D^\star$ meson cross sections as a function of the transverse momentum of the $D^\star$ mesons [Akt07]. The measurement is compared with the leading order predictions of the Pythia (massive) and the Cascade simulation (on the left) and to a FFNS (FMNR) and a GMVFNS next to leading order calculation (on the right).*

similar in the previous analysis as can be infered from figure 8.6 in contrast to figure 8.1.

A further difference difference between this and the previous analysis is given by the treatment of the theoretical uncertainties of the FFNS calculation. In this analysis the theoretical uncertainties are estimated indepedently and afterwards added in quadrature, whereas in the previous analysis only the dominant error is shown.

The Cascade and Pythia (massive) predictions displayed in figure 8.6 show the same tendency as observed in this analysis. Cascade is harder compared to Pythia, which results in higher cross section at low p_t, both have the same normalization at high p_t. However, the data are steeper in this analysis. The harder p_t spectrum is probably related to the extended $W_{\gamma p}$ range studied in this analysis. In order to prove this hypothesis, the phase space of this analysis has been restricted to the phase space of the previous analysis and cross sections as a function of p_t and η determined. Figure 8.7 shows the corresponding cross sections. The Cascade prediction has been as well recalculated for the restricted phase space and is shown for reference in 8.7. This supports the hypothesis that the extended $W_{\gamma p}$ range studied in this analysis leads to the different p_t shape of both analyses.

Previous Measurement by the ZEUS collaboration

A measurement, which has been performed in a phase space compareable to the phase space of this analysis, is given by the latest published ZEUS measurement of the year 1998 [Bre99]. In this analysis inclusive cross section of $D^\star$ mesons have been measured for photon-proton center-of-mass energies in the range $130 < W_{\gamma p} < 285$ GeV and for photon virtualities of $Q^2 < 1$ GeV^2. The analyzed data sample corresponds to an integrated luminosity of 37 pb^{-1}. $D^\star$ mesons had been investigated in the Golden Decay and the five prong chanel with a transverse momentum of $p_t(D^\star) > 2.0$ GeV and in the pseudorapidity range $|\eta(D^\star)| < 1.5$. The analysis is based on a total number of $D^\star$ mesons of 3702 ± 136. Figure 8.8 shows the measurement of the pseudorapidity for different lower values of the transverse momentum of the $D^\star$ meson. The results are compared to different NLO predictions ([Bin98], [Cac97]).

The data shows the same tendency as observed in this analysis. $D^\star$ mesons with low p_t are primarily observed in the backward region. Towards larger $p_t(D^\star)$ more and more $D^\star$ mesons are measured in the forward region. The most prominent result of this measurement

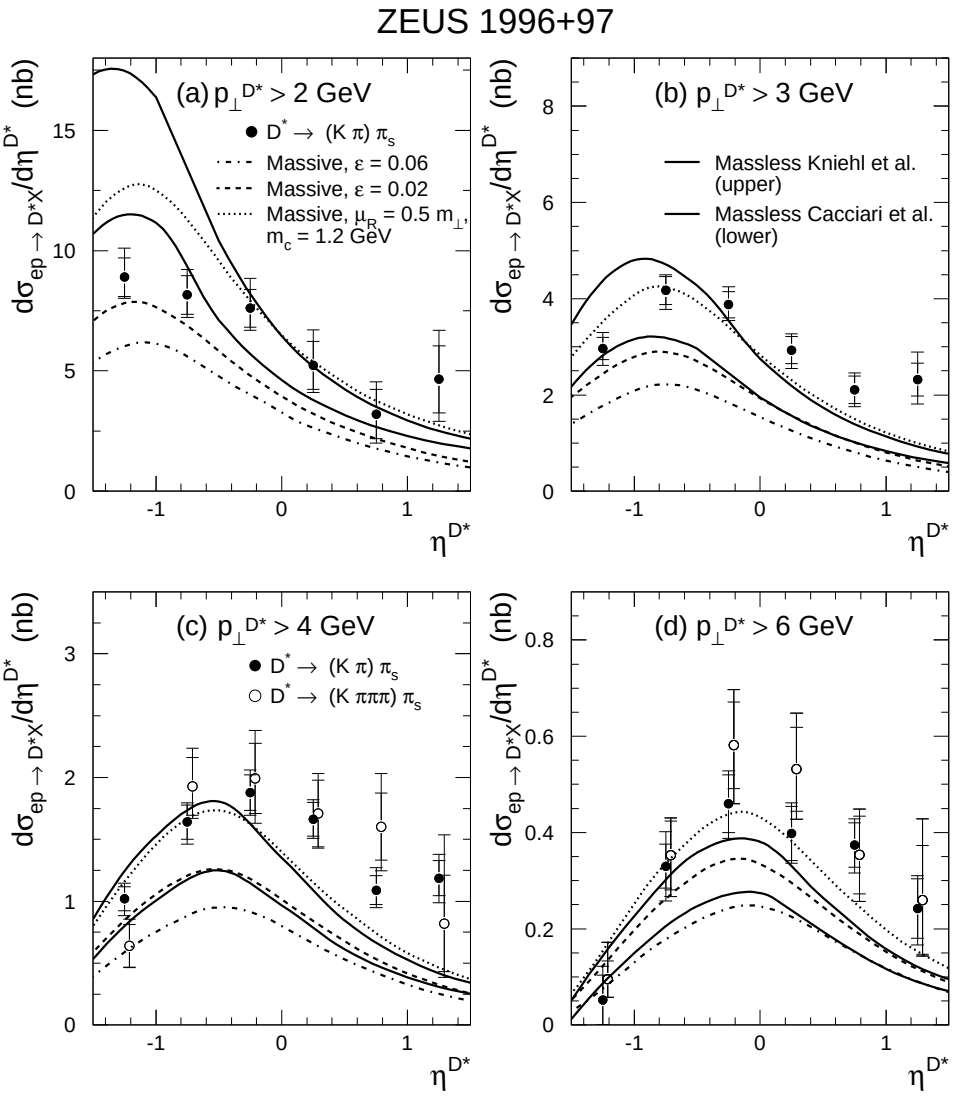

Figure 8.8: *Differential cross sections for $D^\star$ mesons in photoproduction measured by the ZEUS collaboration. The curves are the predictions of the massless charm NLO calculation, corresponding to [Bin98] (a,c) and [Cac97] (b,d) with various photon parton density parameterizations.*

is that the measurement is underestimated in particular towards large transverse momenta and in the forward region. This is in agreement with the result of this analysis (see figure 8.5).

Chapter 9

DiJet Sample

In the inclusive sample one charm quark is tagged by the $D^\star$ meson. This method allows to draw conclusions from the $D^\star$ meson kinematics to the charm quark kinematics. However, this has to be handled with care since the momentum transfer from the charm quark to the $D^\star$ meson depends crucially on the knowledge of the fragmentation. Furthermore this method gives no information about the second hard parton, produced in the BGF or resolved processes (see figure 2.5), which is needed to get a more detailed picture of the production mechanism. In a continuative measurement, which is based on the inclusive data sample, in addition to the $D^\star$ meson at least two jets are reconstructed. It is required that one of the jets is associated to the $D^\star$ meson. The resulting sample is referred to as the DiJet sample. The reconstruction of the charm quark kinematic by means of a jet allows to reduce the influence of fragmentation, since it is expected that the jet incorporates in addition to the $D^\star$ meson most of the hadronic final state particles generated in the fragmentation process of the charm quark. It is assumed that the second hard parton can be associated with the other leading jet.

In the following a description of the jet algorithm used in this analysis is given, subsequently the selection strategy of the jets will be described. Afterwards, the correlation between the charm quarks and the jets is probed on the basis of different QCD models. In the end of this chapter hadronic correction factors, which are needed to correct the NLO prediction from the parton to the hadron level, are presented.

9.1 Jet Algorithm

A jet algorithm defines under which assumptions objects are grouped to jets and how the four vectors of the objects are merged to the resulting four vector of the jet. A well-defined jet algorithm is characterized by a strong correlation between the jets reconstructed either on the parton, hadron or detector level. One of the most important requirements of the algorithm is "infrared safety" that means that processes like soft gluon radiation or gluon splitting do not change the result of the jet algorithm. The most commonly used jet algorithm at the H1 experiment which fulfills "infrared safety" is the so-called k_t algorithm [But03]. The algorithm is divided in two parts. The first part defines under which conditions particles are grouped to jets and the second part defines how the kinematics of the particles are merged to the kinematic of the resulting jet. Several schemes are available to merge the kinematics of the protojets to the final jets. The merging scheme used in this analysis is the E-scheme in which the kinematic of the jets is calculated by adding the four-vectors of the protojets. A second scheme which is widely used at the H1 experiment is the p_t-scheme. This scheme has been tested as well in the context of this analysis (see section 9.8). A detailed description of the iterative grouping and merging procedure follows:

1. For each protojet i and each pair of protojets ij the distances

$$d_i = E_{t,i}^2 \tag{9.1}$$
$$d_{ij} = min(E_{t,i}^2,\, E_{t,j}^2) \cdot [(\eta_i - \eta_j)^2 + (\phi_i - \phi_j)^2]/R_0^2 \tag{9.2}$$

   are calculated. The constant R_0 is related to the opening angle of the jets. In this analysis $R_0 = 1$ is chosen.

2. The minimum d_{min} of all d_i and d_{ij} is found.

3. If d_{min} is a d_{ij} the protojets i and j are replaced by a new protojet k with the merged kinematic quantities. As mentioned above, various approaches exist to calculate the kinematics of the merged jets. The E-scheme has been used in the measurement and is given by adding the four-vectors of the protojets:

$$(p_x, p_y, p_z, E)_k = (p_x, p_y, p_z, E)_i + (p_x, p_y, p_z, E)_j \tag{9.3}$$

   The p_t-scheme is defined as follows:

$$E_{t,k} = E_{t,i} + E_{t,j}, \tag{9.4}$$
$$\eta_k = \frac{E_{t,i} \cdot \eta_i + E_{t,j} \cdot \eta_j}{E_{t,ij}} \tag{9.5}$$
$$\phi_k = \frac{E_{t,i} \cdot \phi_i + E_{t,j} \cdot \phi_j}{E_{t,ij}} \tag{9.6}$$

   The schemes differ in the kinematic of the resulting jets. The most prominent difference of the schemes is that the E-scheme provides massive jets whereas the result of the p_t-scheme are massless jets. It will be shown in section 9.8 that the hadronic correction factors calculated on the basis of the E-scheme are smaller compared to those calculated in the p_t-scheme.

4. If d_{min} is a d_i the protojet i is considered as a final jet and is removed from the list of protojets.

5. If there are protojets left, the procedure goes on with step one.

The algorithm described above produces a list containing a large number of jets. However, only jets with a reasonably high transverse momentum allow perturbative calculations and are therefore of physical interest.

9.2 DiJet Selection

The DiJet selection is performed in addition to the inclusive sample, hence the resulting DiJet sample is a subsample of the inclusive sample with a significantly lower statistics. The jet selection is based on the inclusive k_t algorithm which is run in the E-scheme. At least two jets are required, one jet is associated to the $D^\star$ meson and is in the following referred to as the $Jet_{D^\star}$. The other jet is assumed to be associated to the other hard parton, which did not hadronize into the $D^\star$ meson. This jet is referred to as the Jet_{other}. An illustratration of the jet association on the basis of the BGF process is illustrated in figure 9.1.

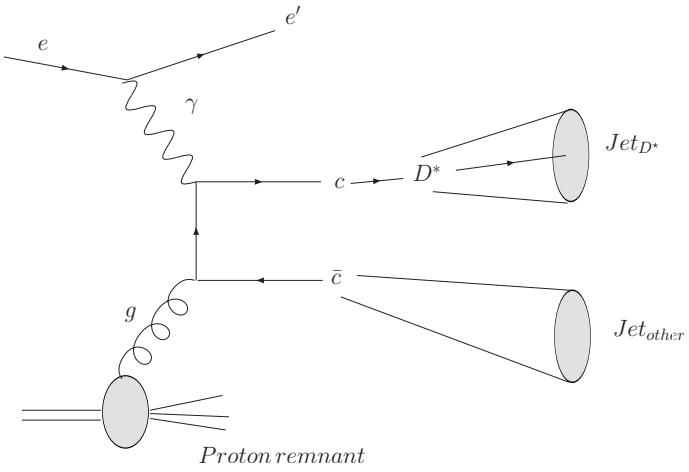

Figure 9.1: *Illustration of the terminology used in this chapter on the basis of the BGF process. The jet associated to the $D^\star$ meson is referred to as $Jet_{D^\star}$. The jet associated to the other hard parton, which is not fragmenting into the $D^\star$ meson is referred to as Jet_{other}.*

Jet Selection Cuts	
$p_t(Jet_1)$	> 4.0 GeV
$p_t(Jet_2)$	> 3.0 GeV
$\lvert\eta(Jet_{1,2})\rvert$	< 1.5
Number of jets	≥ 2

Table 9.1: *Summary of the jet selection cuts. The Jet_1 denotes the leading and Jet_2 the next leading jet. One of these jets has to contain a $D^\star$ meson candidate.*

The DiJet selection proceeds in the following steps. In the first step a list of all HFS particles for each event of the inclusive sample is created. The list is modified such that the decay products of the $D^\star$ meson candidate ($K^\mp\pi^\pm\pi^\pm_{slow}$) are removed from the list and substituted by the corresponding $D^\star$ meson candidate. This prevents that in the resulting $Jet_{D^\star}$ decay particles of the $D^\star$ meson are not incorporated. This list is fed into the k_t algorithm which provides a list of jets ordered by decreasing transverse momenta of the jets. Jets with a transverse momentum lower than 3 GeV and jets which are reconstructed outside the central detector region $|\eta| > 1.5$ are removed from the list. Subsequently only those events are considered in which at least two jets are found. On the basis of these events the identification of the $Jet_{D^\star}$ and the Jet_{other} is performed. For this, the list of jets is searched for a jet which is incorporating the $D^\star$ meson candidate, this jet is then labled as $Jet_{D^\star}$. In 93.6% of the cases this jet is either the leading or the next leading jet. It is assumed that the second hard parton can be associated to the remaining hard jet. Thus the leading jet which has not already been identified as $Jet_{D^\star}$ is labeled as Jet_{other}. If the $D^\star$ meson is found in a jet of even lower p_t than the next-leading jet, then the Jet_{other} is always assigned to the leading jet. Figure 9.2 shows number of events in which the $Jet_{D^\star}$ or Jet_{other} is found as leading jet Jet_1, next-leading jet Jet_2 or a jet with even lower p_t as the next-leading jet Jet_{n+2}.

On the basis of the identified $Jet_{D^\star}$ and Jet_{other} the final selection is performed. An asymmetric requirement on the transverse momenta of the identified jets of $p_t > 4$ GeV or $p_t > 3$ GeV is applied on the $Jet_{D^\star}$ or Jet_{other}, respectively, to avoid divergencies in the NLO calculation. A summary of the applied jet selections can be found in table 9.1. Note that if more than one $D^\star$ candidate is found in an event, which is usually the case, the described procedure is applied for each $D^\star$ candidate. This prevents ambiguousness in those events where partially unequal daughter particles of different $D^\star$ candidates are reconstructed. If

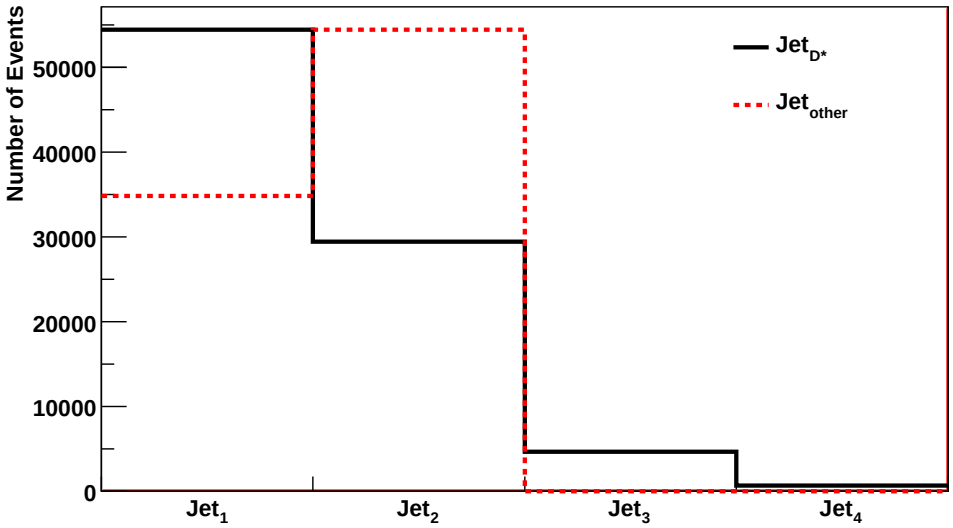

Figure 9.2: *Number of $Jet_{D^\star}$ and Jet_{other} candidates as a function of the ordering of the jets. The Jet_{other} can by definition only be the leading or the next-leading jet.*

the search for jets in events with multiple $D^\star$ candidates is successful more than once, these events contribute multiple times to the jet cross section in the same way as multiple $D^\star$ meson candidates contribute to the inclusive cross section.

9.3 Parton and jet correlation

In this section the correlation between the partons and the jets found on the detector level is studied. These studies are performed on the basis of the Cascade simulation. In Cascade no resolved components are implemented, hence the two outgoing hard partons are always given by a charm and an anticharm quark.

In order to investigate the correlation between the charm quark and the reconstructed $D^\star$ meson, the charm quark before the parton shower and the hadronisation step is matched to the corresponding $D^\star$ meson by comparing the charge of the charm quarks with the charge of the reconstructed $D^\star$ meson. Figure 9.3 a) and b) shows the correlation of the transverse momentum and the pseudorapidity between the charm quark and the corresponding reconstructed $D^\star$ meson. The transverse momentum of the generated charm quark is in comparison to the reconstructed $D^\star$ meson on average about 20% higher. This deviation is caused by the particles, which are produced in addition to the $D^\star$ meson in the hadronisation process. These particles carry a fraction of transverse momentum away. In figure 9.3 b) shows that the fragmentation has only little influence on the pseudorapidity of the $D^\star$ mesons. In figure 9.3 the correlation between the charm quark and the corresponding reconstructed $Jet_{D^\star}$ correlation as a function of p_t a) and in 9.3 b) as a function of η is displayed. As expected a much better p_t correlation is observed in this case. The η correlation is similar to the correlation of the $D^\star$ meson and the charm quark. The better p_t correlation can be explained by the circumstance that most of the particles produced in the hadronisation process are incorporated in the corresponding jet.

The assignment of the Jet_{other} to the second hard parton is based on the assumption that

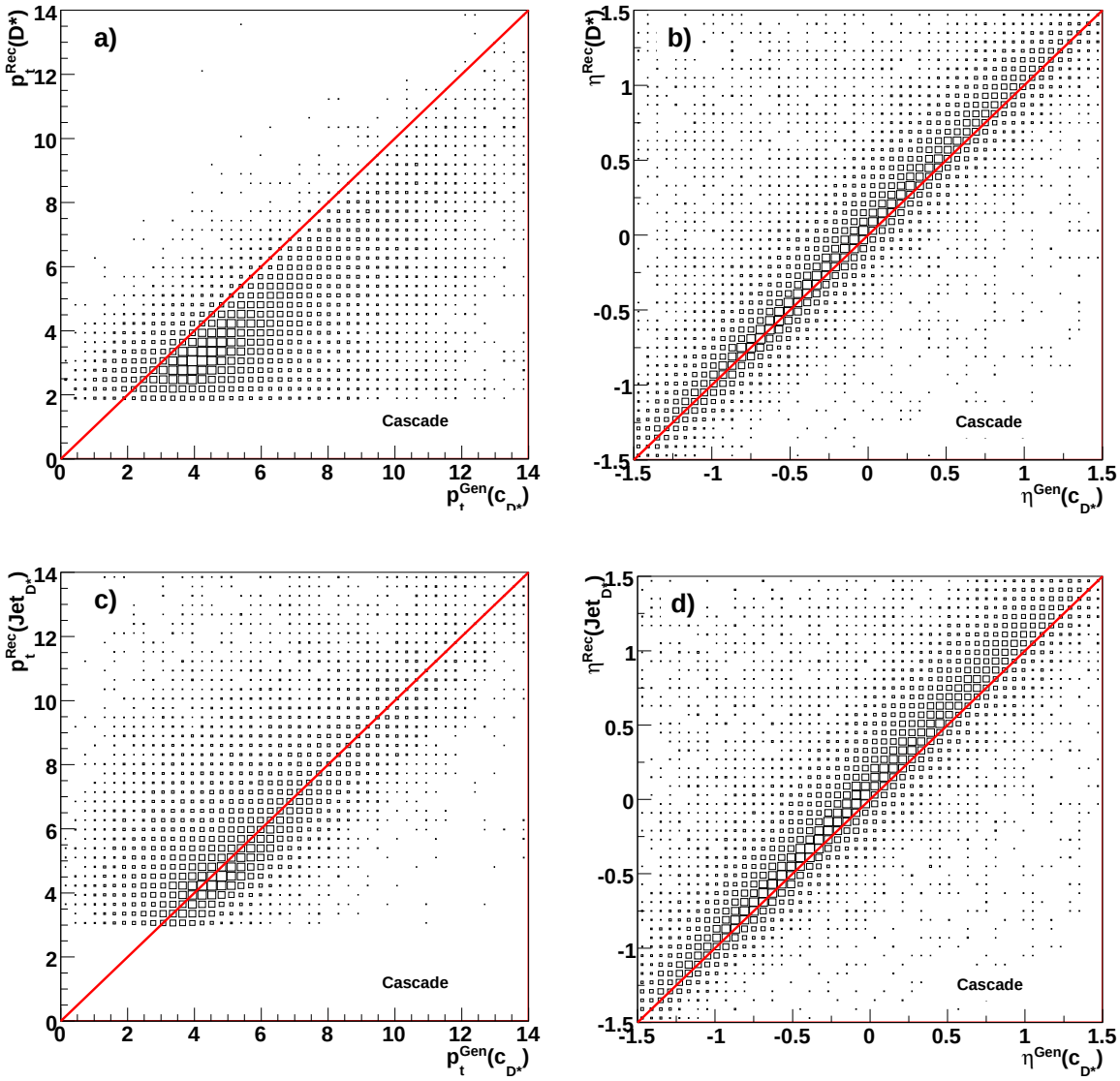

Figure 9.3: Correlation between the charm quarks and the associated reconstructed $D^\star$ meson as a function of the transverse momentum (a) and the pseudorapidity (b).

the charm quarks produced in the hard interaction produce in general two hard jets. In figure 9.4 a) and 9.4 b) the correlation between the Jet_{other} and the charm quark, not hadronizing into the $D^\star$ meson, is displayed for Cascade. This correlation is slightly worse compared to the correlation depicted in figure 9.4 a) and b) but still sufficient and shows that the second hard parton produces in most of the cases the Jet_{other}. It is further interesting to confront the correlation of the Jet_{other} and the corresponding charm quark with a Monte Carlo model in which in addition to the BGF resolved components are implemented. The correlation of the Jet_{other} and the charm quark determined on the basis of the Pythia (massless) simulation is displayed in figure 9.4 c) and d) and for Pythia (massive) in 9.4 e) and f). In Pythia the second hard parton can also be given by a gluon or light flavor as predicted by the resolved components. The accumulation of events in the left lower part of 9.4 e) represents the fraction of events in which the Jet_{other} is not produced by a charm quark, which indicates that the Jet_{other} is in some cases produced by a gluon or light flavor.

Note that the absence of resolved processes in Cascade does not mean that these are ignored in the Cascade simulation, in Cascade part of the charm excitation and NLO effects

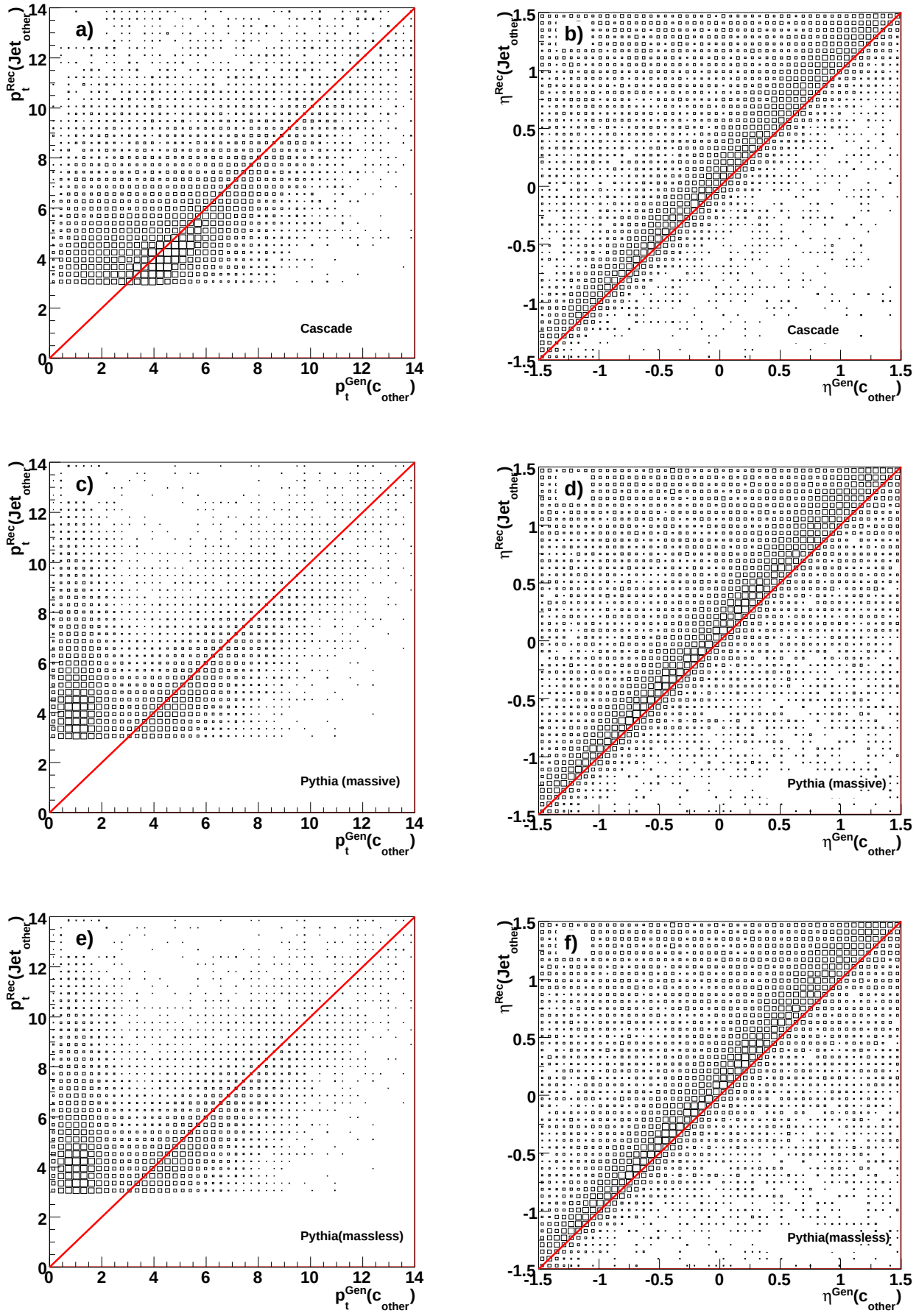

Figure 9.4: Correlation between the charm quarks and the reconstructed jets as a function of the transverse momentum and the pseudorapidity. Figures a)-d) are based on Cascade and e) and f) on Pythia (massless) simulation.

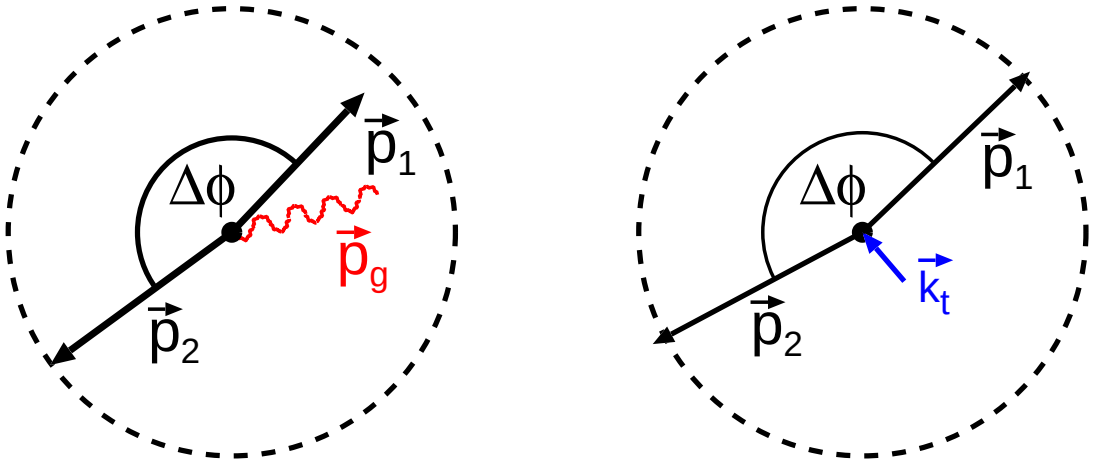

Figure 9.5: *Illustration of charm quark pair production in the rϕ plane. On the left it is shown that initial state gluon radiation can cause a deviation from the back-to-back topology. On right the influence of intrinsic transverse momenta of the incoming gluon is depicted. The picture is adopted from [Flu05].*

are covered by the k_t factorization as described in chapter 2.

9.4 Combined Jet Observables

The reconstruction of both hard partons allows to obtain a more detailed picture of the production mechanism of the charm quarks. Therefore special quantities are studied which are constructed on the basis of both reconstructed jets.

Angular Difference $\Delta\phi$ and $\Delta\eta$

One of these observables is the azimuthal angular difference $\Delta\phi$ between the $Jet_{D^\star}$ and Jet_{other}. This observable is defined as follows:

$$\Delta\phi(Jet_{D^\star},\, Jet_{other}) = \begin{cases} |\phi_{Jet_{D^\star}} - \phi_{Jet_{other}}| & \text{if } |\phi_{Jet_{D^\star}} - \phi_{Jet_{other}}| \leq 180° \\ 360° - |\phi_{Jet_{D^\star}} - \phi_{Jet_{other}}| & \text{if } |\phi_{Jet_{D^\star}} - \phi_{Jet_{other}}| > 180° \end{cases} .$$

The subsequent considerations are based on the assumption that the transverse momentum of the incoming photon can be neglected. This is certainly true for the regime of photoproduction which is investigated in this thesis. Furthermore it is assumed that in first approximation the transverse momentum of the incoming gluon can be neglected as well. With this assumptions it is expected that in a $2 \rightarrow 2$ process, as it is for instance given by the BGF process in the leading order picture, both partons and the corresponding jets are to be back-to-back in the center-of-mass frame of the gluon photon system, which corresponds to $\Delta\phi = 180°$. Deviations from the back-to-back topology indicate the presence of NLO effects. In the LO Monte Carlo models NLO effects are implemented by resolved processes in Pythia and the k_t-factorization in Cascade. On the left side of figure 9.5 the case is illustrated where transverse momentum is carried away by an emitted gluon (NLO), whereas in the case depicted on the right side additional transverse momentum is transfered to the $c\bar{c}$ system by the gluon as for instance calculated by the CCFM equations. Both cases lead to a deviation of the back-to-back topology.

A further variable which is investigated in this thesis is the pseudorapidity difference $\Delta\eta$ of the jets, which is defined as:

$$\Delta\eta = \eta_{Jet_{other}} - \eta_{Jet_{D^\star}} \tag{9.7}$$

Considering again the $2 \to 2$ process as given in the LO picture by the BGF process. In this case it is expected, that both jets show a similar η distribution corresponding to $\Delta\eta$ equal to zero. In the case of resolved processes, it may happen that the Jet_{other} is produced by a gluon which would result in different η distribution for the Jet_{other} and a deviation from $\Delta\eta = 0$.

By measurering $\Delta\phi$ and $\Delta\eta$ the angular correlation of the two hardest partons is investigated. Deviations from $\Delta\phi = 180°$ and $\Delta\eta = 0$ indicate the presence of NLO effects or resolved processes.

Momentum fractions $\mathbf{x_\gamma^{obs}}$ and $\mathbf{x_g^{obs}}$

In the leading order picture the kinematic of the partons produced in the hard interaction is defined by the momentum fractions of the photon and gluon entering the hard interaction which are denoted as x_γ^{LO} or x_g^{LO}. These variables are calculated using energy and momentum conservation by the following formulas:

$$x_\gamma^{LO} = \frac{\sum_i (E - p_z)_i}{2E_\gamma} \tag{9.8}$$

$$x_g^{LO} = \frac{\sum_i (E + p_z)_i}{2E_p} \tag{9.9}$$

Here i denotes a parton in the hadronic final state. For low values of Q^2, the photon energy can be expressed by $E_\gamma = yE_e$. In events with two jets it is possible to approximate x_γ and x_g by replacing the partons in the sum, by the particles in the jets. In this case it can be written:

$$x_\gamma^{obs} = \frac{\sum_j (E - p_z)_j + \sum_k (E - p_z)_k}{2yE_e} \tag{9.10}$$

$$x_g^{obs} = \frac{\sum_j (E + p_z)_j + \sum_k (E + p_z)_k}{2E_p} \tag{9.11}$$

Here the sums run over the all particles j and k in the $Jet_{D^\star}$ or Jet_{other}, respectively. Both quantities are restricted by definition to the range $0 < x < 1$. For heavy quark production values for x_g^{obs} of the order $\simeq 10^{-2}$ are usual. The observable x_g^{obs} is sensitive to the gluon density in the proton and can be used to measure the gluon density as performed in [Adl99]. For the BGF process in LO the HFS consists of only two hard jets and the proton remnant, which goes predominantly into the forward direction and has therefore only a small influence on $E - p_z$. In this case x_γ^{obs} is close to one. Deviations from $x_\gamma^{obs} \simeq 1$ are caused by resolved photon processes and NLO effects for instance. In both cases, an additional jet is present in the HFS, given by the photon remnant or produced by intial state radiation. The third jet does not contribute to the numerator of equation 9.11, thus significantly lower values for x_γ^{obs} than one are observed in these cases. Hence x_γ^{obs} is sensitive to resolved photon processes and NLO effects. Resolved photon processes are expected to be enriched in the range $x_\gamma^{obs} < 0.75$ and the pointlike component in the region $x_\gamma^{obs} > 0.75$.

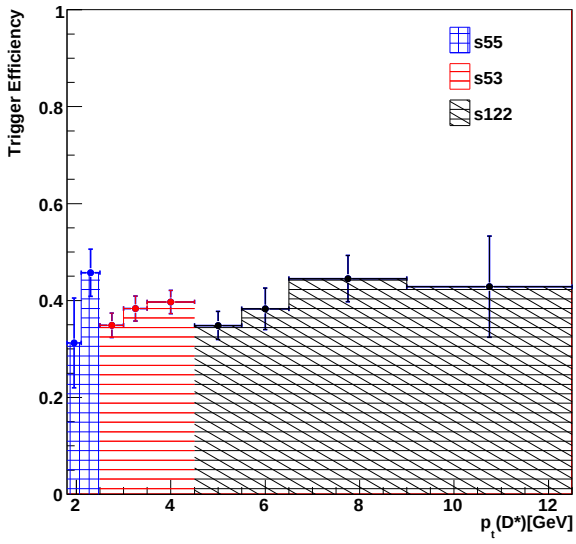

Figure 9.6: *Trigger efficiency as a function of the p_t of all $D^\star$ candidates in the DiJet sample. The phase space covered by the different subtriggers is distinguished by different hatched areas.*

9.5 Data selection strategy in the DiJet sample

In the inclusive sample the trigger efficiency, determined in data, as a function of p_t of the $D^\star$ mesons has been used to simulate the subtriggers in Monte Carlo. For the DiJet sample the same trigger mix, consisting of s55, s53 and s122 and the same combining strategy is applied (see section 5.5). Due to the different event topologies in the DiJet sample compared to the inclusive sample, the trigger efficiency has been redetermined in the DiJet sample. Figure 9.6 shows the trigger efficiency for $D^\star$ mesons as a function of the transverse momentum. In comparison to the trigger efficiency in the inclusive sample (see figure 5.6), the trigger efficiency in the DiJet sample is significantly higher. This is especially true for the low p_t regime, where the efficiency is increased by around 10%. Figure 9.6 shows furthermore, that the relative uncertainty of the triggerefficiency is larger compared to the corresponding uncertainty in the inclusive sample. This can be explained by the additional jet selection which results in a lower statistics in the DiJet sample compared to the inclusive sample.

The ΔM distribution for all events found in the DiJet sample is displayed in figure 9.7. The amount of $D^\star$ mesons is determined to $N(D^\star) = 3243 \pm 104$. Compared to the inclusive sample, the additional jet selection lead to a reduction of the number of $D^\star$ mesons of about 60%.

In order to compare the data with the Monte Carlo simulation the effects of the chosen triggermix have to be transfered to the Monte Carlo beforehand. Therefore the events in the Monte Carlo are weighted according the trigger efficiency (see figure 9.6) determined in the DiJet sample $\epsilon^{DiJet}_{trigger}(p_t)$ and correction factors $L(p_t)$ which take into account the different amount of luminosities in certain p_t ranges seen by the corresponding subtrigger in this range. This procedure is in detail described in section 6.3. The total weight factors $w(p_t)$ applied to the Monte Carlo events are given by $w(p_t) = L(p_t) \cdot \epsilon^{DiJet}_{trigger}(p_t)/\mathcal{L}_{MC}$.

9.6 Control Distributions

Figure 9.8 displays control distributions as a function of the transverse momentum and the pseudorapidity of the $D^\star$ meson. The shape of the distributions are similar to the shapes observed in the inclusive sample (see figure 6.2 and 6.3). The data is compared to the weighted as well to the unweighted prediction given by the Pythia (massless) Monte Carlo simulation. The applied weighting has been determined on the basis of the inclusive

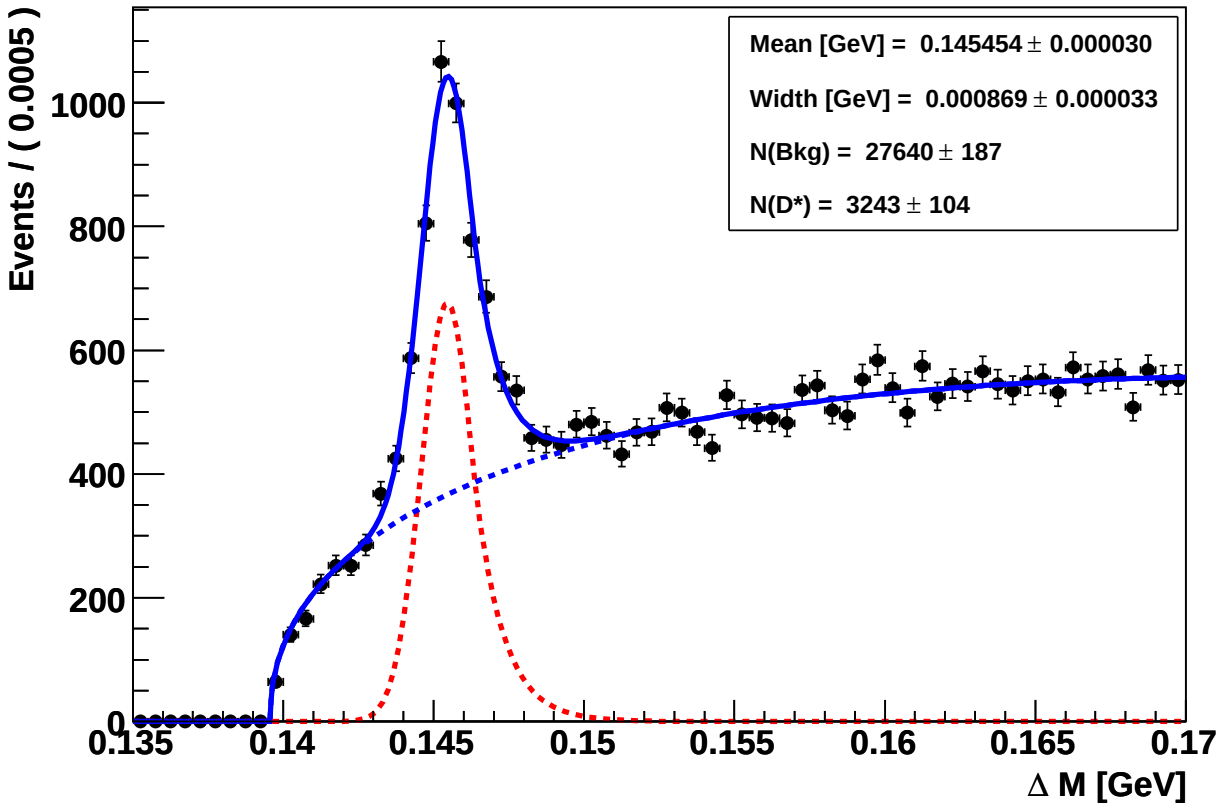

Figure 9.7: ΔM distribution of all selected $D^\star$ meson candidates in the DiJet sample. The number of signal events is extracted by the parameterization described in 4.2.

sample and corresponds to a correction of the $p_t(D^\star)$ and $W_{\gamma p}$ distribution, as described in section 6.3. The kinematic of the $D^\star$ meson is nicely described by the Monte Carlo. The reweighting has as expected an influence on $p_t(D^\star)$. Consistent to the results obtained in the inclusive sample the effect on the $\eta(D^\star)$ distribution is marginal. Figure 9.8 shows that both the unweighted and weighted simulation give a good description of the data within the statistical error.

Figure 9.9 shows the p_t and η control distributions of the $Jet_{D^\star}$ and the Jet_{other}. The shape of the $Jet_{D^\star}$ and Jet_{other} distributions differ significantly. Deviations are in particular observed in the lowest p_t interval, the $p_t(Jet_{D^\star})$ distribution decreases towards low p_t, whereas the $p_t(Jet_{other})$ distributions tends to flatten. The deviation between both distributions is caused by the fact that it is more likely that the $Jet_{D^\star}$ is the leading jet than the Jet_{other}, as displayed in figure 9.2.

The η distribution of the $Jet_{D^\star}$ is as expected to be similar to the η distribution of the $D^\star$ meson. The η distribution of the Jet_{other} shows a completely different behavior and rises towards positive values of η. This indicates that the Jet_{other} receives contributions from NLO effects or resolved processes, otherwise a similar behavior as observed in the $\eta(Jet_{D^\star})$ distribution would be expected.

In order to be consistent with the analysis of the inclusive sample the weighted distribution has been used to unfold the data to the hadron level.

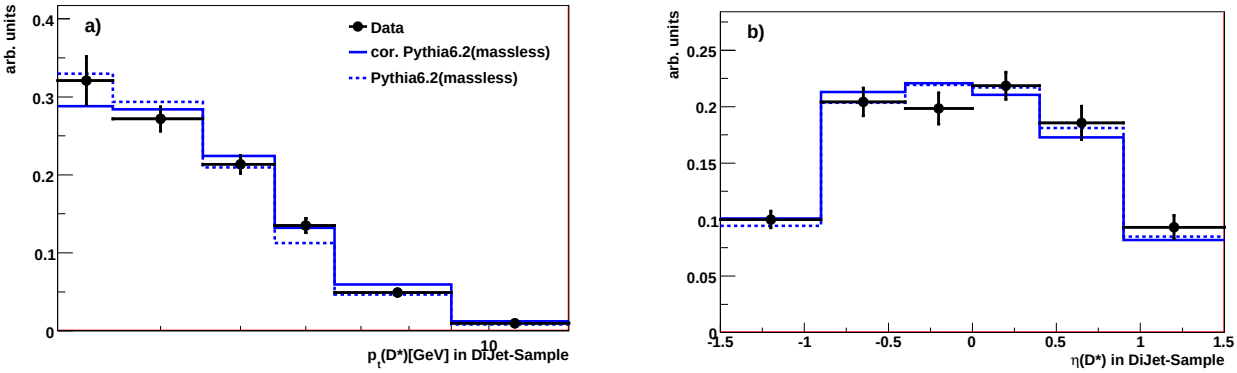

Figure 9.8: Comparison of data and Monte Carlo as a function of the transverse momenta a) and pseudorapidity b) of the $D^{\star}$ meson. The data is represented by the points and the Monte Carlo simulation by the lines. The dotted line corresponds to the uncorrected prediction by the Pythia (massless) prediction and the solid line to the corrected prediction according the reweighting described in section 6.3.

9.7 Systematic Uncertainties in the DiJet Sample

Most of the systematic uncertainty sources discussed in section 7 are also applicable in the DiJet sample. With respect to the additional jet selection criteria, the uncertainties due to trigger efficiency, model dependence and hadronic energy scale have to be redetermined.

Trigger Efficiency

The uncertainty due to trigger efficiency as a function of the measured variables is displayed in figure 9.10. In general an uncertainty twice as large as in the inclusive sample is found (see figure 7.2). This is caused by the lower statistics in the DiJet sample compared to the inclusive sample. The uncertainty rises towards large $p_t(Jet)$ and reaches $\simeq$ 13% in the highest $p_t(Jet_{D^{\star}})$ and $p_t(Jet_{other})$ interval. The uncertainty as function of the other jet quantities is almost flat and amounts on average to $\simeq$ 8.1% in the DiJet.

Jet Energy Scale

The uncertainty due to the hadronic energy scale is determined as described in chapter 7 by a variation of the energy of the HFS particles by $\pm$4%. This includes a variation of the jet energy. The uncertainties as function of the measured jet quantities are displayed in figure 9.11. A clear increase of the uncertainty towards large $p_t(Jet_{D^{\star}})$ is observed. In the highest $p_t(Jet_{D^{\star}})$ bin the uncertainty amounts to 15%. The $p_t(Jet_{other})$ distribution differs clearly from the $p_t(Jet_{D^{\star}})$, which can be explained by the different p_t spectra of the jets (see figure 9.9). Further large uncertainties are found in the highest x_g^{obs} and lowest $\Delta\phi$ bin. On average the uncertainty due to the hadronic energy scale in the DiJet sample amounts to 6.3%, which corresponds to an increase by more than a factor three compared to the inclusive sample.

Model Dependence

The uncertainty due to model dependence is shown in 9.12. It is defined in the same way as discussed in 7 by the total deviation between the acceptance corrections determined with

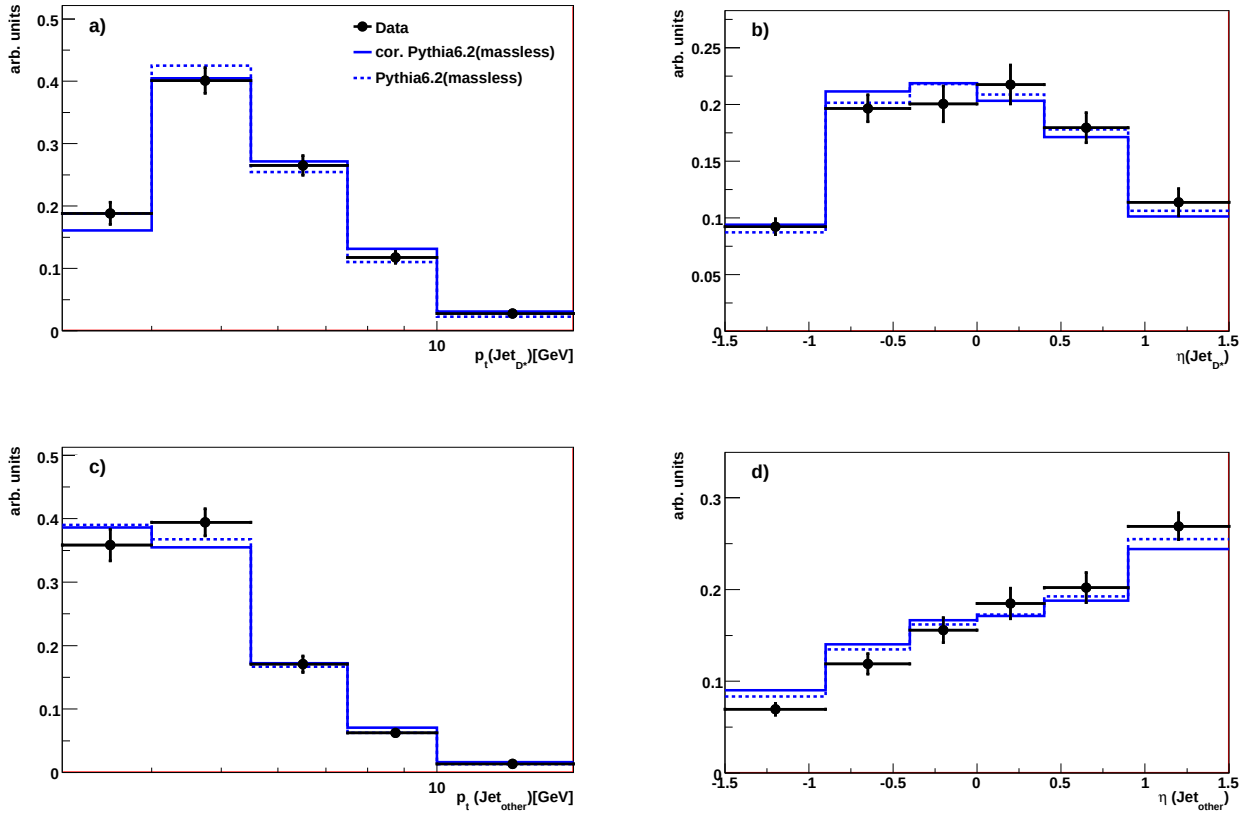

Figure 9.9: Comparison of data and Monte Carlo as a function of the transverse momenta and pseudorapidity of the jets. Figure a) and b) $Jet_{D^\star}$. Figure c) and d) Jet_{other}. The data is represented by the points and the Monte Carlo simulation by the lines. The dotted line corresponds to the uncorrected prediction by the Pythia (massless) prediction and the solid line to the corrected prediction according the reweighting described in section 6.3.

Cascade and Pythia (massless). As in the inclusive sample the uncertainty amounts to ±1% in the DiJet sample.

Summary DiJet Uncertainties

In table 9.2 the total values due to the discussed uncertainty sources are summarized. The uncertainty sources listed in the upper part correspond to global uncertainties, which are applied to each event selected event in the DiJet sample. The uncertainties listed in the lower part are calculated for each interval of the investigated variables, the values correspond to the average uncertainty in the DiJet sample. Four dominant uncertainty sources have been identified, these are the luminosity measurement, trigger efficiency, the jet energy scale and the track finding efficiency. The total uncertainty in the DiJet sample amounts to 13.5%.

9.8 Correction from Parton to Hadron Level

The transverse momentum of the jets on the hadron level is in general lower than the transverse momentum of the corresponding jets on parton level, since it is likely that not all hadrons of a corresponding parton are collected in the jet on the hadron level. That means

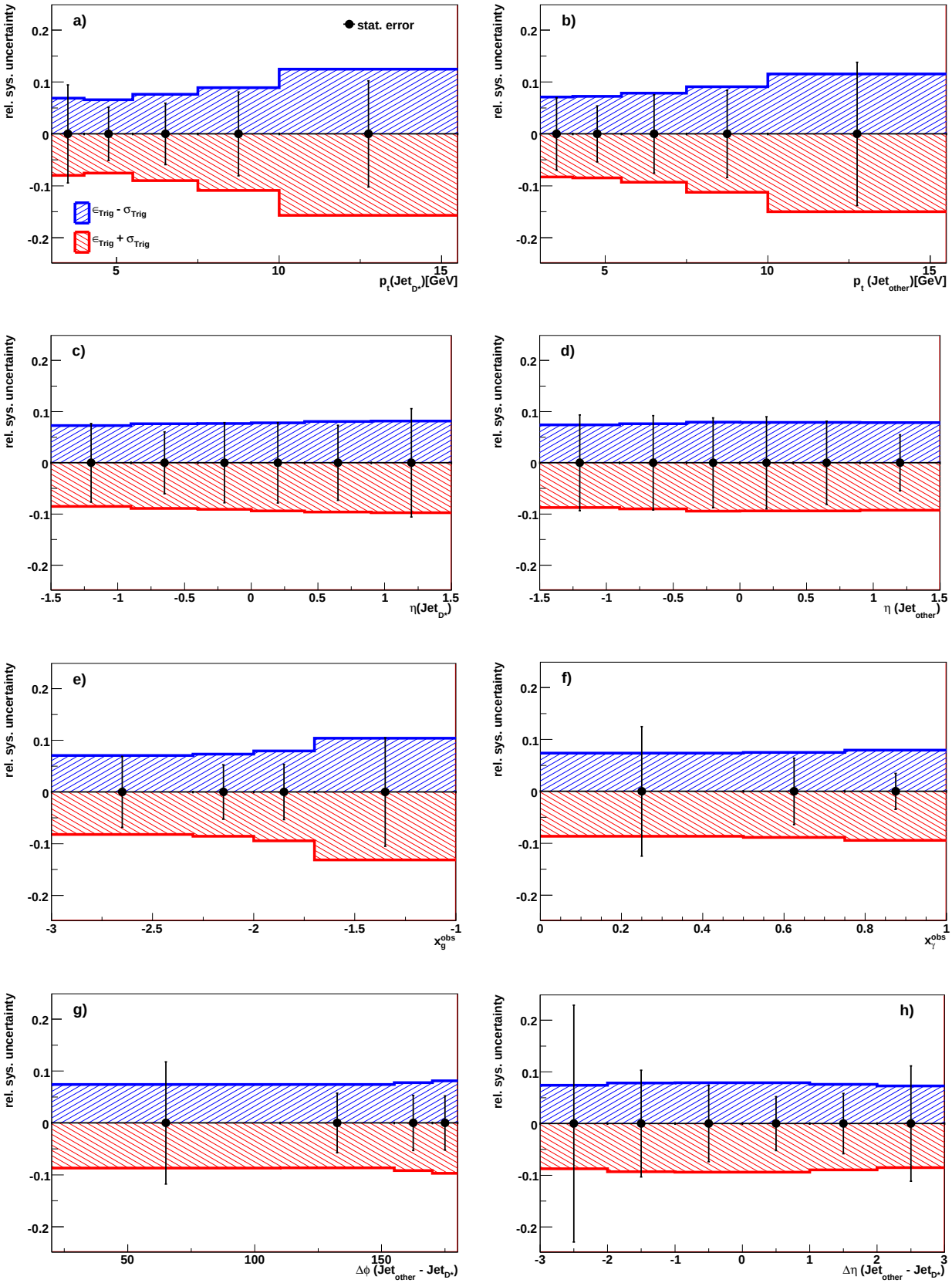

Figure 9.10: *Bin by bin uncertainties due to trigger efficiency as a function of the quantities measured in the DiJet sample. The uncertainties have been estimated on the basis of the Pythia (massless) simulation. For details see section 7.*

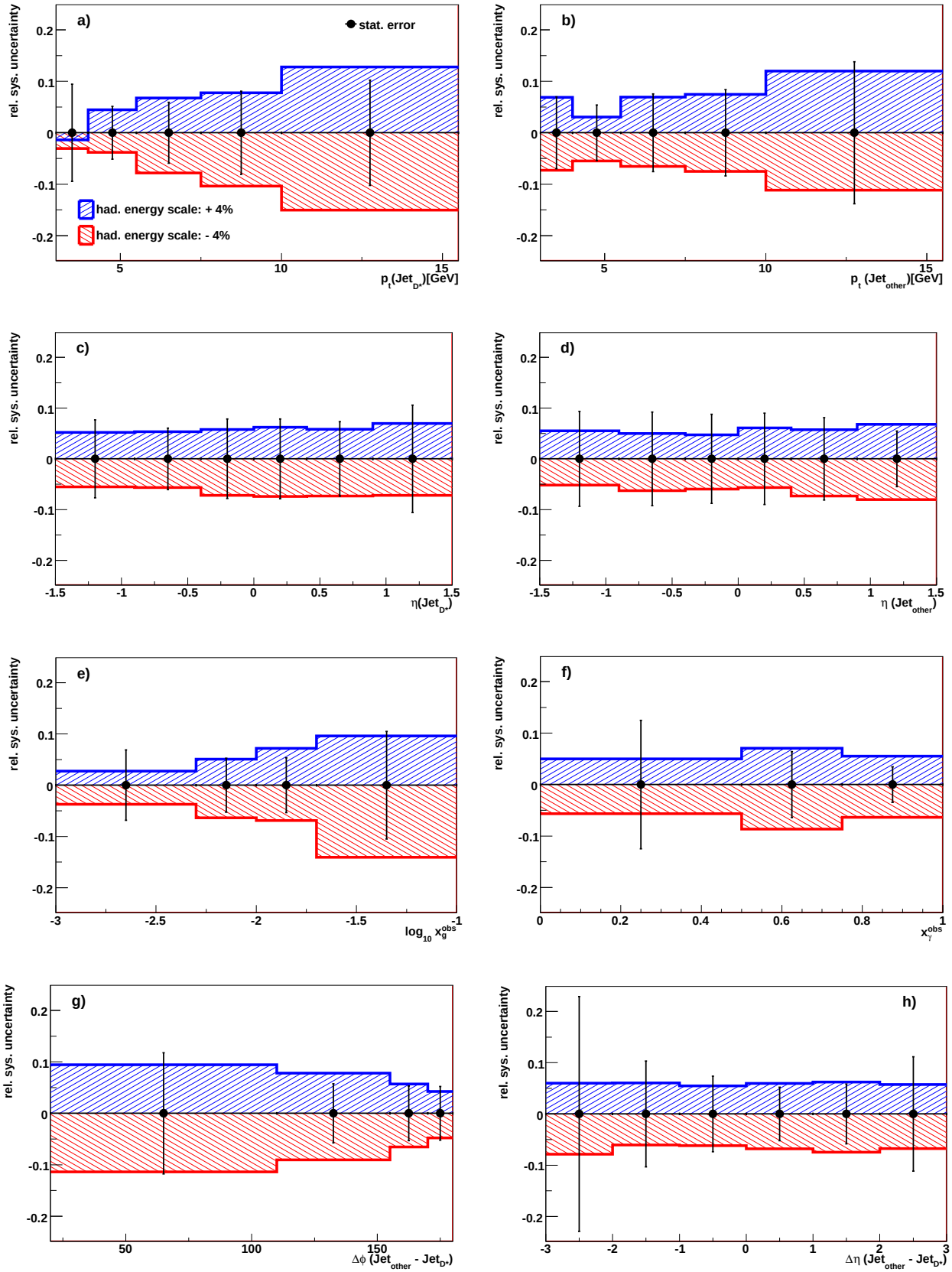

Figure 9.11: *Bin by bin uncertainties due to the hadronic energy scale as a function of the quantities measured in the DiJet sample. The uncertainties have been estimated on the basis of the Pythia (massless) simulation. For details see section 7.*

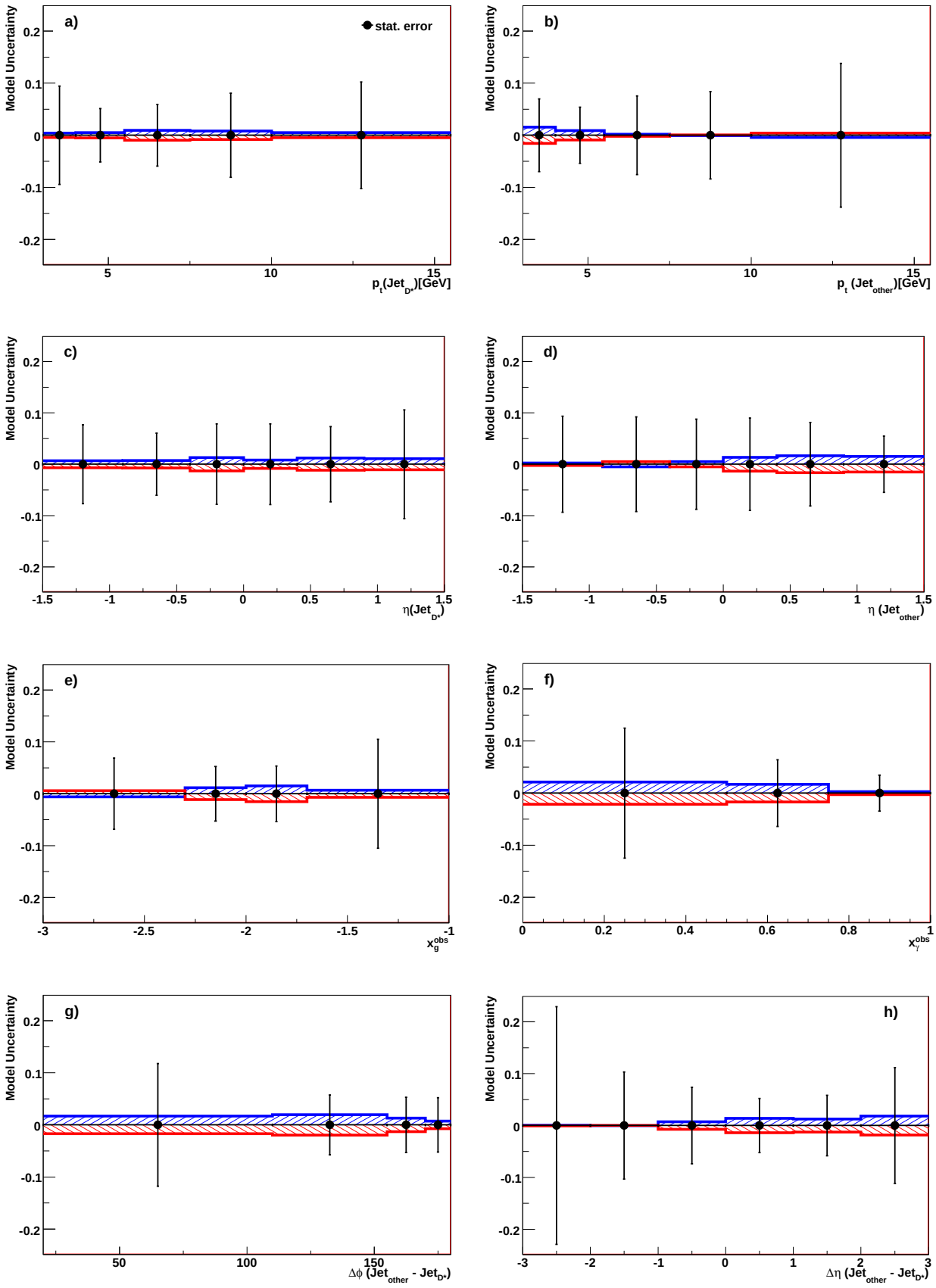

Figure 9.12: *Bin by bin uncertainties due to model uncertainty scale as a function of the quantities measured in the DiJet sample. The uncertainties have been estimated on the basis of the Pythia (massless) simulation. For details see section 7.*

Source	*Uncertainty*
Luminosity	5.0%
Signal Extraction	1.2%
D^0-meson mass cut	1.0%
DIS Background	1.0%
Branching ratio	2.3%
Reflections	1.0%
Primary vertex fit efficiency	2.5%
Track finding efficiency	6.0%
Trigger Efficiency	8.1%
Hadronic energy scale	6.3%
Model Dependence	1.0%
Sum	13.5%

Table 9.2: *Summary of all identified systematic uncertainty sources. The latter three uncertainties correspond to bin by bin uncertainties.*

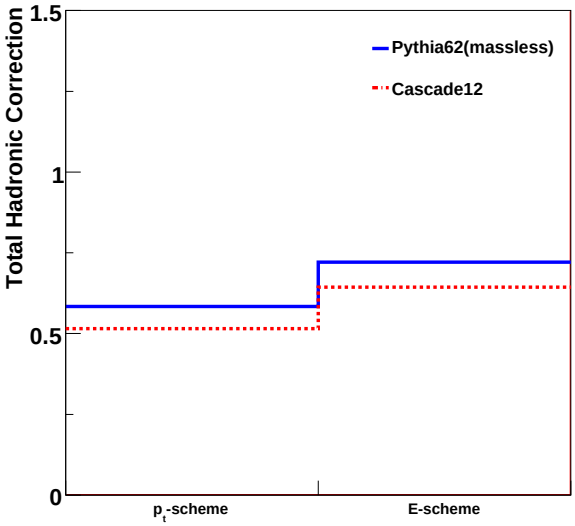

Figure 9.13: *Total hadronic correction factors estimated on the basis of Pythia(massless) and the Cascade Monte Carlo. On the left the correction is estimated in the E - recombination scheme and on the right in the p_t- recombination scheme.*

in particular, that due to the steeply falling p_t distribution the jet cross sections calculated on parton level are in general larger than on the hadron level. Since the cross sections presented in this thesis are corrected to the hadron level, and the NLO prediction provided by the program FMNR corresponds to the parton level, it is necessary to correct the FMNR cross sections to the hadron level.

The hadronic correction factors have been determined on the basis of LO Monte Carlo plus parton shower simulations. Therefore the jet algorithm has been run once on the parton and once on the hadron level. The relative deviation between the jets found on the hadron level to the jets found on the parton level are taken as hadronic correction factor C_h. The hadronic corrections C_h are determined for each measured bin i

$$C_h^i = \left. \frac{N_{PS\oplus had.}}{N_{PS}} \right|_i \tag{9.12}$$

Here $N_{PS\oplus had.}$ represents the amount of particles found in bin i on the hadron level and N_{PS} corresponds to the amount of particles found on the parton level after parton showers but

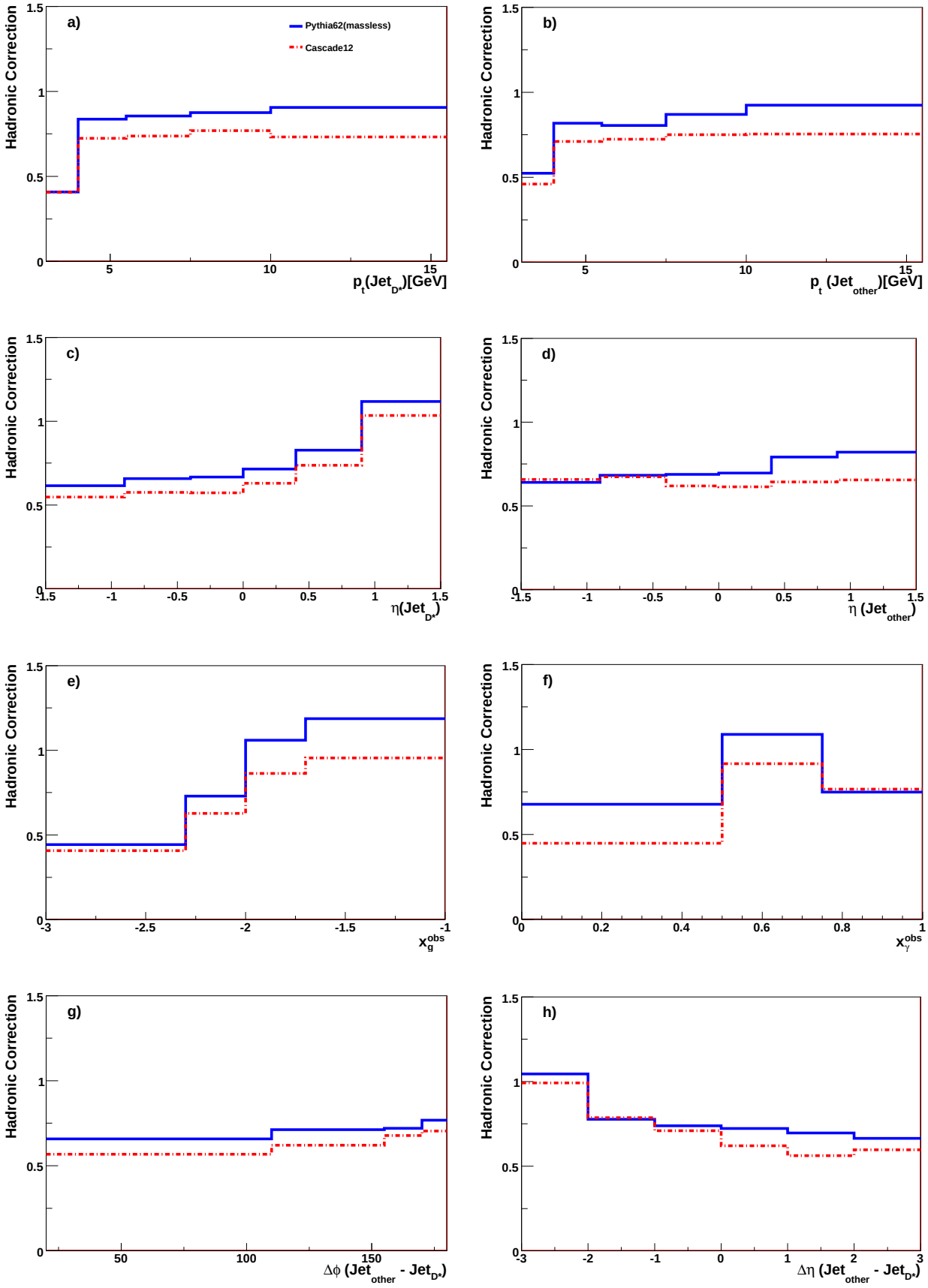

Figure 9.14: *Correction factors due to hadronisation for each bin of the measured quantities. The solid line represents the correction factors estimated by the Pythia(massless) Monte Carlo and the dashed lines represent Cascade.*

before the hadronisation.

The corrections are calculated on the basis of the Monte Carlo generator Cascade and Pythia(massless). The jet algorithm has been run first on the hadron and afterwards on the parton level. The jet selection and the identification of the $Jet_{D^\star}$ and Jet_{other} on the hadron level are the same as described in section 9.2. On the parton level the jet algorithm is applied to the partons after PS and before the hadronisation.

The $Jet_{D^\star}$ and Jet_{other} found on the hadron level have to be matched to the jets found on the parton level. The $Jet_{D^\star}$ is identified by comparing the charge of the of the $D^\star$ in the hadron jets and the charge of the charm quarks in the parton jets. The Jet_{other} identification on the parton level is performed in the same way as on the hadron level, by by assigning the leading jet to the Jet_{other} which has not already identified as $Jet_{D^\star}$.

After the identification of the jets, the selections, described in section 9.2 and summarized in table 9.1, are applied.

Figure 9.13 shows the average hadronisation corrections determined in the DiJet sample. The correction factors are calculated on the basis of the LO Monte Carlo models Pythia (massless) and Cascade with the two different recombination schemes which have been introduced in section 9.1. Significant differences between the average correction factor determined on the basis of the different recombination schemes and Monte Carlos are found. The correction factor closer to one is found with the E-scheme, $\sim 72\%$ for Pythia (massless) and $\sim 64\%$ for Cascade. Thus, this scheme has been used to determine the hadronic correction factors within this analysis. A priori there is no explicit rule whether to use the Cascade or the Pythia (massless) Monte Carlo to correct for hadronisation. The Pythia (massless) simulation has been chosen, since it provides the smallest correction factors. The absolute deviations of the hadronisation correction factors obtained with Pythia (massless) and Cascade simulations, both calculated in the E-scheme, is applied as systematic uncertainty on the prediction given by FMNR. The average uncertainty amounts to $\sim 12\%$.

Figure 9.14 shows the hadronisation corrections determined with Pythia (massless) and Cascade as function of the jet variables studied in this analysis. The hadronisation correction are smallest at high transverse momentum for both the $Jet_{D^\star}$ and the Jet_{other} and largest in the first bin of the $p_t(Jet_{D^\star})$ and the x_g^{obs} distribution.

9.9 Resolution and Purity of Jet Quantities

The measurement of the jets depends on the energy measurement of the HFS particles in the calorimeters, hence it is expected that the resolution of the transverse momentum of the $Jet_{D^\star}$ is worse than the resolution of the transverse momentum of the $D^\star$ mesons in the inclusive sample.

The reconstructed $Jet_{D^\star}$ is matched to the corresponding jet on the hadron level by charge comparison of the charm quark and the $D^\star$ meson. Figure 9.15 a) and 9.15 b) show the relative resolution, defined as $p_t(Jet)^{rec} - p_t(Jet)^{gen}/p_t(Jet)^{gen}$, for $p_t(Jet_{D^\star})$ and $p_t(Jet_{other})$, determined on the basis of the Pythia (massless) Monte Carlo simulation. In order to avoid a bias towards low p_t the p_t cuts on the reconstructed jets are lowered by 0.5 GeV. Both distributions show on average a mean slightly below zero, which is more prominent for the $p_t(Jet_{other})$. The relative resolution decreases slightly towards large transverse momenta. The resolution of the Jet_{other} is worse compared to the resolution of the $Jet_{D^\star}$. The corresponding purities are displayed in figure 9.15 e) and f). The interval sizes for $p_t(Jet_{D^\star})$ have been adjusted such that a constant purity of about 70% is found. In order to allow a good comparison of the final cross sections of both distributions, the same interval sizes

have been chosen for the $p_t(Jet_{other})$ distribution, which leads to a lower purity, due to the lower resolution.

The absolute resolution of the $\eta(Jet_{D^\star})$ and $\eta(Jet_{other})$ is displayed in 9.15 c) and d). The resolution for both quantities is decreasing towards the forward direction. A better resolution is found for the $\eta(Jet_{D^\star})$ than for $\eta(Jet_{other})$. The interval sizes have been adjusted such that a constant purity of about 80% is found as a function of $\eta(Jet_{D^\star})$. For better comparison, the same interval sizes have been chosen for the $\eta(Jet_{other})$ distribution. This leads to a decreasing purity for $\eta(Jet_{other})$ towards the forward direction.

In comparison to the purities determined in section 6.2 for the $D^\star$ meson as function of p_t, a similar purity for $p_t(Jet_{D^\star})$ is only achieved by choosing much larger bin sizes. For the $\eta(Jet_{D^\star})$ the same intervals are applied as for $\eta(D^\star)$. This results on average in a 10% lower purity for the $\eta(Jet_{D^\star})$ than for the $\eta(D^\star)$ distribution due to the lower resolution of the jet quantity.

The resolutions and purities for the other studied jet quantities are displayed in figure 9.16. The lowest purity is found in the lowest bin of the $\Delta\phi$ distribution, where the purity amounts to $\sim$ 40% for the Pythia predictions. For this bin Cascade predicts a purity of $\sim$ 50%. Low purities are also found for low x_γ^{obs} values, where the purity amounts to $\sim$ 50%.

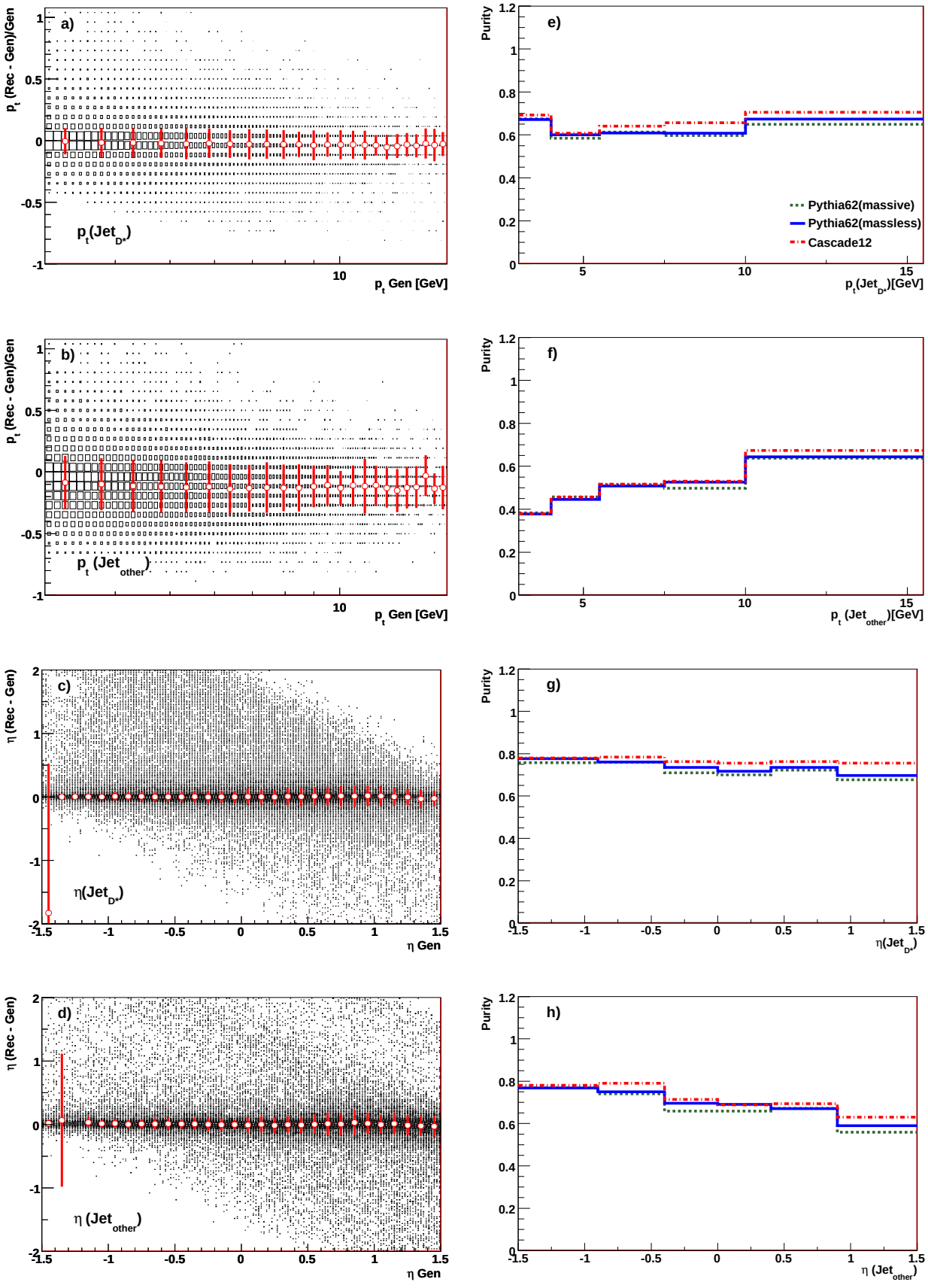

Figure 9.15: *Resolution as a function of the transverse momentum and the pseudorapidity of the jets. The resolution had been estimated on the basis of the Pythia (massless), Pythia (massive) and the Cascade Monte Carlo simulation. The correlations have been divided into slices and each slice fitted by a Gaussian distribution. The points denote the mean of the gauss and the error bars width for each slice.*

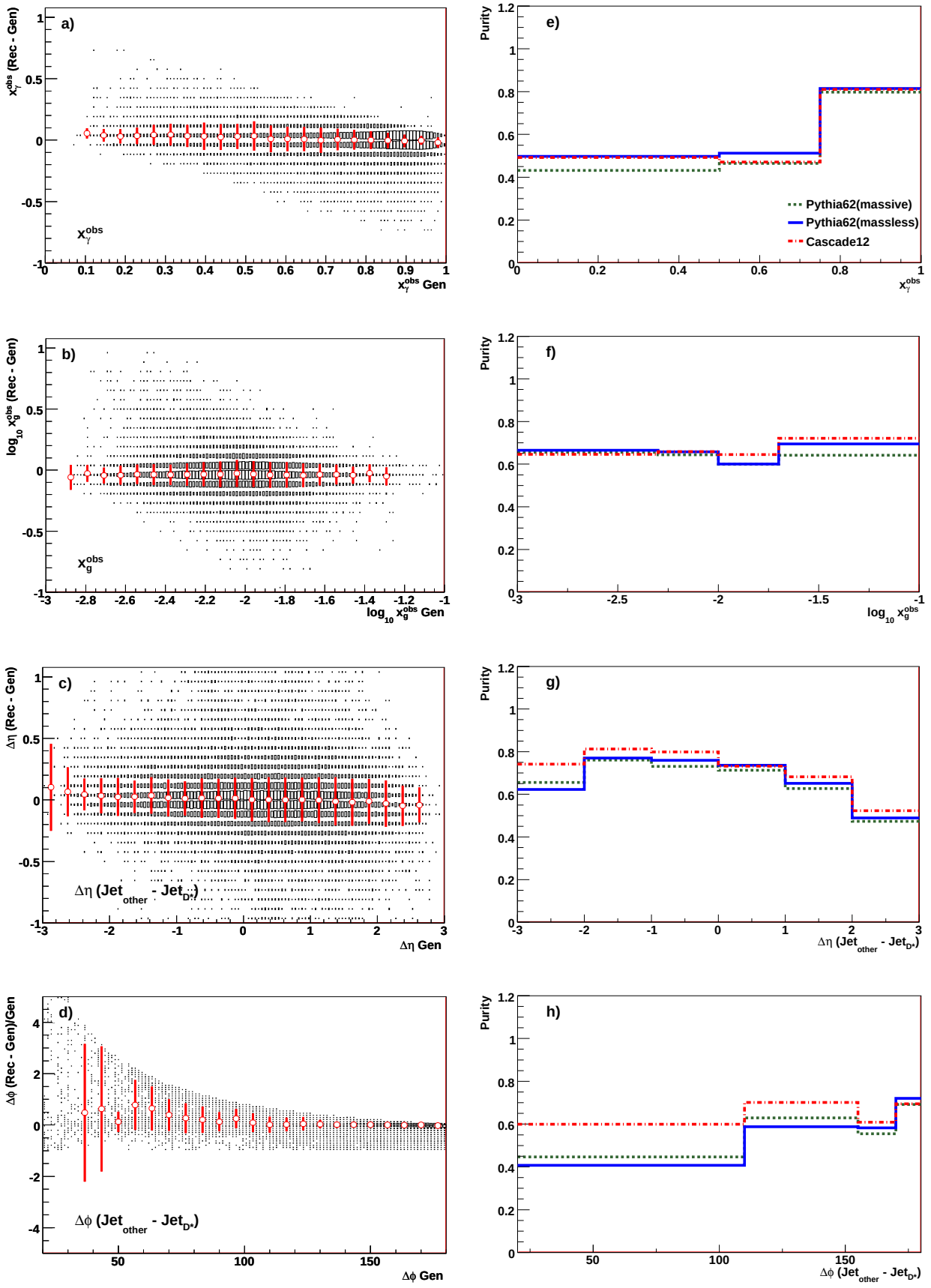

Figure 9.16: *Resolution as a function of the observables x_g^{obs} and x_γ^{obs} of the jets a)-b). The resolution had been determined on the basis of the Pythia (massless) Monte Carlo simulation. The correlations have been divided into slices and each slice fitted by a Gaussian distribution. The points denote the mean of the gauss and the error bars width for each slice.*

Chapter 10

Results: DiJet Sample

In this chapter the results of the $D^\star$ meson tagged DiJet cross section measurement are presented. The measurement is compared to leading order Monte Carlo predictions given by the Pythia (massive), the Pythia (massless) and the Cascade prediction and further to a next-to-leading order predictions based on a FFNS calculation. A GMVFNS calculation is presently not available for two partons in the final state.

10.1 Total DiJet Cross Section

With the total number of reconstructed $D^\star$ mesons of the DiJet sample together with the corrected luminosity of 30.68 pb^{-1}, 68.23 pb^{-1} and 93.39 pb^{-1} and the detector and acceptance correction determined in the previous chapter, the total DiJet cross section in the visible range (see table 10.1) yields:

$$\sigma^{tot}_{vis}(e^{\pm}p \rightarrow e^{\pm}D^{\star\pm}\,Jet\,Jet\,X) = (8.70 \pm 0.29 \pm 1.13)\ \text{nb}^{-1} \tag{10.1}$$

Here the first error denotes the statistical error and the second the systematic uncertainty. Due to the more strongly restricted phase space of the DiJet sample compared to the inclusive sample the total cross section is significantly lower. Table 10.2 gives a summary of the total cross section obtained by the LO Pythia (massive), Pythia (massless) and Cascade predictions as well as for the massive NLO FFNS prediction calculated with the program FMNR. The measurement is compatible within the uncertainties with both Pythia predictions and within the uncertainty of the FFNS calculation. The result of FFNS calculation is denoted before and after applying the hadronisation corrections. The hadronisation correction factor determined with the Pythia (massless) simulation amounts to 0.74 and the uncertainty given by the total deviation between the correction calculated with Pythia (massless) and Cascade amounts to 11.6%. The theoretical uncertainties are estimated by a variation of the charm mass by ± 0.2 GeV and the renormalization and factorization scales by $1/2\mu_0 < \mu_{r,f} < 2\mu_0$ as discussed in chapter 2. The uncertainty into the upward direction is significantly higher than the uncertainty downwards. The positive deviation is primarily caused by the downward variation of the renormalization scale. In comparison to the result obtained for the inclusive cross section (see table 8.1) the uncertainties are significantly lower. However, in contrast to the inclusive sample the measurement is only in agreement with uncertainty. As already observed in the inclusive sample the Cascade prediction is below the data. However, compared to the inclusive sample a better agreement in normalization in the DiJet sample is found. The ratio $\sigma^{data}_{tot}/\sigma^{Cascade}_{tot}$ amounts to 1.5 in the inclusive sample and to 1.3 in the DiJet sample.

visible range	
Q^2	< 2 GeV
$W_{\gamma p}$	$100 - 285$ GeV
$\lvert\eta(D^\star)\rvert$	< 1.5
$p_t(D^\star)$	> 1.8 GeV
$p_t(Jet_1)$	> 4.0 GeV
$p_t(Jet_2)$	> 3.0 GeV
$\lvert\eta(Jet_{1,2})\rvert$	< 1.5
Number of jets	≥ 2

Table 10.1: *Definition of the visible range in the DiJet sample. The Jet_1 denotes the leading and Jet_2 the next leading jet. One of these jets has to be associated to the $D^\star$ meson.*

	σ_{vis}^{tot} [nb]
Data	$8.70 \pm 0.29\,(stat.) \pm 0.83\,(sys.)$
$Pythia62(massive)$	8.54
$Pythia62(massless)$	8.06
$Cascade12$	6.66
$FMNR$	$9.34^{+1.77}_{-0.31}$
$FMNR \otimes had.$	$6.90 \pm 0.43\,(had.unc.)^{+1.77}_{-0.31}\,(theo.unc.)$

Table 10.2: *Total visible cross sections in the DiJet sample and its uncertainties compared with theoretical predictions. The statistical error is determined as described in 4.2. The systematic uncertainty corresponds to the uncertainty sources discussed in chapter 7 and section 9.7. For the FMNR prediction the uncertainty due to scale and mass variation and the uncertainty due to the hadronisation correction are listed separately. The FMNR prediction before applying the hadronisation corrections is given for reference only.*

10.2 Differential DiJet Cross Section

Transverse momenta of the Jets

The differential cross sections as a function of the transverse momentum of the jet associated to the $D^\star$ meson $p_t(Jet_{D^\star})$ and the other leading jet $p_t(Jet_{other})$ are depicted in figure 10.1 a)-d). In figure a) and c) the measurement is compared to LO predictions and in b) and d) to the prediction provided by the FFNS calculation. Both distributions show a similar behavior in shape and are steeply falling towards higher p_t. Differences in shape are observed at low transverse momenta. The measurement as function of the $p_t(Jet_{D^\star})$ decreases below 4 GeV, whereas the measurement as a function of the $p_t(Jet_{other})$ decreases less strongly towards lower transverse momenta. This deviation in shape between both distributions is caused by the fact that it is more likely that the $Jet_{D^\star}$ corresponds to leading jet than the Jet_{other} as displayed in figure 9.2.

A good agreement is found for both jet distributions in the regime of low transverse mo-

menta with the Pythia (massless) and Pythia (massive) prediction. The Cascade prediction tends to be too low in this regime. In the high p_t regime the measurement is slightly underestimated by all QCD models. The measurement is in general compatible with the upper uncertainty band of the NLO calculation. Large influences of the hadronisation corrections are found at low p_t.

Pseudorapidity of the Jets

The differential cross sections as a function of the pseudorapidity for the $Jet_{D^\star}$ and the Jet_{other} as well as the difference between both variables is depicted in figure 10.2 a)-f). By comparing the $\eta(Jet_{D^\star})$ and $\eta(Jet_{other})$ distributions a significant difference in shape is observed. The $\eta(Jet_{D^\star})$ distribution is symmetric and nearly flat, whereas the $\eta(Jet_{other})$ distribution is clearly rising towards positive η values. Considering the boson-gluon-fusion process in the leading order picture with two outgoing charm quarks, both distributions are expected to be similar in shape. The different shape of the $\eta(Jet_{other})$ distribution indicates, that the Jet_{other} is highly influenced by non-charm contributions, for instance from resolved components or NLO effects. The shape of both distributions is well described by all predictions. The normalization is underestimated by Cascade. The measurement is as well compatible with uncertainty band of the NLO prediction. Very small theoretical and hadronisation uncertainties are found at negative $\eta(Jet_{other})$, whereas the uncertainties are large for positive values of $\eta(Jet_{other})$. A small excess in the forward region is observed for the $\eta(Jet_{other})$ distribution.

In order to make the difference of the two jets better visible the difference of the pseudorapidities is shown in figure 10.2 c) and f). This distribution shows that the Jet_{other} usually has a larger η than the $Jet_{D^\star}$, meaning that it is between the $Jet_{D^\star}$ and the proton remnant. This indicates furthermore that resolved or NLO effects are needed to describe the production of charm. The measurement is in good agreement with the Pythia (massless) and Pythia (massive) and the uncertainty of the NLO calculation. Cascade has a different shape and underestimates the measurement.

Combined Jet Observables

The differential cross section as a function of the combined jet observables (see section 9.4) are depicted in the figures 10.3 a)-f). The x_g^{obs} distribution shows a maximum at 10^{-2}. The shape is described by all models. However, the shape is best described by the Pythia (massless) and (massive). Cascade underestimates the peak by a factor 1.3. The measurement is compatible with the upward uncertainty of the FFNS calculation in the last three bins. Large hadronisation corrections are found in the first bin.

The cross section as a function of x_γ^{obs} rises towards its maximum above $x_\gamma^{obs} > 0.75$. The variable x_γ^{obs} can be used to separate the resolved and direct processes. The direct component is expected to be located at $x_\gamma^{obs} > 0.75$ and the resolved at $x_\gamma^{obs} < 0.75$. The shape of the distribution is reasonably well described by all predictions. The best agreement is found with the Pythia (massless) and Pythia (massive) simulation. Roughly 50% of the data are observed at $x_\gamma^{obs} < 0.75$, this indicates large contributions from resolved processes. The measurement is likewise compatible with the uncertainty band of the NLO prediction in the first two bins. The maximum is in agreement with the central value of the prediction. This indicates that the resolved contribution is underestimated in the NLO calculation.

With the presence of two outgoing partons as for instance predicted by the BGF process

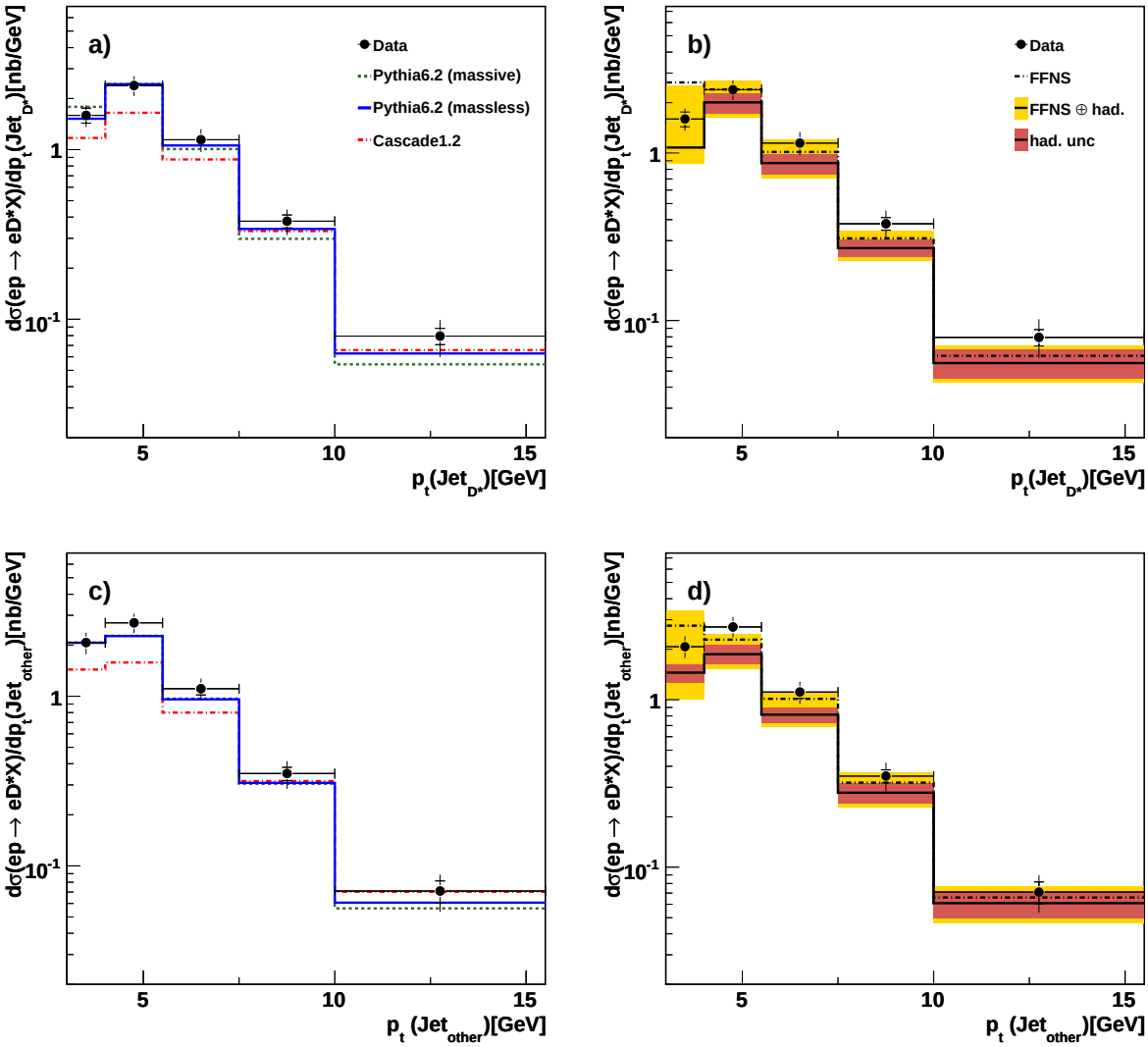

Figure 10.1: *Differential cross sections as a function of p_t of the jets. On the left the data is compared to leading order Monte Carlo predictions and on the right with the NLO prediction given by FMNR. The dark colored error band represents the uncertainty due to hadronisation and the light colored the uncertainty due to charm mass, factorization and renormalization scale.*

in the leading order picture the two partons are expected to be back-to-back, corresponding to $\Delta\phi = 180°$. Deviations from the back-to-back topology indicate NLO effects as described in section 9.4. The $\Delta\phi$ distribution is displayed in figure 10.3 e)-f). The distribution reaches a maximum at 180° and is steeply falling towards lower values. The shape is reasonable well described by the Pythia (massive) prediction decreasing only slightly more to small values of $\Delta\phi$ than the data. The Pythia (massless) is slightly too steep, while the prediction provided by Cascade is too flat. The deviation from the back-to-back topology are caused by the intrinsic transverse momentum of the gluon in Cascade and by parton showers in Pythia, which have been tuned to describe NLO effects. The FFNS calculation does not predict any activity below 110°, which can be explained by the fact that it is not possible to find a configuration with three partons where the angular difference of the two hardest partons is below 120°. NNLO corrections are needed to describ the low $\Delta\phi$ region. The range from $155° - 180°$ is compatible with the measurement.

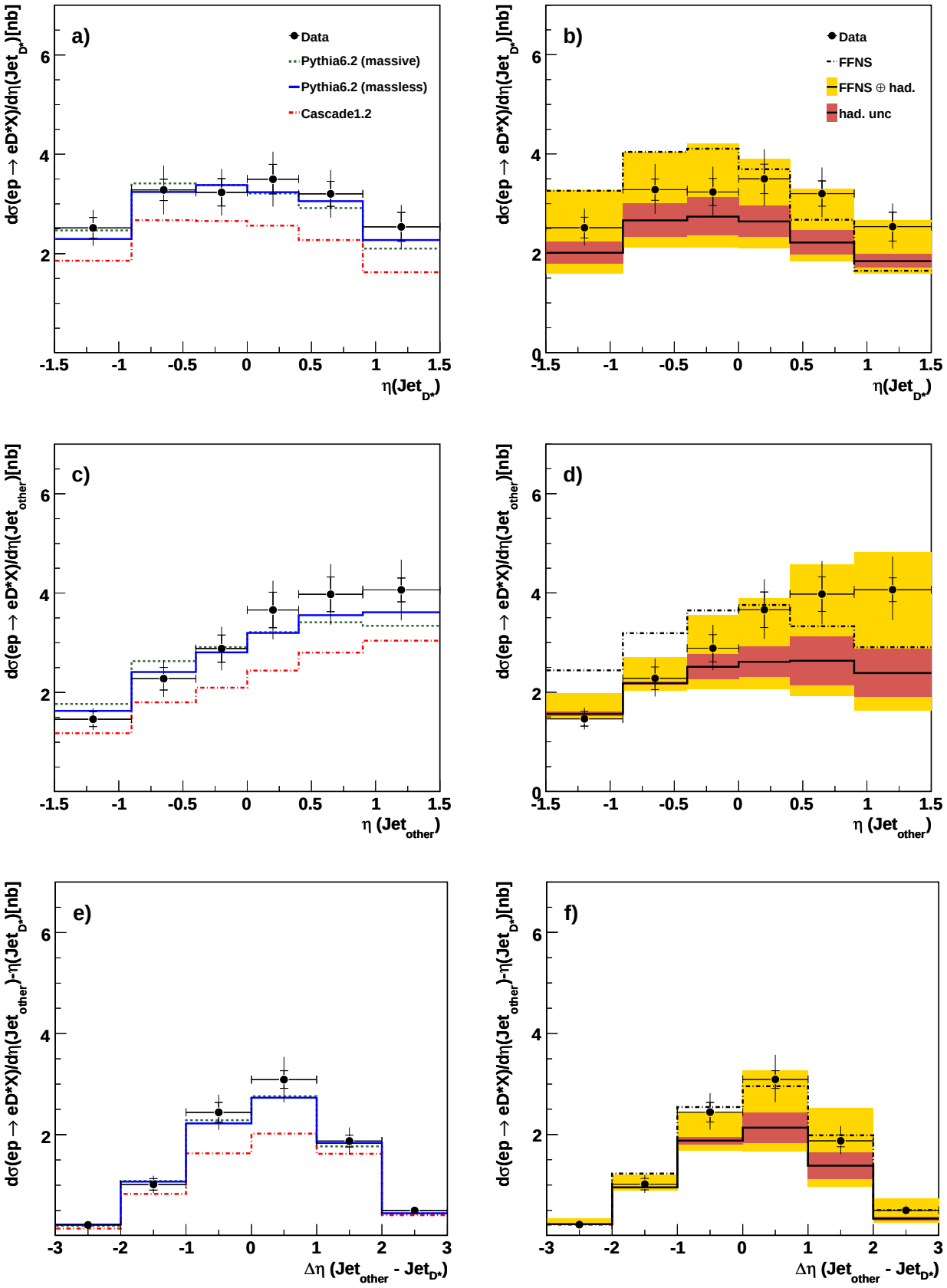

Figure 10.2: *Differential cross sections as a function of η of the jet associated with a $D^\star$ meson and the other jet which is not associated with a $D^\star$meson. On the left the data is compared to leading order Monte Carlo predictions and on the right with the NLO prediction given by FMNR. The dark colored error band represents the uncertainty due to hadronisation and the light colored the uncertainty due to charm mass, factorization and renormalization scale.*

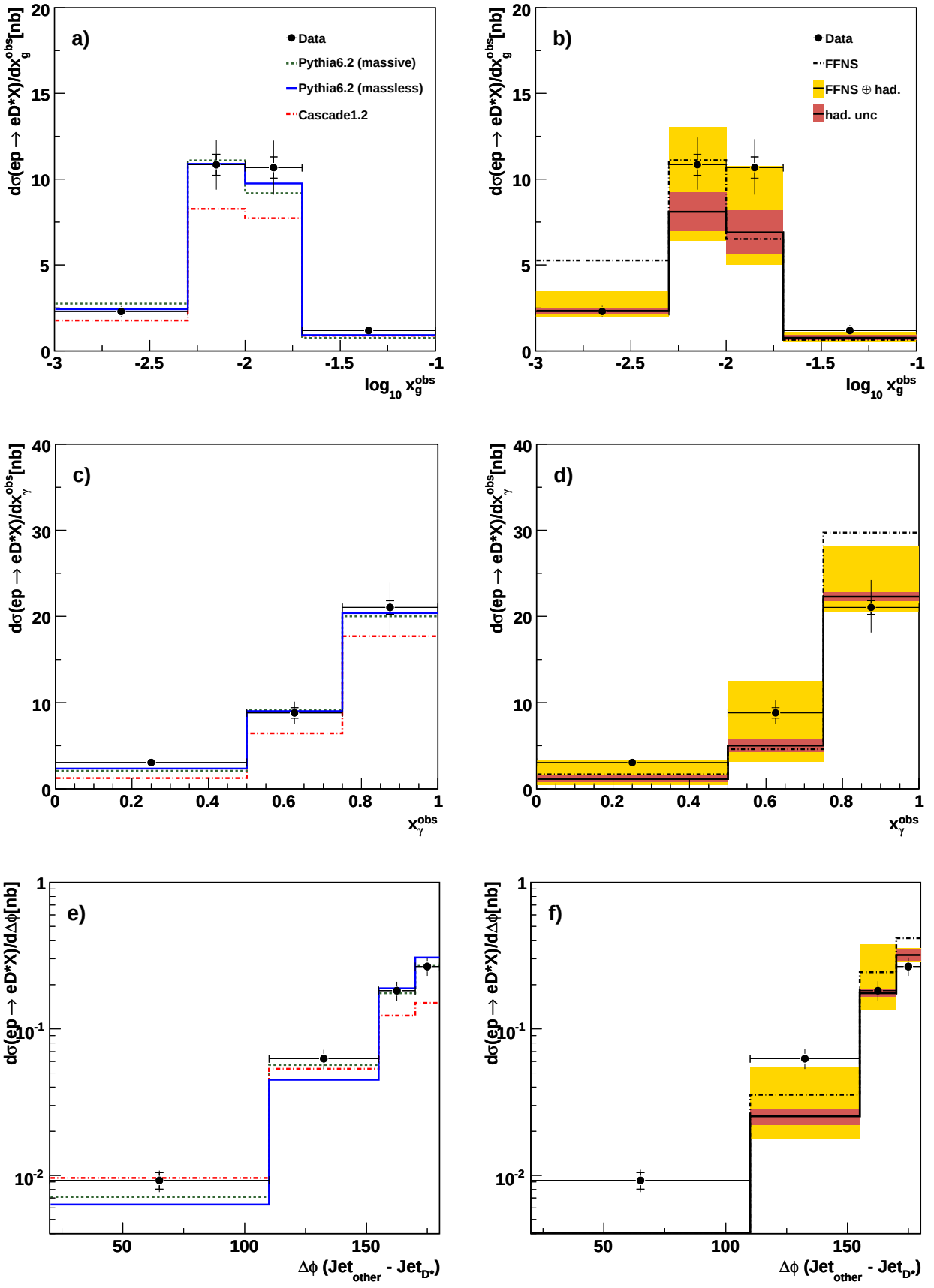

Figure 10.3: *Differential cross sections as a function of x_g^{obs}, x_γ^{obs} and $\Delta\phi$. On the left the data is compared to leading order Monte Carlo predictions and on the right with the NLO prediction given by FMNR. The dark colored error band represents the uncertainty due to hadronisation and the light colored the uncertainty due to charm mass, factorization and renormalization scale.*

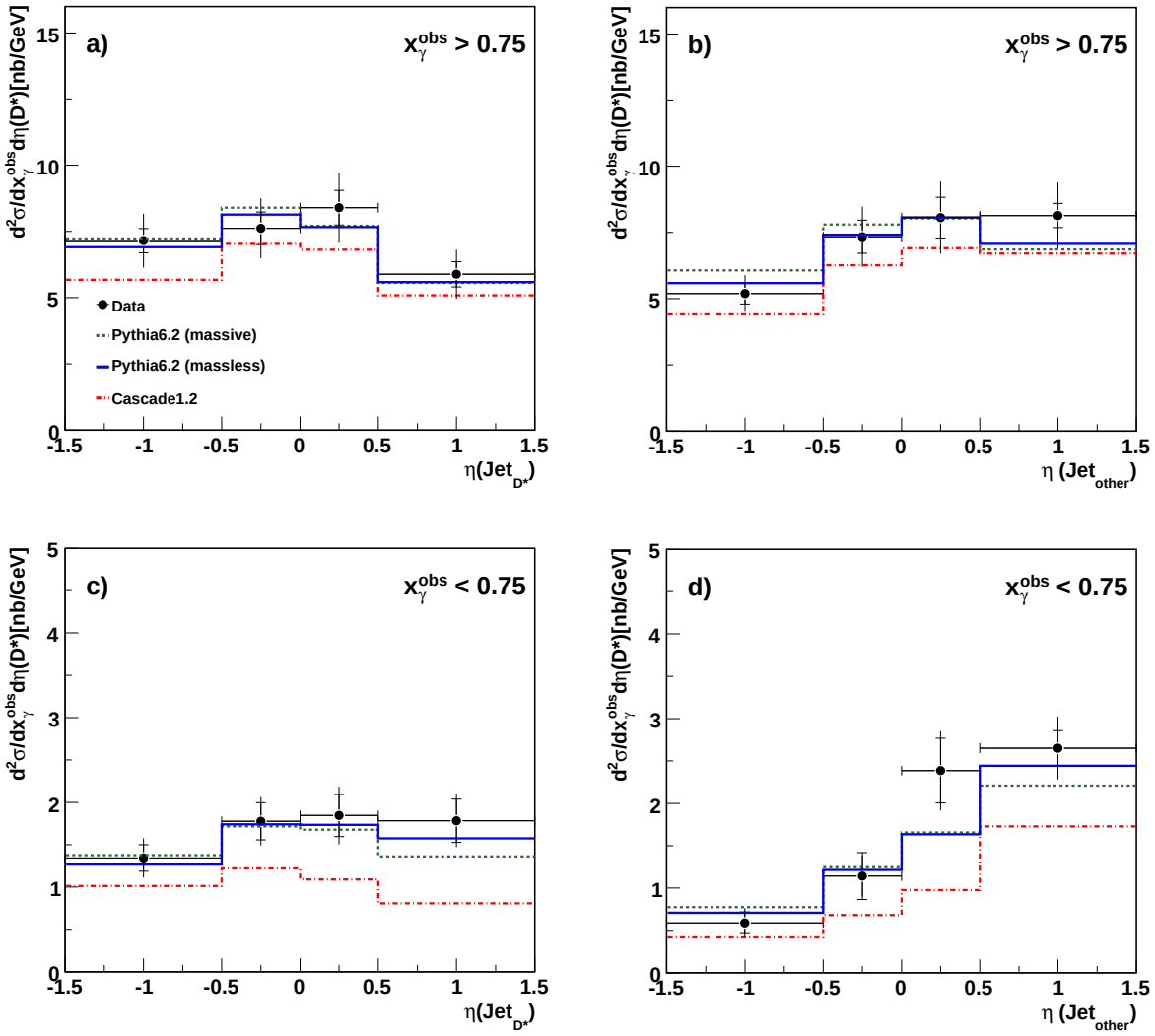

Figure 10.4: *Double differential cross sections in intervals of x_γ^{obs} as a function of η of the jet associated with a $D^\star$ meson and the other jet which is not associated with a $D^\star$meson. The data is compared to LO Monte Carlo predictions.*

10.3 Seperating the Direct and Resolved Components

The previous discussion already indicated that resolved components play an important role in the production mechanism of the charm quarks. Especially the η distributions of the Jet_{other} showed that contributions in addition to the direct BGF are needed to explain the rise towards positive η. For the first time the statistics of the data allows to split the data into a direct enriched ($x_\gamma^{obs} > 0.75$) and a resolved enriched ($x_\gamma^{obs} < 0.75$) sample in an analysis performed at H1.

Figure 10.4 a)-d) shows the double differential measurement in two regions of x_γ^{obs} as a function of η of the $Jet_{D^\star}$ and Jet_{other} compared to LO predictions Pythia (massive), Pythia (massless) and Cascade and figure 10.5 a)-d) the comparsion to the FFNS NLO calculation. The measurement in the direct regime $x_\gamma^{obs} > 0.75$ is displayed in figure 10.4 a) for $\eta(Jet_{D^\star})$ and b) for $\eta(Jet_{other})$. By comparing both distribution only slight differences in the shape are observed. The $\eta(Jet_{D^\star})$ is nearly symmetric, whereas a slight rise of the $\eta(Jet_{other})$ distribution towards positive values of η is observed. A good agreement in shape and normalization is found with all predictions, except for the Cascade predictions which

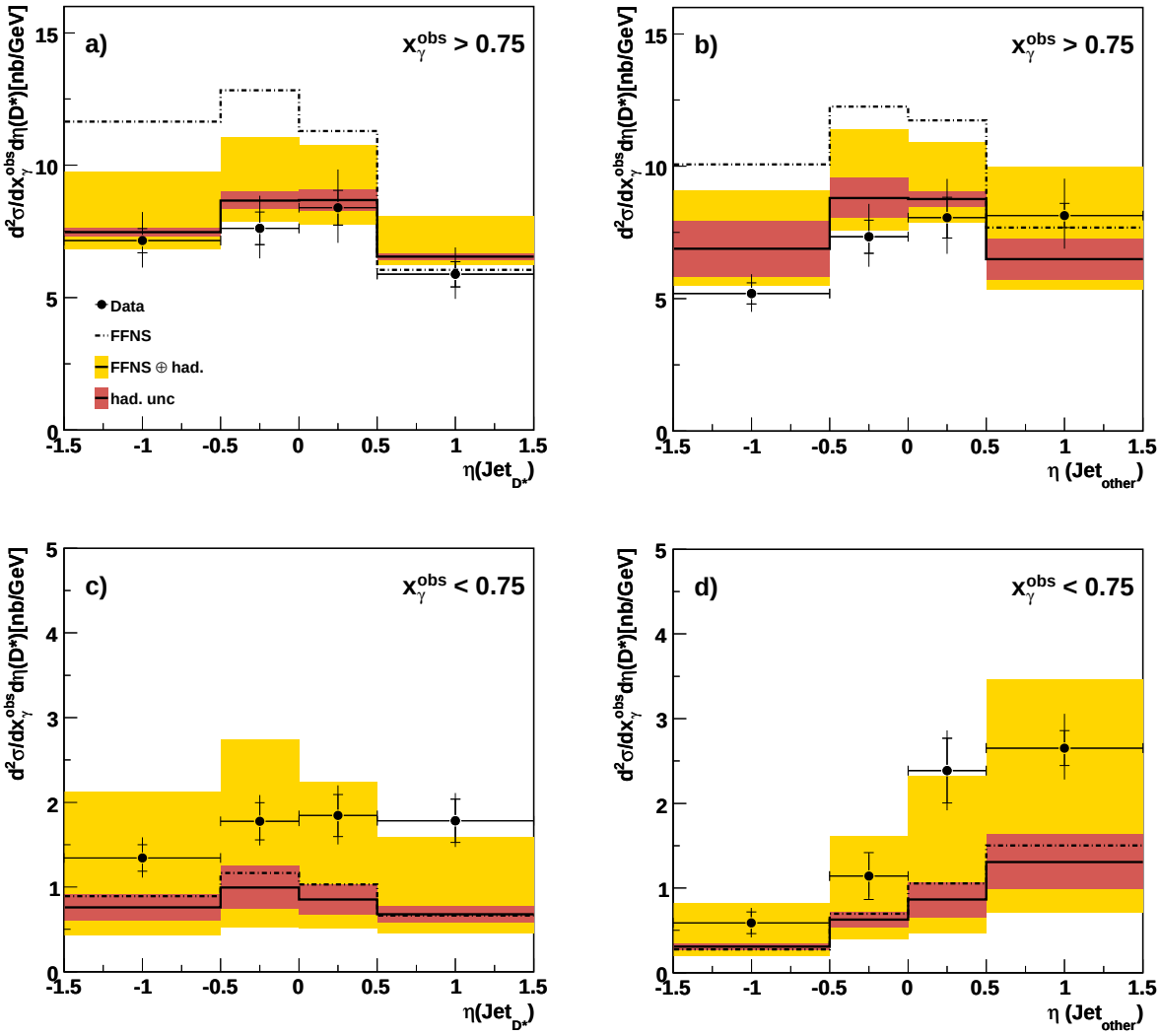

Figure 10.5: *Double differential cross sections in intervals of x_γ^{obs} as a function of $\eta(Jet_{D^\star})$ and $\eta(Jet_{other})$. The data is compared to a FFNS calculation.*

tends to be slightly too low. The measurement in the resolved regime $x_\gamma^{obs} < 0.75$ is depicted in figure 10.4 c) and d). The η distribution of the $Jet_{D^\star}$ in the resolved enriched sample shows a similar behavior as in the direct enriched sample (see figure 10.4 a)). In contrast to this the η distribution of the Jet_{other} shows a stronger rise towards positive values of η. The comparison with the NLO prediction is shown in figure 10.5. A good agreement in shape and normalization is found for the central value of the prediction in the direct component for $\eta(Jet_{D^\star})$ as well as for $\eta(Jet_{other})$. In the resolved regime the measurement is underestimated by the central value by a factor of two. Nevertheless the shape of both distribution is reasonably well described.

10.4 Summary of DiJet Cross Section results

The best agreement is found with the Pythia (massless) and Pythia (massive) simulation. Cascade describes the shape of nearly all distributions but is too low in normalization. The central values of the NLO prediction underestimates the measurements as well. Nevertheless, the measurement is compatible with the uncertainty band of the prediction except for the

$\Delta\phi$ measurement, which is sensitive to higher order contributions. The double differential cross sections as a function of x_γ^{obs} and η of the jets shows that Pythia and Cascade describes both the direct and resolved enriched regions consistently, while the NLO FFNS calculation describes the direct enriched region and the and underestimates the resolved enriched region.

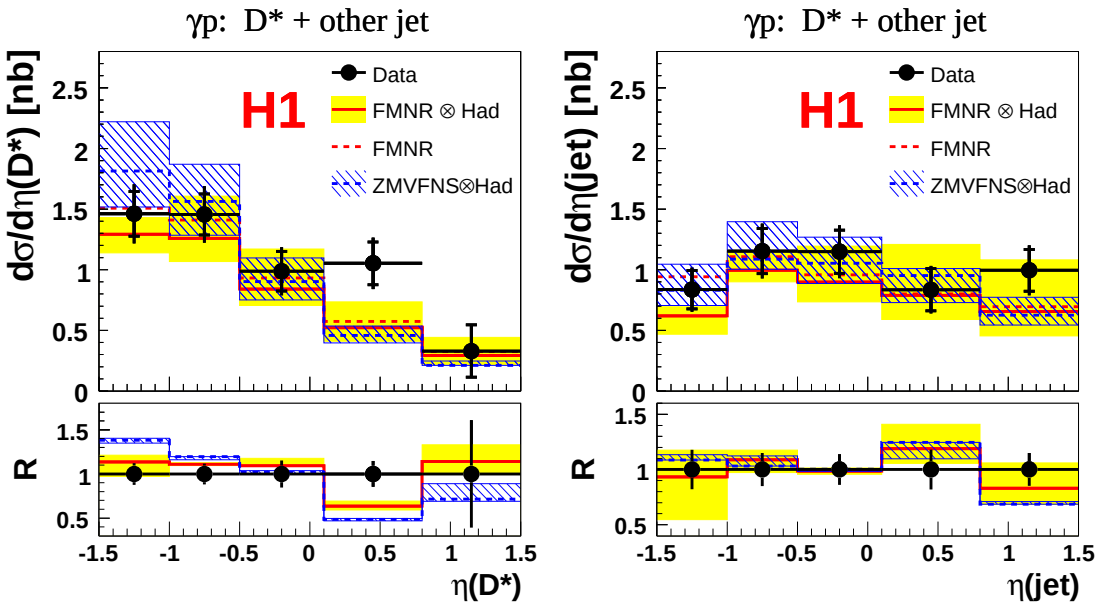

Figure 10.6: *Measurement of the pseudorapidity of the $D^\star$in a jet sample (a) and of the jet not containing a $D^\star$ meson by the H1 collaboration [Akt07]. The measurement is compared with predictions of Pythia (massive) and Cascade (a) and with the next-to-leading order calculation FMNR (b).*

10.5 Comparison to Previous $D^\star$+ Jets Measurements of H1 and ZEUS

The results obtained in the DiJet sample of this analysis are compared to previous measurements of the H1 and ZEUS collaboration.

Differential photoproduction cross sections for events containing $D^\star$ mesons and jets have been measured previously by the H1 collaboration in [Akt07]. The requirements for the photoproduction and the $D^\star$ meson selection in the inclusive sample of this measurements have been given in section 8.5. Events with $D^\star$ mesons and jets are investigated in a sample with a $D^\star$ meson and a jet not containing the $D^\star$ ($D^\star$ + other jet) and in a sample with a $D^\star$ meson and at least two jets ($D^\star$ tagged DiJet). Jets are selected with $p_t(jet) > 3.0$ GeV in the $D^\star$ + other jet sample and with $p_t(jet) > 3.0(4.0)$ GeV in the $D^\star$ tagged DiJet. In both samples only jets measured in the central region are taken into account ($|\eta(jet)| < 1.5$). The $D^\star$ + other jet sample corresponds to a number of $D^\star$ mesons of about 592 ± 57. Figure 10.6 shows the measurement of the cross sections as a function of $\eta(D^\star)$ and $\eta(jet)$ in the $D^\star$ + other jet sample. Both distributions show clear differences in shape. In [Akt07] it is concluded that the jet receives contributions from gluons or light flavors. This result is confirmed by the analysis presented in this thesis see figure 10.2 and the discussion in section 10.2.

A further result presented in [Akt07] is the measurement of the observable x_γ^{obs} in the $D^\star$ tagged DiJet sample. Figure 10.7 shows that the measurement is underestimated at low values of $x_\gamma^{obs} < 0.6$. In this region resolved photon processes or higher order contributions are expected to be enhanced. This is in agreement with the results obtained in this analysis see figure 10.3 a)-b), 10.4 and 10.5. The ZEUS collaboration measured $d\sigma/dx_\gamma^{obs}$ in [Che03]. $D^\star$ mesons and jets have been measured in the range $130 < W_{\gamma p} < 280$ GeV and $Q^2 < 1$ GeV^2 with $p_t(D^\star) > 3$ GeV and $|\eta(D^\star)| < 1.5$. Jets are selected in the range $|\eta(jet)| < 2.4$ and

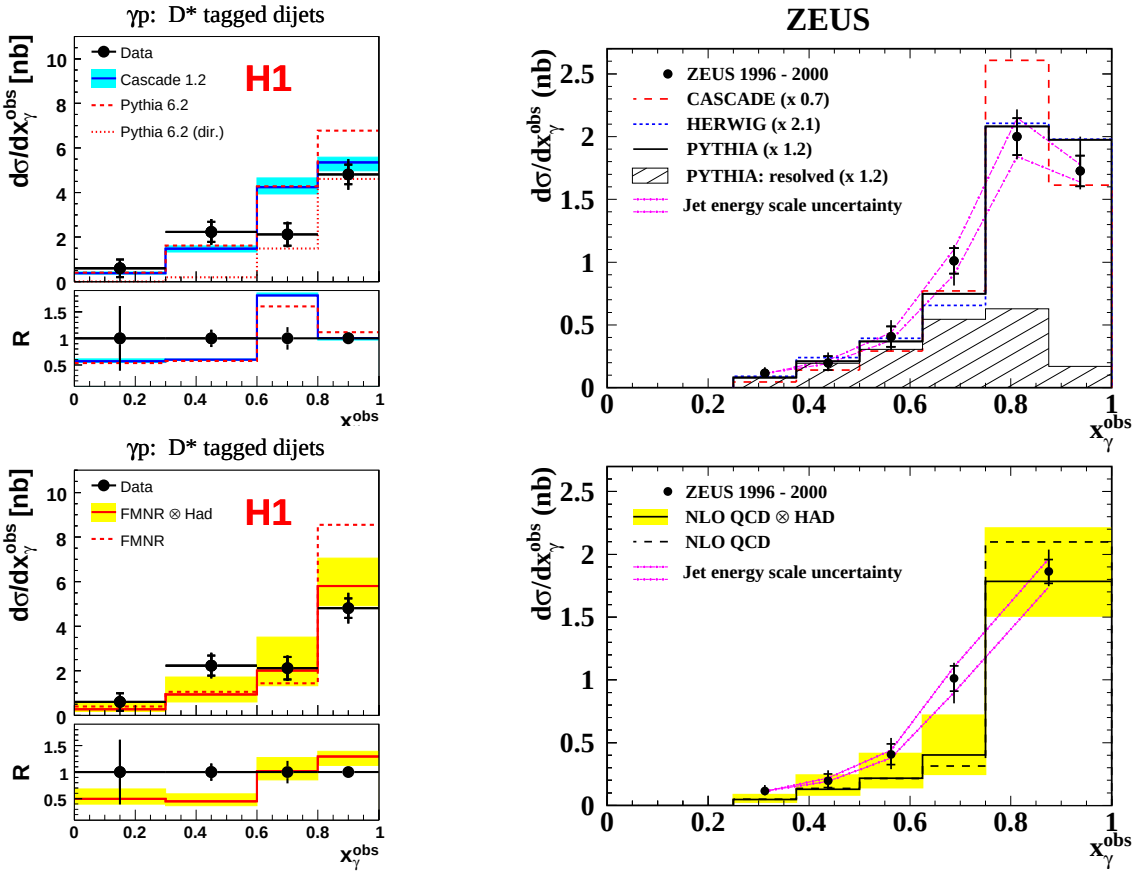

Figure 10.7: *On the left the measurement of DiJet cross sections as a function of x_γ^{obs} by the H1 collaboration [Akt07]. The measurement is compared with predictions of Pythia (massive) and Cascade (a) and with the next-to-leading order calculation FMNR (b). On the right the measurement of the ZEUS collaboration [Che03] is compared to predictions by Herwig (a) and a massive next-to-leading-order calculation.*

with $p_t(jet) > 5$ GeV. The $d\sigma/dx_\gamma^{obs}$ measurement is likewise underestimated at low values of x_γ^{obs} as the previous H1 measurement and the present measurement.

Chapter 11

Summary and Conclusion

The photoproduction of charm quarks is studied with the H1 detector at HERA. Events with charm are tagged by $D^\star$ mesons decaying via the decay $D^\star \to D^0\pi^\pm_{slow} \to K^\mp\pi^\pm\pi^\pm_{slow}$. Employing the new Level 3 system of the Fast Track Trigger yields a significantly extended phase space and a data sample eight times larger than in the previous measurement. Cross sections are determined for events with $D^\star$ mesons (inclusive sample) and events with $D^\star$ mesons and jets (DiJet sample). The investigated kinematic region covers a range of the photon virtuality of $Q^2 < 2$ GeV^2 and of the photon-proton center-of-mass energies of $100 < W_{\gamma p} < 285$ GeV. $D^\star$ mesons are measured with transverse momenta of at least 1.8 GeV and pseudorapidities $|\eta| < 1.5$. In the DiJet sample in addition to a $D^\star$ meson at least two jets are selected in the pseudorapidity range of $|\eta| < 1.5$ with $p_t(Jet_1) > 4$ GeV or $p_t(Jet_2) > 3$ GeV, respectively. The analyzed data sample corresponds to an integrated luminosity of 93.39 pb^{-1}.

The results of the measurement are compared with leading order plus parton shower QCD models provided by the Monte Carlo simulation programs Pythia and Cascade, which are based either on collinear or k_t-factorization. The results are further compared to next-to-leading order predictions based on a FFNS and GMVFNS calculation. The precision of the measurement presented here is much higher than the accuracy of the NLO calculations. The theoretical uncertainties are estimated by scale variations and correspond to missing higher order terms.

In the inclusive measurement, differential cross sections are determined as a function of $p_t(D^\star)$, $\eta(D^\star)$ and $W_{\gamma p}$ and double differential cross sections as a function of $p_t(D^\star)$ and $\eta(D^\star)$. The shape of the $p_t(D^\star)$ spectrum is best described by the Cascade and the NLO FFNS calculation. Part of the NLO effects are taken into account by the k_t-factorization in Cascade, which results in a harder $p_t(D^\star)$ spectrum compared to the prediction provided by Pythia. The good agreement with the FFNS and the Cascade prediction indicate that NLO effects are needed to describe the $p_t(D^\star)$ spectrum. The shape of the $\eta(D^\star)$ spectrum is best described by Pythia. Cascade and the NLO calculations underestimate the measurement in the very forward region $0.9 < \eta(D^\star) < 1.5$. This discrepancy is probably connected to resolved processes which are predominantly expected in the forward region. In Pythia in addition to the BGF processes resolved processes are considered, which are partially covered by the k_t-factorization in Cascade. Indications that the resolved component is underestimated in the NLO calculations have been found in the DiJet measurement of this analysis and previous DiJet mesurements by the H1 [Akt07] and ZEUS [Che03] Collaborations. The cross section as a function of $W_{\gamma p}$ is of particular interest, since the studied $W_{\gamma p}$ range has been significantly extended compared to previous measurements. The shape of the $W_{\gamma p}$ spectrum is not described by any of the QCD models, where all predictions tend to be too steep. In the double differential measurement a very prominent excess is observed in the forward region of the highest p_t interval. An excess in this region of phase space has also been observed by ZEUS in an analysis [Bre99], which was performed in a phase space similar

to the phase space of this analysis. In general, the findings in the inclusive measurement are consistent with a previous measurement of the H1 collaboration performed in a stronger restricted phase space (see section 8.5).

In the DiJet measurement, in addition to the charm tag by the $D^\star$, a second parton is tagged by means of a jet. This allows a more detailed investigation of the charm production mechanism. Compared to the inclusive measurement a slightly higher accuracy of the FFNS NLO calculation is found which corresponds to the larger scale in the DiJet sample compared to the inclusive sample. Cross sections are determined for the jet associated to the $D^\star$ meson ($Jet_{D^\star}$) and the other leading jet (Jet_{other}) as a function of p_t and η and for the combined jet quantities $\Delta\phi$, $\Delta\eta$, x_g^{obs} and x_γ^{obs}. The determined cross sections are found to be consistent with Pythia in normalization and shape and with the uncertainty of the FFNS calculation. The Cascade prediction describes the shape, but generally underestimates the normalization. The variable x_γ^{obs} corresponds to the momentum fraction of the photon transfered to the hard interaction, thus x_γ^{obs} is by definition sensitive to resolved processes. The x_γ^{obs} distribution is well reproduced by all LO predictions. The NLO calculation describes the large values ($x_\gamma^{obs} > 0.75$) region, but tends to underestimate the region of low values ($x_\gamma^{obs} < 0.75$). This indicates that resolved components are underestimated in the FFNS calculation. The η distribution of the jet associated with the $D^\star$ meson and the other jet are clearly different, which indicates that the other jet receives contributions from gluons and light flavors, as predicted by resolved processes. The distributions are in good agreement with the LO predictions. A tendency that the measurement is underestimated by the FFNS NLO calculation is especially observed in the forward region of the $\eta(Jet_{other})$ measurement. The difference between the $\eta(Jet_{other})$ and $\eta(Jet_{D^\star})$ shows a maximum at $\Delta\eta \approx 0.5$, indicating that the resolved component goes predominantly into the forward direction. Double differential cross sections in bins of x_γ^{obs} as a function of η have been extracted to separate the resolved ($x_\gamma^{obs} < 0.75$) from direct component ($x_\gamma^{obs} > 0.75$). Similar η distributions are determined for both jets for $x_\gamma^{obs} > 0.75$, whereas strong deviations in shape are observed in the η distributions for $x_\gamma^{obs} < 0.75$. The $\Delta\phi$ measurement is sensitive to higher order QCD radiations. The shape is not described by any of the QCD models. The k_t-factorization leads to a harder $\Delta\phi$ spectrum for Cascade than for Pythia. The FFNS calculation is not able to describe the distribution, in particular no activity is found in the range $0^\circ < \Delta\phi < 120^\circ$. The variable x_g^{obs} corresponds to the momentum fraction of the gluon transfered to the hard interaction from the proton side and is sensitive to the gluon content in the proton. The variable is well reproduced by the LO predictions and the upper uncertainty of the NLO prediction. The quantity x_g^{obs} can be used to perform a direct measurement of the gluon density in the proton as described in [Adl99].

In general it can be concluded that the charm photoproduction is well described by pQCD. Indications for the need of NLO terms or even higher order to describe the measurement are found in the $p_t(D^\star)$ and $\Delta\phi$ distribution. Consistent with previous measurements, relevant contributions of resolved processes are found to be nessecary to describe the production of charm quarks.

Appendix A

Further Background Reduction Studies

The specific energy loss (dE/dx) depends on the velocity of a particle. For a measured momentum it is sensitive to the particle mass. Thus a measurement of dE/dx can be used for particle identification. The available simulation of the dE/dx information is insufficient and could not be used within this analysis. However, the simulation is currently improved and the dE/dx information is a future option to improve the signal to combinatorial background ratio.

A quantitative expression for the specific energy loss of a charged particle is given by the Bethe-Bloch-Formula:

$$\frac{dE}{dx} = \frac{4\pi e^4 N_A}{m_e c^2} \cdot \frac{Z}{A} \cdot \frac{1}{\beta^2} z^2 \left(\ln \frac{\sqrt{2 m_e c^2 E_{max}} \beta\gamma}{I} - \frac{\beta^2}{2} - \frac{\delta(\beta)}{2} \right) \tag{A.1}$$

Here N_A denotes Avogadro's number, m_e the electron mass, z the charge of the incident particles in units of the elementary charge, Z (A) the atomic number (mass) of the traversed matter. The lorentz variables $\beta = p/E$ and $\gamma = 1/\sqrt{1-\beta^2}$ are defined as usual. The velocity of the charged particles defines the energy loss in a certain material. At small velocities the energy loss is decreasing with β^2, since the interaction time between the electrons in the material and the charged particle decreases. At large velocities of the particles relativistic effects play a dominant role and lead again to an increase of the energy loss, since the electric field is compressed in the direction of movement of the particles. The density effect correction $\delta/2$ has been introduced in equation A.1 to account for the effect that real media become polarized, limiting the field extansion.

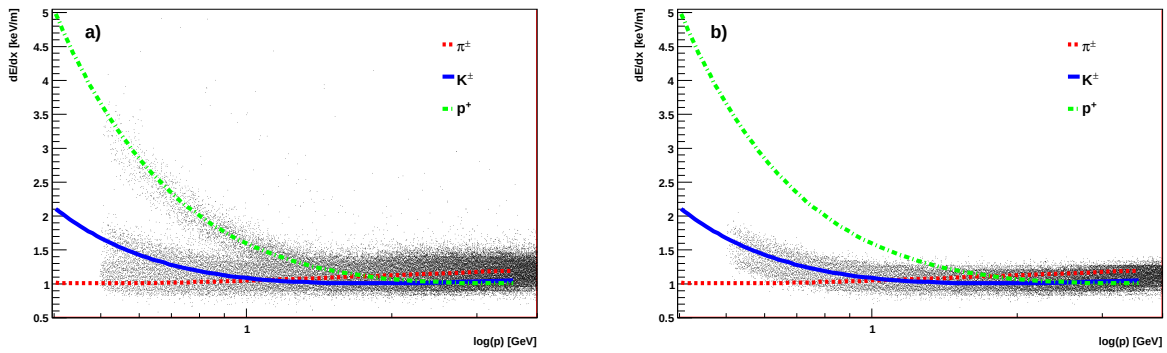

Figure A.1: *Energy loss (dE/dx) as a function of the momentum p for all particle candidates selected within this thesis (a). The same distribution after rejecting all particle candidates with $LH(K) > 98\%$. The lines correspond to an empirical derived parametrization, which takes into account varying detector conditions.*

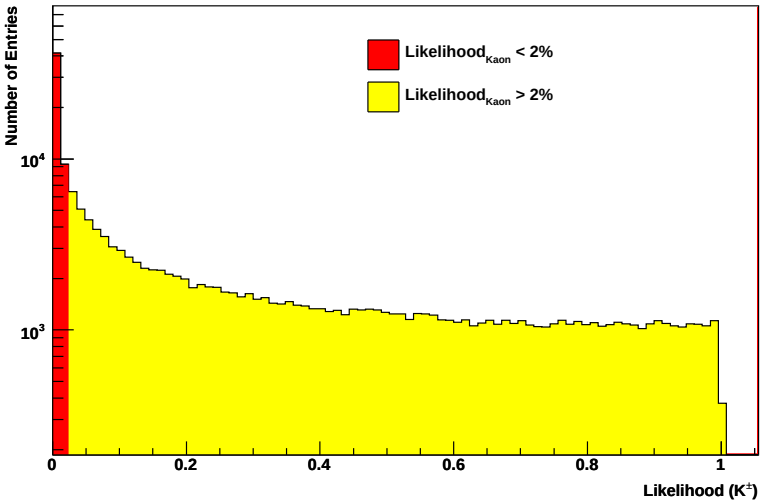

Figure A.2: *The likelihood for particles to be kaon $LH(K)$ is diplayed in a logarithmic scale.*

Due to influences of the track reconstruction, the dE/dx values measured at the H1 experiment differ a priori from the prediction given by equation A.1. An empirical derived parametrization of the measured dE/dx values is used at H1. Detailed information about the H1 specific dE/dx parametrization can be found in [Kle08]. The measured values have to be corrected for varying conditions in the CJC by run dependent correction factors.

Figure A.1 shows the dE/dx of the decay particles of all $D^\star$ meson candidates selected in this analysis as a function of the momentum. To ensure a reliable dE/dx measurement only tracks are taken into account with more than ten hits. The points correspond to the measured dE/dx values and the curves represent the prediction according the H1 specific empirical parametrization for the particle hypothesis of pions, kaons and protons. A clear particle seperation is found at low momenta.

The dE/dx information is used to calculate the probability to find a track of a certain particle kind. The likelihood LH corresponds to the probability to find the measured dE/dx value in a certain distance to the Bethe-Bloch parametrization. Figure A.2 shows the likelihood for all kaon candidates under the hypothesis of a kaon mass. In this distribution real kaons are expected to show a flat behaviour and the fake kaons are expected in the peak at zero. The red shaded region corresponds to kaon candidates which have a probability of less than 2% to be a real kaon. The total $D^\star$ meson signal of the inclusive sample after rejecting all particles with $LH(K) < 2\%$ is displayed in figure A.3. The comparison of figure A.3 with figure 4.3 shows that a further reduction of the combinatorical background of $\simeq 30\%$ is achieved by taking into account the dE/dx information. Within the statistical error no signal loss is observed.

The influence of the dE/dx cut has been studied differentially as a function of the transverse momentum and the pseudorapidity of the $D^\star$ mesons. The signal efficiency and background reduction as a function of $p_t(D^\star)$ and $\eta(D^\star)$ is displayed in figure A.4 a)-d). No dependence, neither on η nor on p_t, is observed. The signal is not reduced within the uncertainties and and the background reduction amounts to $\simeq 30\%$. The absolut statistical error with (solid line) and without (dashed line) a cut on the $LH(K)$ are displayed in figure A.4 e)-f). In addition the relative reduction of the statistical error due to the cut on the likelihood is shown (filled histogram). The reduction of the error is largest at low transverse momenta and in the forward regio, where it amounts to 1%.

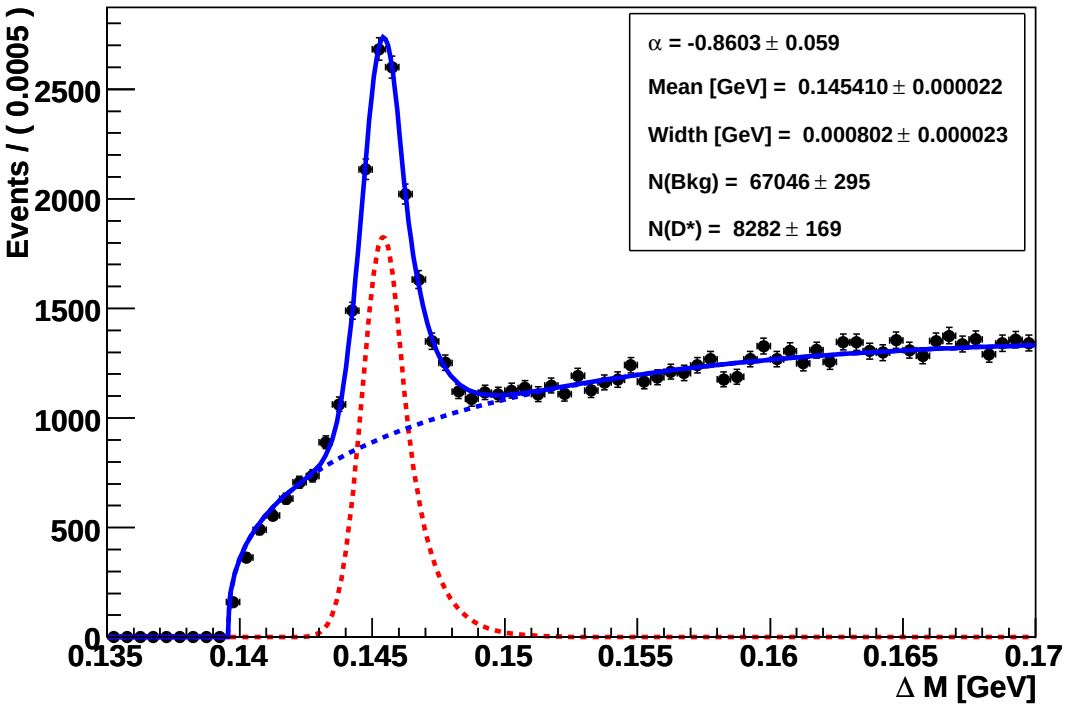

Figure A.3: ΔM *distribution of all selected* $D^\star$ *meson candidates in the inclusive sample after a liklihood cut of* $LH(K) < 2\%$.

Although the background is reduced by $\simeq 30\%$, the improvement in statistical error is small, showing that the fit constrains the seperation into signal and background well. For a cut $LH > 2\%$ a corresponding reduction in the signal of 2% is expected but not found. Without a simulation of dE/dx in the Monte Carlo this would have to be taken into account in the systematic uncertainty. The dE/dx information is therefore not used in this analysis.

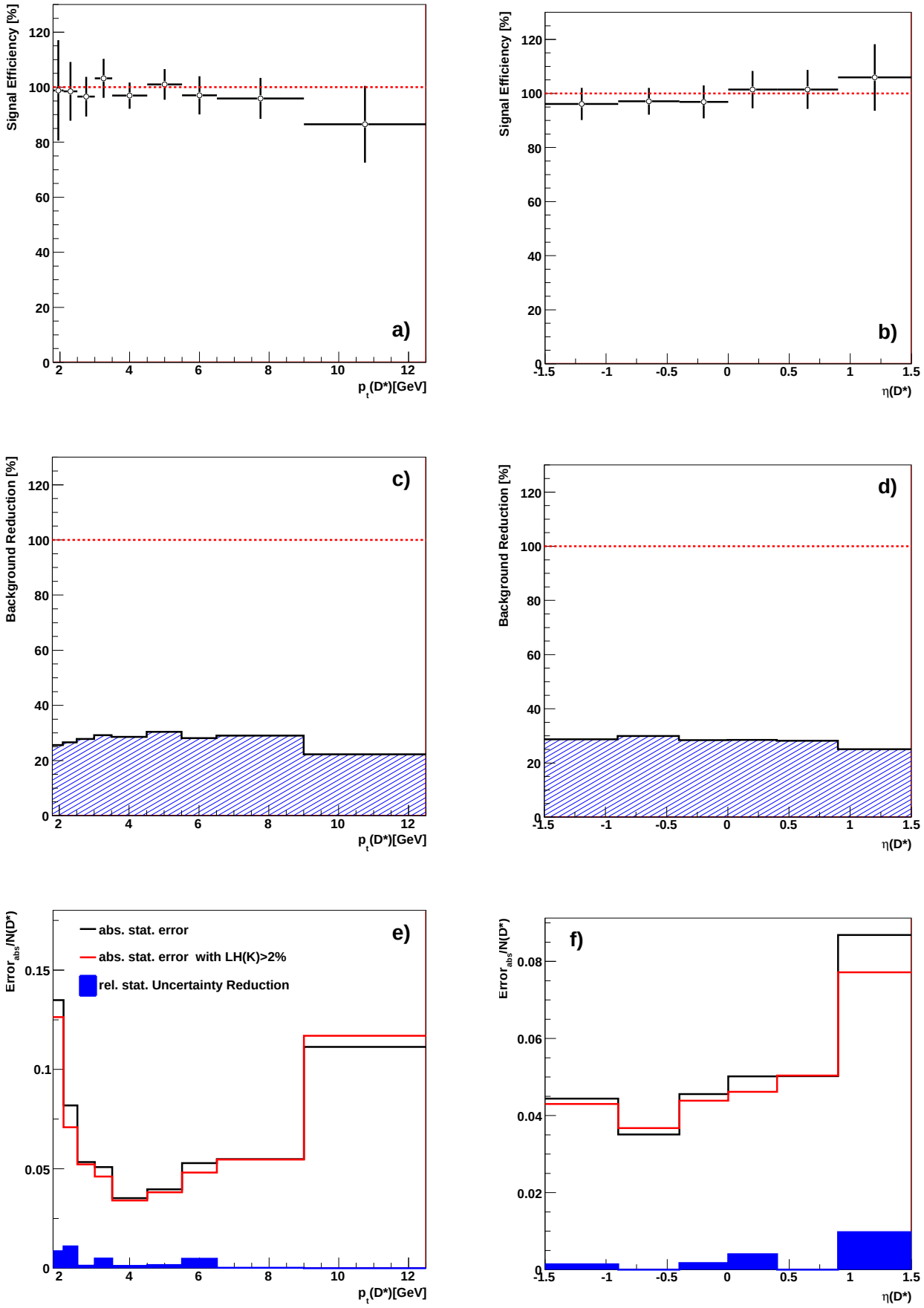

Figure A.4: *Influence of the cut $LH(K) > 2\%$ on $p_t(D^\star)$ and $\eta(D^\star)$. Signal efficiency a)-b), background reduction c)-d) and influcene on the statistical error.*

Appendix B

Result tables of the Inclusive Sample

Bin Border [GeV]	$\frac{d\sigma}{dp_t(D^\star)}$ [nb/GeV]	σ_{stat} [%]	σ_{sys} [%]
$1.80 - 2.10$	31.41	± 14.0	$^{+17.9}_{-19.8}$
$2.10 - 2.50$	22.99	± 8.5	$^{+12.6}_{-13.6}$
$2.50 - 3.00$	14.20	± 5.6	$^{+10.6}_{-11.9}$
$3.00 - 3.50$	9.11	± 5.3	$^{+10.6}_{-11.8}$
$3.50 - 4.50$	5.16	± 3.7	$^{+9.8}_{-11.2}$
$4.50 - 5.50$	2.14	± 4.1	$^{+10.6}_{-11.9}$
$5.50 - 6.50$	0.93	± 5.5	$^{+12.1}_{-13.7}$
$6.50 - 9.00$	0.30	± 5.7	$^{+12.9}_{-15.3}$
$9.00 - 12.50$	0.06	± 11.6	$^{+21.9}_{-29.6}$
Bin Border	$\frac{d\sigma}{d\eta(D^\star)}$ [nb]	σ_{stat} [%]	σ_{sys} [%]
$-1.50 - -0.90$	13.86	± 4.6	$^{+11.2}_{-13.4}$
$-0.90 - -0.40$	15.29	± 3.7	$^{+10.5}_{-12.4}$
$-0.40 - 0.00$	14.04	± 4.7	$^{+10.8}_{-12.3}$
$0.00 - 0.40$	13.24	± 5.2	$^{+10.9}_{-12.0}$
$0.40 - 0.90$	12.18	± 5.2	$^{+11.0}_{-11.8}$
$0.90 - 1.50$	9.39	± 9.1	$^{+13.4}_{-13.8}$
Bin Border [GeV]	$\frac{d\sigma}{dW_{\gamma p}}$ [nb/GeV]	σ_{stat} [%]	σ_{sys} [%]
$100.00 - 140.00$	0.28	± 3.6	$^{+10.9}_{-12.5}$
$140.00 - 180.00$	0.27	± 4.0	$^{+10.4}_{-13.1}$
$180.00 - 230.00$	0.20	± 4.5	$^{+10.6}_{-11.5}$
$230.00 - 285.00$	0.12	± 6.3	$^{+12.4}_{-12.4}$

Table B.1: *Bin by bin results for the inclusive differential cross section as a function of p_t and η of the $D^\star$ meson and $W_{\gamma p}$.*

Bin Border	$\frac{d\sigma}{d\eta(D^\star)dp_t(D^\star)}$ [nb/GeV]	σ_{stat} [%]	σ_{sys} [%]
$1.8 < p_t(D^\star) < 2.5$ GeV			
$-1.50 - -0.80$	10.53	± 10.04	$^{+13.70}_{-13.83}$
$-0.80 - 0.00$	10.73	± 10.46	$^{+14.13}_{-14.07}$
$0.00 - 1.50$	6.84	± 15.53	$^{+18.36}_{-18.35}$
$2.5 < p_t(D^\star) < 4.5$ GeV			
$-1.50 - -1.00$	2.89	± 6.81	$^{+11.23}_{-11.26}$
$-1.00 - -0.50$	3.45	± 5.06	$^{+10.28}_{-10.32}$
$-0.50 - 0.00$	3.27	± 5.36	$^{+10.45}_{-10.44}$
$0.00 - 0.50$	2.84	± 6.68	$^{+11.25}_{-11.18}$
$0.50 - 1.50$	2.14	± 7.50	$^{+11.69}_{-11.69}$
$4.5 < p_t(D^\star) < 12.5$ GeV			
$-1.50 - -1.00$	0.09	± 10.58	$^{+14.49}_{-14.48}$
$-1.00 - -0.50$	0.14	± 6.38	$^{+11.88}_{-11.88}$
$-0.50 - 0.00$	0.19	± 5.94	$^{+11.76}_{-11.76}$
$0.00 - 0.50$	0.24	± 5.71	$^{+11.67}_{-11.65}$
$0.50 - 1.00$	0.21	± 6.19	$^{+12.04}_{-11.99}$
$1.00 - 1.50$	0.15	± 9.95	$^{+14.37}_{-14.37}$

Table B.2: *Bin by bin results for the inclusive double differential cross section as a function of η and p_t of the $D^\star$ meson.*

Appendix C

Result tables of the DiJet Sample

Bin Border [GeV]	$\frac{d\sigma}{dp_t(Jet_{D^\star})}$ [nb/GeV]	σ_{stat} [%]	σ_{sys} [%]
$3.00 - 4.00$	1.60	± 10.2	$^{+15.5}_{-14.7}$
$4.00 - 5.50$	2.39	± 5.5	$^{+13.6}_{-13.2}$
$5.50 - 7.50$	1.14	± 6.4	$^{+16.6}_{-15.3}$
$7.50 - 10.00$	0.38	± 8.7	$^{+19.7}_{-17.2}$
$10.00 - 15.50$	0.08	± 11.1	$^{+28.1}_{-24.6}$
Bin Border [GeV]	$\frac{d\sigma}{dp_t(Jet_{other})}$ [nb/GeV]	σ_{stat} [%]	σ_{sys} [%]
$3.00 - 4.00$	2.07	± 7.5	$^{+15.3}_{-14.6}$
$4.00 - 5.50$	2.71	± 5.8	$^{+14.7}_{-13.2}$
$5.50 - 7.50$	1.11	± 8.2	$^{+15.5}_{-14.9}$
$7.50 - 10.00$	0.35	± 9.0	$^{+20.1}_{-18.7}$
$10.00 - 15.50$	0.07	± 14.9	$^{+26.3}_{-24.7}$

Table C.1: *Bin by bin results for the p_t measurement of the $Jet_{D^\star}$ and Jet_{other}.*

Bin Border	$\frac{d\sigma}{d\eta(Jet_{D^\star})}$ [nb]	σ_{stat} [%]	σ_{sys} [%]
$-1.50 - -0.90$	2.52	± 8.3	$^{+15.2}_{-14.4}$
$-0.90 - -0.40$	3.28	± 6.5	$^{+15.8}_{-14.9}$
$-0.40 - 0.00$	3.23	± 8.5	$^{+15.7}_{-14.5}$
$0.00 - 0.40$	3.50	± 8.5	$^{+17.2}_{-15.8}$
$0.40 - 0.90$	3.20	± 7.9	$^{+16.4}_{-14.9}$
$0.90 - 1.50$	2.54	± 11.4	$^{+18.3}_{-17.4}$
Bin Border	$\frac{d\sigma}{d\eta(Jet_{other})}$ [nb]	σ_{stat} [%]	σ_{sys} [%]
$-1.50 - -0.90$	1.47	± 10.1	$^{+15.2}_{-14.7}$
$-0.90 - -0.40$	2.28	± 10.0	$^{+17.3}_{-16.1}$
$-0.40 - 0.00$	2.88	± 9.5	$^{+16.5}_{-15.2}$
$0.00 - 0.40$	3.66	± 9.7	$^{+16.8}_{-16.1}$
$0.40 - 0.90$	3.98	± 8.8	$^{+16.8}_{-15.3}$
$0.90 - 1.50$	4.06	± 5.9	$^{+16.5}_{-15.0}$

Table C.2: *Bin by bin results for the η measurement of the $Jet_{D^\star}$ and Jet_{other}.*

Bin Border	$\frac{d\sigma}{d\Delta\eta}$ [nb]	σ_{stat} [%]	σ_{sys} [%]
$-3.00 - -2.00$	0.22	± 24.8	$^{+25.7}_{-24.9}$
$-2.00 - -1.00$	1.02	± 11.2	$^{+17.7}_{-16.9}$
$-1.00 - 0.00$	2.44	± 8.0	$^{+15.3}_{-14.2}$
$0.00 - 1.00$	3.09	± 5.6	$^{+15.8}_{-14.5}$
$1.00 - 2.00$	1.88	± 6.3	$^{+15.6}_{-14.3}$
$2.00 - 3.00$	0.50	± 12.0	$^{+20.8}_{-19.7}$
Bin Border	$\frac{d\sigma}{dx_\gamma^{obs}}$ [nb]	σ_{stat} [%]	σ_{sys} [%]
$0.00 - 0.50$	3.06	± 13.5	$^{+16.7}_{-16.0}$
$0.50 - 0.75$	8.81	± 6.9	$^{+16.4}_{-14.9}$
$0.75 - 1.00$	21.03	± 3.7	$^{+15.1}_{-13.8}$
Bin Border	$\frac{d\sigma}{dx_g^{obs}}$ [nb]	σ_{stat} [%]	σ_{sys} [%]
$-3.00 - -2.30$	2.30	± 7.4	$^{+14.2}_{-13.3}$
$-2.30 - -2.00$	10.84	± 5.7	$^{+14.7}_{-13.4}$
$-2.00 - -1.70$	10.68	± 5.8	$^{+15.5}_{-14.7}$
$-1.70 - -1.00$	1.19	± 11.4	$^{+25.9}_{-21.6}$
Bin Border	$\frac{d\sigma}{d\Delta\phi}$ [nb]	σ_{stat} [%]	σ_{sys} [%]
$20.00 - 110.00$	0.01	± 12.7	$^{+18.2}_{-16.8}$
$110.00 - 155.00$	0.06	± 6.2	$^{+16.3}_{-15.0}$
$155.00 - 170.00$	0.18	± 5.7	$^{+16.0}_{-14.7}$
$170.00 - 180.00$	0.27	± 5.6	$^{+14.7}_{-13.6}$

Table C.3: *Bin by bin results for the differential cross section as a function of the* $\Delta\eta$, x_γ^{obs}, x_g^{obs} *and* $\Delta\phi$.

Bin Border	$\frac{d\sigma}{d\eta(Jet_{D^\star})dx_\gamma}$ [nb]	σ_{stat} [%]	σ_{sys} [%]
$x_\gamma > 0.75$			
$-1.50 - -0.50$	7.15	± 6.4	$^{+15.1}_{-14.2}$
$-0.50 - 0.00$	7.62	± 8.1	$^{+16.1}_{-14.9}$
$0.00 - 0.50$	8.39	± 7.8	$^{+17.2}_{-15.8}$
$0.50 - 1.50$	5.88	± 8.1	$^{+17.2}_{-15.8}$
$x_\gamma < 0.75$			
$-1.50 - -0.50$	1.34	± 11.6	$^{+18.2}_{-17.3}$
$-0.50 - 0.00$	1.78	± 12.4	$^{+17.4}_{-16.1}$
$0.00 - 0.50$	1.84	± 13.4	$^{+19.3}_{-18.5}$
$0.50 - 1.50$	1.78	± 14.3	$^{+18.5}_{-17.4}$

Table C.4: *Double differential bin by bin results as a function of* $\eta(Jet_{D^\star})$ *and* x_γ.

Bin Border	$\frac{d\sigma}{d\eta(Jet_{other})dx_\gamma}$ [nb]	σ_{stat} [%]	σ_{sys} [%]
$x_\gamma > 0.75$			
$-1.50 - -0.50$	5.19	± 7.7	$^{+14.1}_{-13.4}$
$-0.50 - 0.00$	7.34	± 8.5	$^{+16.8}_{-15.5}$
$0.00 - 0.50$	8.06	± 9.6	$^{+18.2}_{-17.0}$
$0.50 - 1.50$	8.14	± 5.6	$^{+17.1}_{-15.3}$
$x_\gamma < 0.75$			
$-1.50 - -0.50$	0.59	± 21.7	$^{+30.0}_{-29.3}$
$-0.50 - 0.00$	1.14	± 24.2	$^{+22.5}_{-21.4}$
$0.00 - 0.50$	2.39	± 16.0	$^{+19.9}_{-19.6}$
$0.50 - 1.50$	2.65	± 7.7	$^{+15.2}_{-14.0}$

Table C.5: *Double differential bin by bin results as a function of* $\eta(Jet_{other})$ *and* x_γ.

Bibliography

[Aar08] F. D. Aaron et al. (H1), *Measurement of the Proton Structure Function F_L at Low x*, Phys. Lett. **B665** (2008), 139, 0805.2809.

[AB79] F. J. A. Blondel, *Proceedings of the Study of an ep facility for Europe, ed. Amaldi*, DESY 79/48 (1979) 391 (1979).

[Abt97a] I. Abt et al. (H1), *The H1 detector at HERA*, Nucl. Instrum. Meth. **A386** (1997), 310.

[Abt97b] I. Abt et al. (H1), *The Tracking, calorimeter and muon detectors of the H1 experiment at HERA*, Nucl. Instrum. Meth. **A386** (1997), 348.

[Adl96] C. Adloff et al. (H1), *Inclusive D0 and D*+- production in neutral current deep inelastic e p scattering at HERA*, Z. Phys. **C72** (1996), 593, hep-ex/9607012.

[Adl97] C. Adloff et al. (H1), *Measurement of charged particle transverse momentum spectra in deep inelastic scattering*, Nucl. Phys. **B485** (1997), 3, hep-ex/9610006.

[Adl98] C. Adloff et al., *Proposal for an Upgrade of the H1 Luminosity System and its Associated Electronics for HERA 2000*, Proposal submitted to the DESY PRC 98/05, 1998 (1998).

[Adl99] C. Adloff et al. (H1), *Measurement of D^* meson cross sections at HERA and determination of the gluon density in the proton using NLO QCD*, Nucl. Phys. **B545** (1999), 21, hep-ex/9812023.

[Adl03] C. Adloff et al. (H1), *Measurement and QCD analysis of neutral and charged current cross sections at HERA*, Eur. Phys. J. **C30** (2003), 1, hep-ex/0304003.

[Akt07] A. Aktas et al. (H1), *Inclusive $D^*\pm$ meson cross sections and $D^{*\pm}$ jet correlations in photoproduction at HERA*, Eur. Phys. J. **C50** (2007), 251, hep-ex/0608042.

[Alt77] G. Altarelli und G. Parisi, *Asymptotic Freedom in Parton Language*, Nucl. Phys. **B126** (1977), 298.

[Alt79] G. Altarelli, R. K. Ellis und G. Martinelli, *Large Perturbative Corrections to the Drell-Yan Process in QCD*, Nucl. Phys. **B157** (1979), 461.

[And83] B. Andersson, G. Gustafson, G. Ingelman und T. Sjostrand, *Parton Fragmentation and String Dynamics*, Phys. Rept. **97** (1983), 31.

[And93] B. Andrieu et al. (H1 Calorimeter Group), *The H1 liquid argon calorimeter system*, Nucl. Instrum. Meth. **A336** (1993), 460.

[App96] R. D. Appuhn et al. (H1 SPACAL GROUP), *Hadronic response and e/pi separation with the H1 lead/fibre calorimeter*, Nucl. Instrum. Meth. **A382** (1996), 395.

[App97] R. D. Appuhn et al. (H1 SPACAL Group), *The H1 lead/scintillating-fibre calorimeter*, Nucl. Instrum. Meth. **A386** (1997), 397.

[Bai99a] S. Baird et al., *Addendum to the proposal: A Fast Track Trigger with high Resolution for H1*, H1-09/99-576 (H1 internal Note) (1999).

[Bai99b] S. Baird et al., *A Fast Track Trigger with high Resolution for H1*, H1-06/99-573 (H1 internal Note) (1999).

[Bal78] *The Pomeranchuk Singularity in Quantum Chromodynamics*, Sov. J. Nucl. Phys. **28** (1978), 822.

[Bar78] W. A. Bardeen, A. J. Buras, D. W. Duke und T. Muta, *Deep Inelastic Scattering Beyond the Leading Order in Asymptotically Free Gauge Theories*, Phys. Rev. **D18** (1978), 3998.

[Ber06] N. Berger, *Measurement of diffractive ϕ meson photoproduction with the Fast Track Trigger at H1*, Dissertation, ETH Zürich (2006).

[Bet34] H. Bethe und W. Heitler, *On the Stopping of fast particles and on the creation of positive electrons*, Proc. Roy. Soc. Lond. **A146** (1934), 83.

[Bin98] J. Binnewies, B. A. Kniehl und G. Kramer, *Predictions for D*+- photoproduction at HERA with new fragmentation functions from LEP1*, Phys. Rev. **D58** (1998), 014014, hep-ph/9712482.

[Biz97] J. Bizot et al., *Strategy Studies for the H1 Topological L2 Trigger (L2TT)*, H1-01/97-508 (H1 internal Note) (1997).

[Boe07] M.-O. Boenig, *Messung des $D^\star$-Meson-Produktionsquerschnitts in tiefinelastischer Streuung mit dem H1-Experiment*, Dissertation, University Dortmund (2007).

[Bow81] M. G. Bowler, *e+ e- Production of Heavy Quarks in the String Modell*, Zeit. Phys. **C11** (1981), 169.

[Bre99] J. Breitweg et al. (ZEUS), *Measurement of inclusive $D^{*\pm}$ and associated dijet cross sections in photoproduction at HERA*, Eur. Phys. J. **C6** (1999), 67, hep-ex/9807008.

[Bro94] R. Brock et al. (CTEQ), *Handbook of perturbative QCD; Version 1.1: September 1994* (1994), fERMILAB-PUB-94-316.

[But03] J. M. Butterworth, J. P. Couchman, B. E. Cox und B. M. Waugh, *KtJet: A C++ implementation of the K(T) clustering algorithm*, Comput. Phys. Commun. **153** (2003), 85, hep-ph/0210022.

[Cac97] M. Cacciari, M. Greco, S. Rolli und A. Tanzini, *Charmed mesons fragmentation functions*, Phys. Rev. **D55** (1997), 2736, hep-ph/9608213.

[Cat90a] S. Catani, F. Fiorani und G. Marchesini, *QCD Coherence in Initial State Radiation*, Phys. Lett. **B234** (1990), 339.

[Cat90b] S. Catani, F. Fiorani und G. Marchesini, *Small x Behavior of Initial State Radiation in Perturbative QCD*, Nucl. Phys. **B336** (1990), 18.

[Che03] S. Chekanov et al. (ZEUS), *Dijet angular distributions in photoproduction of charm at HERA*, Phys. Lett. **B565** (2003), 87, hep-ex/0302025.

[Che04] S. Chekanov et al. (ZEUS), *High-Q^2 neutral current cross sections in e+ p deep inelastic scattering at $s^{1/2}$ = 318-GeV*, Phys. Rev. **D70** (2004), 052001, hep-ex/0401003.

[Cia88] M. Ciafaloni, *Coherence Effects in initial Jets at small Q^2/s*, Nucl. Phys. **B296** (1988), 49.

[Dok77] Y. L. Dokshitzer, *Calculation of the Structure Functions for the Deep Inelastic Scattering and e+ e- Annihilation by the pertubation theory in Quantum Chromodynamics.*, Sov. Phys. JETP **46** (1977), 641.

[Els92] E. Elsen, *Aspects Of The H1 Trigger And Data Acquisition System*, 2nd Annual Conference on Electronics for Future Colliders (1992).

[Erd96] W. Erdmann, *Untersuchung der Photoproduktion von $D^\star$-Mesonen am ep-Speichering HERA*, Dissertation, ETH Zuerich IPP (1996).

[Fie78] R. D. Field und R. P. Feynman, *A parametrization of the properties of quark jets*, Nucl. Phys. **B136** (1978), 1.

[Flu05] G. Flucke, *Photoproduction of $D^\star$ Mesons and $D^\star$ Mesons Associated with Jets at HERA*, Dissertation, University Hamburg (2005).

[Fri95a] S. Frixione, M. L. Mangano, P. Nason und G. Ridolfi, *Total cross-sections for heavy flavor production at HERA*, Phys. Lett. **B348** (1995), 633, hep-ph/9412348.

[Fri95b] S. Frixione, P. Nason und G. Ridolfi, *Differential distributions for heavy flavor production at HERA*, Nucl. Phys. **B454** (1995), 3, hep-ph/9506226.

[Glu92] M. Gluck, E. Reya und A. Vogt, *Photonic parton distributions*, Phys. Rev. **D46** (1992), 1973.

[Gra78] P. Granet et al. (French-Soviet), *Inclusive Production Cross-Sections of Resonances in 32-GeV/c K+ p Interactions*, Nucl. Phys. **B140** (1978), 389.

[Gri72] V. N. Gribov und L. N. Lipatov, *Deep inelastic e p scattering in perturbation theory*, Sov. J. Nucl. Phys. **15** (1972), 438.

[Gro73] D. J. Gross und F. Wilczek, *Ultraviolet Behavior of Non-Abelian Gauge Theories*, Phys. Rev. Lett. **30** (1973), 1343.

[H108] H1 et al., *Study of Charm Fragmentation into $D^{*\pm}$ Mesons in Deep- Inelastic Scattering at HERA* (2008).

[Han03] M. Hansson und H. Jung, *Status of CCFM: Un-integrated gluon densities* (2003), hep-ph/0309009.

[Jun01] H. Jung und G. P. Salam, *Hadronic final state predictions from CCFM: The hadron- level Monte Carlo generator CASCADE*, Eur. Phys. J. **C19** (2001), 351, hep-ph/0012143.

[Jun02] H. Jung, *The CCFM Monte Carlo generator CASCADE*, Comput. Phys. Commun. **143** (2002), 100, hep-ph/0109102.

[Jun04] A. Jung, *Inbetriebnahme der dritten Stufe des schnellen Spurtriggers für das H1 Experiment*, Diplomarbeit, University Dortmund (2004).

[Jun07] A. Jung, *FTT level3 performance*, private comunication (2007).

[Jun08] A. W. Jung, *Measurement of the $D^\star$ meson Cross Section and Extraction of the charm contribution to the Proton Structure in Deep Inelastic ep Scattering with the H1 Detector at HERA*, Dissertation, University Heidelberg (2008).

[Kar78] V. G. Kartvelishvili, A. K. Likhoded und V. A. Petrov, *On the Fragmentation Functions of Heavy Quarks Into Hadrons*, Phys. Lett. **B78** (1978), 615.

[Kar91] V. Karimaki, *Effective circle fitting for particle trajectories*, Nucl. Instrum. Meth. **A305** (1991), 187.

[Kle06] *H1 Alignment Experience*, Proceedings of the Workshop "First LHC Detector Alignment Workshop", CERN(2006) (2006).

[Kle08] C. Kleinwort, *Energy loss measurement with the H1 Central Jet Chamber*, H1-IN-630 (H1 internal Note) (2008).

[Kne08] T. Kneesch, B. A. Kniehl, G. Kramer und I. Schienbein, *Charmed-Meson Fragmentation Functions with Finite-Mass Corrections*, Nucl. Phys. **B799** (2008), 34, 0712.0481.

[Kni05a] B. A. Kniehl, G. Kramer, I. Schienbein und H. Spiesberger, *Collinear subtractions in hadroproduction of heavy quarks*, Eur. Phys. J. **C41** (2005), 199, hep-ph/0502194.

[Kni05b] B. A. Kniehl, G. Kramer, I. Schienbein und H. Spiesberger, *Inclusive D*+- production in p anti-p collisions with massive charm quarks*, Phys. Rev. **D71** (2005), 014018, hep-ph/0410289.

[Kur77] E. A. Kuraev, L. N. Lipatov und V. S. Fadin, *The Pomeranchuk Singularity in Nonabelian Gauge Theories*, Sov. Phys. JETP **45** (1977), 199.

[Köh97] J. K. Köhne et al., *Realization of a second level neural network trigger for the H1 experiment at HERA*, Nucl. Instrum. Meth. **A389** (1997), 128.

[Lai00] H. L. Lai et al. (CTEQ), *Global QCD analysis of parton structure of the nucleon: CTEQ5 parton distributions*, Eur. Phys. J. **C12** (2000), 375, hep-ph/9903282.

[Lev06] S. Levonian, *Status of the offline lumi corrections for e-p HERA2 data*, https://www-h1.desy.de/idet/ilumi/online/levonian/lumi_06_ele.ps.gz (2006).

[Lip75] L. N. Lipatov, *The parton model and perturbation theory*, Sov. J. Nucl. Phys. **20** (1975), 94.

[Mar88] G. Marchesini und B. R. Webber, *Monte Carlo Simulation of General Hard Processes with Coherent QCD Radiation*, Nucl. Phys. **B310** (1988), 461.

[Mar95] G. Marchesini, *QCD coherence in the structure function and associated distributions at small x*, Nucl. Phys. **B445** (1995), 49, hep-ph/9412327.

[MP05] E. S. M. Peez, B. Portheault, *An energy flow algorithm for Hadronic Reconstruction in OO: Hadroo2*, h1-01/05-616 (H1 internal note) (2005).

[Nau03] J. Naumann, *Entwicklung und Test der dritten Triggerstufe*, Dissertation, University Dortmund (2003).

[Nic96] T. Nicholls et al. (H1 SPACAL Group), *Performance of an electromagnetic lead / scintillating fiber calorimeter for the H1 detector*, Nucl. Instrum. Meth. **A374** (1996), 149.

[Pet83] C. Peterson, D. Schlatter, I. Schmitt und P. M. Zerwas, *Scaling Violations in Inclusive e+ e- Annihilation Spectra*, Phys. Rev. **D27** (1983), 105.

[Pit00] D. Pitzl et al., *The H1 silicon vertex detector*, Nucl. Instrum. Meth. **A454** (2000), 334, hep-ex/0002044.

[Pol73] H. D. Politzer, *Reliable Pertubative Results for Strong Interactions?*, Phys. Rev. Lett. **30** (1973), 1346.

[Ric97] H. Rick et al., *Calculating Event Weights in Case of Downscaling on Trigger Levels 1-4*, H1-04/97-517 (H1 internal Note) (1997).

[Sch04] A. Schoning (H1), *A fast track trigger for the H1 collaboration*, Nucl. Instrum. Meth. **A518** (2004), 542.

[Sch08] S. Schmidt, *Lumi Status Report*, Presentation on the H1 Physics Plenary Meeting (2008).

[Sjo94] T. Sjostrand, *High-energy physics event generation with PYTHIA 5.7 and JETSET 7.4*, Comput. Phys. Commun. **82** (1994), 74.

[Spi08a] H. Spiesberger, *$D^\star$ Mesons in Photoproduction at HERA*, New Trends in HERA Physics 2008, Ringberg, Germany (2008).

[Spi08b] H. Spiesberger, *A GMVFNS calculation for $D^\star$ mesons in photoproduction at HERA, private comunication* (2008).

[Str04] I. Strauch, *Jets with high transverse momenta in photoproduction*, Dissertation, University Hamburg (2004).

[Tun02] W.-K. Tung, S. Kretzer und C. Schmidt, *Open heavy flavor production in QCD: Conceptual framework and implementation issues*, J. Phys. **G28** (2002), 983, hep-ph/0110247.

[Urb04] M. Urban, *The new CIP2k z-vertex trigger for the H1 experiment at HERA*, Dissertation, University Zürich (2004).

[Urb05] K. Urban, *Triggerstudien für eine Messung der Protonstrukturfunktion F_2 bei H1*, Diploma Thesis (2005).

[V.B95] V.Boudry et al., *The Inclusive Electron Trigger for the SpaCal: Design and CERN-Test Results (1995)*, h1-03/95-430 (H1 internal note) (1995).

[Ver] W. Verkerke und D. Kirkby, *http://roofit.sourceforge.net*, Internet page.

[vW34] C. F. von Weizsacker, *Radiation emitted in collisions of very fast electrons*, Z. Phys. **88** (1934), 612.

[Wil34] E. J. Williams, *Nature of the high-energy particles of penetrating radiation and status of ionization and radiation formulae*, Phys. Rev. **45** (1934), 729.

[Wis03] C. Wissing, *Entwicklung eines Simulationsprogramms und Implementierung schneller Spurfitalgorithmen für den neuen H1-Driftkammertrigger*, Dissertation, University Dortmund (2003).

[Yao06] W. M. Yao et al. (Particle Data Group), *Review of particle physics*, J. Phys. **G33** (2006), 1.

[ZEU00] ZEUS et al., *Measurement of charm fragmentation function in D^* photoproduction at HERA* (2000).

Danksagung

An dieser Stelle möchte ich mich bei allen Personen bedanken, die diese Doktorarbeit ermöglicht haben.

Meinem Doktorvater Herrn Prof. Dr. Hans-Christian Schultz-Coulon danke ich für die hervorragende Betreuung. Sein andauerndes Vertrauen in diese Arbeit war die Grundvoraussetzung dafür, dass sie gelingen konnte.

Weiterhin möchte ich Herrn Prof. Dr. Ulrich Uwer für die Bereitschaft danken das Zweitgutachten dieser Arbeit zu erstellen.

Am DESY in Hamburg war es vor allen anderen Frau Dr. Katja Krüger, die durch kompetente Betreuung, stete Diskussionsbereitschaft und engagiertes Korrekturlesen maßgeblich an der Durchführung der Analyse und Fertigstellung dieser Arbeit beteiligt war.

Ich danke Herrn Dr. Andre Schöning und Herrn Dr. Benno List dafür, dass sie ihr Wissen mit mir geteilt und mich im richtigen Moment motiviert haben. Besonders Herrn Dr. Andre Schönings Fachkenntnis über das Herzstück dieser Analyse (FTT) war bei der Entstehung dieser Arbeit von großer Hilfe. Außerdem danke ich Herrn Dr. David South und Herrn Dr. Hannes Jung für das Korrekturlesen dieser Dissertation.

Für eine tolle Atmosphäre im Büro haben meine Mitdoktoranden Andreas Jung, Eva Hennekemper und Michael Herbst gesorgt. Vor allem Andreas Jung, der Höhen und Tiefen unserer gemeinsamen Zeit nicht nur als Kollege, sondern als Freund mit mir durchlebt hat, gilt mein herzlicher Dank.

Allen weiteren Mitgliedern der Atlas und ILC Gruppe in Heidelberg danke ich für die stets freundliche Aufnahme. Insbesondere die Grillabende und die spannenden Kickerspiele werden mir immer in guter Erinnerung bleiben.

Mein größter Dank gilt meinen Eltern und Geschwistern. Ohne eure Liebe und Rückhalt wäre all dies nicht möglich gewesen.

Ein liebevoller Dank geht an Nancy. Nancy, du bist das Schöne und die stete Erinnerung daran, was wirklich wichtig ist in meinem Leben.

Diese Arbeit wurde mit Mitteln des Bundesministeriums für Bildung und Forschung unter der Projektnummer 05H16VHB gefördert.